

UNIVERSITY OF KWAZULU-NATAL

Microwave and Millimetre Radio Wave Propagation  
Modelling for Terrestrial Line-of-Sight Links in Central  
Africa.

By

Djuma Sumbiri



June, 2018

Supervisor: Professor Thomas Joachim Odhiambo Afullo

MICROWAVE AND MILLIMETRE RADIO WAVE  
PROPAGATION MODELLING FOR TERRESTRIAL LINE-OF-  
SIGHT LINKS IN CENTRAL AFRICA.

Djuma Sumbiri

In fulfilment of the Degree of Doctor of Philosophy in Electronic Engineering,  
College of Agriculture, Engineering and Science, University of KwaZulu-Natal,  
Durban



June, 2018

Supervisor:

As the candidate's Supervisor, I agree/~~do not agree~~ to the submission of this thesis

Professor T.J. Afullo



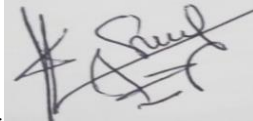
Date: 15th June, 2018

## DECLARATION 1- PLAGIARISM

I, Djuma Sumbiri, with Student Number 214584638, with the thesis entitled “Microwave and Millimetre Radio Wave Propagation Modelling for Terrestrial Line-of-Sight Links in Central Africa,” declare that

1. The research reported in this thesis, except otherwise indicated, is my original research.
2. This thesis has not been submitted for any degree or examination in any other university.
3. This thesis does not contain any other person’s data, pictures, graphs or other information unless specifically acknowledged as being sourced from other persons.
4. This thesis does not contain other persons’ writing, unless specifically acknowledged as being sourced from other researchers. Where other written sources have been quoted, then:
  - a) Their words have been re-written but the general information attributed to them has been referenced,
  - b) Where their exact words have been used, then their writing has been placed in italics and inside quotation marks, and referenced.
5. This thesis does not contain text, graphics or tables copied and pasted from the internet, unless specifically acknowledged, and the source being detailed and in the thesis and in the reference sections.

Signed...



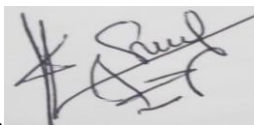
Date: 15th, June 2018

## DECLARATION 2 – PUBLICATIONS

DETAILS OF CONTRIBUTIONS TO PUBLICATIONS that form part and/or include research presented in this thesis (include publications in preparation, submitted, *in press* and published and give details of the contributions of each author to the experimental work and writing of each publication)

- Sumbiri, Djuma, Afullo, T., Alonge, A., “Rainfall Zoning and Rain Attenuation Mapping for Microwave and Millimetric Applications in Central Africa,” (2016) *International Journal on Communications Antenna and Propagation (IRECAP)*, 6 (4), pp. 198-210.
- Djuma. Sumbiri, T. J. O. Afullo and A. Alonge, "Rain attenuation prediction for terrestrial links at microwave and millimeter bands over Rwanda," 2016 *Progress in Electromagnetic Research Symposium (PIERS)*, Shanghai, 2016, pp. 4233-4236.
- Djuma. Sumbiri, T. J. O. Afullo and A. Alonge, “Geoclimatic Factor estimation for Central Africa” *Southern Africa Telecommunication Networks and Applications Conference (SATNAC)* 2016, At Fancourt, George, South Africa.
- Djuma. Sumbiri, T. J. O. Afullo and A. Alonge,” Modelling of Rain Drop Size Distribution for Microwave and Millimeter Wave in Central Africa,” *Progress in Electromagnetic Research Symposium (PIERS)*, 2017 Singapore, 2017, pp. 2398-2404

Signed...

A handwritten signature in black ink, appearing to be 'T. J. O. Afullo', written over a light grey rectangular background.

## Acknowledgements

Above all, my sincere appreciation goes to the Almighty God for granting me the gift of life and good health for the completion of this work. Secondly, my profound gratitude and appreciation goes to my supervisor, Professor Thomas J. Afullo for his guidance, suggestions and criticisms during the undertaking of this research.

I would also like to thank all staff members in the School of Electrical, Electronics and Computer Engineering, University of KwaZulu-Natal, South Africa, for their contribution in the success of this research work. A big thank you to Dr. Akintunde Alonge and Dr. Mosalaosi Modisa for their constructive suggestions; and to Mr. Khaye Dlamini and Mr. Sphamandla Nqanyi, the school administrator, for their great assistance.

To my postgraduate colleagues and friends, a big thank you – especially Dr. Feyisa Debo Diba, Dr. Efe Orumwense, Dr. Mike Asiyo, Mr. Afolayan Babajide, Mr. Steven Awino, Mr. Ayele Legesse, Mr. Wehib Abubeker, Mr. Olabamidele Kolawole, Mr. Edwin Kataka, Mr. Oyedeji Okikioluwa, Mr. Thabelang Sefako, Mr. Daudi Ayanda, Mr. Babatunde Adejumobi and Mr. Nicholas Oyie. I also acknowledge the support of Mr. Mathew Habyarimana and Mr. Jean Damascene Munyeshyaka.

I will be forever grateful to my wife, Mukayiranga Epiphany Merriam and my son Sumbiri Kayenzi Naim for their moral support and boundless understanding that greatly assisted me escape the study-related stress during my study period in Durban.

## Dedication

*This thesis is dedicated to my mother Nyiragasigwa Therese, my late father Semunkima Shabani Ibrahim Birara, my step mother, Kankindi Theresia Ashura, my brother Kayenzi Jean Nepomuscene Abdoul Karim, my sisters Zainab and Furaha Nakure Clementine, my wife, Mukayiranga Epiphany Merriam and my son Sumbiri Kayenzi Naim.*

*I would not be who I am today without their genuine prayer, love and support.*

*To God be the Glory.*

## Abstract

The rapid expansion of the global telecommunication has led to an exponential growth in the demand of wireless services. This has led to the migration to higher frequency bands in the microwave and millimeter wave spectrum. Research has shown that rainfall is the most dominant factor affecting the provision of network services in these bands. Rainfall attenuation is among the major factors often considered in the design of wireless networks operating at higher bands within microwave and millimeter wave spectrum. At tropical and equatorial locations, not only is the occurrence frequency of rainfall events of serious concern to terrestrial and satellite communication systems, but also the high intensity of rain rates and drop size distribution result in extreme fading of **line of sight (LOS)** system during such events.

In this work, daily rainfall measurements from the Rwanda Meteorology Agency (Meteo Rwanda) are obtained for 60 locations within equatorial Rwanda (between latitudes of 1°2'S and 2°45'S and longitudes of 28°45'E and 30°52'E), in Central Africa, to develop rain rate and rain attenuation maps for wireless radio links. From these long term annual rainfall measurements spanning a minimum of 10 years at these locations, rainfall rate statistics estimated from appropriate models are applied to determine fade margin for radio link availabilities between 99% and 99.999%. Furthermore, specific attenuation estimates due to rainfall are proposed from International Telecommunication Union (ITU) recommendations at selected frequencies of the microwave and millimeter bands, for the design of wireless networks. Results obtained from this approach incorporating both rainfall rate zones and specific attenuation over Rwanda are presented as spatial contour maps representations for different ranges of link availability.

Further, disdrometer data collected in Butare, Rwanda (2°35' 53.88" S and 29°44' 31.5" E) for a period of 32 months between 2012 and 2015 have been use to develop a suitable model on drop size distribution in the region. Rainfall data was classified into four different regimes, namely, drizzle, widespread, shower and thunderstorm. Different raindrop size distribution (DSD) models such as Lognormal, Gamma, Marshall-Palmer and Weibull distributions are selected and the method of moment technique is applied for estimating input DSD fit-parameters for those DSD models. From the results, it is observed that different models have varying performances as the rainfall regime varies from drizzle to widespread, shower and later as thunderstorm, except the Marshall- Palmer model which shows the inadequacy for the region. It is found that neither the Lognormal nor other models match perfectly wel

l with the measured DSD, particularly at high rainfall rates. Therefore, a new rainfall DSD model for Central Africa is developed and found to be an improvement over the existing models. The



Mie Scattering technique (spherical method) is employed to derive the scattering parameters. Therefore, the derived scattering parameters with DSD models are used for the estimation of rainfall attenuation in the region of Central Africa. Finally, the synthetic storm techniques (SST) is applied for comparison with other rainfall attenuation models.

# Table of Contents

DECLARATION 1- PLAGIARISM.....	iii
DECLARATION 2 – PUBLICATIONS .....	iv
Acknowledgements .....	v
Dedication .....	vi
<b>Abstract</b> .....	vii
<b>Chapter One</b> .....	1
<b>General Introduction</b> .....	1
1.1 Introduction.....	1
1.2 Research Motivation .....	2
1.3 Objectives of Research.....	3
1.4 Dissertation Overview.....	3
1.5 Contribution to knowledge.....	4
<b>Chapter Two</b> .....	5
<b>Literature Review</b> .....	5
2.1 Introduction.....	5
2.2 The Atmosphere.....	5
2.3 Tropospheric Effects .....	7
2.4 Clear-Air Radio Climatic Effect on Line of Sight (LOS) Links. ....	7
2.4.1 Clear-Air Multipath Fading Prediction .....	7
2.4.1.1 Overview of the Geo-climatic factor.....	8
2.4.1.2 Work Reported for Sub-Saharan Africa.....	10
2.4.2 Diffraction Fading.....	15
2.5 Fading due to Precipitation .....	21
2.5.1 Rainfall Types .....	21
2.6 Rainfall Rate Distribution Models .....	21
2.6.1 The ITU-R Rainfall Rate prediction Model .....	22
2.6.2 The Global Crane Rainfall Rate Prediction Model .....	23
2.7. Rain Drop Size Distribution Models.....	24

2.7.1 Lognormal Rainfall Drop Size Distribution Model .....	25
2.7.2 Modified Gamma Rainfall Drop Size Distribution Model.....	26
2.7.3 Negative Exponential Drop Size Distribution Model .....	28
2.7.4. Weibull Rainfall Drop Size Distribution Model. ....	29
2.8 Rainfall Specific Attenuation.....	29
2.9 Chapter Summary and Conclusion.....	30
<b>Chapter Three</b> .....	<b>31</b>
<b>Rainfall Zoning and Rain Attenuation Mapping for Microwave and Millimetric Applications in Central Africa</b> .....	<b>31</b>
3.1 Introduction.....	31
3.2 Climatic characteristics of Rwanda and rainfall rate models .....	31
3.2.1 Rwanda climatic features .....	31
3.2.2 Rainfall rate distribution modelling .....	33
3.3 Determination of rainfall rate statistics over Rwanda.....	35
3.3.1 Local Rainfall Measurements at Locations in Rwanda.....	35
3.3.2 Rainfall Rate Distribution over Rwanda .....	37
3.3.3 Rain Rate Contour Mapping over Rwanda .....	42
3.4 Rainfall Specific Attenuation.....	44
3.4.1 Rainfall Specific Attenuation Statistics over Rwanda for Ku and Ka Bands.....	44
3.4.2 Specific Attenuation Contour Mapping for Rwanda at 15 GHz and 27 GHz.....	45
3.5 Conclusion Chapter Summary and Conclusion .....	54
<b>Chapter Four</b> .....	<b>55</b>
<b>Comparison of Rainfall Drop-Size Distribution Models for Microwave and Millimetric radio propagation in Butare</b> .....	<b>55</b>
4.1 Introduction.....	55
4.2 Data measurements and processing .....	55
4.3 Rainfall Rate Analysis for Butare .....	58
4.3.1 Monthly Distribution of Rainfall Rate. ....	58
4.3.2 Seasonal Distribution of Rainfall Rate.....	59
4.3.3 Regime Distribution of Rainfall Rate.....	61

4.3.4 Annual Distribution of Rainfall Rate. ....	62
4.4 Rainfall Drop Size Distribution Modelling Using Existing Models for Butare, Rwanda. 62	
4.4.1 Drop Size Distribution Models with the Method of Moments Estimation Technique63	
4.4.1.1 Lognormal Rainfall Drop Size Distribution Moments Estimation.....	64
4.4.1.2 Modified Gamma Rainfall Drop Size Distribution Moments Estimation.....	65
4.4.1.3 Negative Exponential Drop Size Distribution Moments Estimation. ....	66
4.4.1.4 Weibull Rainfall Drop Size Distribution Moments Estimation. ....	67
4.5 Variability of Drop Size Distribution Modelling for Butare, Rwanda.....	67
4.6 Chapter Summary and Conclusion.....	73
<b>Chapter Five</b> .....	74
<b>Proposed Rain Drop Size Distribution Model for Microwave and Millimeter Wave in Central Africa</b> .....	74
5.1 Introduction.....	74
5.2 Development of a New Rainfall Drop Size Distribution Model for Rwanda. ....	74
5.3 Method of Maximum Likelihood Estimation Technique.....	76
5.4 Measurement and Data Processing .....	80
5.5 Comparison of the new proposed DSD model with other DSD models in Butare, Rwanda. ....	81
5.5.1 Regime Variation of Rainfall Drop Size Distribution.....	81
5.5.2 Annual Variation of Rainfall Drop Size Distribution. ....	85
5.5.3 Seasonal Variation of Rainfall Drop Size Distribution. ....	87
5.6 Chapter Summary and Conclusion.....	97
<b>Chapter Six</b> .....	98
<b>Specific Rainfall Attenuation Patterns over Butare, Rwanda</b> .....	98
6.1 Introduction.....	98
6.2 Specific Rain Attenuation over Butare. ....	98
6.2.1 Seasonal Variation of Specific Attenuation. ....	102
6.2.2 Regime Variation of Specific Attenuation. ....	105
6.3 Specific Attenuation Constants .....	108
6.4 Attenuation Prediction Models .....	110

6.4.1 ITU-R Rain Attenuation Model .....	110
6.4.2 Synthetic Storm Techniques Rain Attenuation Model.....	111
6.4.3 Lognormal Rain Attenuation Model .....	112
6.4.4 Modified Gamma Rain Attenuation Model .....	113
6.4.5 Negative Exponential Rain Attenuation Model .....	114
6.4.6 Weibull Rain Attenuation Model.....	114
6.4.7 Proposed Rain Attenuation Model.....	115
6.5 Calculation of rain attenuation statistics .....	116
6.6 Chapter Summary and Conclusion.....	160
<b>Chapter Seven</b> .....	162
<b>Conclusions and Recommendations</b> .....	162
7.1 Introduction.....	162
7.2. Chapter Three: Rainfall zoning and rain attenuation mapping for microwave and millimetric applications in Central Africa.....	162
7.3 Chapter Four: Comparison of Rainfall Drop-Size Distribution Models for Microwave and Millimetric radio propagation in Butare. ....	162
7.4 Chapter Five: Proposed Rain Drop Size Distribution Model for Microwave and Millimeter Wave in Central Africa .....	163
7.5 Chapter Six: Specific Rainfall Attenuation patterns over Butare, Rwanda .....	163
7.6 Recommendations for Future Work.....	163
References.....	164
Appendices.....	174

## List of Figures

- Figure 2-1: Layers of Earth's atmosphere [37]
- Figure 2-2: Map of Tanzania, Rwanda, Burundi
- Figure 2-3: Average monthly variation of refractivity in Bukoba, Mwanza, Kigoma, and Musoma
- Figure 2-4: Point refractivity gradient for Bukoba, Mwanza, Kigoma and Musoma
- Figure 2-5: Geo-climatic factor (K) variation for Bukoba, Mwanza, Kigoma and Musoma
- Figure 2-6: Comparison of Kernel estimates of k-factor for Rwanda.
- Figure 2-7: Comparison of Kernel estimates of k-factor for North-West Tanzania
- Figure 2-8: Prediction map of k-factor spatial distribution, ordinary kriging, 0-100 m a.g.l. [53]
- Figure 2-9: Prediction map of k-factor spatial distribution, ordinary kriging, 0-200 m a.g.l. [53]
- Figure 2-10: World ITU-R rainfall rate map [12]
- Figure 2-11: Global Crane rainfall climatic zone [21]
- Figure 3-1: The geographical map of Rwanda, Central Africa.
- Figure 3-2: Rwanda rain accumulation contour map
- Figure 3-3: Cumulative distribution of rainfall rate for Southern Province, Rwanda using Moupfouma model.
- Figure 3-4: Cumulative distribution of rainfall rate for Northern Province, Rwanda using Moupfouma model
- Figure 3-5: Cumulative distribution of rainfall rate for Western Province, Rwanda using Moupfouma model.
- Figure 3-6: Cumulative distribution of rainfall rate for Eastern Province and Kigali City, Rwanda using Moupfouma model.
- Figure 3-7: Rainfall Rate (mm/h) contour maps for 0.1% of time in Rwanda
- Figure 3-8: Rainfall Rate (mm/h) contour maps for 0.01% of time in Rwanda
- Figure 3-9: Frequency characteristics of specific rain attenuation signal for South Province, Rwanda (a) vertical polarization (b) horizontal polarization.
- Figure 3-10: Frequency characteristics of specific rain attenuation signal for North Province, Rwanda (a) vertical polarization (b) horizontal polarization.
- Figure 3-11: Frequency characteristics of specific rain attenuation signal for West Province, Rwanda (a) vertical polarization (b) horizontal polarization.
- Figure 3-12: Frequency characteristics of specific rain attenuation signal for Eastern Province and Kigali City, Rwanda (a) vertical polarization (b) horizontal polarization.
- Figure 3-13. Rain specific attenuation contour map for link at 15 GHz frequency for link availability of 0.01% in Rwanda (a) Vertical polarization (b) Horizontal polarization

Figure 3-14. Rain specific attenuation contour map for link at 27 GHz frequency for link availability of 0.01% in Rwanda (a) Vertical polarization (b) Horizontal polarization

Figure 4-1a: Joss-Waldvogel RD-80 impact disdrometer system connected to a personal computer [104].

Figure 4-1b: Block diagram of the Joss-Waldvogel RD-80 Distrometer [104]

Figure 4-2: Monthly cumulative distribution of rainfall rate in Butare, Rwanda between 2012 and 2014-2015.

Figure 4-3: Seasonal cumulative distribution of Rainfall rate in Butare, Rwanda between 2012 and 2015

Figure 4.4: Regime Cumulative Distribution of Rainfall rate in Butare, Rwanda between 2012 and 2015.

Figure 4-5: Annual cumulative distribution of rainfall rate in Butare, Rwanda between 2012 and 2015.

Figure 4-6: Different DSD models for Butare, Rwanda ( $R = 1.53$  mm/h)

Figure 4-7: Different DSD models for Butare, Rwanda ( $R = 4.95$  mm/h)

Figure 4.8: Different DSD models for Butare, Rwanda ( $R = 9.54$  mm/h)

Figure 4-9: Different DSD models for Butare, Rwanda ( $R = 26.86$  mm/h)

Figure 4-10: Different DSD models for Butare, Rwanda ( $R = 60.08$  mm/h)

Figure 4-11: Different DSD models for Butare, Rwanda ( $R = 118.5$  mm/h)

Figure 5-1: Rain size distribution in Butare, Rwanda based on rainfall regimes. (a) Drizzle at 4.95 mm/h (b) Widespread at 9.9 mm/h (c) Shower at 27.7 mm/h (d) Thunderstorm at 75.28 mm/h.

Figure 5-2: .Annual Rain drop size distribution in Butare, Rwanda (a) Drizzle at 4.97 mm/h (b) Widespread at 9.9 mm/h (c) Shower at 25.55 mm/h (d) Thunderstorm at 60.08 mm/h.

Figure 5-3: Seasonal rainfall DSDs for drizzle rains in Butare, Rwanda. (a) Short dry season at 3.91 mm/h (b) Long rainy season at 3.88 mm/h (c) Long dry season at 3.92 mm/h (d) Short rainy season at 3.88 mm/h.

Figure 5-4: Seasonal rainfall DSDs for widespread rains in Butare, Rwanda. (a) Short dry season at 9.93 mm/h (b) Long rainy season at 9.99 mm/h (c) Long dry season at 9.97 mm/h (d) Short rainy season at 9.94 mm/h.

Figure 5-5: Seasonal rainfall DSDs for Shower rains in Butare, Rwanda. (a) Short dry season at 38.7 mm/h (b) Long rainy season at 38.73 mm/h (c) Long dry season at 37.44 mm/h (d) Short rainy season at 38.58 mm/h.

Figure 5-6: Seasonal rainfall DSDs for Thunderstorm rains in Butare, Rwanda. (a) Short dry season at  $R_{0.01}=89$  mm/h (b) Long rainy season at  $R_{0.01}=94$  mm/h (c) Long dry season at  $R_{0.01}=70$  mm/h (d) Short rainy season at  $R_{0.01}=114$  mm/h.

Figure 6-1: Specific rain attenuation estimation in Short dry season in Butare, Rwanda for  $R_{0.01}=89.26$  mm/h

Figure 6-2: Specific rain attenuation estimation in Long rain season in Butare, Rwanda for  $R_{0.01}=97.82$  mm/h

Figure 6-3: Specific rain attenuation estimation in Long dry season in Butare, Rwanda for  $R_{0.01}=70.8$  mm/h

Figure 6-4: Specific rain attenuation estimation in Short rain season in Butare, Rwanda for  $R_{0.01}=114.01$  mm/h

Figure 6-5: Comparison of Specific rain attenuation for various models in Butare, Rwanda for drizzle rainfall regime at 4.9 mm/h.

Figure 6-6: Comparison of Specific rain attenuation for various models in Butare, Rwanda for widespread rainfall regime at 9.9 mm/h.

Figure 6-7: Comparison of Specific rain attenuation for various models in Butare, Rwanda for shower rainfall regime at 39.1 mm/h.

Figure 6-8: Comparison of Specific rain attenuation for various models in Butare, Rwanda for thunderstorm rainfall regime at 96.02 mm/h.

Figure 6-9: Variation of coefficient  $k$  with frequency over Butare, Rwanda at 20°C

Figure 6-10: Variation of coefficient  $\alpha$  with frequency over Butare, Rwanda at 20°C

Figure 6-11: Rain rate time series measurements during the rain event of 06/12/2013 in Butare, Rwanda

Figure 6-12: Rain rate time series measurements during the rain event of 01/10/2014 in Butare, Rwanda

Figure 6-13: Rain rate time series measurements during the rain event of 18/05/2015 in Butare, Rwanda

Figure 6-14: Rain rate and rain attenuation time series converted by: (a) SST (b) various models for a measured rainy event on 06/12/2013 at frequency  $f=8$  GHz and path length  $L=1$  km

Figure 6-15: Rain rate and rain attenuation time series converted by: (a) SST (b) various models for a measured rainy event on 06/12/2013 at frequency  $f=8$  GHz and path length  $L=5$  km

Figure 6-16: Rain rate and rain attenuation time series converted by: (a) SST (b) various models for a measured rainy event on 06/12/2013 at frequency  $f=8$  GHz and path length  $L=8$  km

Figure 6-17: Rain rate and rain attenuation time series converted by: (a) SST (b) various models for a measured rainy event on 06/12/2013 at frequency  $f=12$  GHz and path length  $L=2$  km

Figure 6-18: Rain rate and rain attenuation time series converted by: (a) SST (b) various models for a measured rainy event on 06/12/2013 at frequency  $f=12$  GHz and path length  $L=5$  km

Figure 6-19: Rain rate and rain attenuation time series converted by: (a) SST (b) various models for a measured rainy event on 06/12/2013 at frequency  $f=12$  GHz and path length  $L=8$  km

Figure 6-20: Rain rate and rain attenuation time series converted by: (a) SST (b) various models for a measured rainy event on 06/12/2013 at frequency  $f=19$  GHz and path length  $L=2$  km



Figure 6-21: Rain rate and rain attenuation time series converted by: (a) SST (b) various models for a measured rainy event on 06/12/2013 at frequency  $f=19$  GHz and path length  $L=5$  km

Figure 6-22: Rain rate and rain attenuation time series converted by: (a) SST (b) various models for a measured rainy event on 06/12/2013 at frequency  $f=19$  GHz and path length  $L=8$  km

Figure 6-23: Rain rate and rain attenuation time series converted by: (a) SST (b) various models for a measured rainy event on 01/10/2014 at frequency  $f=8$  GHz and path length  $L=1$  km

Figure 6-24: Rain rate and rain attenuation time series converted by: (a) SST (b) various models for a measured rainy event on 01/10/2014 at frequency  $f=8$  GHz and path length  $L=5$  km

Figure 6-25: Rain rate and rain attenuation time series converted by: (a) SST (b) various models for a measured rainy event on 01/10/2014 at frequency  $f=8$  GHz and path length  $L=8$  km

Figure 6-26: Rain rate and rain attenuation time series converted by: (a) SST (b) various models for a measured rainy event on 01/10/2014 at frequency  $f=12$  GHz and path length  $L=2$  km

Figure 6-27: Rain rate and rain attenuation time series converted by: (a) SST (b) various models for a measured rainy event on 01/10/2014 at frequency  $f=12$  GHz and path length  $L=5$  km

Figure 6-28: Rain rate and rain attenuation time series converted by: (a) SST (b) various models for a measured rainy event on 01/10/2014 at frequency  $f=12$  GHz and path length  $L=8$  km

Figure 6-29: Rain rate and rain attenuation time series converted by: (a) SST (b) various models for a measured rainy event on 01/10/2014 at frequency  $f=19$  GHz and path length  $L=2$  km

Figure 6-30: Rain rate and rain attenuation time series converted by: (a) SST (b) various models for a measured rainy event on 01/10/2014 at frequency  $f=19$  GHz and path length  $L=5$  km

Figure 6-31: Rain rate and rain attenuation time series converted by: (a) SST (b) various models for a measured rainy event on 01/10/2014 at frequency  $f=19$  GHz and path length  $L=8$  km

Figure 6-32: Rain rate and rain attenuation time series converted by: (a) SST (b) various models for a measured rainy event on 18/05/2015 at frequency  $f=8$  GHz and path length  $L=1$  km

Figure 6-33: Rain rate and rain attenuation time series converted by: (a) SST (b) various models for a measured rainy event on 18/05/2015 at frequency  $f=8$  GHz and path length  $L=5$  km

Figure 6-34: Rain rate and rain attenuation time series converted by: (a) SST (b) various models for a measured rainy event on 18/05/2015 at frequency  $f=8$  GHz and path length  $L=8$  km

Figure 6-35: Rain rate and rain attenuation time series converted by: (a) SST (b) various models for a measured rainy event on 18/05/2015 at frequency  $f=19$  GHz and path length  $L=2$  km

Figure 6-36: Rain rate and rain attenuation time series converted by: (a) SST (b) various models for a measured rainy event on 18/05/2015 at frequency  $f=19$  GHz and path length  $L=5$  km

Figure 6-37: Rain rate and rain attenuation time series converted by: (a) SST (b) various models for a measured rainy event on 18/05/2015 at frequency  $f=19$  GHz and path length  $L=8$  km

Figure 6-38: Annual rainfall rate distribution in Butare, Rwanda in 2012, 2014 and 2015

Figure 6-39: Comparison between synthesized rain attenuation converted by SST and other rain attenuation models at frequency  $f=8$  GHz and path length  $L=1$  km over Butare, Rwanda in 2012.

Figure 6-40: Comparison between synthesized rain attenuation converted by SST and other rain attenuation models at frequency  $f=8$  GHz and path length  $L=5$  km over Butare, Rwanda in 2012.

Figure 6-41: Comparison between synthesized rain attenuation converted by SST and other rain attenuation models at frequency  $f=8$  GHz and path length  $L=8$  km over Butare, Rwanda in 2012.

Figure 6-42: Comparison between synthesized rain attenuation converted by SST and other rain attenuation models at frequency  $f=19$  GHz and path length  $L=2$  km over Butare, Rwanda in 2012.

Figure 6-43: Comparison between synthesized rain attenuation converted by SST and other rain attenuation models at frequency  $f=19$  GHz and path length  $L=5$  km over Butare, Rwanda in 2012.

Figure 6-44: Comparison between synthesized rain attenuation converted by SST and other rain attenuation models at frequency  $f=19$  GHz and path length  $L=8$  km over Butare, Rwanda in 2012.

Figure 6-45: Comparison between synthesized rain attenuation converted by SST and other rain attenuation models at frequency  $f=8$  GHz and path length  $L=1$  km over Butare, Rwanda in 2014.

Figure 6-46: Comparison between synthesized rain attenuation converted by SST and other rain attenuation models at frequency  $f=8$  GHz and path length  $L=5$  km over Butare, Rwanda in 2014.

Figure 6-47: Comparison between synthesized rain attenuation converted by SST and other rain attenuation models at frequency  $f=8$  GHz and path length  $L=8$  km over Butare, Rwanda in 2014.

Figure 6-48: Comparison between synthesized rain attenuation converted by SST and other rain attenuation models at frequency  $f=19$  GHz and path length  $L=2$  km over Butare, Rwanda in 2014.

Figure 6-49: Comparison between synthesized rain attenuation converted by SST and other rain attenuation models at frequency  $f=19$  GHz and path length  $L=5$  km over Butare, Rwanda in 2014.

Figure 6-50: Comparison between synthesized rain attenuation converted by SST and other rain attenuation models at frequency  $f=19$  GHz and path length  $L=8$  km over Butare, Rwanda in 2014.

Figure 6-51: Comparison between synthesized rain attenuation converted by SST (a) and other rain attenuation models (b) at frequency  $f=8$  GHz and path length  $L=1$  km over Butare, Rwanda in 2015.

Figure 6-52: Comparison between synthesized rain attenuation converted by SST and other rain attenuation models at frequency  $f=8$  GHz and path length  $L=5$  km over Butare, Rwanda in 2015.

Figure 6-53: Comparison between synthesized rain attenuation converted by SST and other rain attenuation models at frequency  $f=8$  GHz and path length  $L=8$  km over Butare, Rwanda in 2015.

Figure 6-54: Comparison between synthesized rain attenuation converted by SST and other rain attenuation models at frequency  $f=19$  GHz and path length  $L=2$  km over Butare, Rwanda in 2015.

Figure 6-55: Comparison between synthesized rain attenuation converted by SST (a) and other rain attenuation models (b) at frequency  $f=19$  GHz and path length  $L=5$  km over Butare, Rwanda in 2015.

Figure 6-56: Comparison between synthesized rain attenuation converted by SST and other rain attenuation models at frequency  $f=19$  GHz and path length  $L=8$  km over Butare, Rwanda in 2015.

## List of Tables

- Table 1-1: Standard microwave and millimetre wave bands
- Table 2-1: Geo-climatic factor (K) for different months for Bukoba, Mwanza, Kigoma and Musoma
- Table 2-2: Geo-climatic factor (K) for different months for Durban, Cape Town, Pretoria, Bloemfontein and Polokwane in South Africa [48]
- Table 2-3: Common values of k-factor and refractivity gradient [49]
- Table 2-4: Values of mean k-factor and ISE for kernel estimates, 0-100m a.g.l. [53]
- Table 2-5: Values of mean k-factor and ISE for kernel estimates, 0-200m a.g.l. [68]
- Table 2-6: ITU-R Rain rate climatic zones [12]
- Table 2-7: The Global Crane Rain Rate Model [21]
- Table 2-8: Lognormal DSD parameters for tropical rains by Ajay and Olsen in 1985 [24].
- Table 2-9: Lognormal DSD parameters for different rainfall types by Ajayi and Adimula in 1996 [79]
- Table 2-10: Estimated parameter of Lognormal Model in Durban using MoM technique [25]
- Table 2-11: Estimated parameter of Lognormal Model in Durban using MLE technique [25]
- Table 2-12: Seasonal Model parameters for different rainfall DSD models in Durban, South Africa [80]
- Table 2-13: Negative exponential parameters for different rainfall types [86]
- Table 3-1a: Climatic characteristics of measurement Sites for Southern Province, Rwanda
- Table 3-1b: Climatic characteristics of measurement Sites for Northern Province, Rwanda
- Table 3-1c: Climatic characteristics of measurement Sites for Western Province, Rwanda
- Table 3-1d: Climatic characteristics of measurement Sites for Eastern Province and Kigali city, Rwanda
- Table 3-2a: Rain rate exceeded at 0.01 (R0.01) for different locations in Southern Province, Rwanda from Chebil Model
- Table 3-2b: Rain rate exceeded at 0.01 (R0.01) for different locations in Northern Province, Rwanda from Chebil Model
- Table 3-2c: Rain rate exceeded at 0.01 (R0.01) for different locations in Western Province, Rwanda from Chebil Model
- Table 3-2d: Rain rate exceeded at 0.01 (R0.01) for different locations in Eastern Province and Kigali City, Rwanda from Chebil Model
- Table 3-3: Estimated specific attenuation at R0.01 for Ka and Ku bands for different locations over Rwanda

Table 4-1: Statistical summary of the RD-80 disdrometer for Butare, Rwanda between 2012 and 2015.

Table 4-2: Monthly statistics on rainfall rate exceeded (mm/h) in Butare, Rwanda

Table 4-3. Seasonal statistics on rainfall rate exceeded (mm/h) in Butare, Rwanda

Table 4.4. Rainfall regime statistics on rainfall rate exceeded (mm/h) in Butare- Rwanda

Table 4-5. Model parameters for different rainfall DSD statistical models based on annual rainfall analysis in Butare, Rwanda

Table 4-6. Model parameters for different rainfall DSD statistical models analysis in Butare, Rwanda based on rainfall regimes.

Table 5-1. Rainfall DSD measurements over Butare, Rwanda between 2012 and 2015

Table 5.2. Model parameters for the new proposed DSD statistical model analysis in Butare, Rwanda based on rainfall regimes

Table 5-3. Error estimation from different rainfall DSD models for Butare based on rainfall regimes.

Table 5-4. Error estimation from different annual rainfall DSD models in Butare.

Table 5-5: Model parameters for different rainfall DSD statistical models for Short dry season analysis in Butare, Rwanda

Table 5-6: Model parameters for different rainfall DSD statistical models for Long rainy season analysis in Butare, Rwanda

Table 5-7: Model parameters for different rainfall DSD statistical models for long dry season analysis in Butare, Rwanda

Table 5-8: Model parameters for different rainfall DSD statistical models for Short rainy season analysis in Butare, Rwanda

Table 5-9: Error estimation from different seasonal rainfall DSD models in Butare, Rwanda. (a) Short dry and Long rainy season. (b) Long dry and Short rainy season.

Table 6-1: Extinction cross section power-law coefficients at 20oC using Mie scattering technique

Table 6-2: Regression coefficients  $k$  and  $\alpha$  for various models for Butare, Rwanda at 20°C

Table B-1: ITU-R Parameters ( $k$  and  $\alpha$ ) for rainfall specific Attenuation Estimation [91]

Table C-1 Estimated specific attenuation at R0.01 for Ka and Ku bands for all the 60 locations over Rwanda

## List of Abbreviations

CDF	Cumulative Distribution Function
CHI	Chi Square Error technique
D-D	Dutton and Dougherty Model
D-S	Douglas and Sims Model
DSD	Drop Size Distribution
ECS	Extinction Cross Section
GIS	Geographic Information System
ISE	Integral Square Error
ITU-R	International Telecommunication Union – Radio communication Sector
JW	Joss-Waldvogel
LGN	Lognormal Model
LOS	Line-of-Sight
MoM	Method of Moments
MLE	Maximum Likelihood Estimation
MGM	Modified Gamma Model
M-P	Marshal-Palmer Model
PDF	Probability Density Function
QoS	Quality of Service
RMSE	Root Mean Square Error
R-H	Rice and Holmberg model
SST	Synthetic Storm Technique
SHF	Super High Frequency
SAWS	South African Weather Service
WBL	Weibull Model
UHF	Ultra High Frequency
VHF	Very High Frequency

# Chapter One

## General Introduction

### 1.1 Introduction

Frequency bands within the microwave and millimeter spectra are increasingly becoming important to service providers and system designers because of their larger data-carrying capacity required to match the expectations of end-users of wireless communication systems. These bands are projected to provide larger bandwidths, which is necessary for enhanced network performances, especially in areas of high-speed data transmission and video diffusion [1], [2]. However, various environmental design factors such as rainfall, atmospheric gas, and diffraction fading due to multipath affect wave propagation, leading to signal fading in microwave and millimeter bands [3-6]. Among these factors, rainfall is one of the major causes of signal attenuation and network outages at these bands [7-12]. The presence of rainfall globally results in attenuation of transmitted signals at these bands, although the scale of causality is highly dependent on climatic characteristics and geographical features. Depending on the climate of the considered region, there exists a frequency threshold above which the rain attenuation becomes the most important parameter degrading the performance of signal transmission between line-of-sight (LOS) microwave links [13]. In temperate climates, signal impairments due to rainfall become noticeable from 10 GHz; while at tropical and equatorial climates, this occurs from about 7 GHz because of the influence of large raindrops [13], [14]. Based on the foregoing, it is therefore important to include the effect of rain attenuation on wave propagation over LOS radio links, to guarantee a satisfactory level of network performance [15]-[19]. **Table 1-1 shows the standard microwave and millimeter wave bands.**

To mitigate the effects of rain attenuation while improving link performance, system designers often adopt standards of the International Telecommunication Union (ITU) embedded in different recommendation series [3]. For example, the ITU-R P.837 is well known for its global mapping of rainfall rate distribution curves from different regions into 15 climatic zones [20]. However, some studies have found these recommendations as unsuitable for radio planning in tropical regions, whereas a great degree of agreement has been found for temperate regions [21]. For example, it has been shown that the Indian sub-continent consists of 12 climatic zones against two proposed by ITU-R [22]. Further examples include Brazil with 11 zones compared to ITU-R's two zones [22], China with 12 climatic zones instead of five, and finally, South Africa with 8 zones instead of ITU-R's five zones [13].

Table 1-1: Standard microwave and millimetre wave bands [23]

Frequency Band	Frequency range	Wavelength	Mode of propagation
L band	1-2 GHz	15 cm-30 cm	Strictly LOS. They are space waves.
S band	2-4 GHz	7.5 cm-15 cm	
C band	4-8 GHz	3.75 cm-7.5 cm	Strictly LOS. Microwaves (3GHz-30 GHz) and Millimeter waves (30 GHz-300 GHz)
X band	8-12 GHz	25 mm-37.5 cm	
Ku band	12-18 GHz	16.7 mm-25 mm	
K band	18-26.5 GHz	11.3 mm-16.7 mm	
Ka band	26.5-40 GHz	5.0 mm-11.3 mm	
Q band	33-50 GHz	6.0 mm-9.0 mm	
U band	40-60 GHz	5.0 mm -7.5 mm	

In the current work, the focus is on Butare, Rwanda, located in the Central African region, which is characterized by equatorial climatic features. Based on ITU-R P.837-1, rainfall patterns in Central Africa are classified into four climatic zones namely: Q, P, N and K. Further investigation based on the current ITU-R P.837-6 publication suggests that rain rate exceedence at 0.01% ( $R_{0.01}$ ) over Rwanda, falls between 60 to 70mm/h [12]. This falls short of recent investigations at the same location where  $R_{0.01}$  is found to be much greater than 70 mm/h [24] suggesting that estimates from ITU-R P.837-6 recommendations may result in gross under-estimation of rainfall fading statistics in this region. Based on this observation, it is obvious that there is a great need to harness the knowledge of local rainfall measurements at equatorial Rwanda. Unfortunately, as observed in many African locations, there is paucity of proper research highlighting rainfall campaigns and rainfall attenuation studies in this region. As Rwanda is rapidly experiencing massive growth in the wireless communication industry, with future plans for space and satellite communication industries, it is important that an assessment of rainfall attenuation be undertaken at this equatorial country.

In this study, point rainfall measurements spanning a minimum of 10 years are obtained from the Rwanda Meteorology Agency databank for 60 different locations in Rwanda. Results from the rainfall data analysis are subsequently applied in the mapping of rainfall rate and rain attenuation statistics required for link budget purposes in terrestrial and satellite communication systems in Rwanda. Using four years of disdrometer data collected in Butare, Rwanda, the study focuses on determining and modelling the regional raindrop size distribution, as well as the corresponding rainfall attenuation in the Central African region.

## 1.2 Research Motivation

In radio propagation, modelling of rainfall rate, rain attenuation and drop size distribution is highly location-dependent and thus requires availability of reliable data from various locations. Models and mathematical predictions obtained based on data from one location often prove

inadequate when applied to another location with either slightly or radically different rainfall pattern.

The problem of data availability for location-specific modelling has been tackled with good results in various regions of the world. The earliest of such models were based on data from temperate regions [25]. Other regions such as the subtropical regions of Southern Africa [26, 27], the tropical regions of West Africa [28] and Ethiopia [29] have also amassed extensive data and have developed and tested fitting models based on their data.

The primary motivation of the present work is to develop a reliable database of rainfall measurements and to utilize it to provide an empirical basis for modelling rainfall rate, attenuation and drop size distribution fitted specifically to the equatorial region of Central Africa and its unique rainfall pattern. The work aims to explore the specific peculiarities that might appear when rain data from the Central Africa region is applied to implement the well-known models which were developed based on measurements carried out elsewhere, and to develop mathematical tools and methods that factor these peculiarities into the key radio propagation expressions employed in communication planning.

### **1.3 Objectives of Research**

The objectives of this study are as follows:

1. Development of rainfall rate distribution maps for the entire Rwanda.
2. Development of rainfall attenuation distribution and contour maps for the entire Rwanda.
3. Measurement of appropriate rainfall drop size distribution for Rwanda.
4. Application of the proposed rainfall DSD in 3 to estimate the specific attenuation coefficients for Rwanda at different microwave and millimetre frequencies
5. Determination of a new rainfall DSD model for Central Africa.
6. Comparison of the ITUR, SST and other rain attenuation models for Central Africa.

### **1.4 Dissertation Overview**

Chapter one is an introduction to the research work. It presents the research motivation, the objectives of the research, the dissertation overview, the contribution to knowledge and list of publications.

Chapter two focuses on the literature review. In this chapter, we focus on clear-air modelling for Central Africa, Rwanda. We deal with both Geo-climatic factor,  $K$ , and effective earth radius factor,  $k$ . The former is responsible for multipath fading while the latter is responsible for diffraction fading. Later we introduce fading due to precipitation.



Chapter three presents climatic characteristics of Rwanda, rainfall rate distribution modelling, rainfall specific attenuation, contour maps of rainfall rate and rainfall specific attenuation for Rwandan links.

In Chapter four, rainfall data is classified into annual, seasonal, monthly and regime events and their respective rainfall rate exceedences are calculated. Different DSD models such as Lognormal, Gamma, Marshall-Palmer and Weibull distributions are involved and the method of moment technique is applied for estimating the corresponding model parameters.

Chapter five focuses on the development of a new rainfall drop size distribution model for equatorial Africa. The maximum likelihood estimation technique is applied to construct estimates of input DSD fit parameters of the developed statistical distribution for rainfall DSD in Rwanda. Thereafter, the newly obtained distribution is compared to the existing rainfall DSD models.

In Chapter six, the specific rain attenuation is estimated using results from chapter four and five. The Mie Scattering technique is used to derive the scattering parameters. The derived scattering parameters with DSD models are used to estimate the attenuation due to rain in the region of Central Africa. To this end, the synthetic storm technique (SST) and ITU-R models are applied for comparison with other distributions.

Chapter seven gives conclusions and recommendations.

## **1.5 Contribution to knowledge**

Listed here are parts of this thesis that have been published in journals and conference proceedings.

- Sumbiri, Djuma, Afullo, T., Alonge, A., “Rainfall Zoning and Rain Attenuation Mapping for Microwave and Millimetric Applications in Central Africa,” (2016) *International Journal on Communications Antenna and Propagation (IRECAP)*, 6 (4), pp. 198-210.
- Djuma. Sumbiri, T. J. O. Afullo and A. Alonge, "Rain attenuation prediction for terrestrial links at microwave and millimeter bands over Rwanda," 2016 *Progress in Electromagnetic Research Symposium (PIERS)*, Shanghai, 2016, pp. 4233-4236.
- Djuma. Sumbiri, T. J. O. Afullo and A. Alonge, “Geoclimatic Factor estimation for Central Africa” *Southern Africa Telecommunication Networks and Applications Conference (SATNAC)* 2016, At Fancourt, George, South Africa.
- Djuma. Sumbiri, T. J. O. Afullo and A. Alonge,” Modelling of Rain Drop Size Distribution for Microwave and Millimeter Wave in Central Africa” *Progress in Electromagnetic Research Symposium (PIERS)*, Singapore, pp. 2398-2404.

# Chapter Two

## Literature Review

### 2.1 Introduction

Line-of-sight radio links play an important part in long distance communication networks. With the rising demand for higher bandwidths partly supported by current developments in radio communication technology, higher reliability and better performance of radio links are still required for the transmission of high quality signals. As a wireless medium, the troposphere affects the propagation of radio waves between radio link terminals. Poor propagation conditions lead to a fluctuation of the output signal, thus resulting in fades on microwave links [30]. This phenomenon affects the transmitted signal and the overall communication system may thus not perform well [31]. Therefore, when designing a highly reliable radio communication network, these fades or signal variations have to be taken into account [32]. To solve this impairment related to radio propagation in different areas of the world, various techniques have been proposed by many authors. These techniques were developed based on the radio propagation data of the regions in question [33-37].

According to [35], most predictions of tropospheric propagation effects are made either for the average worst month or the average year. However, the radio-climatological frameworks for such predictions are more than thirty years old for clear-air effects and more than twenty years old for precipitation effects. Radioclimatological data required to improve on even the existing frameworks have been sparse for some regions of the world, including Africa. Radio propagation data for testing prediction techniques based on radioclimatological models have been even sparser. A recent effort by the international community to update the radio climatological data base for tropospheric propagation predictions has involved an increase in the number of meteorological stations included in the analysis, the introduction of new potential prediction variables, and improved mapping and other presentation procedures. This effort has been hampered, however, by the use of sensors of variable quality in different parts of the world, and again a shortage of data for certain regions.

In this chapter, we focus on clear-air modelling for Sub-Saharan Africa, and thereafter introduce precipitation attenuation models.

### 2.2 The Atmosphere

The atmosphere is known as a mixture of gases and vapours surrounding the earth. It is divided into four main layers according to the variability of the temperature gradient with altitude [38]. These layers are commonly known as troposphere, stratosphere, mesosphere and **thermosphere**.

The boundaries of the layers are referred to as pauses with an identifying prefix. Those pauses are considered as transition zones in which the temperature remains constant with height [38]. The variation of these layers with altitude is shown in Figure 2-1 [40]. In this study, we will be interested in the troposphere where its weather variations affect the propagation of radio wave.

The troposphere may extend from the ground surface to an altitude of about 10 km at the poles and 17 km at the equator with some variation due to weather. It is the thinnest and the lowest layer, the warmest and the wettest, but also the most dense with 72% of the total mass of the atmosphere. The troposphere is often thought of as the zone of weather since it is where all weather takes place. It is the region of rising and falling packets of air. The air pressure at the top of the troposphere is only 10% of that at sea level [41]. On average, the temperature decreases with height in this layer.

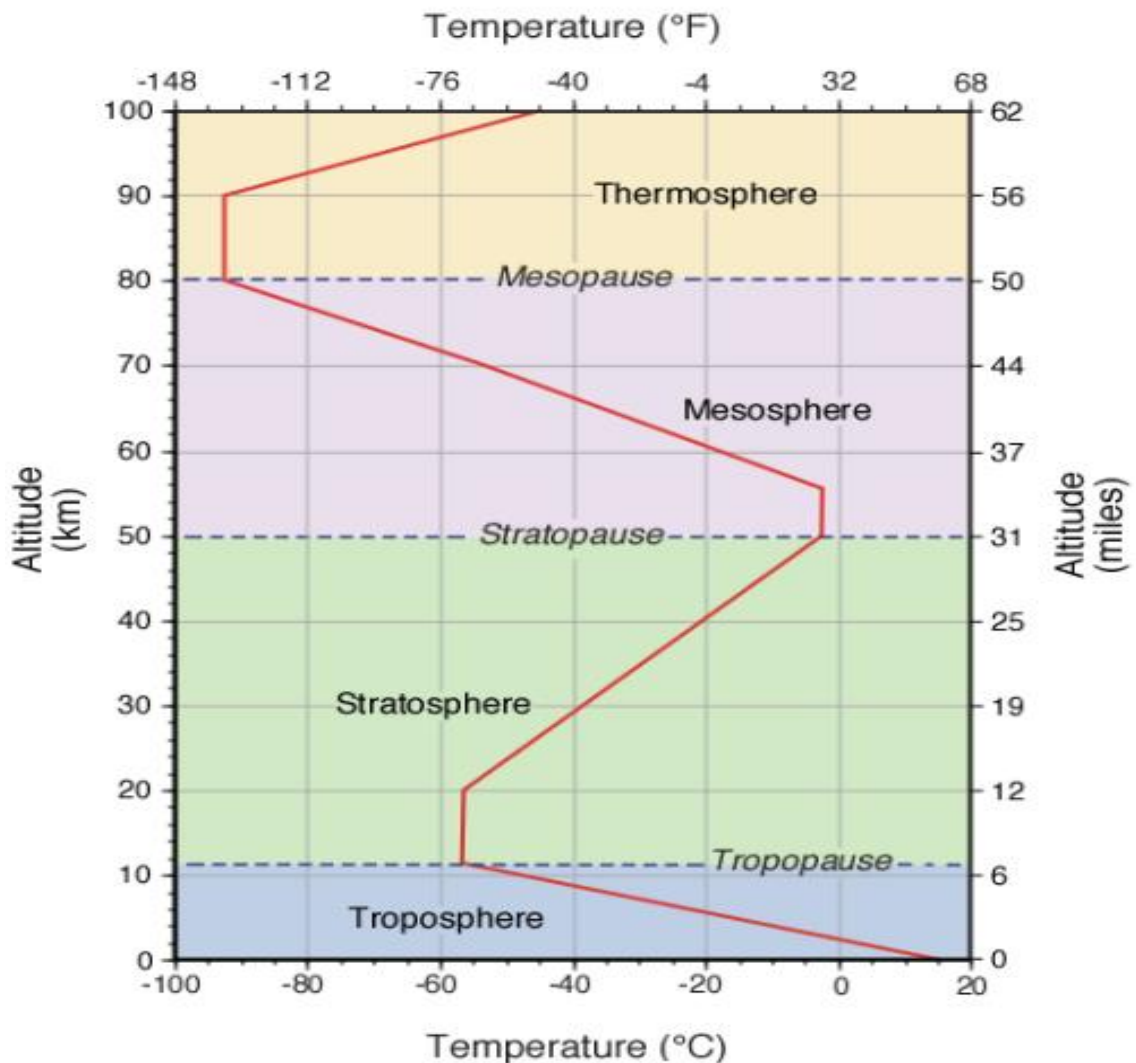


Figure 2-1: Layers of Earth's atmosphere [38]

## **2.3 Tropospheric Effects**

In the troposphere, the refractive index is slightly above one and it reduces with height. This change with height has influence on radio frequencies; waves experience absorption and scattering due to clouds, rain, snow, etc. The decrease of refractive index as the altitude increase causes the radio waves to move downwards. For this reason, the electromagnetic waves propagating through the troposphere may bend downward so that they can be received beyond the optical LOS. This effect is important for communication at VHF, UHF, and SHF [42].

In addition to this effect the troposphere has several effects on terrestrial radio paths such as [13, 43]:

- Attenuation caused by atmospheric gases (mainly oxygen and water vapour) and hydrometeors (rain, fog, hail, snow, mist, Clouds, ...);
- Interference with other signals that causes multipath fading in microwave radio links and scintillation in satellite links;

Variations in the index of refraction with height are determined by meteorological conditions such as temperature, pressure and humidity, so that successful communication via tropospheric bending is difficult to predict [44]. In general, subject to the causative agent, tropospheric effects can be classified in two categories, namely, the clear-air effects and the precipitation effects.

## **2.4 Clear-Air Radio Climatic Effect on Line of Sight (LOS) Links.**

Any change of atmospheric parameter such as temperature, pressure and humidity in the lower layer of the atmosphere leads to the variation of the refractive index of the atmosphere. Therefore, these parameters can be used to describe the way a microwave link is affected while propagating in the atmosphere under clear-air conditions. These parameters are very important and are measured directly from meteorological equipment; such as thermometer for temperature, barometer for both pressure and humidity. These three quantities can be used to derive other secondary radio climatic data such as refractivity, refractive gradient, effective earth radius factor ( $k$ ), and the Geo-climatic factor ( $K$ ). These effects can be defined in terms of gaseous absorption, scintillation, multipath fading and diffraction fading.

### **2.4.1 Clear-Air Multipath Fading Prediction**

The transmitted signal may arrive at the receiver through several paths: it can come directly along line of sight, through reflections from buildings and terrain, and through atmospheric refraction. These results in multipath propagation and the latter can lead to the phenomenon known as multipath fading. This phenomenon affects the transmitted signal and the system may thus not

perform well [31]. The Geo-climatic factor which, is both indicative of geographical and climatic characteristics of the region of interest, is a very important parameter for clear-air multipath fading prediction.

#### 2.4.1.1 Overview of the Geo-climatic factor

The Geo-climatic factor cannot be determined without first determining other propagation parameters such as refractivity and refractivity gradient [45]. By following steps recommended by the International Telecommunication Union Radio (ITU-R) in Recommendation P.453-8, we can determine the radio refractivity and its gradient. The atmospheric refractive index is computed using [45]:

$$n = 1 + N \cdot 10^{-6} \quad (2.1)$$

Where  $N$  is the radio refractivity in  $N$ -units, expressed by [45]:

$$N = \frac{77.6}{T} \left( P + 4810 \frac{e}{T} \right) \quad (2.2)$$

Where  $P$  is the atmospheric pressure expressed in hector-Pascal ( $hPa$ ),  $e$  is the water vapour pressure ( $hPa$ ), and  $T$  is the absolute temperature expressed in degrees Kelvin ( $^{\circ}K$ ). Equation (2.2) may be used for all radio frequencies, and for frequencies up to 100 GHz, the error is less than 0.5%. As stated in P.453-8, the water vapour pressure,  $e$ , can be calculated from the relative humidity,  $H$ , and saturated water vapour  $e_s$ , by the following expression [45]:

$$e = H \frac{e_s}{100} \quad (2.3)$$

Where  $e_s$  is expressed by the following equation [45]:

$$e_s = a \exp\left(\frac{bt}{t+c}\right) \quad (2.4)$$

By combining (2.3) and (2.4), we get the expression [45]:

$$e = H \frac{a \exp\left(\frac{bt}{t+c}\right)}{100} \quad (2.5)$$

Where  $H$  is the relative humidity (%),  $t$  is the Celsius temperature ( $^{\circ}C$ ),  $e_s$  is the saturation vapour pressure (hPa) at the temperature  $t$  ( $^{\circ}C$ ). For water, the coefficients  $a=6.1121$ ;  $b=17.502$ ;  $c=240.97$  and are valid between  $-20^{\circ}$  to  $50^{\circ}$  with an accuracy of  $\pm 0.20\%$  while for ice,  $a=6.1115$ ;  $b=22.452$ ;  $c=272.55$  and are valid between  $-50^{\circ}$  to  $0^{\circ}$  with an accuracy of  $\pm 0.20\%$ .

For water, equation (2.5) becomes:

$$e = H \frac{6.1121 \exp\left(\frac{17.502t}{t + 240.97}\right)}{100} \quad (2.6)$$

It has been found out that the long-term mean dependence of the refractive index  $n$  upon the height  $h$  is well expressed as follows [45]:

$$n(h) = 1 + N_o \cdot 10^{-6} \exp\left(-\frac{h}{h_o}\right) \quad (2.7)$$

Where  $N_o$  is average value of atmospheric refractivity extrapolated to sea level, and  $h_o$  is the scale height (km).  $N_o$  and  $h_o$  can be obtained statistically for different climates.  $N_o=315$  and  $h_o=7.35$  km for terrestrial paths [45]. This is used to calculate the value of refractivity  $N_s$  at the earth's surface from  $N_o$  by:

$$N_s = N_o \exp\left(-\frac{h}{h_o}\right) \quad (2.8)$$

With  $h_s$  (km), the height of the earth's surface above sea level. The radio refractivity gradient  $G$  N-units/km is expressed as [45]:

$$G = \frac{dN}{dh} = \frac{N_1 - N_2}{h_1 - h_2} \quad (2.9)$$

Here  $N_1$  and  $N_2$  are radio refractivity values at heights  $h_1$  and  $h_2$ , respectively [46]. The procedure for determination of the Geo-climatic factor ( $K$ ) is stated in [47]. In order to calculate  $K$ , a fairly accurate estimate can be made from the expression [47]:

$$K = 10^{-4.2 - 0.00029dN_1} \quad (2.10)$$

Where  $K$  is the geo-climatic factor and  $dN_i$  is the point refractivity gradient in the lowest 65 m of the atmosphere not exceeded for 1% of an average year and can be estimated as follows [35]:

$$dN_1 = \left. \frac{dN}{dh} \right|_{h \leq 65m} \quad (2.11)$$

#### 2.4.1.2 Work Reported for Sub-Saharan Africa

The data used in this sub-section was obtained for the North-Western region of Tanzania (from January 2001 to December 2010) in four different meteorological stations in the region close to Rwanda. The first meteorological station is Bukoba with coordinates ( $1^{\circ}19'13.33''S$ ,  $31^{\circ}48'31.17''E$ ) and elevation of 1150.1 m above sea level. The second is Mwanza station ( $2^{\circ}21'58.25''S$ ,  $32^{\circ}53'46.16''E$ ) and elevation of 1173.8 m above sea level. The third is Kigoma ( $4^{\circ}55'11.93''S$ ,  $29^{\circ}37'49.83''E$ ) with elevation of 767.8 m above sea level, and the last is Musoma station situated at ( $1^{\circ}30'00.00''S$ ,  $33^{\circ}48'00.00''E$ ) with elevation of 1150.0 m above sea level. Note that Kigoma is based on the North-Eastern shores of Lake Tanganyika, Bukoba at the western shores of Lake Victoria, Mwanza on the southern shores of Lake Victoria, and Musoma on the eastern shores of Lake Victoria. In terms of proximity to the Kagera basin and Rwanda, Bukoba would be the closest, followed by Kigoma and Mwanza, while Musoma would be the farthest.

The parameters extracted are monthly records of pressure,  $P$  ( $hPa$ ), temperature,  $T$  ( $^{\circ}C$ ) and the relative humidity, (%). The values of humidity were converted to water vapour pressure,  $e$  ( $hPa$ ) by using equation (2.6). In the processing of data, we used the average values for each month over the period 2001 to 2010. The monthly data was used to calculate the values of refractivity at the ground level and at 100 m altitude using equation (2.2). From the calculated values of refractivity, we calculated the values of refractivity gradient at heights of 65 m and at 100 m using equations (2.11) and (2.9). Finally after determining  $dN_1$ , the Geo-climatic factor ( $K$ ) was calculated using equation (2.10) and the results presented in Figures 2-3 to 2-5 and Table 2-1 [48].



Figure 2-2: Map of Tanzania, Rwanda, Burundi

A major item in multipath fade margin determination is the value of  $K$  at the worst month. This corresponds to the month with the highest value of  $K$ . For Bukoba, the months of February to April give the highest peaks of  $K$ , with  $K=0.00322$  in February. In Kigoma, the highest values of  $K$  again take place in January to April with a peak  $K=0.0046$  in January and April. For Mwanza, which is based on the southern shores of Lake Victoria, the highest values of  $K$  occur from December to March, with the peak  $K=0.00321$  in December. Finally, for Musoma, the highest values of  $K$  occur in March and April, with a peak  $K=0.02588$  occurring in April. Thus Musoma exhibits the highest values of  $K$  in the region, and is thus most prone to high rates of multipath fading.



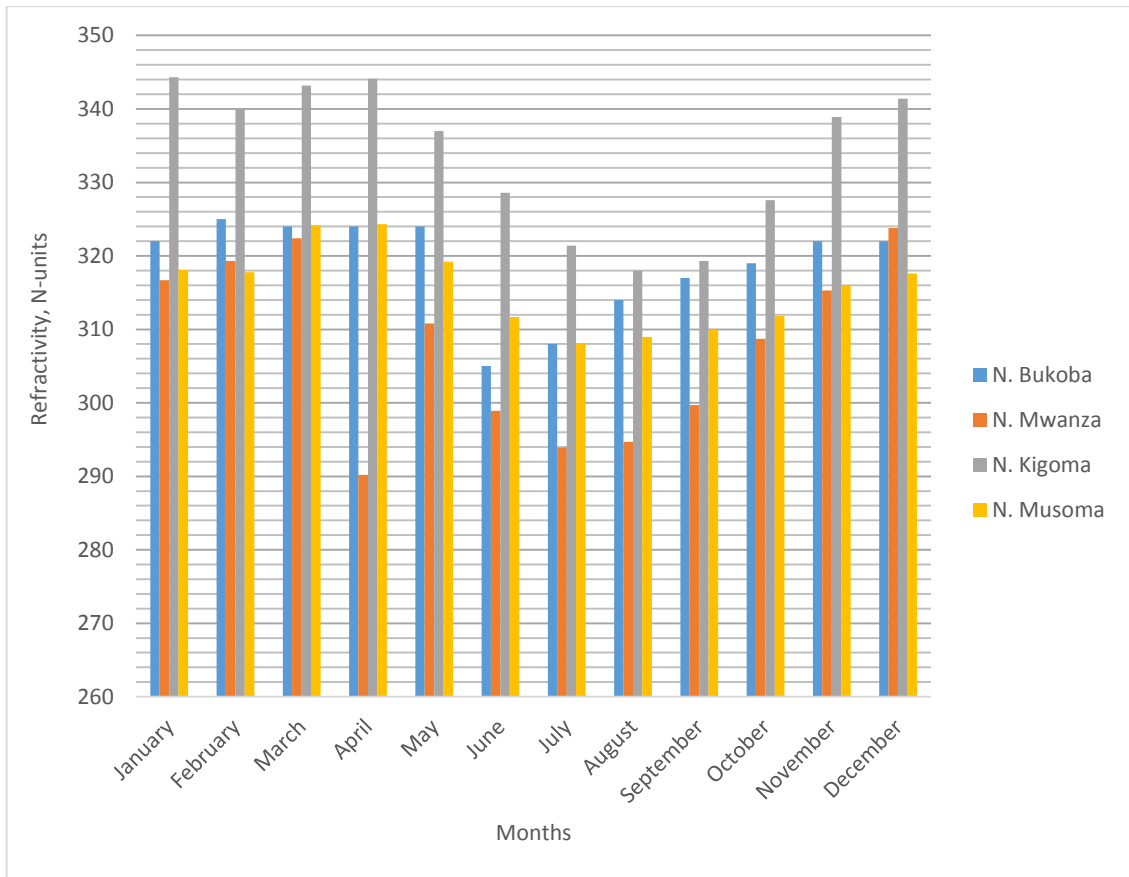


Figure 2-3: Average monthly variation of refractivity in Bukoba, Mwanza, Kigoma, and Musoma

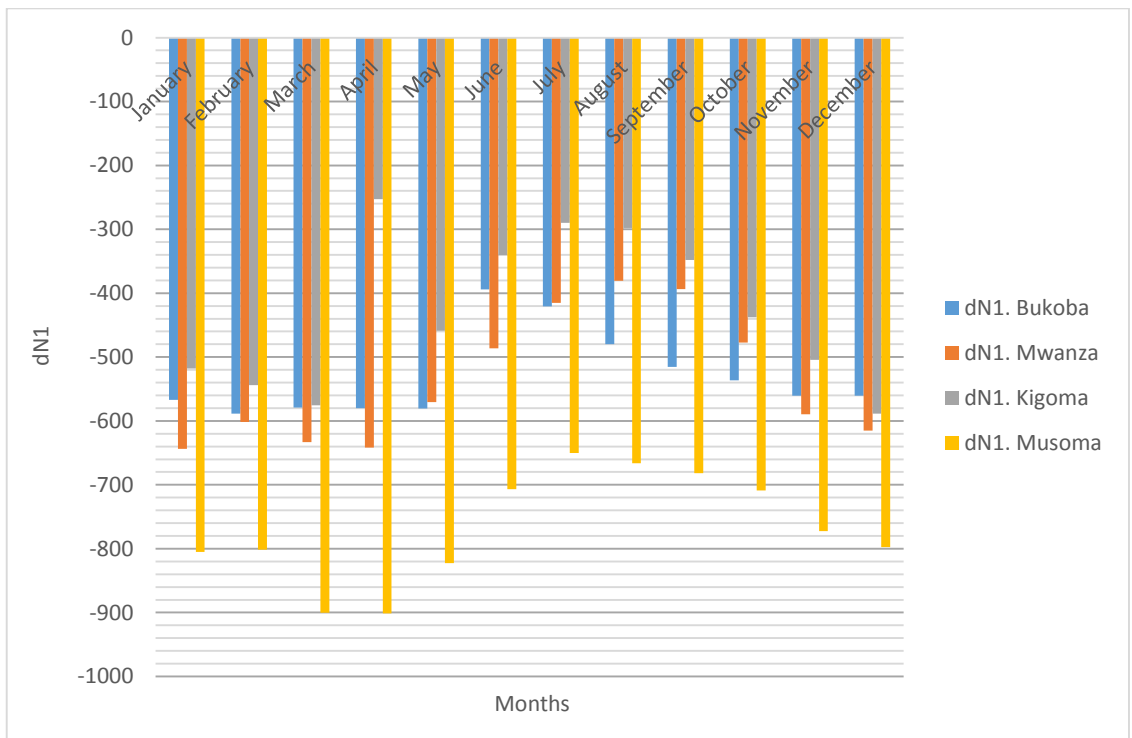


Figure 2-4: Point refractivity gradient for Bukoba, Mwanza, Kigoma and Musoma

Table 2-1: Geo-climatic factor ( $K$ ) for different months for Bukoba, Mwanza, Kigoma and Musoma

Calendar Months	Geo-climatic factor, $K$			
	Bukoba	Mwanza	Kigoma	Musoma
January	0.00278	0.0046	0.00201	0.01362
February	0.00322	0.0035	0.00238	0.01333
March	0.00301	0.0043	0.00294	0.02573
April	0.00304	0.0046	0.00034	0.02588
May	0.00304	0.0028	0.00135	0.01534
June	0.00088	0.0016	0.00061	0.00708
July	0.00105	0.001	0.00044	0.00484
August	0.00155	0.0008	0.00046	0.00539
September	0.00197	0.0009	0.00065	0.00598
October	0.00226	0.0015	0.00117	0.00717
November	0.00267	0.0032	0.00183	0.01098
December	0.00266	0.0038	0.00321	0.01297
Average	0.00234	0.0027	0.00145	0.01236

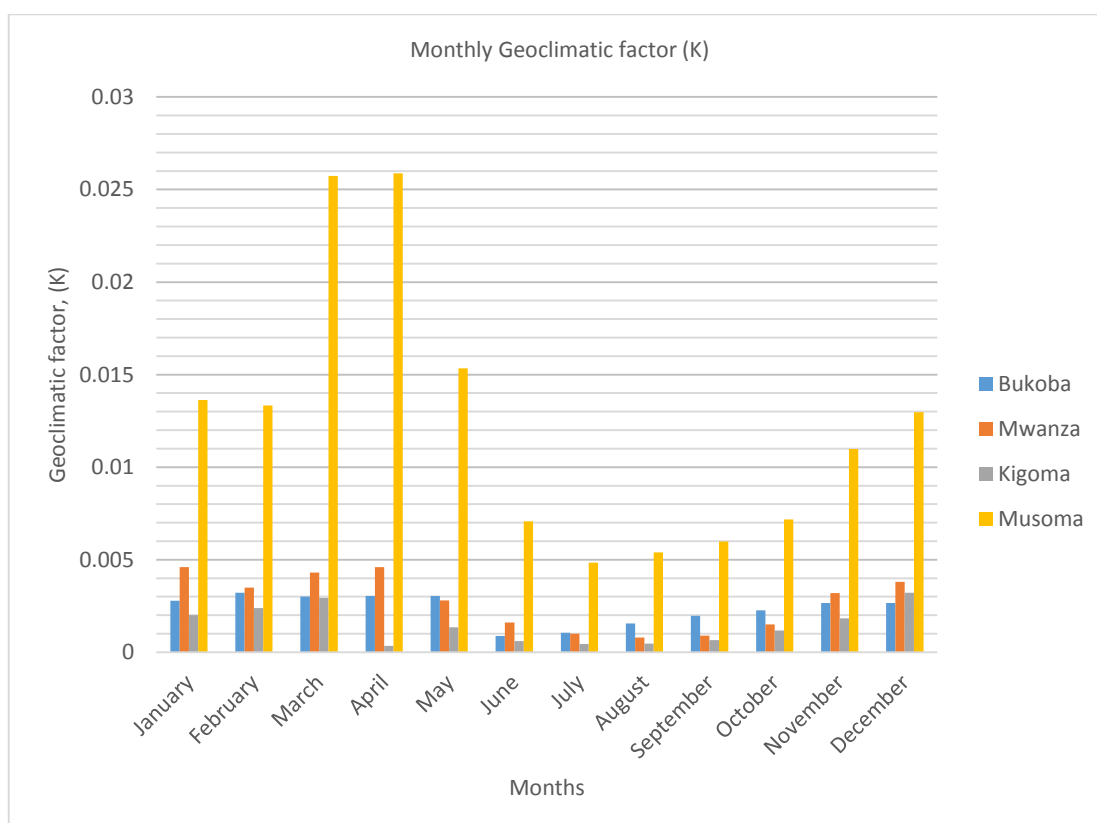


Figure 2-5: Geo-climatic factor ( $K$ ) variation for Bukoba, Mwanza, Kigoma and Musoma

Table 2-2: Geo-climatic factor ( $K$ ) for different months for Durban, Cape Town, Pretoria, Bloemfontein and Polokwane in South Africa [49]

Calendar Months	Geo-climatic factor, $K$				
	Durban	Cape Town	Pretoria	Bloemfontein	Polokwane
January	0.000627	0.000451	0.008420	0.000308	0.000486
February	0.002770	0.000411	0.002870	0.000213	0.001250
March	0.000648	0.000203	0.005070	0.000263	0.000596
April	0.000301	0.000284	0.001930	0.000133	0.000470
May	0.000399	0.000859	0.000339	0.000223	0.000528
June	0.000405	0.000464	0.000265	0.000207	0.000316
July	0.000172	0.000409	0.000220	0.000233	0.000115
August	0.000735	0.000418	0.000193	0.000174	0.000128
September	0.000531	0.000406	0.000228	0.000534	0.000134
October	0.000184	0.000233	0.000314	0.000642	0.000195
November	0.000406	0.000321	0.000276	0.000201	0.000214
December	0.000234	0.000142	0.000885	0.000473	0.000300

The Geo-climatic factor ( $K$ ) variable, which is one of the most important radio climatic variables in the planning of the radio links in the region, has been calculated for Bukoba, Mwanza, Kigoma and Musoma in Tanzania in the region close to Rwanda, in central Africa. It is observed that as the values of  $dN_1$  become more negative, the Geo-climatic factor increases. The average of the Geo-climatic factor is 0.00234 for Bukoba, 0.0027 for Mwanza, 0.00145 for Kigoma, and 0.01236 for Musoma. The worst month values of  $K$  are determined to be 0.00322 for Bukoba in February, 0.0046 for Mwanza in April, and 0.00321 for Kigoma in December, and a high value of 0.02588 for Musoma in April. Thus regionally, for planning purposes, we can state that the worst value of Geo-climatic Factor ( $K$ ) for Rwanda is 0.0032.

From previous work, in 2013, Asiyo and Afullo [49] have determined the Geo-climatic factor ( $K$ ) values for various locations in South Africa (Durban, Cape Town, Pretoria, Bloemfontein and Polokwane) using three years (2004 to 2006) radiosonde data obtained from South Africa Weather Service (SAWS), and their results are presented in Table 2-2. The worst month values of  $K$  are 0.00277 for Durban in February, 0.00142 for Cape Town in December, 0.00842 for Pretoria in January, 0.00133 for Bloemfontein in April, and 0.00125 for Polokwane in February [49].

### 2.4.2 Diffraction Fading

In a line-of-sight propagation, diffraction takes place when a radio wave is blocked by a sharp or round obstacle with large dimensions compared to the wavelength [50]. A radio path can also be diffracted by other obstacles such as buildings, hills, trees, etc.

The refractive index of the troposphere and the effective earth radius factor (k-factor) are given by [51]:

$$n = \frac{c}{v} = 1 + N \cdot 10^{-6} \quad (2.12)$$

$$k = \left[ 1 + \left( \frac{dN}{dh} \right) / 157 \right]^{-1} \quad (2.13)$$

Where  $c$  is the speed of a radio wave in free space,  $v$  is the speed of a radio wave in air,  $k$  and  $dN/dh$  are the effective earth radius factor and the vertical refractivity gradient, respectively.

When low k-factor values are observed, the radio rays will be bent upwards. The radio path between transmitter and receiver is thus blocked by the earth bulge, leading to the loss of direct visibility between these radio link terminals. The loss of signal strength under these conditions is called diffraction fading. This fading is an important factor for determining the appropriate antenna heights of a radio link [3].

Equation (2.13) shows the k-factor is a function of the vertical refractivity gradient, which is in turn a function of the meteorological variables. The k-factor variability is a very useful way of describing non-standard propagations. These types of propagations are generally classified as super-refraction, sub-refraction and ducting as presented in Table 2-3.

Super-refraction occurs if the temperature increases with height (temperature inversion) and/or the water vapor content decreases quickly with height. In this case, the refractivity gradient will decrease from the standard value of -40 N-units/km [52]. Thus, the k-factor will be greater than the standard value of 4/3, and radio rays will be bent more towards the Earth's surface than under normal propagation conditions. If the refractivity gradient becomes more negative, radio rays become more bent downwards and cannot arrive at the receive antenna [50].

Sub-refraction occurs when the refractivity gradient is greater than -40 N-units/km, and k-factor is less than the standard value of 4/3. In this case, the curvature of radio rays is reduced, and the radio rays are bent upwards relative to the Earth's surface. This will cause the propagation ranges to become smaller than those of the normal propagation conditions [52].

Table 2-3: Common values of k-factor and refractivity gradient [50]

Types of propagation	Refractivity gradient ( $dN/dh$ )	K-factor
Super-refraction	$-40 > dN/dh > -157$	$4/3 < k < \infty$
Sub-refraction	$dN/dh > -40$	$0 < k < 4/3$
Ducting	$dN/dh < -157$	$-\infty < k < 0$

If the refractive gradients are extremely negative, typically  $< -157$  N-units/km, the radius of radio rays becomes less than the Earth's radius. This refractive condition is called ducting or trapping, since the radio waves are confined to a narrow tropospheric layer. In the presence of ducts, radio waves can propagate over great ranges, and the received signal strength may reach its free-space strength [53].

Table 2-4: Values of mean k-factor and ISE for kernel estimates, 0-100 m a.g.l. [54]

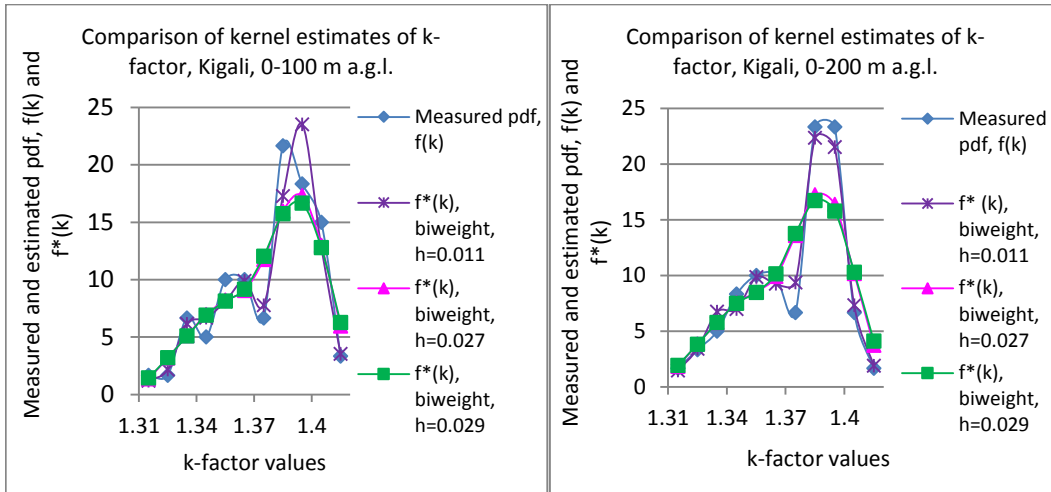
Locations	Bandwidth, h	Gaussian kernel		Triangular kernel		Biweight kernel	
		Mean	ISE	Mean	ISE	Mean	ISE
Kigali	0.011	1.340	0.840	1.377	0.618	1.365	0.596
	0.027	1.165	2.540	1.343	0.907	1.347	0.832
	0.029	1.142	2.725	1.334	1.020	1.342	0.932
Kamembe	0.006	1.325	1.843	1.456	0.178	1.482	0.266
	0.016	1.124	7.800	1.327	2.692	1.325	2.384
	0.017	1.103	8.136	1.317	3.076	1.320	2.769
Gisenyi	0.004	1.358	0.106	1.339	0.709	1.295	0.829
	0.010	1.337	2.484	1.364	0.148	1.368	0.087
	0.011	1.332	2.970	1.365	0.241	1.366	0.154
Kigoma	0.019	1.373	0.660	1.428	0.028	1.429	0.030
	0.047	1.144	2.199	1.374	0.790	1.381	0.685
	0.051	1.112	2.291	1.362	0.957	1.371	0.846
Mwanza	0.014	1.366	0.891	1.368	0.037	1.394	0.041
	0.033	1.208	2.875	1.370	0.942	1.375	0.832
	0.036	1.179	3.075	1.364	1.146	1.371	1.040
Bukoba	0.007	1.385	0.076	1.194	0.419	1.078	0.814
	0.017	1.367	1.791	1.369	0.109	1.283	0.511
	0.018	1.362	1.969	1.370	0.155	1.290	0.547
Musoma	0.009	1.387	0.010	1.356	0.162	1.337	0.115
	0.021	1.308	0.959	1.379	0.011	1.393	0.016
	0.023	1.290	1.254	1.375	0.019	1.385	0.009

Table 2-5: Values of mean k-factor and ISE for kernel estimates, 0-200m a.g.l. [69]

Location	Bandwidth, h	Gaussian kernel		Triangular kernel		Biweight kernel	
		Mean	ISE	Mean	ISE	Mean	ISE
Kigali	0.011	1.348	1.498	1.377	0.227	1.376	0.175
	0.027	1.185	3.768	1.350	1.671	1.353	1.539
	0.029	1.161	3.966	1.345	1.849	1.350	1.738
Kamembe	0.006	1.356	0.331	1.318	0.036	1.322	0.037
	0.015	1.225	4.415	1.349	0.442	1.358	0.270
	0.017	1.187	5.133	1.348	0.808	1.354	0.532
Gisenyi	0.004	1.344	0.119	1.197	0.324	1.149	0.513
	0.010	1.338	2.257	1.354	0.160	1.364	0.099
	0.011	1.333	2.747	1.352	0.256	1.367	0.165
Kigoma	0.019	1.310	1.717	1.405	0.328	1.415	0.213
	0.046	1.054	3.527	1.301	1.852	1.324	1.739
	0.050	1.021	3.631	1.283	2.055	1.305	1.950
Mwanza	0.014	1.366	0.571	1.369	0.039	1.347	0.018
	0.033	1.222	2.298	1.367	0.606	1.369	0.499
	0.036	1.193	2.487	1.366	0.764	1.368	0.645
Bukoba	0.007	1.413	0.024	1.568	0.726	1.338	0.887
	0.016	1.357	1.640	1.439	0.035	1.266	0.480
	0.018	1.347	2.062	1.416	0.059	1.261	0.506
Musoma	0.009	1.350	0.061	1.331	2.133	1.300	2.202
	0.021	1.335	0.830	1.371	0.078	1.348	0.062
	0.023	1.321	1.125	1.377	0.045	1.363	0.030

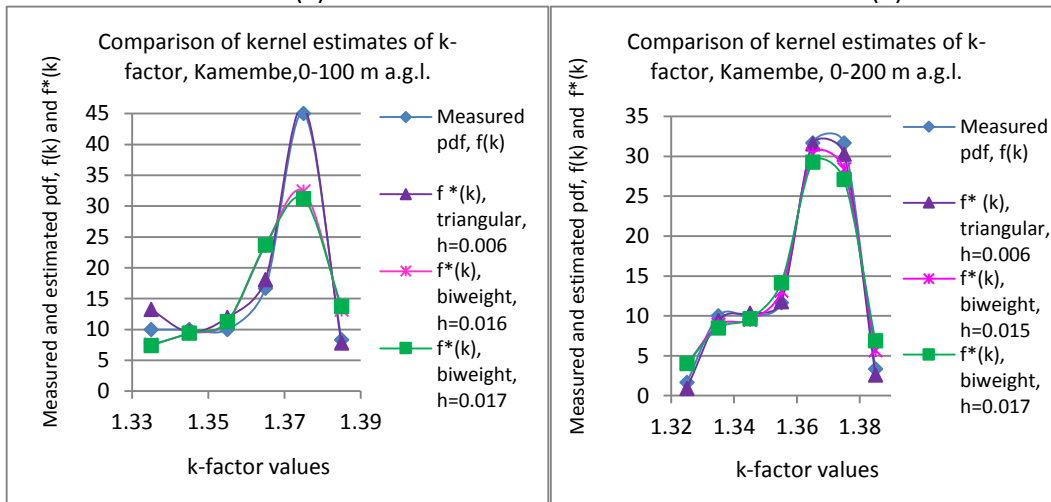
From previous work, in 2012, Fulgence Dushimimana, has determined the k-factor values for various locations in Rwanda (Kigali, Kamembe, Gisenyi, Kibungo, Byumba) and North-Western Tanzania (Kigoma, Mwanza, Bukoba, Musoma, Tabora) using five years (2006-2010) meteorological data collected in these regions. Then, he has proposed a model for the k-factor distribution and extending the spatial distribution of the observed k-factor values to other locations in the region of Central Africa. The all-year mean k-factor of 1.366 and median k-factor of 1.367 within 0-200 m were obtained for Rwanda. For North-Western Tanzania, the respective values of the all-year mean and median k-factors were 1.403 and 1.398 within 0-200 m

Comparing these *k*-factor values to those obtained for Botswana (mean  $k=1.09$ ) and Southern Africa (mean  $k= 1.21$ ) [55], he observed that the use of the *k*-factor values from these countries can overestimate the diffraction loss and antenna heights in the regions under study. The *k*-factor variation showed that the radio propagation over Rwanda and North-Western Tanzania is mostly super-refractive [54].



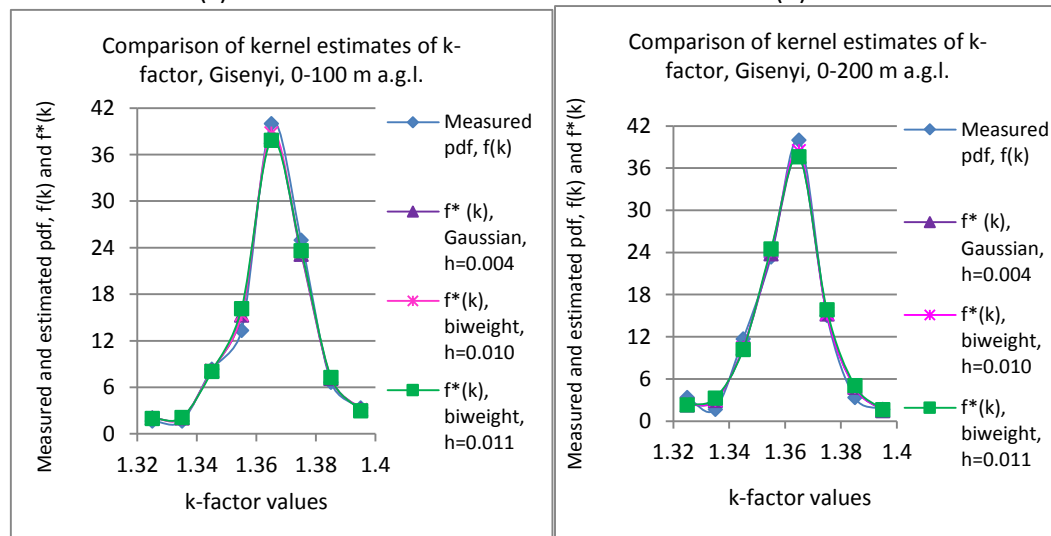
(a)

(b)



(c)

(d)



(e)

(f)

Figure 2-6: Comparison of Kernel estimates of k-factor for Rwanda. (a) Kigali, 0-100 m a.g.l. (b) Kigali, 0-200 m a.g.l. (c) Kamembe, 0-100 m a.g.l. (d) Kamembe, 0-200 m a.g.l. (e) Gisenyi, 0-100 m a.g.l. (f) Gisenyi, 0-200 m a.g.l. [54]

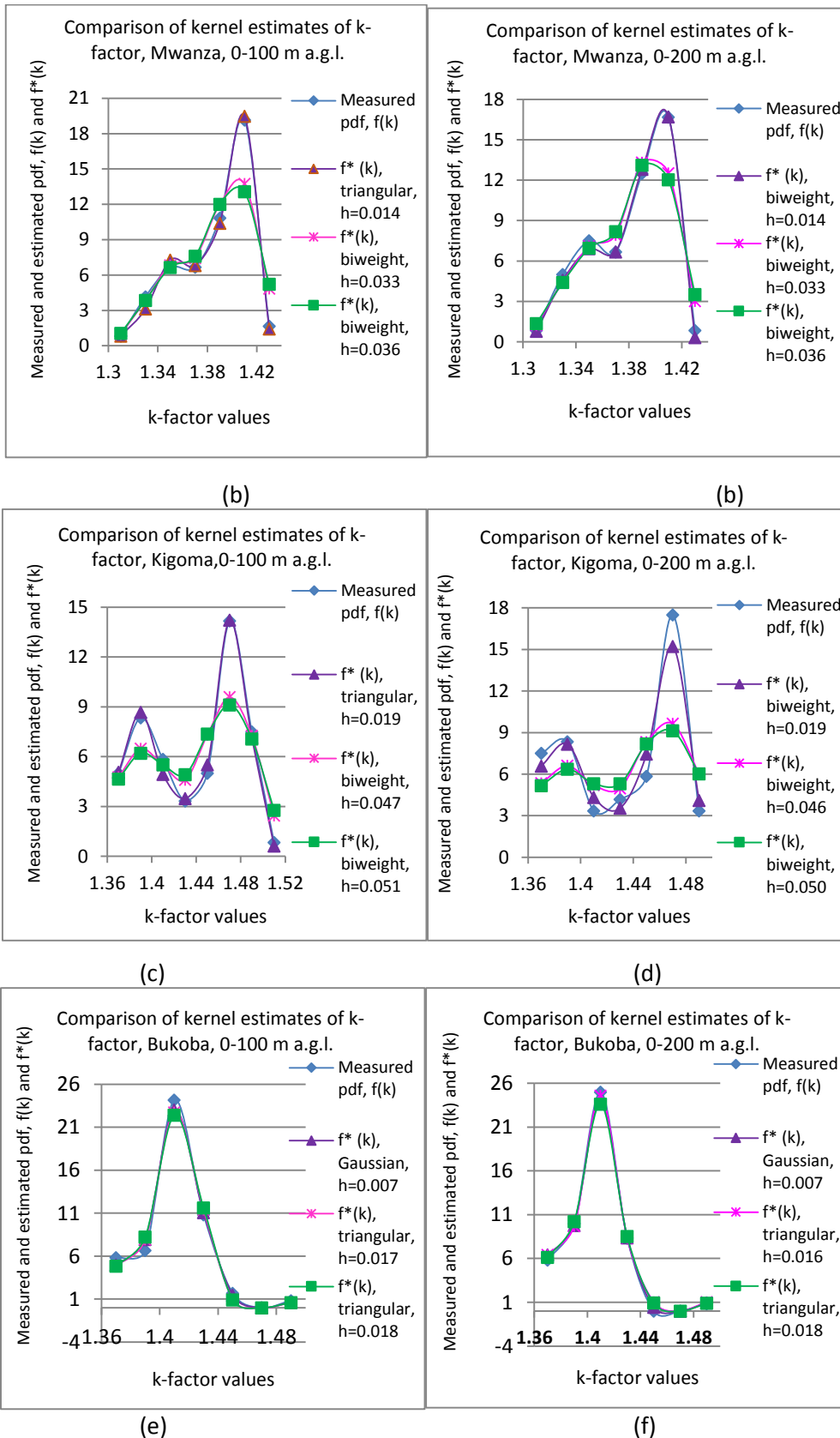


Figure 2-7: Comparison of Kernel estimates of k-factor for North-West Tanzania. (a) Mwanza, 0-100 m a.g.l. (b) Mwanza, 0-200 m a.g.l. (c) Kigoma, 0-100 m a.g.l. (d) Kigoma, 0-100 m a.g.l. (e) Bukoba, 0-100 m a.g.l. (f) Bukoba, 0-200 m a.g.l. [54]



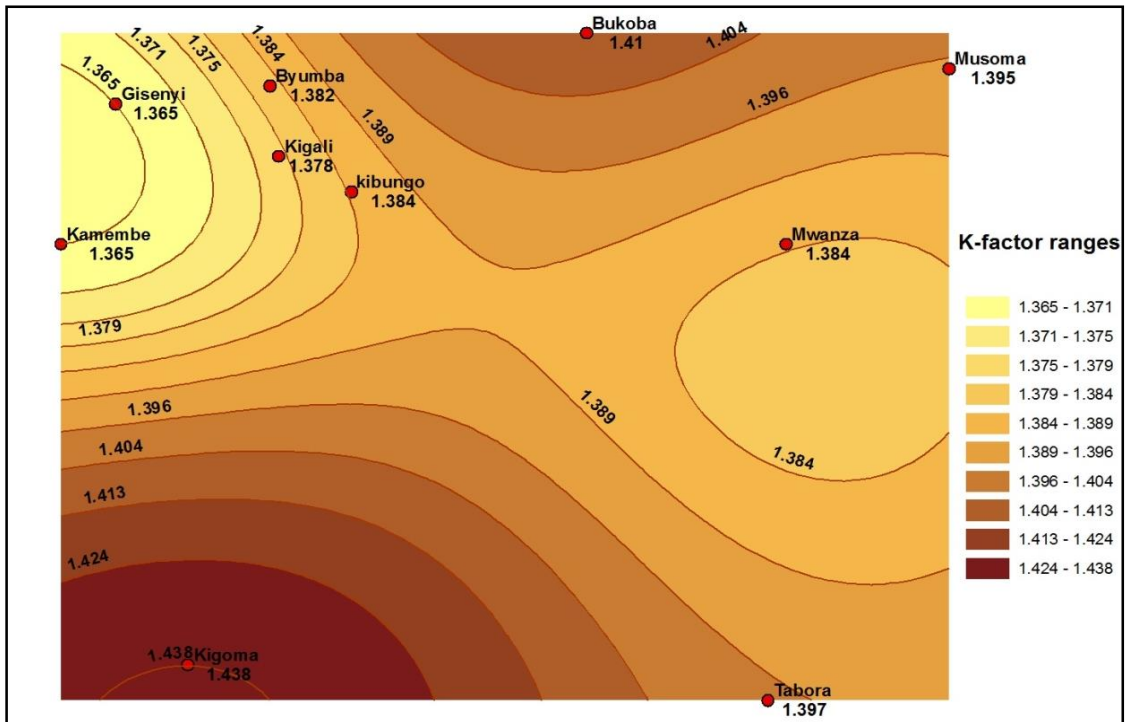


Figure 2-8: Prediction map of k-factor spatial distribution, ordinary kriging, 0-100 m a.g.l. [54]

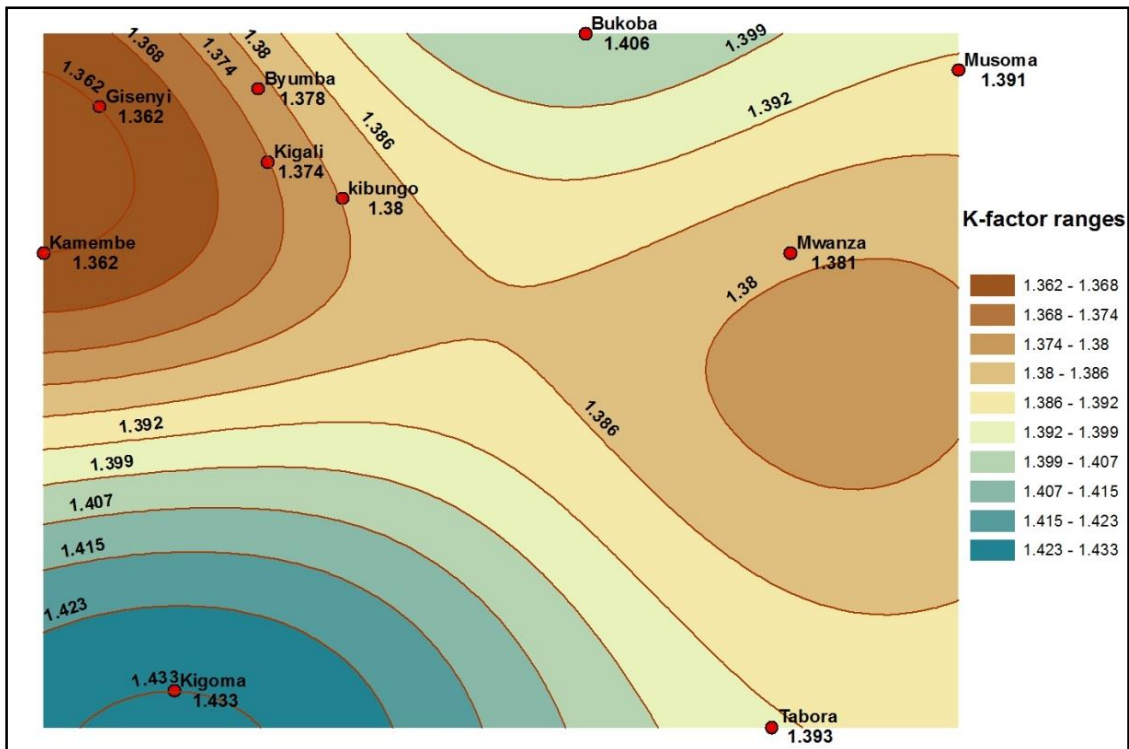


Figure 2-9: Prediction map of k-factor spatial distribution, ordinary kriging, 0-200 m a.g.l. [54]

The results of modeling the k-factor distribution showed that the biweight kernel estimate is the best model for most of the locations, except for Kamembe and Bukoba where the triangular and

Gaussian kernel estimates are respectively the best models [54]. Some of his results are presented in Tables 2-4 to 2-5 and Figures 2-6 to 2-7.

From the results of extending the observed k-factor values to other locations, he concluded that the ordinary kriging (with the Gaussian semivariogram model) is the best interpolation technique for predicting the spatial distribution of the k-factor. The k-factor prediction map for the regions of interest are presented in Figures 2-8 and 2-9 [54].

## **2.5 Fading due to Precipitation**

When cloud particles are saturated with water vapour, they become too heavy to remain suspended in the troposphere and they fall under gravity to the ground as precipitation. Precipitation which is one of the classes of hydrometeors is called rain when it falls in form of liquid water.

Rainfall is a natural phenomenon which causes an attenuation considered as the most dominant fading mechanism for different microwave and millimetric line of sight links [31]. The severity of rain impairment increases with frequency and varies from year to year with location to locations especially in equatorial and tropical regions [56]. There exists a frequency threshold above which the rain attenuation becomes the most important parameter the performance of a microwave link. In the temperate climates this frequency threshold is about 10 GHz, while it is about 7 GHz in the tropical and equatorial climates due to the larger size of raindrops.

### **2.5.1 Rainfall Types**

Rainfall is classified into two major categories, namely: stratiform and convective rainfall [57, 58]; which are dependent on nature of cloud formation, condensation and strength of the rainfall. Stratiform rainfall is formed by weak nimbostratus clouds resulting in light drizzle and widespread rain usually in a large area. They extend up to 1 km across the vertical profile of the isotherm height with rain rates usually less than 10 mm/h [22]. On the other hand, convective rainfall is formed by strong cumulonimbus clouds which are often localized and reaching rain rates of up to 100 mm/h [57]. Ajayi et al. and Moupfouma in their studies, indicated that these types of rainfall (shower and thunderstorm) are normal at equatorial and tropical climates [32, 34]. In recent rainfall campaigns in Southern African regions, the rainfall is thus classified into four regimes as follows: drizzle ( $0 \text{ mm/h} \leq R < 5 \text{ mm/h}$ ); widespread ( $5 \text{ mm/h} \leq R < 10 \text{ mm/h}$ ); shower ( $10 \text{ mm/h} \leq R < 40 \text{ mm/h}$ ); and thunderstorm ( $R > 40 \text{ mm/h}$ ) [27].

## **2.6 Rainfall Rate Distribution Models**

Rainfall rate is the rate at which rain water reaches the ground [28]. The rainfall is a natural time varying phenomena which varies from year to year over different regions of the world [47]. When

it rains intensively, raindrops absorb and scatter radio waves in the lower atmosphere, leading to signal attenuation and reduction of the system availability and reliability. Rainfall rate distribution models are used to determine the point rainfall rate cumulative distribution  $R_{0.01}$  at 0.01% of time exceedance, which is a very important parameter to estimate the rainfall attenuation for a given location. Many statistical distributions of rainfall rate have been developed by earlier researchers. These include the Rice and Holmberg (R-H) [59], Dutton and Dougherty (D-D) [60,61], Moupfouma [58], Moupfouma and Martins [62], Douglas and Sims (D-S) [63], Ito and Hosoya (KIT) [64], ITU-R P.837 [12] and Crane global rain rate distribution [65-67] models, among others.

### 2.6.1 The ITU-R Rainfall Rate prediction Model

The ITU-R rainfall rate model has classified the whole globe into fifteen climatic rainfall zones based mainly on the temperature, terrain height, average rainfall and type of vegetations from different part of the world. This model is derived from ITU-R recommendation P.837-1 to P.837-7. The ITU-R P.837 Rain rate Model uses expressions from ITU-R P.838 to estimate the rainfall attenuation values for both terrestrial and earth-space microwave links. Figure 2-10 and Table 2-6 present ITU-R Rain rate climatic zones and their corresponding exceedance values.

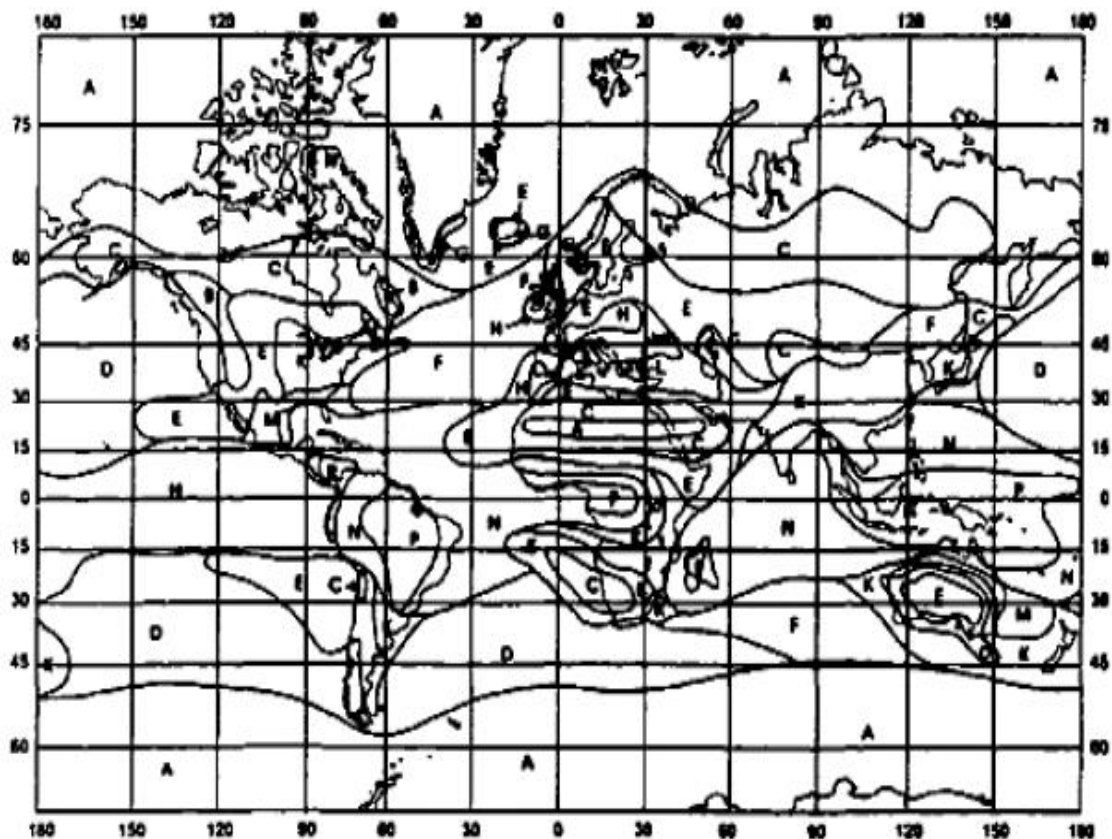


Figure 2-10: World ITU-R rainfall rate map [12]

Table 2-6: ITU-R Rain rate climatic zones [12]

Percentage of time (%)	A	B	C	D	E	F	G	H	J	K	L	M	N	P	Q
1.0	<0.1	0.5	0.7	2.1	0.6	1.7	3	2	8	1.5	2	4	5	12	24
0.3	0.8	2	2.8	4.5	2.4	4.5	7	4	13	4.2	7	11	15	34	49
0.1	2	3	5	8	6	8	12	10	20	12	15	22	35	65	72
0.03	5	6	9	13	12	15	20	18	28	23	33	40	65	105	96
0.01	8	12	15	19	32	28	30	32	35	42	60	63	95	145	115
0.003	14	21	26	29	41	54	45	55	45	70	105	95	140	200	142
0.001	22	32	42	42	70	78	65	83	55	100	150	120	180	250	170

### 2.6.2 The Global Crane Rainfall Rate Prediction Model

Crane classified the world into eight climatic rainfall rate zones (A to H), varying from dryness to wetness [67] based on total rain accumulation from maps published by Landsberg in 1974 [68]. A and B are the driest zones (arctic) while G and H correspond to the wettest zones (Tropical) [50]. E and F represent the sub-tropical zone while, C represents the temperate region. From available data, zone D was subdivided into three zones (D1, D2 and D3) while B into B1 and B2. Figure 2-11 and Table 2-7 present the Global Crane Rain rate climatic zones and their corresponding exceedance values.

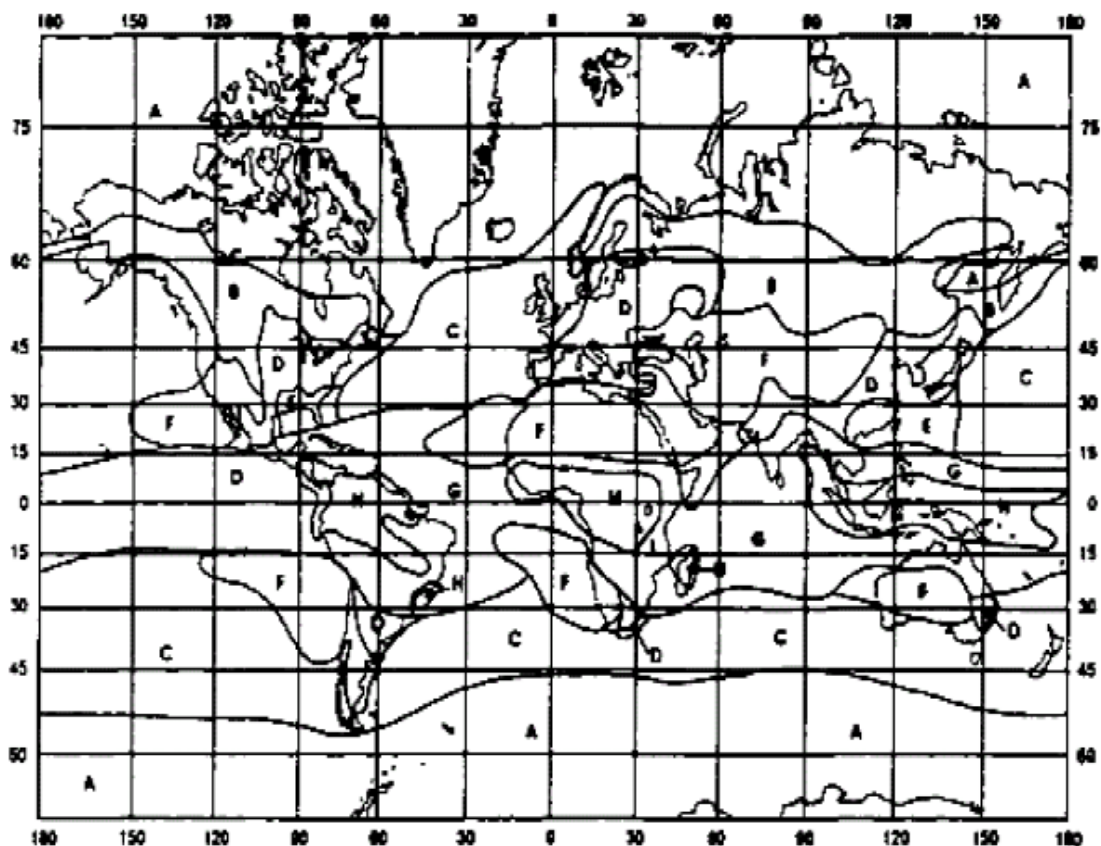


Figure 2-11: Global Crane rainfall climatic zone [21]

Table 2-7: The Global Crane Rain Rate Model [21]

% of the year	A	B	B1	B2	C	D1	D2	D3	E	F	G	H
1.0	0.2	1.2	0.8	1.4	1.8	2.2	3.0	4.6	7.0	0.6	8.4	12.4
0.5	0.5	2.0	1.5	2.4	2.9	3.8	5.3	8.2	12.6	1.4	13.2	22.6
0.3	1.1	2.9	2.2	3.4	4.1	5.3	7.6	11.8	18.4	2.2	17.7	33.1
0.2	1.5	3.8	2.9	4.4	5.2	6.8	9.9	15.2	24.1	3.1	22.0	43.5
0.1	2.5	5.7	4.5	6.8	7.7	10.3	15.1	22.4	36.2	5.3	31.3	66.5
0.05	4.0	8.6	6.8	10.3	11.5	15.3	22.2	31.6	50.4	8.5	43.8	97.2
0.03	5.5	11.6	9.0	13.9	15.6	20.3	28.6	39.9	62.4	11.8	55.8	125.9
0.02	6.9	14.6	11.3	17.6	19.9	25.4	34.7	47.0	72.2	15.0	66.8	152.4
0.01	9.9	21.1	16.1	25.8	29.5	36.2	46.8	61.6	91.5	22.2	90.2	209.3
0.005	13.8	29.2	22.3	35.7	44.4	49.2	62.1	78.7	112.0	31.9	118.0	283.4
0.003	17.5	36.1	27.8	43.8	50.6	60.4	75.6	93.5	130.0	41.4	140.8	350.3
0.002	20.9	41.7	32.7	50.9	58.9	69.0	88.3	106.6	145.4	50.4	159.6	413.9
0.001	28.1	52.1	42.6	63.8	71.6	86.6	114.1	133.2	176.0	70.7	197.0	542.6

## 2.7. Rain Drop Size Distribution Models

The raindrop size distribution (DSD), denoted by  $N(D)$ , is the number of raindrops at a given diameter per unit volume. It varies with respect to the region, season, year and depends on factors such as rainfall rate wind and rainfall types [69]. The knowledge of the drop size distribution is a very important parameter for a system designer to make a proper estimate of the attenuation due to rain. That is why there is need to develop a statistical model for rainfall DSD from measurements in the region of interest to facilitate a reliable prediction of the rain attenuation. Generally, according to Afullo [27], Marzuki et al. [70], Owolawi [71], the measured rainfall DSD can be estimated as:

$$N(D) = N_T f(D) \quad (2.14)$$

Where  $N_T (m^{-3})$  is the raindrop concentration per unit volume of rainfall drops and  $f(D)$  is the probability density function of the raindrop distribution in  $mm^{-1}$ . Many researchers such as: Marshall and Palmer [72], Atlas and Ulbrich [73,74], Sekine and Lind [75], Ajayi and Olsen [25], Jiang et al. [76] have developed several DSD models in different climatic regions and their corresponding input fit-parameters are estimated by the method of moments and maximum likelihood estimation techniques [27,69]. Several DSD models are proposed. These comprise the Negative exponential (Marshall-Palmer), Lognormal, Weibull and the modified Gamma drop size distributions.

### 2.7.1 Lognormal Rainfall Drop Size Distribution Model

The three parameter Lognormal rainfall DSD model is given in [25, 77-79] as:

$$N(D) = \frac{N_T}{\sigma D \sqrt{2\pi}} \exp \left\{ -\frac{1}{2} \left[ \frac{\ln(D) - \mu}{\sigma} \right]^2 \right\} \quad [m^{-3}mm^{-1}] \quad (2.15)$$

Where  $N_T$  is the drop concentration,  $\mu$  is the mean shape parameter,  $\sigma$  is the standard deviation of the drop sizes and  $D$  is the mean drop diameter which is obtained directly from rainfall data. In 1985, Ajayi and Olsen applied the method of moment technique to estimate the input DSD fit-parameters for this distribution using rainfall measurement collected at Ile-Ife in Nigeria. Using regression technique, the three lognormal parameters  $N_T$ ,  $\mu$  and  $\sigma$  are derived from the observed spectrum for rain event and they are related to rainfall rate,  $R$ , as given by [25]:

$$N_T = a_o R^{b_o} \quad (2.16)$$

$$\mu = A_\mu + B_\mu \ln(R) \quad (2.17)$$

$$\sigma^2 = A_\sigma + B_\sigma \ln(R) \quad (2.18)$$

Where  $R$  is the rainfall rate,  $a_o$ ,  $b_o$ ,  $A_\mu$ ,  $B_\mu$ ,  $A_\sigma$ , and  $B_\sigma$  are regression coefficients which depend on the region of interest and are presented in Table 2-8. In 1996, Adimula and Ajayi extended their results using three years rainfall data collected at Ile-Ife and other two locations, (Zaria and Calabar) in Nigeria. They arranged and categorised the rainfall measurement into four different rainfall regimes based on rainfall rates as follows: drizzle ( $0 \text{ mm/h} \leq R < 5 \text{ mm/h}$ ); widespread ( $5 \text{ mm/h} \leq R < 10 \text{ mm/h}$ ); shower ( $10 \text{ mm/h} \leq R < 40 \text{ mm/h}$ ); and thunderstorm ( $R > 40 \text{ mm/h}$ ). The authors averaged and optimised their results to obtain expressions for the four different rain regimes; and their results are shown in Table 2-9.

In later studies researchers such as Das and Maitra in 2010 [69], Alonge and Afullo in 2011 [27], Adetan and Afullo in 2012 [26], have shown that the Lognormal DSD model tends to give a better fit with the observed drop size distributions in tropical and sub-tropical regions; as it gives good estimation in the region with high rainfall rates and poor rainfall drop size distribution estimation at low rainfall rates.

Table 2-8: Lognormal DSD parameters for tropical rains by Ajay and Olsen in 1985 [25].

Type of rain	$N_T = a_o R^{b_o}$		$\mu = A_\mu + B_\mu \ln(R)$		$\sigma^2 = A_\sigma + B_\sigma \ln(R)$	
	$a_o$	$b_o$	$A_\mu$	$B_\mu$	$A_\sigma$	$B_\sigma$
Tropical rains	108	0.363	-0.195	0.199	0.137	0.013

Table 2-9: Lognormal DSD parameters for different rainfall types by Ajayi and Adimula in 1996 [80]

Type of rain	$N_T = a_0 R^{b_0}$		$\mu = A_\mu + B_\mu \ln(R)$		$\sigma^2 = A_\sigma + B_\sigma \ln(R)$	
	$a_0$	$b_0$	$A_\mu$	$B_\mu$	$A_\sigma$	$B_\sigma$
Drizzle ( $0 \text{ mm/h} \leq R < 5 \text{ mm/h}$ )	718	0.399	-0.505	0.128	0.038	0.013
Widespread ( $5 \text{ mm/h} \leq R < 10 \text{ mm/h}$ )	264	0.232	-0.473	0.174	0.161	0.018
Shower ( $10 \text{ mm/h} \leq R < 40 \text{ mm/h}$ )	137	0.370	-0.414	0.234	0.223	-0.034
Thunderstorm ( $R > 40 \text{ mm/h}$ )	63	0.491	-0.178	0.195	0.209	-0.030

Table 2-10. Estimated parameter of Lognormal Model in Durban using MoM technique [26]

Type of rain	$N_T = a_0 R^{b_0}$		$\mu = A_\mu + B_\mu \ln(R)$		$\sigma^2 = A_\sigma + B_\sigma \ln(R)$	
	$a_0$	$b_0$	$A_\mu$	$B_\mu$	$A_\sigma$	$B_\sigma$
Drizzle	284.81	0.5662	-0.3312	0.1252	0.0755	0.0106
Widespread	342.25	0.4225	-0.3981	0.2431	0.0784	-0.0008
Shower	452.27	0.1222	-0.4794	0.2952	0.0725	0.0049
Thunderstorm	41.461	0.3871	0.2183	0.0875	0.0621	0.0085

Table 2-11. Estimated parameter of Lognormal Model in Durban using MLE technique [26]

Type of rain	$N_T = a_0 R^{b_0}$		$\mu = A_\mu + B_\mu \ln(R)$		$\sigma^2 = A_\sigma + B_\sigma \ln(R)$	
	$a_0$	$b_0$	$A_\mu$	$B_\mu$	$A_\sigma$	$B_\sigma$
Drizzle	266.78	0.5662	-0.224	0.1239	0.213	0.0423
Widespread	263.3	0.4225	-0.2214	0.1339	0.1691	0.0897
Shower	458.11	0.1222	-0.3605	0.209	0.1647	0.1024
Thunderstorm	225.9	0.3871	-0.6496	0.2755	0.8082	-0.083

Later in 2012, using disdrometer data collected at the University of KwaZulu-Natal, Durban over twenty seven months (October 2008 to December 2010), Adetan [28], applied the method of moment (MoM) and the maximum likelihood estimation (MLE) technique to compute the model parameter for the Lognormal distribution and results are presented in Table 2-10 and 2-11. In his findings, Lognormal distribution parameters with MoM were found to give a better prediction compared with those obtained with MLE technique.

### 2.7.2 Modified Gamma Rainfall Drop Size Distribution Model

The modified Gamma rainfall DSD model was initially proposed by Atlas and Ulbrich in 1974, and it is given by [73-74, 78, 81]:

$$N(D) = N_m(D)^\mu \exp(-\Lambda D) \quad [m^{-3}mm^{-1}] \quad (2.19)$$

Where  $N(D)$  is the rain drop size distribution,  $D$  is the mean drop diameter,  $N_m$  is the scaling parameter,  $\mu$  is the shape parameter, and  $\Lambda$  is the slope parameter of the distribution.

The shape parameter  $\mu$  is fixed to 2 or 3 in most cases. The other remaining parameters  $\Lambda$  and  $N_m$ , are fitted against measured rainfall rate,  $R$  as:

$$N_m = a_m(R)^{b_m} \quad (2.20)$$

$$\Lambda = a_\Lambda(R)^{b_\Lambda} \quad (2.21)$$

Where  $a_m, b_m, a_\Lambda$  and  $b_\Lambda$  are regression coefficients. The modified Gamma distribution has been applied in both tropical and sub-tropical region of Singapore and Taiwan [82-83], India [69], USA [84] South Africa [27, 71, 85], Malaysia [86], Nigeria [25] and so on. It has responded well to the observed drop size distributions at both low and high rainfall rates [73]. Alonge used the modified gamma distribution in Durban and determined its annual and seasonal (Table 2-12) input fit parameters. For the annual,  $\mu=2$ , and  $N_m = 53522R^{-0.183}$  and  $\Lambda = 5.98R^{-0.172}$ . For Singapore, Timothy et al. [79] arrived on  $\mu=3$ ,  $N_m = 31444.3R^{0.244}$  and  $\Lambda = 5.753R^{0.032}$ .

Table 2-12: Seasonal Model parameters for different rainfall DSD models in Durban, South Africa [81]

Lognormal DSD model						
Input parameters	$N_T = a_0 R^{b_0}$		$\mu = A_\mu + B_\mu \ln(R)$		$\sigma^2 = A_\sigma + B_\sigma \ln(R)$	
	$a_0$	$b_0$	$A_\mu$	$B_\mu$	$A_\sigma$	$B_\sigma$
Summer	376.7	0.4505	-0.416	0.116	0.0816	0.0125
Autumn	139.13	0.3752	-0.2671	0.1454	0.0667	0.0081
Winter	35.78	0.163	0.2467	0.2163	0.0611	0.003
Spring	155.6	0.4077	-0.1922	0.1338	0.0849	0.0099
Modified Gamma DSD Model						
Input parameters	$\mu$	$N_m = a_m(R)^{b_m}$		$\Lambda = a_\Lambda(R)^{b_\Lambda}$		
		$a_m$	$b_m$	$a_\Lambda$	$b_\Lambda$	
Summer	2	132000	-0.103	6.8345	-0.16	
Autumn	2	68944	-0.194	6.2056	-0.174	
Winter	2	2420.9	-0.535	3.7854	-0.227	
Spring	2	26524	-0.156	5.4019	-0.168	
Weibull DSD model						
Input parameters	$\beta = a_\beta(R)^{b_\beta}$		$\gamma = a_\gamma(R)^{b_\gamma}$		$N_w = a_w(R)^{b_w}$	
	$a_\beta$	$b_\beta$	$a_\gamma$	$b_\gamma$	$a_w$	$b_w$
Summer	2.5048	-0.153	0.616	0.1014	571.78	0.4677
Autumn	2.8453	-0.11	0.7438	0.1404	345.78	0.3806
Winter	3.0063	-0.046	1.2564	0.2162	51.78	0.1622
Spring	2.3298	-0.121	0.7799	0.1234	233.43	0.4211



For Europe, Jiang et al. [76] also used the gamma distribution and arrive at parameters  $\mu=2$ ,  $N_m = 64500R^{-0.5}$  and  $\Lambda = 7.09R^{-0.27}$ .

### 2.7.3 Negative Exponential Drop Size Distribution Model

A special case of (2.19) occurs when the shape parameter  $\mu=0$  then, the modified Gamma rainfall drop size distribution becomes the Negative exponential rainfall DSD model given by [72]:

$$N(D) = N_0 \exp(-\Lambda D) \quad [m^{-3}mm^{-1}] \quad (2.22)$$

Where the inputs parameters for the Negative exponential rainfall DSD model are similar to those of the modified Gamma rainfall DSD model in (2.19). The Negative exponential rainfall DSD model was initially proposed by Marshall-Palmer in 1948 [72] for all rain types and later in 1968 by Joss et al. for different rainfall types [87]. In their work, Marshall-Palmer in 1948, the model parameters were determined as:

$$N_0 = 8000 \text{ mm}^{-1}m^{-3} \quad 2.22(a)$$

$$\Lambda = 4.1^{-0.21} \quad 2.22(b)$$

Where  $N_0$  and  $\Lambda$  are Marshall-Palmer scale and slope parameters, respectively.

In 1968, using rain drop size distribution data collected with a disdrometer installed in Switzerland, Joss *et al.* observed that the drop distribution varies with rainfall type noticeably. The model parameter values for drizzle, widespread and thunderstorm rainfall types are presented in Table 2-13. Researchers such as: Ajayi and Olsen [25], Massambani [88], Green [89], and Jiang et al. [75] have identified the inadequacy of the Marshall-Palmer model in the regions with high rainfall rates. It is found to perform best only in the regions with low rainfall intensity and temperate climates.

Table 2-13: Negative exponential parameters for different rainfall types [87]

Type of rain	N <sub>0</sub>	$\Lambda = a_{\Lambda}(R)^{b_{\Lambda}}$	
		$a_{\Lambda}$	$b_{\Lambda}$
Drizzle	30000	5.7	-0.21
Widespread	7000	4.1	-0.21
Thunderstorm	1400	3.0	-0.21

#### 2.7.4. Weibull Rainfall Drop Size Distribution Model.

In 1982, Sekine and Lind first proposed the Weibull distribution to estimate the attenuation due to rain in the range of centimetric, milimetric and sub-milimetric waves. This distribution is expressed as proposed by Sekine et al. [75-76,90] by:

$$N(D_i) = N_w \left(\frac{\beta}{\gamma}\right) \left(\frac{D}{\gamma}\right)^{\beta-1} \exp \left[ -\left(\frac{D}{\gamma}\right)^\beta \right] \quad (2.23)$$

Where  $D$  (mm) is drop diameter,  $\beta$  is the shape parameter,  $\gamma$  is the scale parameter and  $N_w$ , the modified parameter. In 1997, Jiang, Sano and Sekine used this distribution and found that,  $N_o=1000 \text{ m}^{-3}$ ,  $\beta=0.95R^{0.14}$  and  $\gamma=0.26R^{0.44} \text{ mm}$  where  $R$  (mm/h) is the rainfall rate for drizzle, widespread and shower rain types.

The power law regression coefficients of the Weibull DSD Model in (2.23) are given by:

$$N_w = a_w (R)^{b_w} \quad (2.24)$$

$$\beta = a_\beta (R)^{b_\beta} \quad (2.25)$$

$$\gamma = a_\gamma (R)^{b_\gamma} \quad (2.26)$$

Where  $a_w$ ,  $b_w$ ,  $a_\beta$ ,  $b_\beta$ ,  $a_\gamma$  and  $b_\gamma$  are regression coefficients of the model parameters. The Weibull distribution performs closer to the modified gamma as it performs well for low and high rainfall rates [76]. Recently, Alonge applied the Weibull distribution to Durban rainfall data and arrived on  $N_o = 328.68R^{0.4042}$ ,  $\beta = 2.5771R^{-0.125}$  and  $\gamma = 0.7264R^{0.1272}$  [91]

## 2.8 Rainfall Specific Attenuation

The rainfall specific attenuation or attenuation per unit length over a fixed radio link is a fundamental quantity in the calculation of the attenuation due to rain statistics for both terrestrial and earth-space paths. The total value of specific rain attenuation can be computed by integrating each raindrop contribution as given by [22]:

$$A_s [dB/Km] = 4.343 \times 10^{-3} \int_0^\infty Q_{ext}(D) N(D) dD \quad (2.27)$$

Where  $A_s$  is the specific rain attenuation,  $N(D)$  is the drop size distribution,  $N(D) dD$  is the number density of raindrops with diameter  $D$  in the interval  $dD$  and;  $Q_{ext}$ , the extinction cross-section, which is determined from classical scattering theory developed by Mie for frequencies above 3 GHz.

Research has also shown that, the rainfall specific attenuation  $A_S$  (dB/km), can be determined from the rainfall rate  $R$  (mm/h) using the following power law expression [92-94]:

$$A_S = kR^\alpha \quad [dB/Km] \quad (2.28)$$

Where  $k$  and  $\alpha$  are the power-law coefficients depending on frequency of transmission, raindrop size distribution, rain temperature and polarization. They are obtained from expressions below:

$$k = [k_H + k_V + (k_H - k_V)\cos^2\theta \cos 2\tau]/2 \quad (2.29)$$

$$\alpha = [k_H\alpha_H + k_V\alpha_V + (k_H\alpha_H - k_V\alpha_V)\cos^2\theta \cos 2\tau]/2k \quad (2.30)$$

Where  $\theta$  is the path elevation angle and  $\tau$  is the polarization tilt angle relative to the horizontal; circular polarization,  $\tau=45^\circ$ . Where coefficients,  $k_H$  and  $\alpha_H$  are for horizontal polarization while,  $k_V$  and  $\alpha_V$  are for vertical polarization accessible in ITU-R P.838-3 (see Appendix B-1) [92].

## 2.9 Chapter Summary and Conclusion

In this chapter, clear-air multipath propagation fading, diffraction, attenuation due to rain and other tropospheric effects on a microwave and millimetre link have been presented. Rainfall as the main impairment to the quality of the received signal, is examined in details. A review of different rainfall rate, raindrop size distribution and specific rain attenuation models are discussed. The next chapter will focus on the rainfall zoning and rain attenuation mapping for microwave and millimetric applications in Central Africa.

## **Chapter Three**

### **Rainfall Zoning and Rain Attenuation Mapping for Microwave and Millimetric Applications in Central Africa**

#### **3.1 Introduction**

In this chapter, point rainfall measurements spanning a minimum of 10 years are obtained from the Rwanda Meteorology Agency (Meteo Rwanda) databank for 60 locations in Rwanda. Results from rainfall data analysis are subsequently applied in the mapping of rainfall rate and rain attenuation statistics required for link budget in terrestrial and satellite communication systems in Rwanda. The rest of this chapter shall be as follows. Section 3.2 discusses climatic characteristics of Rwanda; Section 3.3 focuses on the determination of rainfall statistics of rain rate distribution over Rwanda; Section 3.4 gives an insight into the determination of specific attenuation for different locations; and finally, Section 3.5 gives the conclusion of this chapter.

#### **3.2 Climatic characteristics of Rwanda and rainfall rate models**

In this section, the climatic features of Rwanda are discussed and some candidate rainfall rate models are presented.

##### **3.2.1 Rwanda climatic features**

Rwanda is a landlocked country located in the Central African belt geographically lying between latitudinal coordinates of 1°04'S and 2°51'S and longitudinal coordinates of 28° 45'E and 30°15'E [95]. The country area covers about 26,338 km<sup>2</sup> in landmass and is bordered by four countries: Democratic Republic of Congo to the West, Uganda to the North, Tanzania to the East, and Burundi to the South as presented in Figure 3-1. The countryside area consists of grasslands and rolling hills with altitude varying from 900 m to 4500 m, from the south-western area to the northern part of the country [96]. With close proximity to the equator, the generic terrain is of high elevation rendering the temperate with tropical features. In general, the average annual temperature around the country varies between 18°C and 24°C, although areas with altitude above 2000 m above surface level may experience temperature as low as 0°C [96].

The country experiences four seasons in a yearly cycle, which are determined by the variability of rainfall. More often, these seasons include a dual rainy season (from March to the beginning of June and from mid-September to December) interspersed between two dry seasons (from January to February and from June to mid-September). The annual rainfall accumulation ranges

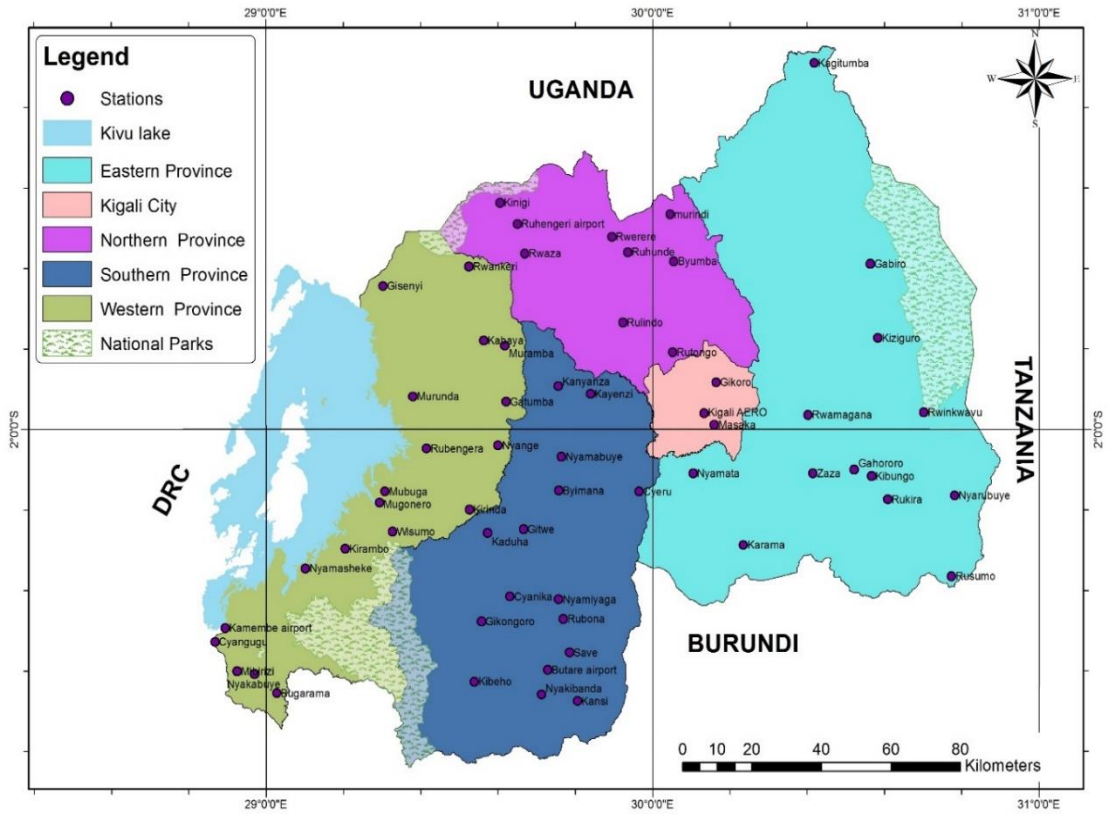


Figure 3-1: The geographical map of Rwanda, Central Africa.

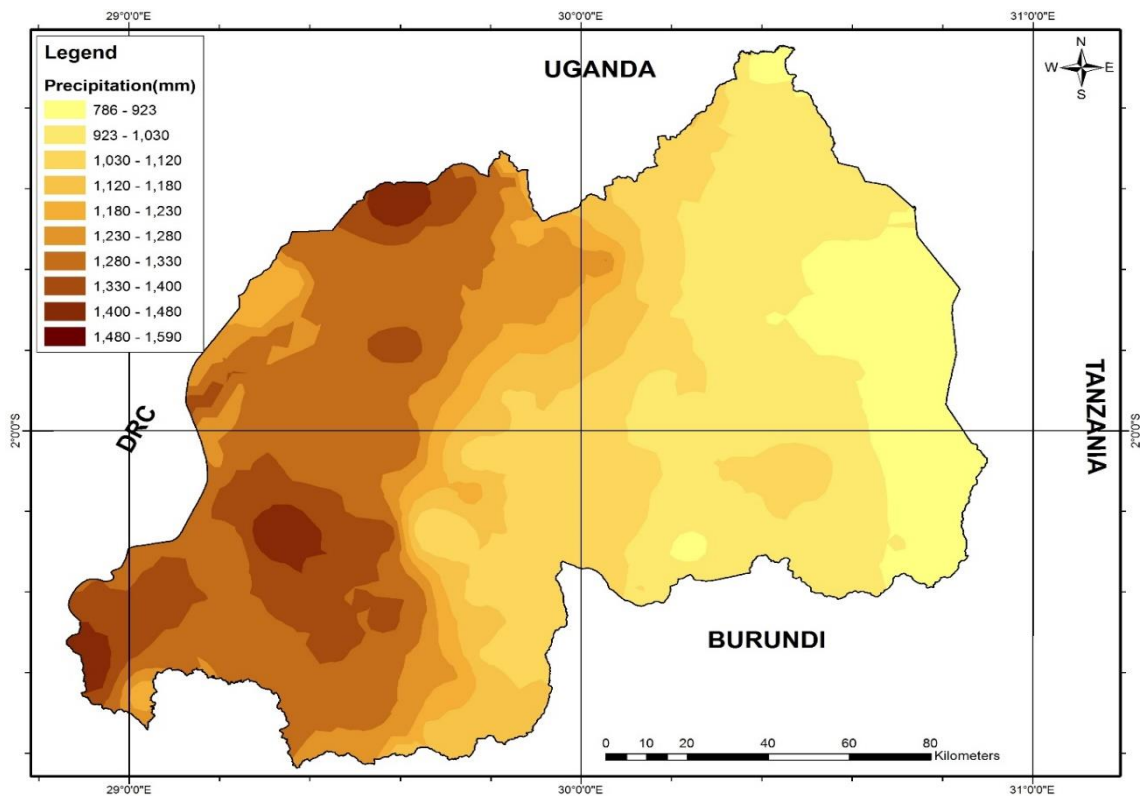


Figure 3-2: Rwanda rain accumulation contour map.

between 900 mm and 1600 mm, but with more intense rainfall in the Western and North-western mountains than the Eastern savanna [96] as shown in Figure 3-2.

The classification of the Rwanda climate is undertaken using the Köppen-Geiger climatic classification by matching the native vegetation and climatic phenomenon around the country [97]. Using this approach, the Southern province has two classes (Aw, Cwb) but dominated by Aw; Northern province has three classes (Aw, Cwb, Cfb), but mostly dominated by Aw; and the Western province has three classes (Aw, Cfb, Cwb), but mostly dominated by Aw and Cfb. Areas around the capital city, Kigali, and the Eastern province all belong to the tropical class given by Aw. Broadly speaking, according to the Köppen-Geiger climate classification, Rwanda can therefore be categorized as having equatorial-continental temperate type of climate, otherwise known as Tropical Savanna (Aw) [98].

### **3.2.2 Rainfall rate distribution modelling**

The reliability of wireless networks operating at microwave and millimetre-wave bands is often constrained by the intensity of rainfall for a particular locality. It is therefore usual for radio engineers to include the contribution of rainfall attenuation to overall link budget to guarantee satisfactory performance of radio links all year round. To achieve this, the point rain rate  $R_{0.01}$  (in mm/h), *i.e.* rainfall rate exceeded for 0.01% of an average year, is determined from rain rate measurements of one-minute integration time. Not unusually, rainfall measurements at one-minute integration time are often scarce to obtain in Africa, and by extension, in Rwanda. However, many meteorological agencies across different African countries regularly archive rainfall data of longer integration time often hourly and daily measurements which are obtained from networks of rain gauges. In the absence of appropriate one-minute data rainfall data, there exist some other valid rain rate climatological models to convert rainfall data from long integration time to short integration time. These rain rate models may suffice as alternatives for evaluating rainfall parameters for designing wireless communication systems operating at microwave and millimetre wave bands. For example, Ojo *et al.* [56] approached this peculiar problem by considering a combination of Chebil model [99], Moupfouma model [100] and the International Telecommunication Union (ITU) standards in [12], [3], and [94] to develop rain attenuation maps over Nigeria. In their publication, the Chebil model was initially used to compute rainfall rate exceeded at 0.01% from hourly rain gauge rainfall measurements. Thereafter, the Moupfouma model was used to generate series of exceedance values and their corresponding rainfall rates from the generated distribution curve.

Following the approach by Ojo *et al.* [56], the parameter,  $R_{0.01}$ , over Rwanda is first determined using the rainfall dataset obtained from long-term measurements of mean annual rainfall

accumulation,  $M$ , from various locations. An approximation of this parameter is obtained from the Chebil power-law function given by [99]:

$$R_{0.01} = \alpha M^\beta \quad (3.1)$$

Where,  $\alpha$  and  $\beta$  are power-law coefficients dependent on  $M$  (mm), obtained from rainfall measurements undertaken at tropical locations of Malaysia, Indonesia, Singapore, Brazil and Vietnam [99]. The Chebil coefficients of  $\alpha$  and  $\beta$  in (3.1) are defined as 12.2903 and 0.2973, respectively [99].

Secondly, the Moupfouma model is applied to generate rain rate distribution dataset from specific parameters. This model is a location-specific tool for describing the rainfall rate distribution while giving preference to regional and climatic characteristics [19,100]. The model is derived from 1-minute integration time rain rate measured from tipping bucket rain gauges and is most appropriate for both tropical and temperate climates. The cumulative distribution of rain rate from this model is given by:

$$P(R \geq r) = 10^{-4} \left( \frac{R_{0.01}}{r + 1} \right)^b \exp[u(R_{0.01} - r)] \quad (3.2)$$

Where  $r$  is the rain rate exceeded for a specified period of time in mm/h,  $R_{0.01}$  is the rainfall rate availability at 99.99% or rain rate exceedance at 0.01 %, in an average year (mm/h). The parameter  $b$  is defined as:

$$b = \left( \frac{r}{R_{0.01}} - 1 \right) \ln \left( 1 + \frac{r}{R_{0.01}} \right) \quad (3.3)$$

The parameter  $u$  determines the slope of rain rate cumulative distribution in (3.2) and is heavily dependent on both the climatic and geographic characteristics of the investigated locality. This parameter is given by:

$$u = \frac{\ln(10^4)}{R_{0.01}} \exp \left( -\lambda \left[ \frac{r}{R_{0.01}} \right]^\gamma \right) \quad (3.4)$$

In (3.4), the parameters of  $\lambda$  and  $\gamma$  are given as 1.066 and 0.214 for tropical and subtropical regions respectively. By combining the Chebil and Moupfouma models, rain rate cumulative distributions of one-minute integration time for different locations in tropical Rwanda can be estimated.

Furthermore, the prediction of specific attenuation due to rain at these locations can be embarked upon given the knowledge of rain exceedences.

### 3.3 Determination of rainfall rate statistics over Rwanda

This section presents rainfall statistics from the Chebil and Moupfouma models, as generated from long term rainfall data for Rwanda. Rainfall rate contour maps for 0.1% and 0.01% of time exceeded in Rwanda are presented.

#### 3.3.1 Local Rainfall Measurements at Locations in Rwanda

To facilitate the application of the proposed rain rate distribution models, a reliable source of long term rainfall measurements is required for different sites in Rwanda. For this purpose, daily rainfall measurements for 60 stations were obtained from the Rwanda Meteorology Agency (Meteo Rwanda) databank, spanning a minimum period of 10 years. Meteo Rwanda employs rain gauge networks to collect rainfall rate measurements on a daily basis across different field stations in Rwanda. These measurements are indexed as rainfall accumulation data at different locations within the four provincial districts in Rwanda and the capital, Kigali. Tables 3-1a to 3-1d present some important information related to the climatic characteristics of the locations under study. In these tables, information provided for each station includes the geographic coordinates (Latitude and Longitude), measurement period, altitude of stations and the corresponding Köppen classification.

Table 3-1a: Climatic characteristics of measurement Sites for Southern Province, Rwanda

Province	Station Name	Period (years)	Latitude (°S)	Longitude (°E)	Altitude(m)	Köppen class
Southern	Butare airport	29	02°36'	29°44'	1768	Aw
	Kansi	61	02°42'	25°45'	1670	Aw
	Nyamiyaga	45	02°24'	29°47'	1800	Aw
	Nyakibanda	51	02°38'	29°44'	1750	Aw
	Rubona	62	02°29'	29°46'	1706	Aw
	Save	83	02°33'	29°46'	1725	Aw
	Nyamabuye	10	02°05'	29°47'	1830	Cwb
	Byimana	31	2°11'	29°44'	1750	Aw
	Cyeru	29	02°13'	29°58'	1450	Aw
	Kanyanza	29	01°54'	029°47'	1500	Cfb
	Gitwe	12	02°14'	029°42'	1750	Aw
	Kayenzi	10	01°54'	029°51'	1800	Aw
	Gikongoro	29	02°29'	29°33'	1900	Cfb
	Cyanika	53	02°24'	29°35'	1950	Cwb
	Kaduha	34	02°14'	29°32'	1900	Cwb
Kibeho	55	02°39'	29°33'	1894	Cwb	



**Table 3-1b: Climatic characteristics of measurement Sites for Northern Province, Rwanda**

Province	Station Name	Period (years)	Latitude (°S)	Longitude (°E)	Altitude(m)	Köppen class
Northern	Kinigi	43	01°58'	30°08'	2200	Cfb
	Ruhengeri airport	63	01°30'	29°40'	1878	Cfb
	Rwaza	54	01°32'	29°41'	1800	Aw
	Rwerere	30	01°32'	29°53'	2312	Aw
	Byumba	59	01°36'	30°03'	2250	Cfb
	Ruhunde	31	01°56'	29°56'	2235	Aw
	Rulindo	61	01°43'	29°55'	1800	Aw
	Rutongo	29	01°48'	30°03'	1900	Aw
	murindi	10	01°29'	30°03'	2100	Aw

**Table 3-1c: Climatic characteristics of measurement Sites for Western Province, Rwanda**

Province	Station Name	Period (years)	Latitude (°S)	Longitude (°E)	Altitude(m)	Köppen class
Western	Kamembe airport	32	02°28'	28°55'	1591	Aw
	Bugarama	25	02°41'	29°00'	900	Aw
	Cyangugu	62	02°29'	28°53'	1525	Aw
	Mibirizi	54	02°00'	29°57'	1750	Cfb
	Nyamasheke	11	02°20'	29°05'	1500	Aw
	Nyakabuye	10	02°36'	29°02'	1400	Aw
	Rubengera	10	02°01'	29°25'	1700	Aw
	Kirambo	52	02°18'	29°11'	1465	Aw
	Kilinda	59	02°11'	29°34'	1650	Aw
	Mubuga	55	02°10'	29°19'	1650	Aw
	Mugonero	51	02°11'	29°17'	1680	Aw
	Murunda	58	01°54'	29°22'	1875	Aw
	Wisumo	21	02°17'	29°18'	2400	Aw
	Rwankeri	54	01°35'	29°32'	2250	Aw
	Nyange	12	02°03'	29°35'	1700	Aw
	Gisenyi	62	01°40'	29°15'	1554	Aw
	Kabaya	55	01°44'	29°32'	2550	Aw
Muramba	61	01°46'	29°37'	1950	Aw	
Gatumba	11	01°54'	29°38'	1600	Aw	

As seen from these tables, the average measurement period at each location is about 40 years, with the measurement range between 10 and 83 years. The average altitude for each location is about 1700 m, with Bugarama and Wisumo having the lowest and highest altitudes of 900 m and 2400 m, respectively. For Köppen classification, the considered locations broadly fall under two categories: tropical savanna (denoted by Aw) and warm temperate (denoted by Cfb and Cwb). In the summary in Tables 3-1a to 3-1d, there are ten measurement sites classified as warm temperate climate, while other sites are classified as tropical savanna.

Table 3-1d: Climatic characteristics of measurement Sites for Eastern Province and Kigali city, Rwanda

Province	Station Name	Period (years)	Latitude (°S)	Longitude (°E)	Altitude(m)	Köppen class
Eastern	Kibungo	57	02°10'	30°32'	1580	Aw
	Gahororo	29	02°10'	30°30'	1700	Aw
	Rukira	62	02°13'	30°35'	1500	Aw
	Rusumo	29	02°16'	30°44'	1450	Aw
	Rwamagana	29	01°57'	30°25'	1550	Aw
	Zaza	64	02°08'	30°25'	1515	Aw
	Rwinkwavu	12	01°58'	30°38'	1420	Aw
	Nyarubuye	29	02°12'	30°45'	1750	Aw
	Gabiro	29	1°38'	30°24'	1472	Aw
	Kagitumba	49	02°03'	30°27'	1280	Aw
	Karama	62	02°17'	30°16'	1403	Aw
	Kiziguro	59	01°46'	30°25'	1550	Aw
Nyamata	28	02°09'	30°05'	1428	Aw	
Kigali	Kigali Airport	38	01°58'	30°08'	1495	Aw
	Gikoro	29	01°55'	29°15'	1650	Aw
	Masaka	20	02°00'	30°15'	1550	Aw

### 3.3.2 Rainfall Rate Distribution over Rwanda

As the focus of this study is to develop rain attenuation maps for application in link budget estimate for different parts of Rwanda, the initial step requires the estimation of point rain rate at 0.01% exceedence. This is obtained by considering the Chebil power-law model for tropical locations already described in (3.1). This model is applied by considering the average annual rainfall accumulation for the years under audit at different locations.

In Tables 3-2a to 3-2d, results obtained from the application of Chebil model over rainfall measurements over Rwanda is presented for 60 stations under consideration. From the tables, it is observed that locations with higher rain accumulation have a corresponding higher rain rate at 0.01%. A breakdown of provincial locations with the highest and lowest values of  $R_{0.01}$  is briefly discussed. In the Southern Province, locations of Kaduha and Gitwe have  $R_{0.01}$  of 105.8 and 93.4 mm/h as the highest and lowest values, respectively. In the Northern Province, the paired location of Kinigi and Rutongo record 109.9 and 99.8 mm/h as the highest and lowest values of  $R_{0.01}$ . In the Western Province, these extremes are found at Wisumo and Gisenyi with values of 109.6 and 99.5 mm/h, respectively. In the East, Gahororo and Nyarubuye have the lowest and highest extremes of  $R_{0.01}$  with 89.2 and 99.9 mm/h, respectively.

Countrywide, the lowest and highest values of  $R_{0.01}$  are observed in Nyarubuye and Kinigi at 89.2 mm/h and 109.9 mm/h, respectively. Broadly speaking, locations around the Eastern Province

generally have the lowest values of  $R_{0.01}$  around the country; while the Northern and Western provinces are observed to experience higher values of  $R_{0.01}$  than any other province in Rwanda.

According to ITU-R P.838-3, the recommended rainfall rate,  $R_{0.01}$ , for Rwanda is roughly 70 mm/h [12]. This value is considerably lower than our current estimations from Chebil function, thereby under-estimating the actual rain rate occurrence across the country.

Having obtained  $R_{0.01}$  from the Chebil model, the Moupfouma rain rate model can be applied to determine rain rate cumulative distribution of one-minute integration time across locations in Rwanda. By applying equations (3.2) to (3.4), rainfall rate exceedences at 1%, 0.1%, 0.01% and 0.001% are obtained for 60 locations under study.

Table 3-2a: Rain rate exceeded at 0.01 ( $R_{0.01}$ ) for different locations in Southern Province, Rwanda from Chebil Model

Province	Station Name	Latitude (°S)	Longitude (°E)	$M(mm/year)$	$R_{0.01}(mm/h)$
Southern	Butare airport	02°36'	29°44'	1254	102.5
	Kansi	02°42'	25°45'	1158.1	100.1
	Nyamiyaga	02°24'	29°47'	1084.6	98.2
	Nyakibanda	02°38'	29°44'	1207.8	101.4
	Rubona	02°29'	29°46'	1175.2	100.5
	Save	02°33'	29°46'	1088.2	98.3
	Nyamabuye	02°05'	29°47'	1040.6	97.0
	Byimana	2°11'	29°44'	1240.8	102.2
	Cyeru	02°13'	29°58'	1042.5	97.0
	Kanyanza	01°54'	029°47'	1219.4	101.6
	Gitwe	02°14'	029°42'	918.95	93.4
	Kayenzi	01°54'	029°51'	1091.2	98.3
	Gikongoro	02°29'	29°33'	1354.7	104.9
	Cyanika	02°24'	29°35'	1331.9	104.3
	Kaduha	02°14'	29°32'	1397.1	105.8
Kibeho	02°39'	29°33'	1306.4	103.7	

Figures 3-3 to 3-6 present results obtained in Rwanda based on the four provinces and Kigali city at different exceedences. From these graphs, it is observed that values of rain rate at exceedence of 0.1% ( $R_{0.1}$ ) obtained from Moupfouma model are quite similar at all locations. However, at exceedence of 0.001% ( $R_{0.001}$ ), rain rates are higher in the Northern and Western provinces with values ranging between 160 and 190 mm/h. Again, we find that  $R_{0.001}$  values are lower at the Southern and Eastern provinces of Rwanda, largely as a result of lower average rainfall accumulation recorded from long term measurements.

Table 3-2b: Rain rate exceeded at 0.01 ( $R_{0.01}$ ) for different locations in Northern Province,  
Rwanda from Chebil Model

Province	Station Name	Latitude (°S)	Longitude (°E)	$M(mm/year)$	$R_{0.01}(mm/h)$
Northern	Kinigi	01°58'	30°08'	1588.1	109.9
	Ruhengeri airport	01°30'	29°40'	1331	104.3
	Rwaza	01°32'	29°41'	1285.7	103.3
	Rwerere	01°32'	29°53'	1212.1	101.5
	Byumba	01°36'	30°03'	1291.4	103.4
	Ruhunde	01°56'	29°56'	1302.7	103.7
	Rulindo	01°43'	29°55'	1238.7	102.1
	Rutongo	01°48'	30°03'	1146.9	99.8
	murindi	01°29'	30°03'	1156.9	100.1

Table 3-2c: Rain rate exceeded at 0.01 ( $R_{0.01}$ ) for different locations in Western Province,  
Rwanda from Chebil Model

Province	Station Name	Latitude (°S)	Longitude (°E)	$M(mm/year)$	$R_{0.01}(mm/h)$
Western	Kamembe airport	02°28'	28°55'	1425.9	106.5
	Bugarama	02°41'	29°00'	1155.5	100.0
	Cyangugu	02°29'	28°53'	1409.5	106.1
	Mibirizi	02°00'	29°57'	1504.7	108.2
	Nyamasheke	02°20'	29°05'	1353.5	104.8
	Nyakabuye	02°36'	29°02'	1326.8	104.2
	Rubengera	02°01'	29°25'	1197.6	101.1
	Kirambo	02°18'	29°11'	1202.6	101.2
	Kilinda	02°11'	29°34'	1307.8	103.8
	Mubuga	02°10'	29°19'	1371.5	105.3
	Mugonero	02°11'	29°17'	1363.6	105.1
	Murunda	01°54'	29°22'	1341.6	104.6
	Wisumo	02°17'	29°18'	1570.9	109.6
	Rwankeri	01°35'	29°32'	1262.6	102.7
	Nyange	02°03'	29°35'	1358.2	105.0
	Gisenyi	01°40'	29°15'	1136.7	99.5
	Kabaya	01°44'	29°32'	1358.4	105.0
	Muramba	01°46'	29°37'	1370.9	105.2
Gatumba	01°54'	29°38'	1271.4	102.9	

Table 3-2d: Rain rate exceeded at 0.01 ( $R_{0.01}$ ) for different locations in Eastern Province and Kigali City, Rwanda from Chebil Model

Province	Station Name	Latitude (°S)	Longitude (°E)	$M(mm/year)$	$R_{0.01}(mm/h)$
Eastern	Kibungo	02°10'	30°32'	984.7	95.4
	Gahororo	02°10'	30°30'	1151.3	99.9
	Rukira	02°13'	30°35'	1004.9	96.0
	Rusumo	02°16'	30°44'	906.1	93.1
	Rwamagana	01°57'	30°25'	981.1	95.3
	Zaza	02°08'	30°25'	1088.2	98.3
	Rwinkwavu	01°58'	30°38'	843.8	91.1
	Nyarubuye	02°12'	30°45'	786	89.2
	Gabiro	1°38'	30°24'	842.9	91.1
	Kagitumba	02°03'	30°27'	794.9	89.5
	Karama	02°17'	30°16'	836.4	90.9
	Kiziguro	01°46'	30°25'	904.1	93.0
Nyamata	02°09'	30°05'	1094.4	98.4	
Kigali	Kigali Airport	01°58'	30°08'	1008.4	96.1
	Gikoro	01°55'	29°15'	976.7	95.2
	Masaka	02°00'	30°15'	996.2	95.7

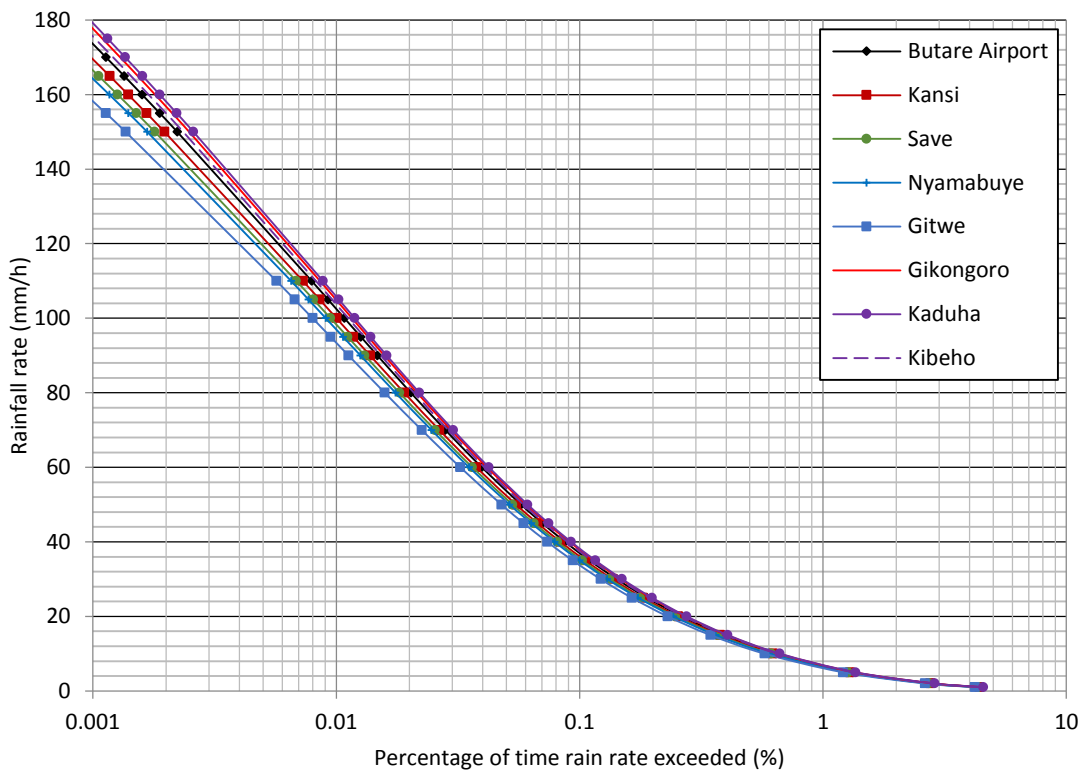


Figure 3-3: Cumulative distribution of rainfall rate for Southern Province, Rwanda using Moupfouma model.

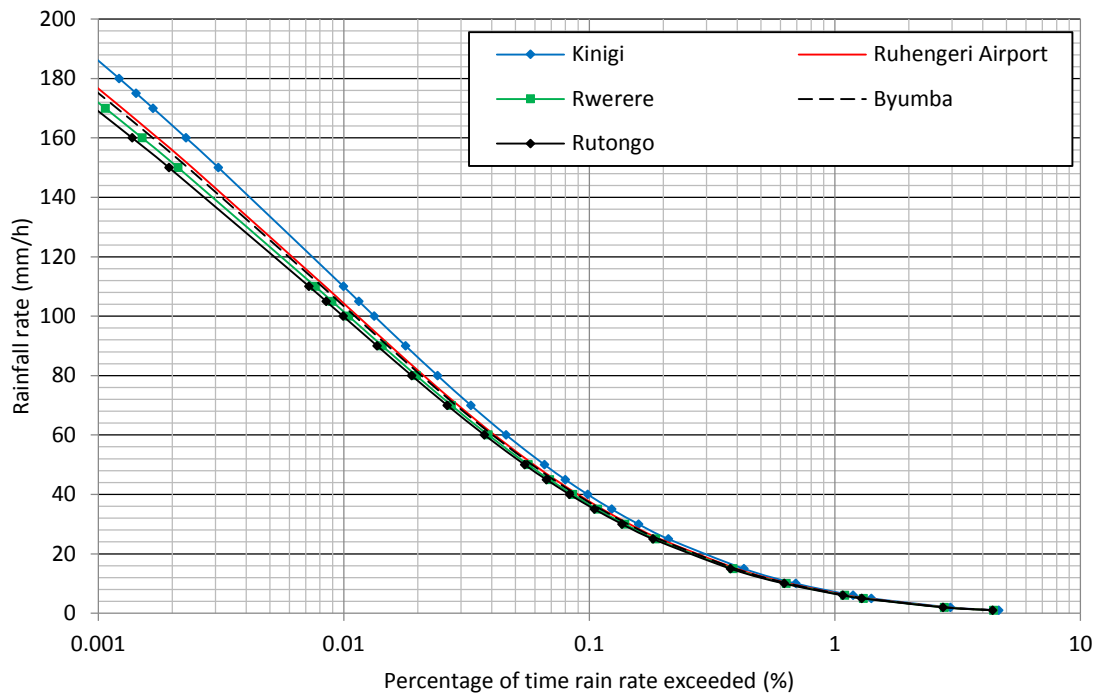


Figure 3-4: Cumulative distribution of rainfall rate for Northern Province, Rwanda using Moupfouma model.

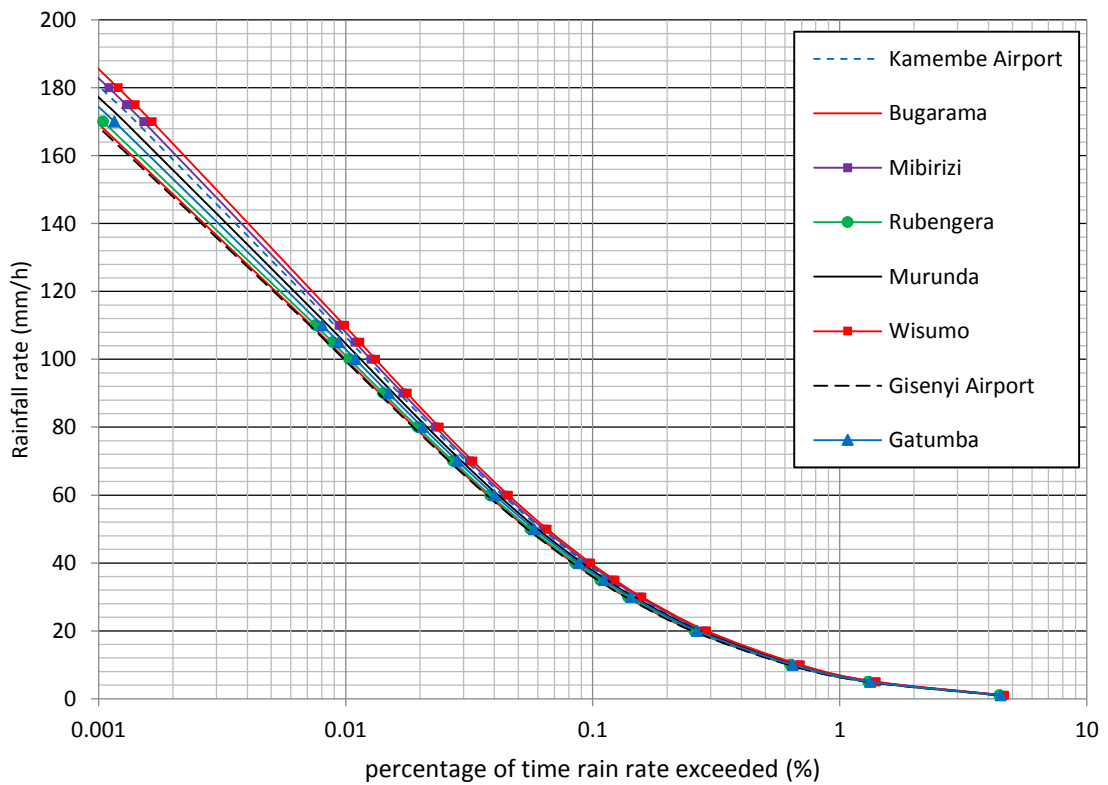


Figure 3-5: Cumulative distribution of rainfall rate for Western Province, Rwanda using Moupfouma model.

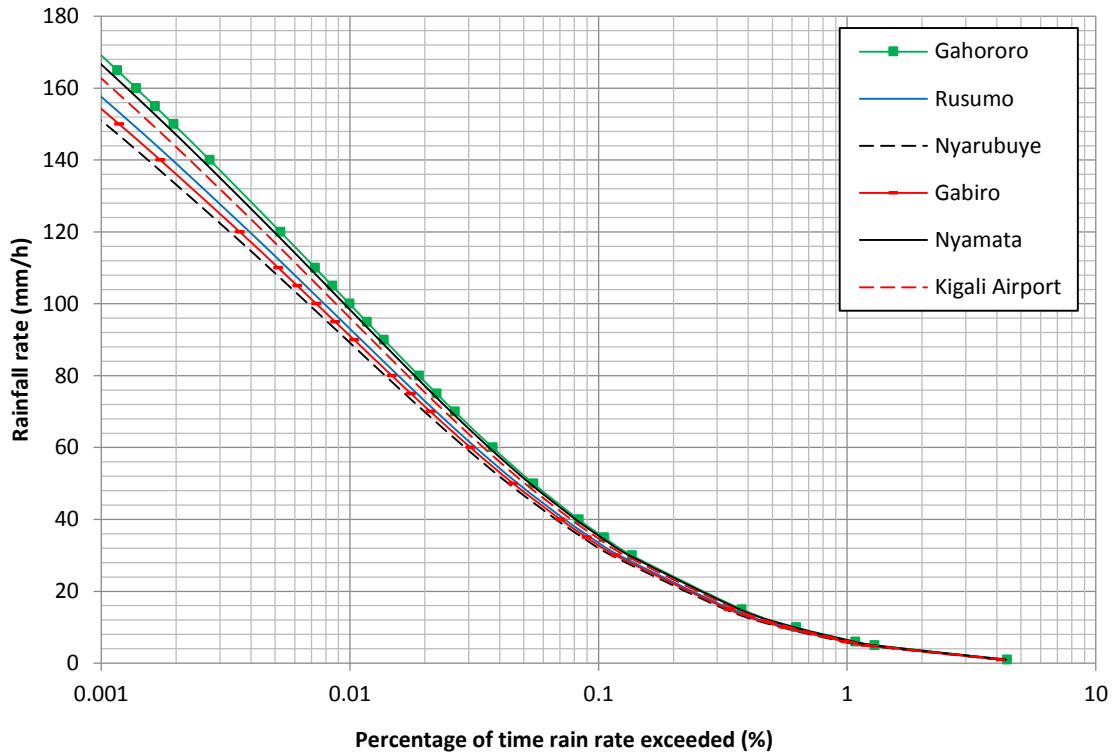


Figure 3-6: Cumulative distribution of rainfall rate for Eastern Province and Kigali City, Rwanda using Moupfouma model.

### 3.3.3 Rain Rate Contour Mapping over Rwanda

For the development of rain rate contour maps, dataset obtained from Moupfouma model in conjunction with Chebil model are applied as inputs. Therefore, by applying procedures described in equations (3.1) to (3.4) and using the equivalent parameters of all stations presented in Tables 3-2a to 3-2d as inputs, one-minute rain rate contour maps for Rwanda are developed. Contour maps for rain rate exceedences at 0.1% and 0.01% are shown in Figure 3-7 and 3-8 respectively. Each of these gridded contour maps were developed using a Geographic Information System (GIS) software platform, the ArcGIS®. Contour results from this software were sequenced by applying inbuilt gridding technique via the Kriging interpolation method, and, consequently mapping the generated contour outputs into targeted coordinate points on the digital map of Rwanda.

A quick look at Figure 3-7 shows that  $R_{0.1}$  varies from 31 to 38 mm/h, while in Figure 3-8,  $R_{0.01}$  varies from 89 to 110 mm/h, depending on the location. It is observed that locations lying around the Northern, Western and South-Western parts of Rwanda have the highest rainfall rates at both 0.1% and 0.01% rain rate exceedences. With the exception of some locations in the Western, Southern and Eastern with lower rain rate exceedences,  $R_{0.1}$  and  $R_{0.01}$  can be approximated to 37 mm/h and 105 mm/h respectively as seen from contour maps.

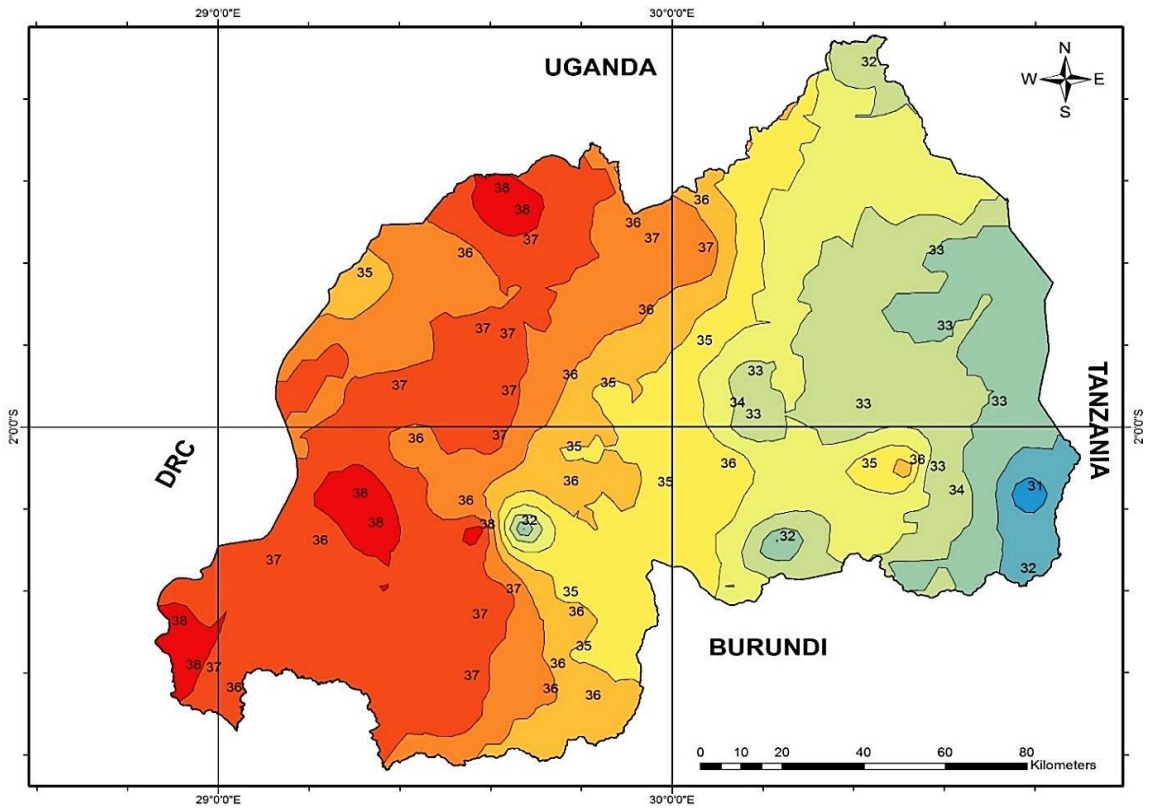


Figure 3-7: Rainfall Rate (mm/h) contour maps for 0.1% of time in Rwanda

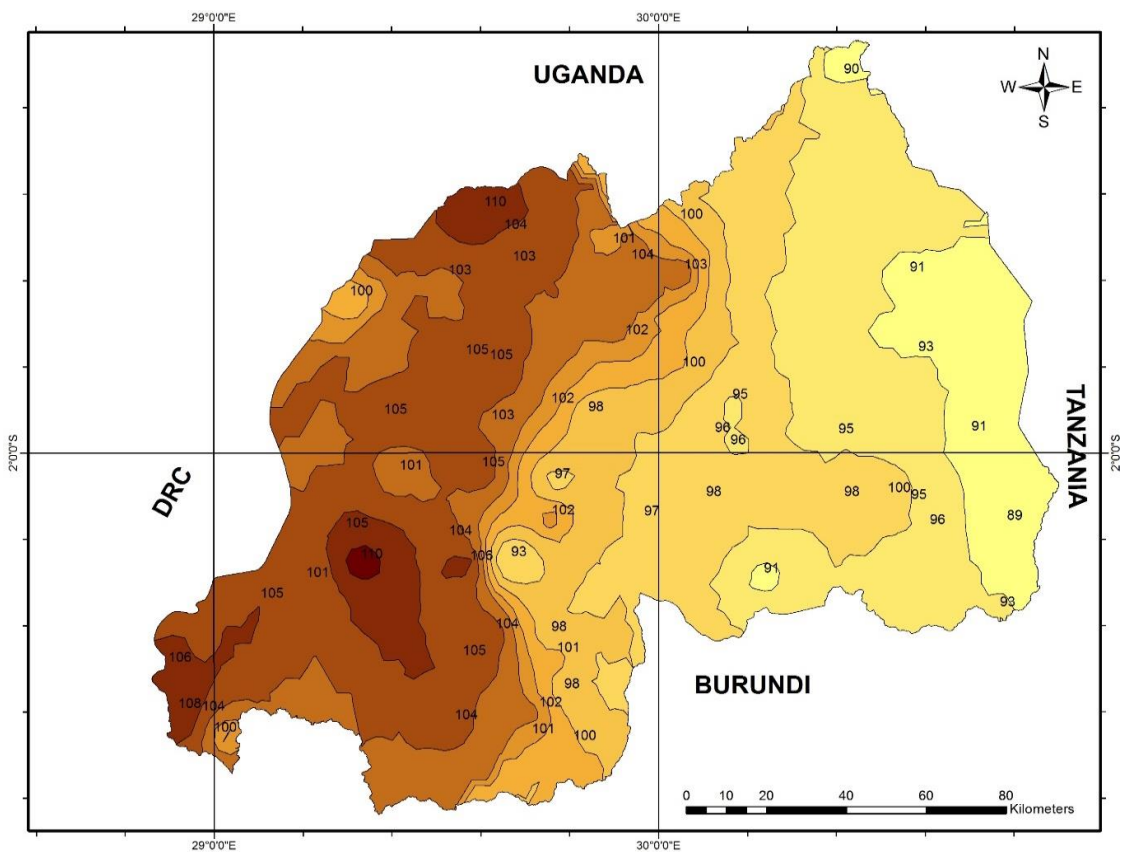


Figure 3-8: Rainfall Rate (mm/h) contour maps for 0.01% of time in Rwanda



It is also observed that at stations with close proximity to central Rwanda and some portion of the Eastern province close to Kigali,  $R_{0.1}$  and  $R_{0.01}$  may be roughly approximated to 35 mm/h and 95 mm/h respectively. Also, at other areas closer to the Eastern Province, approximations of 33 mm/h and 90 mm/h may suffice for  $R_{0.1}$  and  $R_{0.01}$ . In comparison to recommended value of  $R_{0.01}$  by ITU which ranges between 60-70 mm/h, we observe that higher values have been obtained in this current study everywhere in Rwanda [12]. It is proposed that the ITU-R rain rate zones in Rwanda be grouped as lying between the two zones of N and P depending on the location. Conclusively, variations in the estimated spatial values of  $R_{0.01}$  in Rwanda suggest that the Western part of the country tends to fall into rain zone P and Eastern part falls into rain zone N.

### 3.4 Rainfall Specific Attenuation

This section gives an insight into the determination of specific attenuation for different locations in Rwanda.

#### 3.4.1 Rainfall Specific Attenuation Statistics over Rwanda for Ku and Ka Bands

The description of specific attenuation per unit length over a fixed radio link is a fundamental quantity in the determination of rain attenuation statistics for both terrestrial and earth-space paths [20], [22]. Theoretically, ITU-R P.838-3 defines specific attenuation as having a power-law relationship with point rain rate given by [101]:

$$A_s = kR_{0.01}^\alpha \quad [dB/km] \quad (3.5)$$

Where  $k$  and  $\alpha$  are power-law coefficients related to the frequency of transmission for a given radio link.

In ITU-R P.838-3, design values for  $k$  and  $\alpha$  are presented for transmitting frequency ranging between 1 to 1000 GHz for proposed radio links operating at horizontal and vertical polarizations [101]. Therefore, these set of design parameters are utilized to estimate the expected specific attenuation due to rain for various radio links over Rwanda. As an expectation of future deployment of countrywide high-capacity terrestrial wireless networks, there is an inevitable migration towards carrier frequencies of Ku (15 GHz) and Ka (27 GHz) bands in the microwave and millimetre-wave spectrum. It is envisaged that these proposed bands will particularly improve the Quality of Service (QoS) of licensed wireless networks, while matching population growth in the future.

However, rainfall attenuation being an important factor in link budget analysis needs to be appropriately considered. Hence, by applying (3.5), specific attenuation due to rain at 60 locations across Rwanda is estimated from ITU standards.

Figures 3-9 to 3-12 present the computed cumulative distribution of specific attenuation of rain versus frequency for different locations in Rwanda based on the four provinces and the city of Kigali. From the plots, it is seen that, the specific attenuation increases sharply for 0-50 GHz, followed by a more gradual increment for 50-100 GHz; then remains practically constant up to 150 GHz; and finally decreases up to 300 GHz. For all those cases, it is seen that the specific rain attenuation for horizontal polarization is greater than vertical polarization for any frequency as expected.

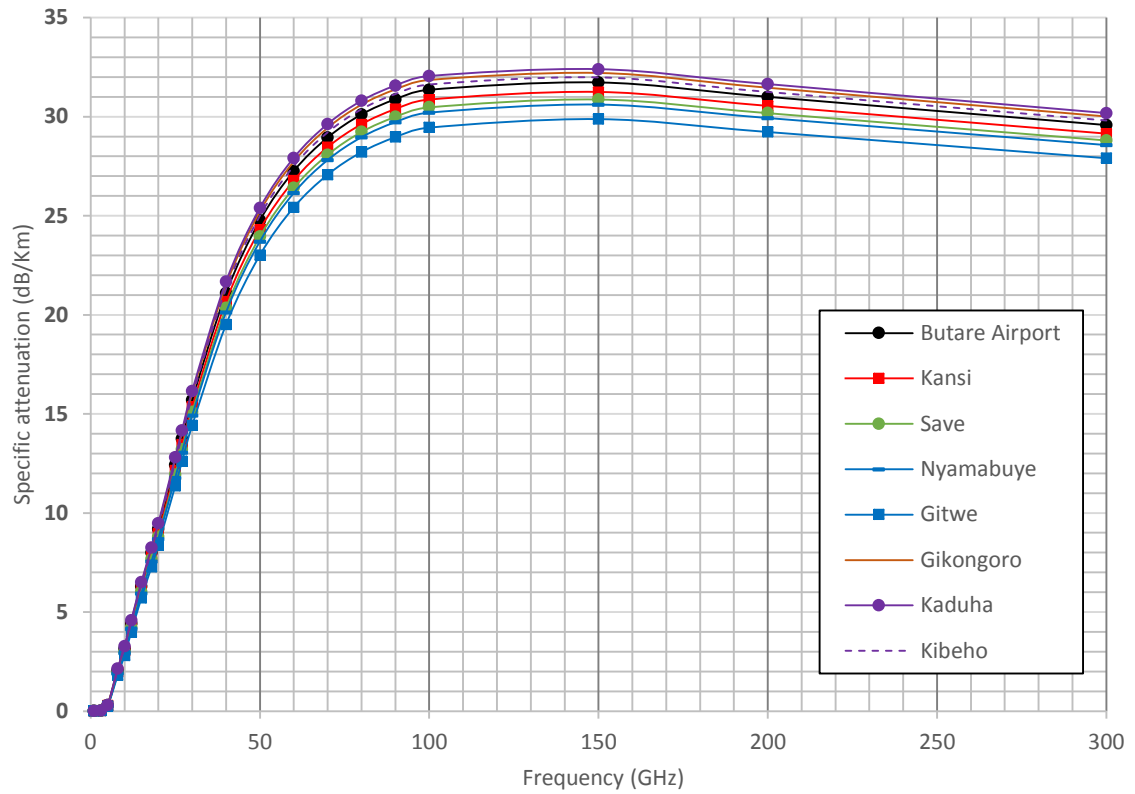
Table 3-3 presents the estimated specific attenuation at these different locations across Rwanda at a rain rate exceedance of 0.01%. As expected, the specific attenuation for horizontal polarization is greater than vertical polarization for any frequency, with a general average margin of 1.79 dB/km and 3.62 dB/Km at 15 and 27 GHz respectively, as seen in Table 3-3. These results imply that terrestrial radio links over Rwanda at 99.99% availability require more fade margins to resolve rain fade occurrences at the Northern and Western provinces, than other provinces, over the same path length. Otherwise, proposed radio links at these provinces must have shorter hop lengths to perform optimally during periods of rainfall at the same frequency.

As a direct consequence of the lower rainfall accumulation noticed at the Eastern province in subsection 3.3.2, specific attenuation is also found to follow the same trend at both 15 GHz and 27 GHz. Among various locations in this province, Nyarubuye is observed to have the least fade margin required to correct rain fade effects in Rwanda.

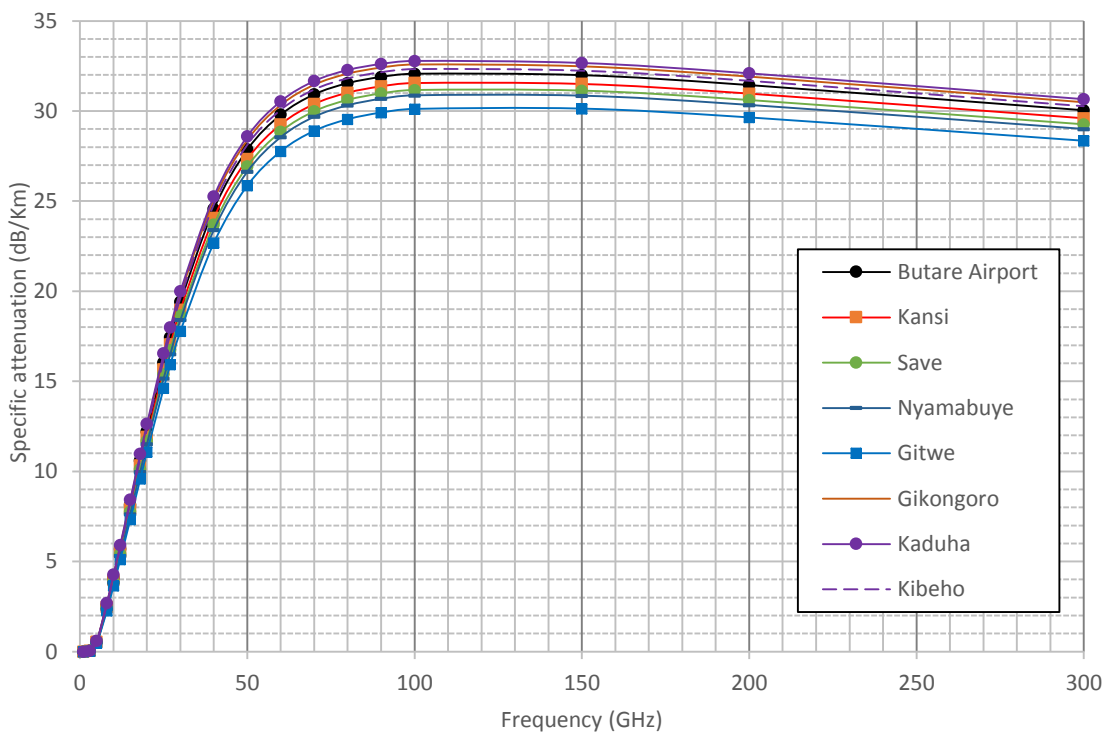
#### **3.4.2 Specific Attenuation Contour Mapping for Rwanda at 15 GHz and 27 GHz**

As part of the efforts to ensure minimum interference of wireless network service by rainfall events, radio link design should appropriately address signal deterioration at microwave and millimetre bands, especially in tropical and equatorial regions where Rwanda is located [7],[ 13]. Therefore, it is imperative to develop contour maps from ITU recommendations at 99.99% link availability, for terrestrial link deployments across Rwanda.

In line with this, specific attenuation was initially computed for different locations at rain rate exceedances of 0.1% and 0.01% of time. Thereafter, results from these computations were exported to ArcGIS® software to generate contour maps which demonstrate the spatial variation of specific attenuation over Rwanda. To this end, rainfall specific attenuation contour maps have been produced for the entire country for the design of future radio links operating at carrier frequencies of Ku-band (15 GHz) and Ka band (27 GHz). These bands are highly susceptible to rain attenuation effect, yet they present great opportunities in the future for network operators,

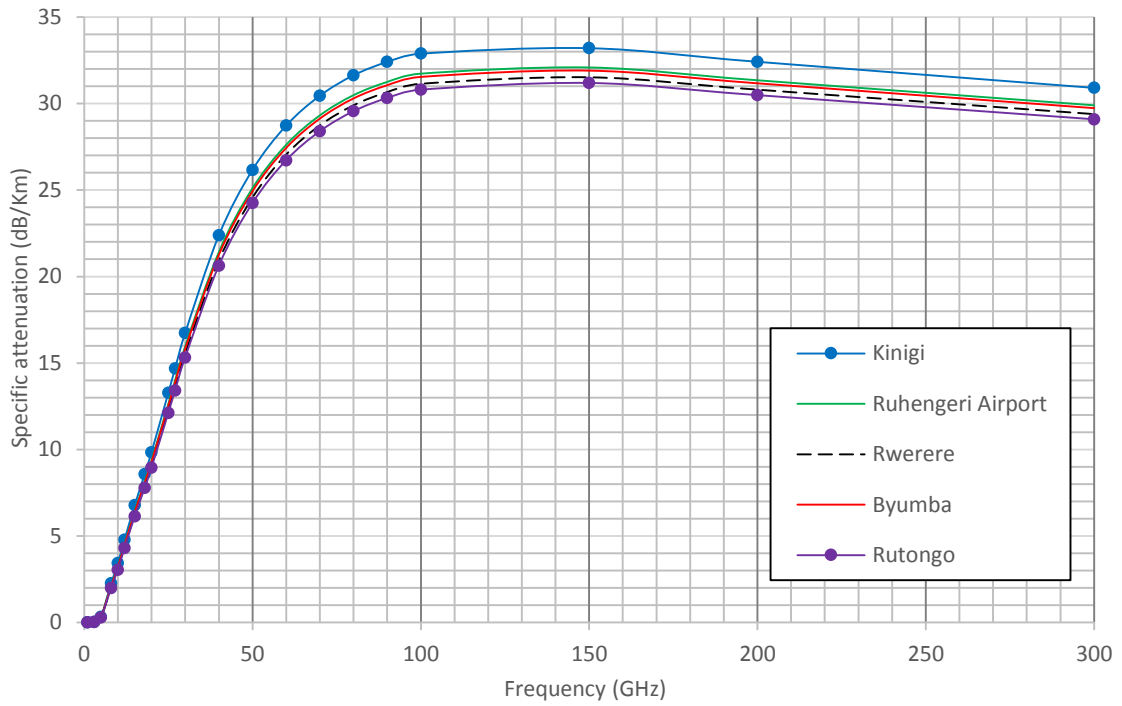


(a)

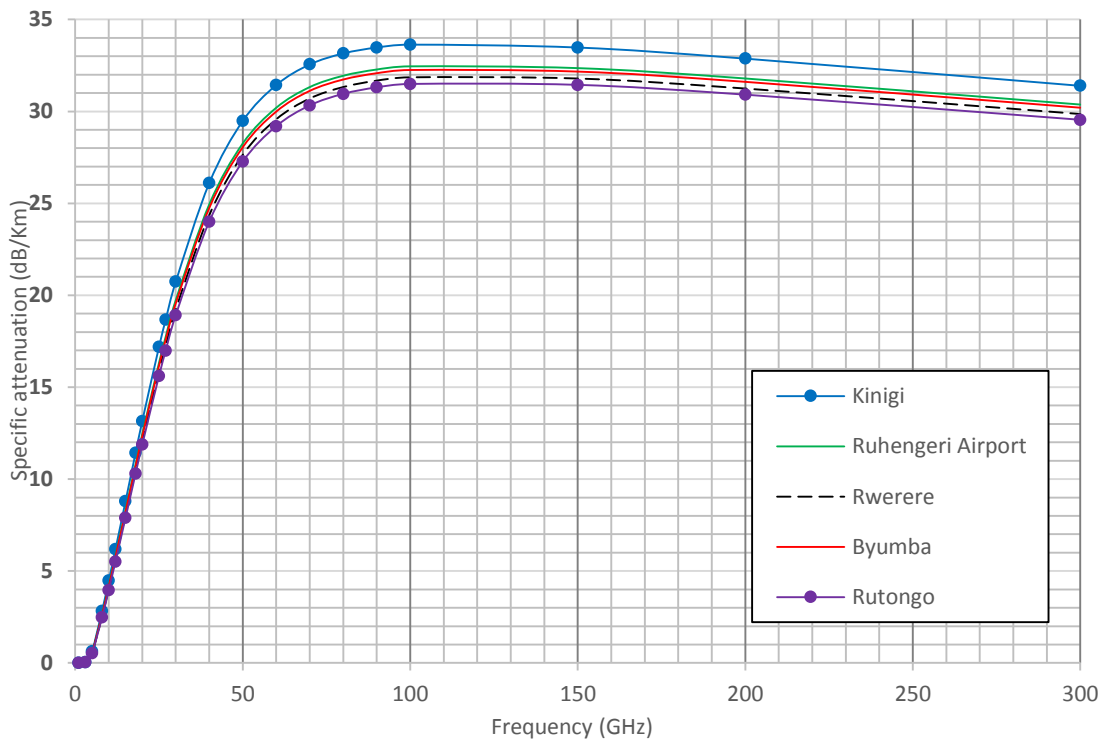


(b)

Figure 3-9: Frequency characteristics of specific rain attenuation signal for South Province, Rwanda (a) vertical polarization (b) horizontal polarization.

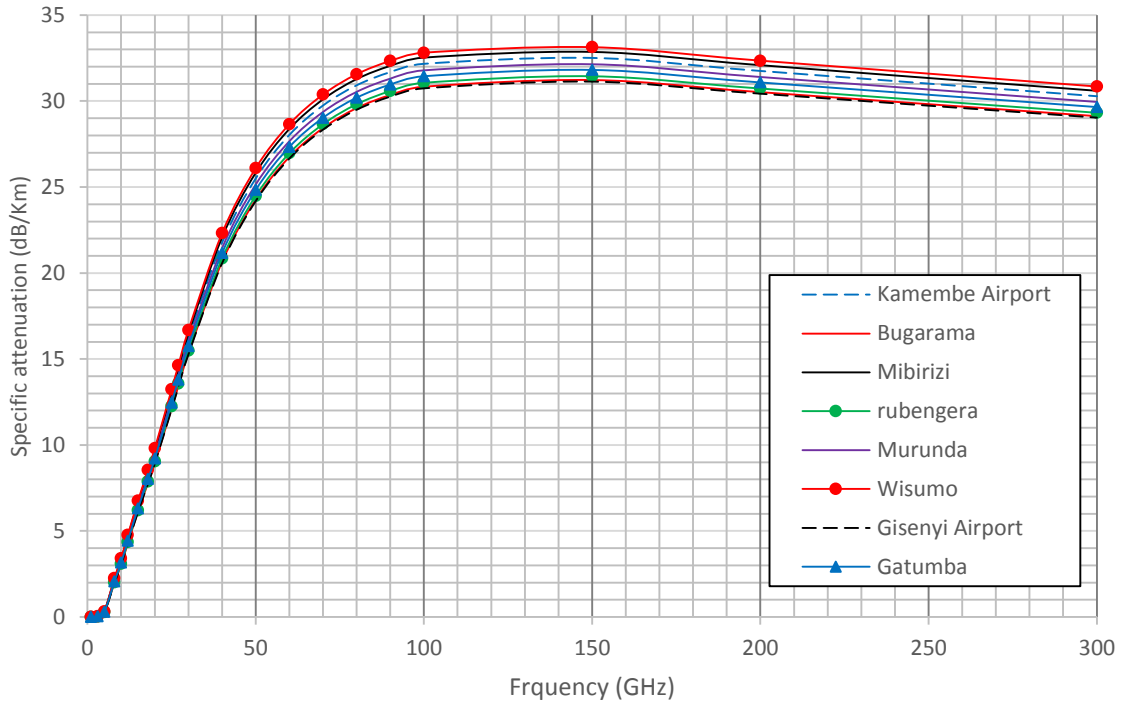


(a)

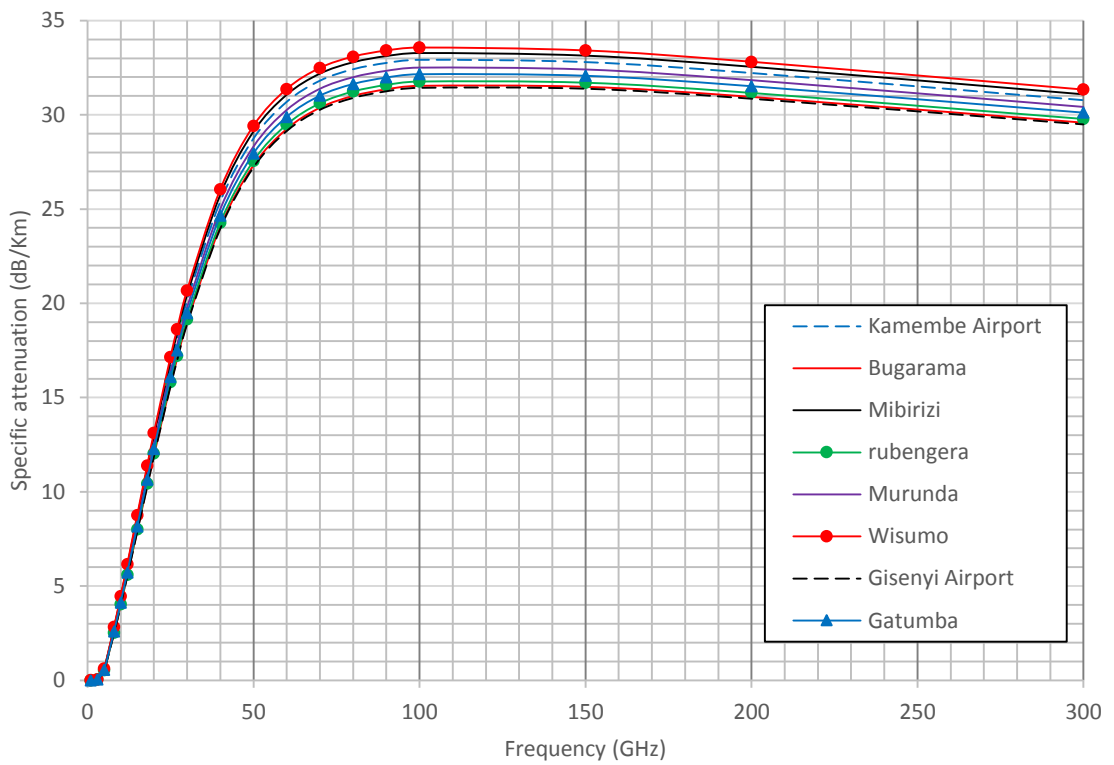


(b)

Figure 3-10: Frequency characteristics of specific rain attenuation signal for North Province, Rwanda (a) vertical polarization (b) horizontal polarization.

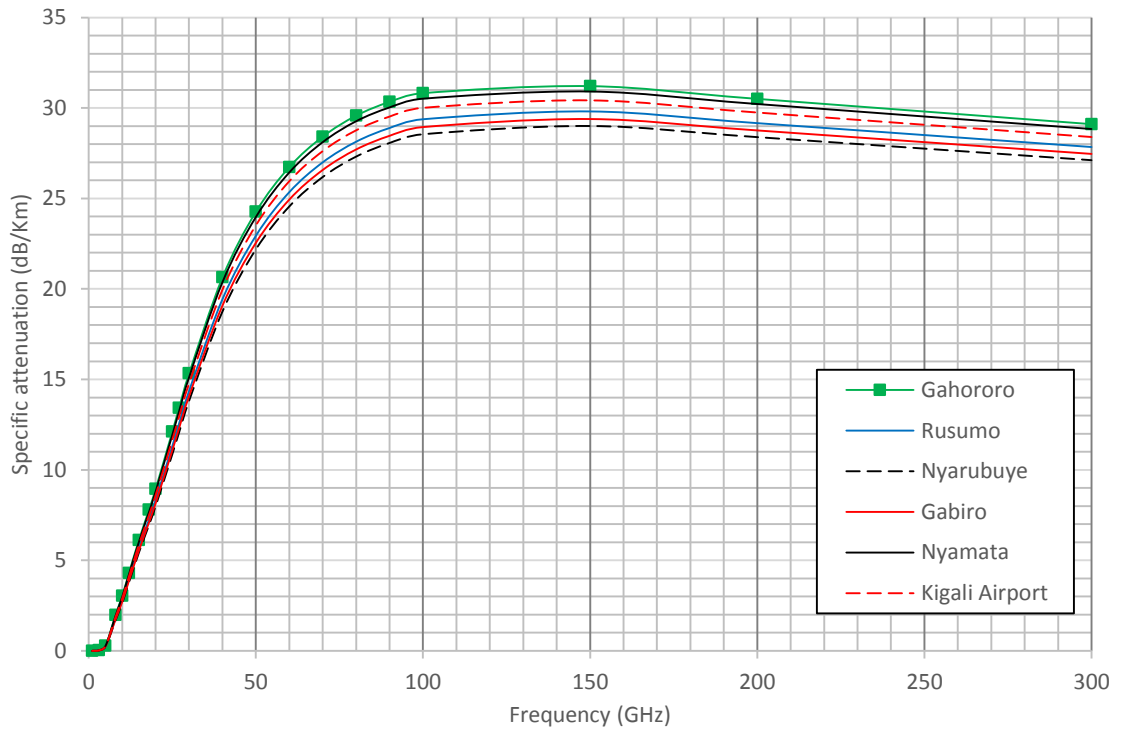


(a)

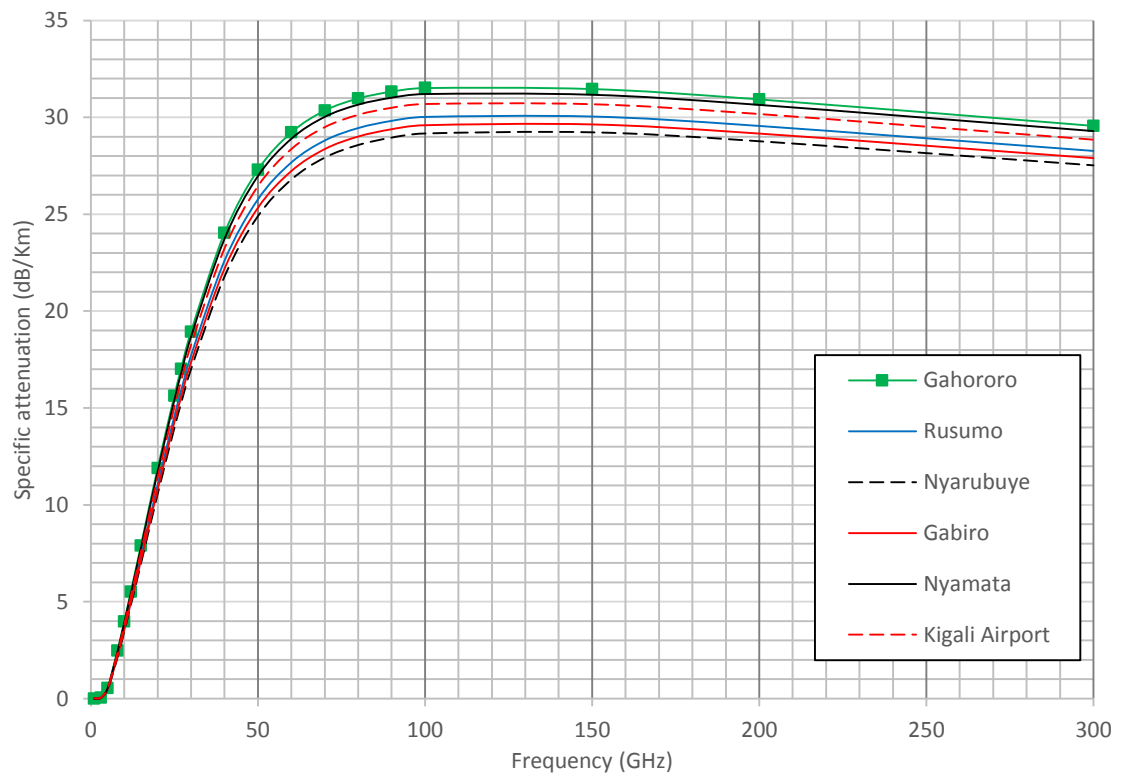


(b)

Figure 3-11: Frequency characteristics of specific rain attenuation signal for West Province, Rwanda (a) vertical polarization (b) horizontal polarization.



(a)



(b)

Figure 3-12: Frequency characteristics of specific rain attenuation signal for Eastern Province and Kigali City, Rwanda (a) vertical polarization (b) horizontal polarization.

Table 3-3: Estimated specific attenuation at  $R_{0.01}$  for Ka and Ku bands for different locations over Rwanda

Province	Station Name	$R_{0.01}$ (mm/h)	Rain Specific attenuation(dB/Km)			
			Vertical Polarization		Horizontal Polarization	
			15GHz	27GHz	15GHz	27GHz
Southern	Butare airport	102.5	6.3	13.7	8.1	17.4
	Kansi	100.1	6.1	13.4	7.9	17
	Save	98.3	6	13.2	7.8	16.7
	Nyamabuye	97.0	5.9	13.1	7.6	16.5
	Byimana	102.2	6.3	13.7	8.1	17.4
	Gitwe	93.4	5.7	12.6	7.3	15.9
	Kayenzi	98.3	6	13.2	7.8	16.7
	Gikongoro	104.9	6.4	14	8.3	17.8
	Kaduha	105.8	6.5	14.2	8.4	18
	Kibeho	103.7	6.4	13.9	8.2	17.6
Northern	Kinigi	109.9	6.8	14.7	8.8	18.7
	Ruhengeri airport	104.3	6.4	14	8.3	17.7
	Rwerere	101.5	6.2	13.6	8	17.3
	Byumba	103.4	6.3	13.9	8.2	17.6
	Rulindo	102.1	6.3	13.7	8.1	17.4
	Rutongo	99.8	6.1	13.4	7.9	17
	murindi	100.1	6.1	13.4	7.9	17
Western	Kamembe airport	106.5	6.6	14.2	8.5	18.1
	Bugarama	100.0	6.1	13.4	7.9	17.1
	Mibirizi	108.2	6.7	14.5	8.6	18.4
	Rubengera	101.1	6.2	13.6	8	17.2
	Murunda	104.6	6.4	14	8.3	17.8
	Wisumo	109.6	6.7	14.6	8.8	18.6
	Gisenyi	99.5	6.1	13.4	7.9	17.8
	Gatumba	102.9	6.3	13.8	8.1	17.5
Eastern	Kibungo	95.4	5.8	12.8	7.9	16.3
	Gahororo	99.9	6.1	13.4	7.9	17
	Rusumo	93.1	5.7	12.6	7.2	15.9
	Nyarubuye	89.2	5.4	12.1	7	15.2
	Gabiro	91.1	5.6	12.3	7.1	15.5
	Nyamata	98.4	6	13.2	7.8	16.8
Kigali City	Kigali airport	96.1	5.9	12.9	7.5	16.4
	Masaka	95.7	5.9	13	7.5	16.3

because of their channel capacity for larger carrier bandwidths required to meet the growing traffic demand of wireless services [102]. Generated contour maps for the required rain fade margin to mitigate rain attenuation at 0.01% are presented for 15 GHz and 27 GHz bands in Figure 3-13 and 3-14. For each figure, a set of contour maps showing vertical and horizontal polarization

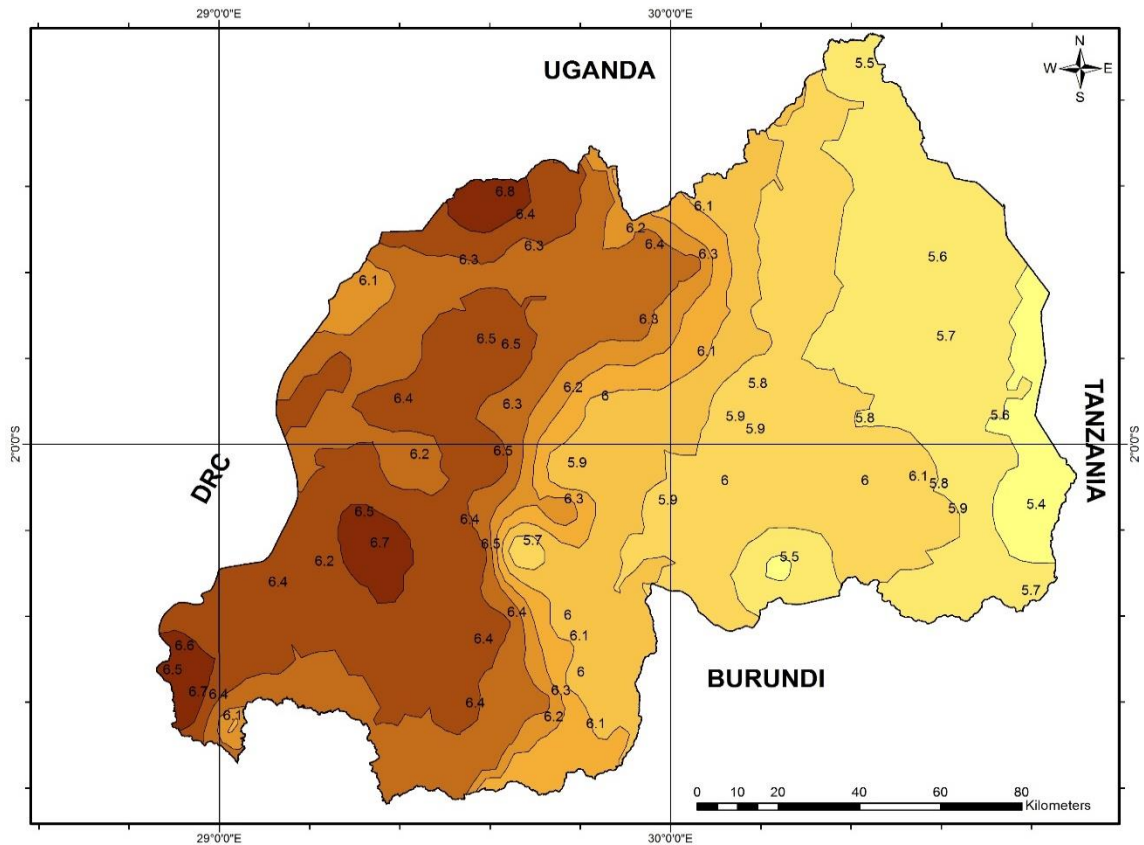
at each bands are available. Dataset used for this nationwide mapping considers the entire 60 locations in Rwanda investigated in this work.

From results in Figure 3-13, it is observed that in the Western, North-western and South-western parts of Rwanda where heavy rainfall is prevalent, predicted specific attenuation for 15 GHz at 0.01% exceedance varies from 6.4 to 6.8 dB/km for vertically polarization; and 8.2 to 8.8 dB/km for horizontally polarized links. In central Rwanda, specific attenuation values at 0.01% exceedance ranges from 5.9 to 6.4 dB/km for vertically polarized paths; and from 7.5 to 8.2 dB/km for 15 GHz horizontally polarized links. Towards the Eastern fringes, where lower rainfall is experienced, specific attenuation values are also lower, ranging between 5.4 to 5.9 dB/km for vertically polarized paths; and 7 to 7.5 dB/km for horizontally polarized paths. Applying this same analysis to Figure 3-14, the same trends are observed but with higher specific attenuation values since the carrier frequency is slightly higher at 27 GHz. Again, at the Western, North-western and South-western parts of Rwanda, specific attenuation for 27 GHz at 0.01% exceedance varies from 13.9 to 14.7 dB/km for vertically polarization; and 17.5 to 18.7 dB/km for horizontally polarized paths. In central Rwanda, specific attenuation values at 0.01% exceedance varies from 12.9 to 13.9 dB/km for vertically polarized paths and from 16.5 to 17.5 dB/km for horizontally polarized paths.

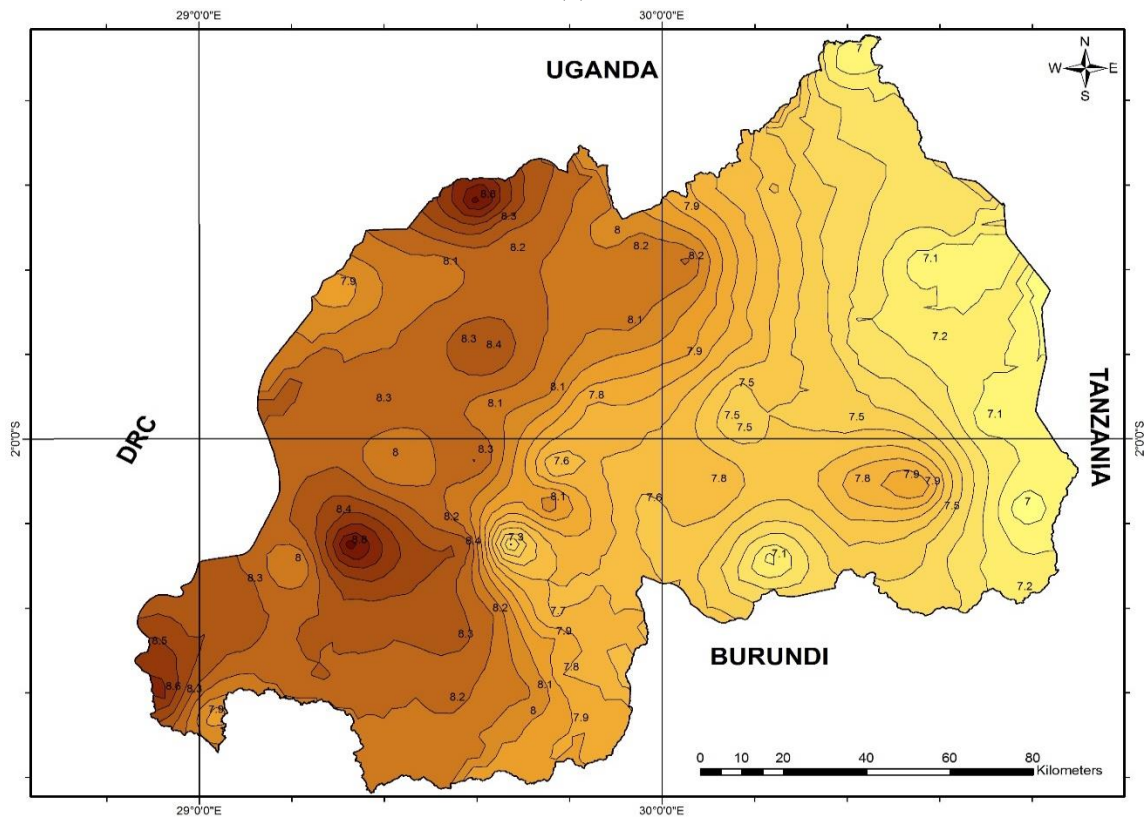
Towards the Eastern fringes, where lower rainfall is experienced, specific attenuation values are also lower, ranging between 12.1 to 12.9 dB/km for vertically polarized paths and 15.2 to 16.5 dB/km for horizontally polarized paths.

It is obvious from our results that irrespective of the proposed frequency of any designed radio links in Rwanda, higher fade margin will always be required in Western, North-western and South-western parts of the country, compared to the Eastern areas. This suggests that higher EIRP levels might be required in these areas to maintain service availability when designing radio links for terrestrial and satellite communication systems.



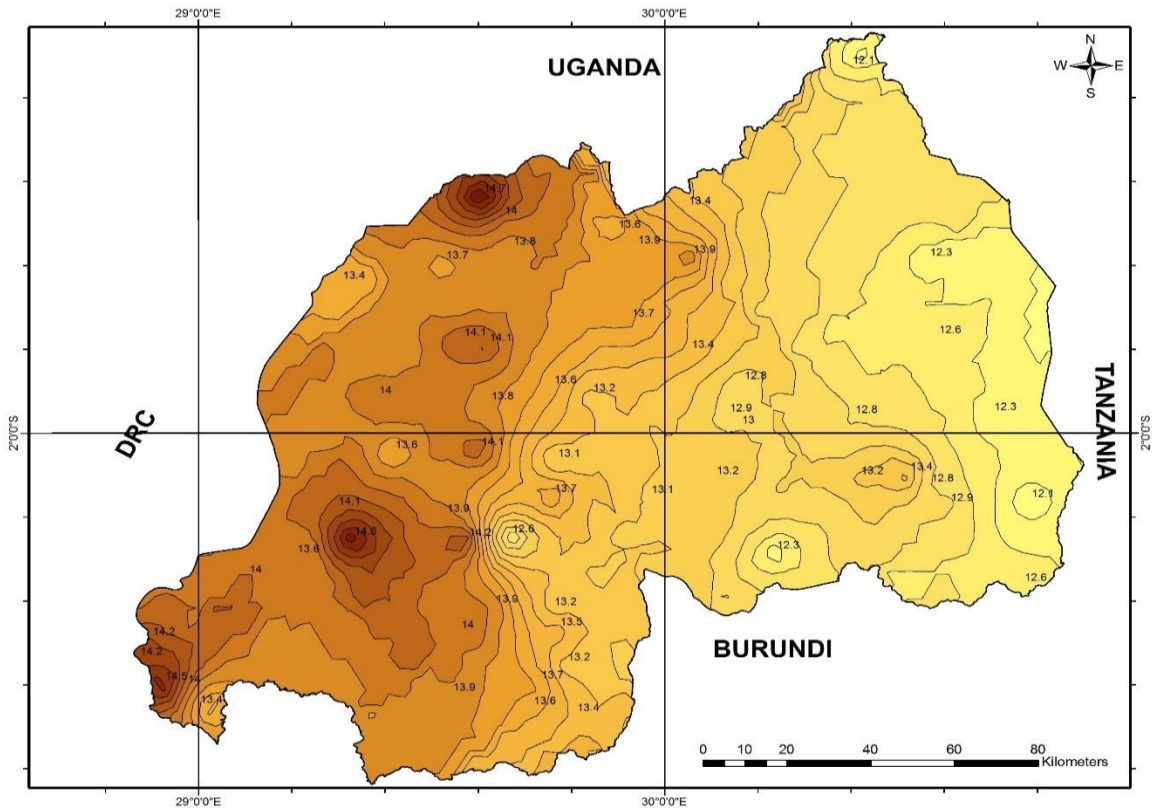


(a)

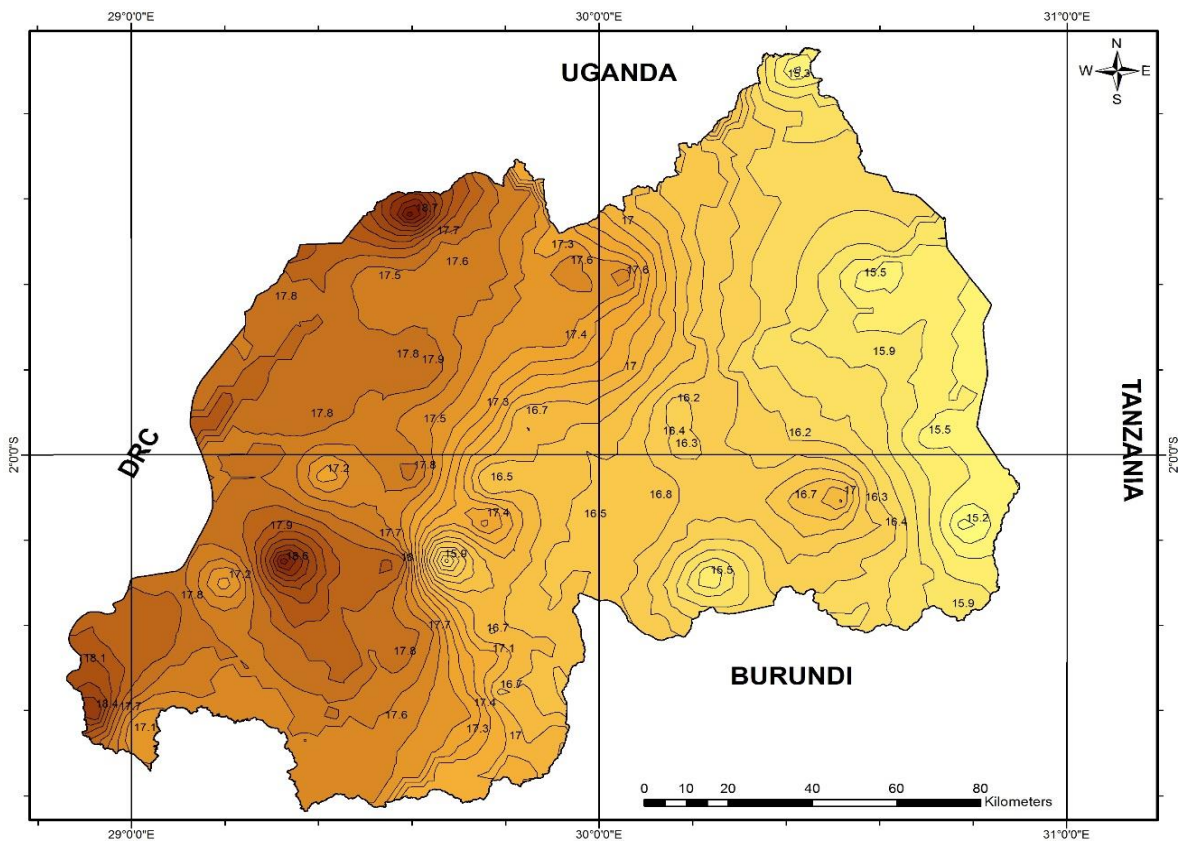


(b)

Figure 3-13. Rain specific attenuation contour map for link at 15 GHz frequency for link availability of 0.01% in Rwanda (a) Vertical polarization (b) Horizontal polarization



(a)



(b)

Figure 3-14. Rain specific attenuation contour map for link at 27 GHz frequency for link availability of 0.01% in Rwanda (a) Vertical polarization (b) Horizontal polarization

### **3.5 Conclusion Chapter Summary and Conclusion**

In this chapter, the rain rate conversion models have been obtained from long term annual rainfall data obtained for 60 different locations obtained from Meteo Rwanda for a period of 10 years and above. Subsequent conversion of rainfall data into equivalent one-minute rainfall rate statistics has resulted in the development of rain rate and rain specific attenuation contour maps for radio links in the Central African state of Rwanda. Results obtained have shown that the ITU-R specification for  $R_{0.01}$  for terrestrial planning is much lower than the values obtained. It is proposed that the ITU-R rain rate zones in Rwanda be grouped as lying between the two zones of N and P depending on the location with the Western province tending to P and the Eastern province to N. From the results, radio links in the Western, North-western and South-western parts of Rwanda thus are prone to suffer more from rain-induced network outages compared to other parts of the country. It is thus proposed, for radio links design, whether for terrestrial or satellite communication systems, these maps could be utilized to enhance the network performance in the presence of rainfall.

## Chapter Four

### Comparison of Rainfall Drop-Size Distribution Models for Microwave and Millimetric Radio Propagation in Butare.

#### 4.1 Introduction

Rainfall is an important fading mechanism for different radio propagation paths especially for millimetric wave and microwave line of sight links. At microwave and millimetric frequencies, the rainfall drops absorb and scatter radio waves, leading to signal attenuation and reduction of the system availability and reliability [56]. An in-depth knowledge of the drop size distribution is a very important parameter for a system designer to make a proper estimate of the attenuation due to rain.

In this chapter, the equatorial Butare region of Rwanda in Central Africa ( $2^{\circ}35'53.88''$  S and  $29^{\circ}44'31.5''$  E) characterized with voluminous levels of rainfall is investigated based on its cyclical rainfall pattern. Measurements of rain rate and rain drop size distributions (DSD), have been carried out using a Joss-Waldvogel RD-80 disdrometer for a period of 32 months between 2012 and 2015 to determine a suitable model of drop size distribution in the region. Rainfall data is classified into annual, seasonal, monthly and regime events, and their respective rainfall rate exceedences are calculated. Different DSD models such as Lognormal, Gamma, Marshall- Palmer and Weibull distributions are tested and the method of moment technique is applied for estimating input DSD fit-parameters for those different DSD models.

#### 4.2 Data measurements and processing

Rainfall measurement data was acquired using the Joss-Waldvogel (JW) RD-80 disdrometer installed at the roof of ICT building, University of Rwanda, Huye Campus, Butare ( $2^{\circ}35'53.88''$ S,  $29^{\circ}44'31.53''$ E at 1769 m a.s.l) in the Southern province of Rwanda for a period of 32 months between 2012 and 2015. This disdrometer has two main components: a sensor and a processor, as shown in Figure 4-1a and 4-1b. The sensor is an outdoor equipment exposed to the rain drops to be measured, while the processor processes the signal pulses caused by drops hitting the sensor. The drop size measurements from the processor are recorded and evaluated on a personal computer by using disdrodata software. This software enables the user to record and evaluate drop size measurements with a windows-based personal computer or notebook [103]. The Joss-Waldvogel RD-80 distrometer is capable of processing rainfall data into 20 drop size channels via the indoor unit. Each of the channels is related to rain drops with diameter,  $D$ , in the range  $0.313 \text{ mm} \leq D \leq 5.373 \text{ mm}$ .

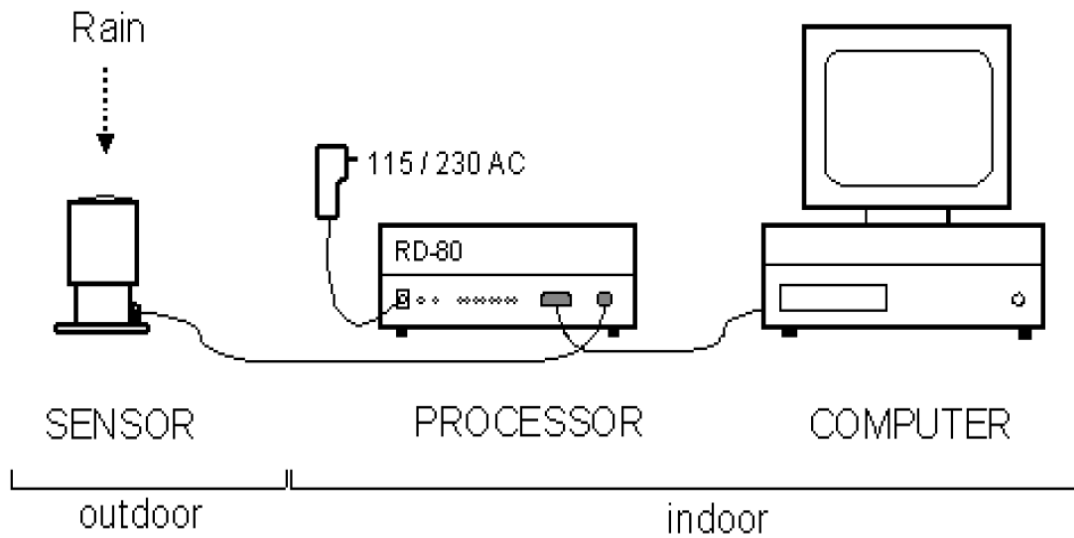


Figure 4-1a: Joss-Waldvogel RD-80 impact disdrometer system connected to a personal computer [104].

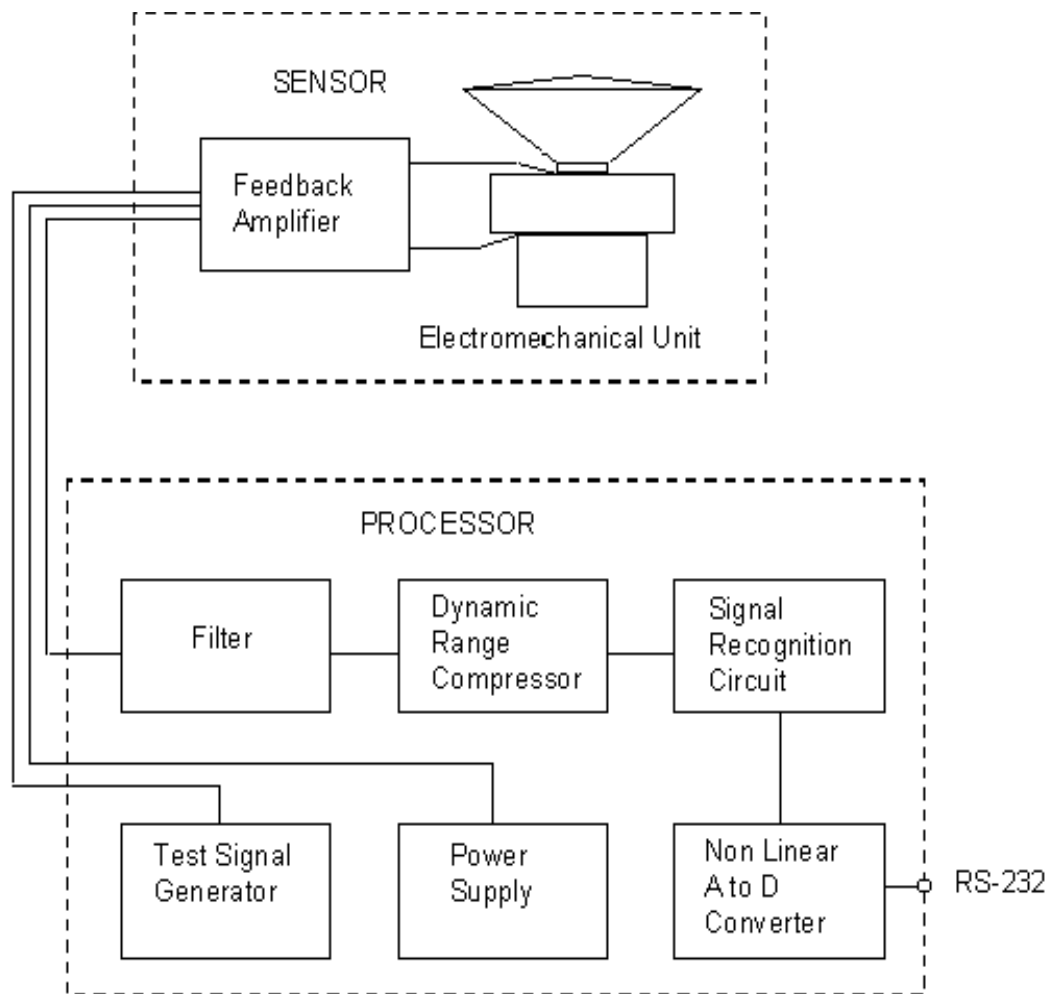


Figure 4-1b: Block diagram of the Joss-Waldvogel RD-80 Distrometer [103]

The accuracy of this instrument is  $\pm 5\%$ , the sampling time T is 60 seconds with a sampling area of  $0.005 \text{ m}^2$ , and it can measure quantities such as rainfall rate, rainfall drop-size, radar reflectivity and the rainfall accumulation [103].

During the period of measurement (2012 to 2015), a total of 1113707 rainfall samples (rainfall events) were recorded, with minimal equipment outage during the period of data collection. Based on recommendations on filtering and processing of disdrometer data [69], rainfall events (rainfall samples) with total sum of drops less than 10 were discarded from the data samples to compensate for the dead-time errors as they are considered to be within the noise level [104]. The maximum and the minimum rainfall rates recorded in the measurement period were 118.5 mm/h and 0.0029 mm/h, with a total of 56620 filtered rainfall samples. Then, the 56620 samples were considered and regrouped based on monthly, seasonal and regime variation of rainfall rate.

Table 4-1: Statistical summary of the RD-80 disdrometer for Butare, Rwanda between 2012 and 2015.

Category	Number of samples	Maximum Rainfall rate(mm/h)	Total rainfall time (hours)	Data percentage (%)
Annual	56620	118.516	943.67	100
Monthly				
January	4445	74.46	74.08	7.85
February	5899	103.08	104.1	10.42
March	5517	81.43	91.95	9.74
April	5922	78.5	98.7	10.46
May	5393	83.4	89.88	9.52
June	3271	71.84	54.52	5.78
July	386	2.9	6.43	0.68
August	2687	74.91	44.78	4.75
September	3355	72.13	55.92	5.93
October	8517	118.516	141.95	15.04
November	5917	111.97	98.62	10.45
December	5311	98.56	88.52	9.38
Seasonal				
Short dry season	9756	98.56	162.6	17.23
Long rainy season	22407	103.086	373.45	39.57
Long dry season	10023	74.91	167.05	17.7
Short rainy season	14434	118.51	240.57	25.5
Regime				
Drizzle	50920	4.99	848.67	89.93
Widespread	2713	9.99	45.22	4.79
Shower	2536	39.98	42.27	4.48
Thunderstorm	451	118.516	7.52	0.8

The data was arranged and categorized into different rainfall regimes based on rainfall rates [27,105-110] as follows: drizzle ( $0 \text{ mm/h} \leq R < 5 \text{ mm/h}$ ); widespread ( $5 \text{ mm/h} \leq R < 10 \text{ mm/h}$ ); shower ( $10 \text{ mm/h} \leq R < 40 \text{ mm/h}$ ); and thunderstorm ( $R > 40 \text{ mm/h}$ ). From this Joss-Waldvogel RD-80 distrometer, the rain rate,  $R$ , is related to the mean drop diameter,  $D_i$ , and given by [85,103,105,111-112]:

$$R = \frac{6\pi \times 10^{-4}}{A \times T} \sum_{i=1}^{20} n_i D_i^3 \quad (\text{mm/h}) \quad (4.1)$$

Where  $n_i$  represents the number of drops measured in the class  $i$ ,  $T$  is the sampling time (one-minute sampling time) and  $A$  is the sampling area ( $0.005 \text{ m}^2$ ). Table 4-1 gives the summary of rainfall data recorded for the period of measurement between 2012 and 2015.

### 4.3 Rainfall Rate Analysis for Butare

While designing a microwave link, it is recommended by the International Telecommunication Union (ITU-R) to target 99.99 % system availability; therefore the rainfall rate ( $R_{0.01}$ ) exceeded for 0.01% of the time in the region of interest has to be determined. The statistical information obtained is based on the cumulative distribution function (CDF) for rainfall rates in Butare, Rwanda. The analysis is done based on annual, seasonal, monthly and regime rainfall rate using the above disdrometer data between 2012 and 2015.

#### 4.3.1 Monthly Distribution of Rainfall Rate.

Figure 4-2 shows the monthly cumulative distribution of rainfall rate distributions for each of the months in Butare, Rwanda. The rainfall rate percentage exceedences at 10%, 1%, 0.1% and 0.01% taken from Figure 4-2 are presented in Table 4-2 respectively.

The month of the highest point rainfall rate is October with  $R_{0.01} = 116 \text{ mm/h}$ , while July has the lowest point rainfall rate in the year. Generally, as shown in Table 4-2, the monthly point rainfall rate values  $R_{0.01}$  are observed to be high from October to December and February to May in the short and long rainy season in Rwanda. A decrease in the values of  $R_{0.01}$  from December to January in the short rainy season and other low  $R_{0.01}$  values are observed from June to September in the long dry season, noting that the point rainfall rate is close to zero in July because there is almost no rain in that period of the year. From the above analysis, it is evident that October to December and February to May are the wettest periods, hence intense microwave attenuation due to rainfall in Butare, Rwanda.

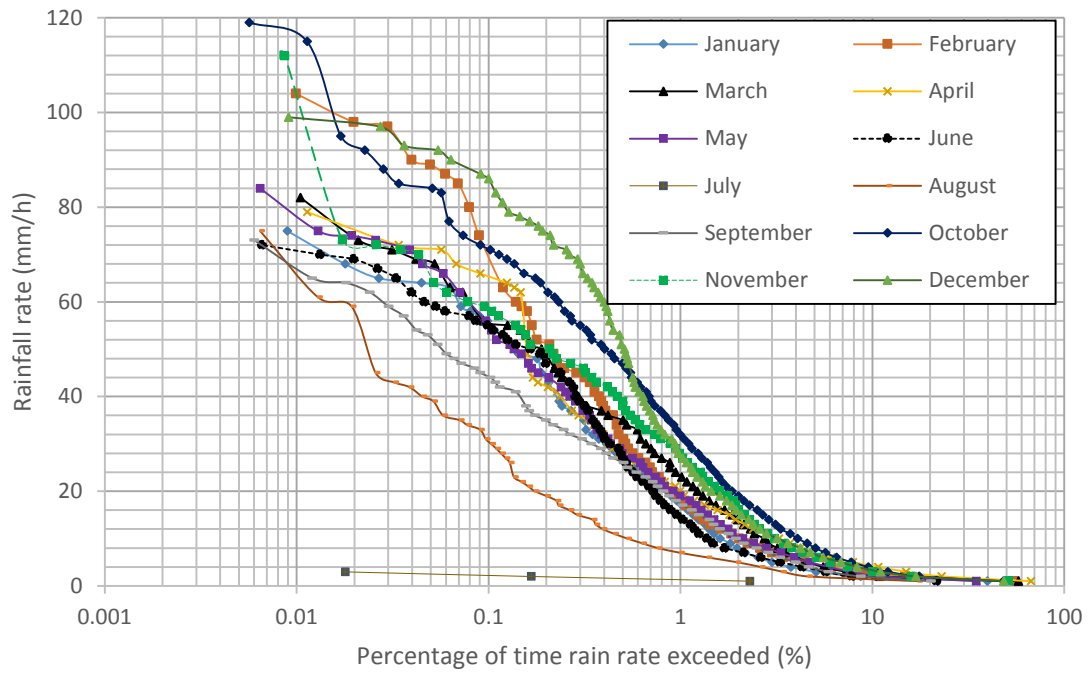


Figure 4-2: Monthly cumulative distribution of rainfall rate in Butare, Rwanda between 2012 and 2014-2015.

Table 4-2: Monthly statistics on rainfall rate exceeded (mm/h) in Butare, Rwanda

Months	Percentage of time rain rate is exceeded (%)			
	10%	1%	0.10%	0.01%
January	2	17	56	73
February	3	18	68	103
March	2	23	56	81
April	4	20	66	78
May	2	19	55	78
June	2	14	55	71
July		1.75	2.25	
August	2	7	31	65
September	2	17	44	67
October	4	32	71	116
November	3	28	59	103
December	3	27	86	98

#### 4.3.2 Seasonal Distribution of Rainfall Rate.

Figure 4-3 presents the seasonal cumulative distribution of rainfall rate for the same period of measurement. From the graph of Figure 4-3, it is observed that the short rainy season has the highest seasonal point rainfall rate values of  $R_{0.01}$  followed by the long rainy season, short dry season and long dry season, respectively.



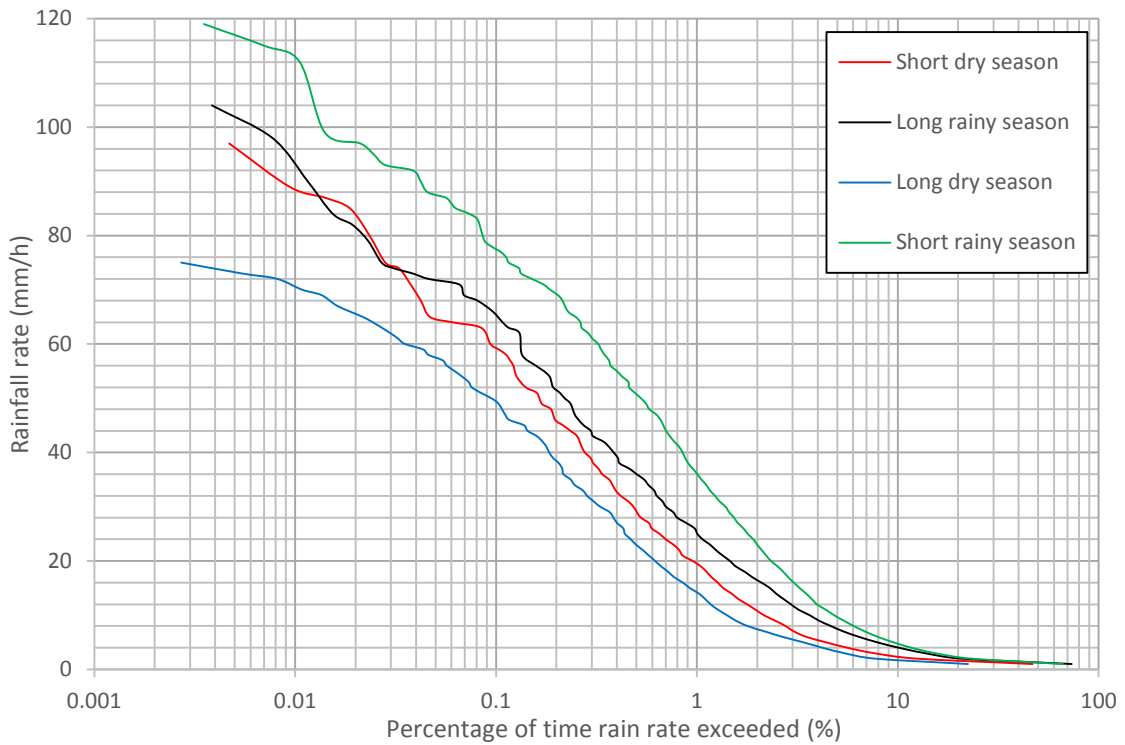


Figure 4-3: Seasonal cumulative distribution of Rainfall rate in Butare, Rwanda between 2012 and 2015.

Table 4-3. Seasonal statistics on rainfall rate exceeded (mm/h) in Butare, Rwanda

Season	Percentage of time rain rate is exceeded (%)			
	10 %	1%	0.1%	0.01%
Short dry season	3	19	59	89
Long rainy season	4	25	66	98
Long dry season	2	12	49	70
Short rainy season	5	36	78	114

From results in Figure 4-3, the rainfall rate exceedence for the short rainy season at  $R_{0.01}$  is 114 mm/h. This high value might result on the overlapping seasonal transition between the long dry season and the short rainy season in October. The short dry season and long rainy seasons are observed to have  $R_{0.01}$  at 89 mm/h and  $R_{0.01}$  at 98 mm/h respectively. The long dry season has the lowest point rainfall rate,  $R_{0.01}$  at 70 mm/h. Table 4-3 presents the summary of the seasonal values of rainfall rate at 10%, 1%, 0.1% and 0.01% percentage of time respectively.

The seasonal distribution of rainfall in Butare seems to suggest rainfall attenuation frequently peaks at months close to the advent of long rainy season around February and short rainy season around October.

### 4.3.3 Regime Distribution of Rainfall Rate.

In this section, the standard four rainfall regimes (drizzle, widespread, shower and thunderstorm) are analysed. As shown in Table 4-1, in Butare 89.93 % of the total rainfall event in the period of measurement are in the drizzle band; followed by widespread, shower and thunderstorm at 4.79 %, 4.48 % and 0.8 %, respectively. Results are presented in Figure 4-4 and Table 4-4. Therefore, it is found that the rainfall rate exceedences for drizzle events is  $R_{0.01}=4.9$  mm/h, widespread events at  $R_{0.01} = 9.9$  mm/h; shower events at  $R_{0.01} = 39.1$  mm/h and thunderstorm events at  $R_{0.01} = 93$  mm/h. Since microwave and millimeter wave links are mostly attenuated by rainfall droplets at high rainfall rate, therefore, Thunderstorm events links will be considered in rainfall design.

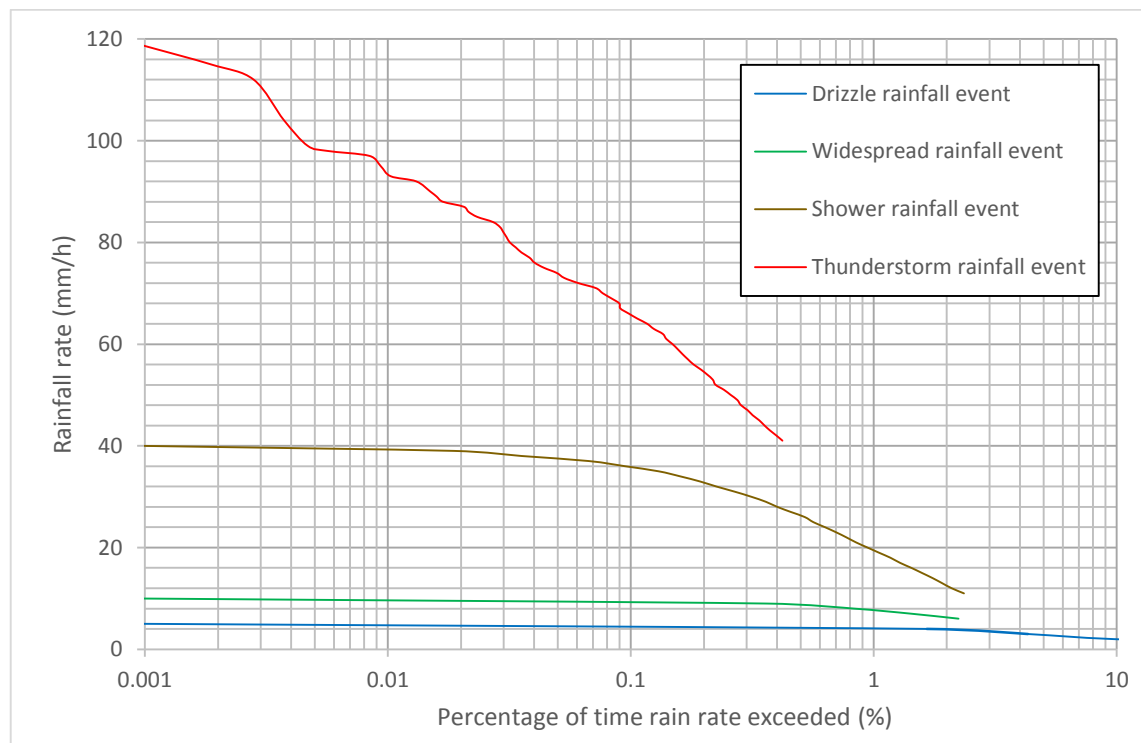


Figure 4.4: Regime Cumulative Distribution of Rainfall rate in Butare, Rwanda between 2012 and 2015.

Table 4.4. Rainfall regime statistics on rainfall rate exceeded (mm/h) in Butare- Rwanda

Regime	Percentage of time rain rate is exceeded (%)		
	1%	0.1%	0.01%
Drizzle	4	4.5	4.9
Widespread	7.5	9.2	9.9
Shower	19.5	36	39.1
Thunderstorm	-	66	93

#### 4.3.4 Annual Distribution of Rainfall Rate.

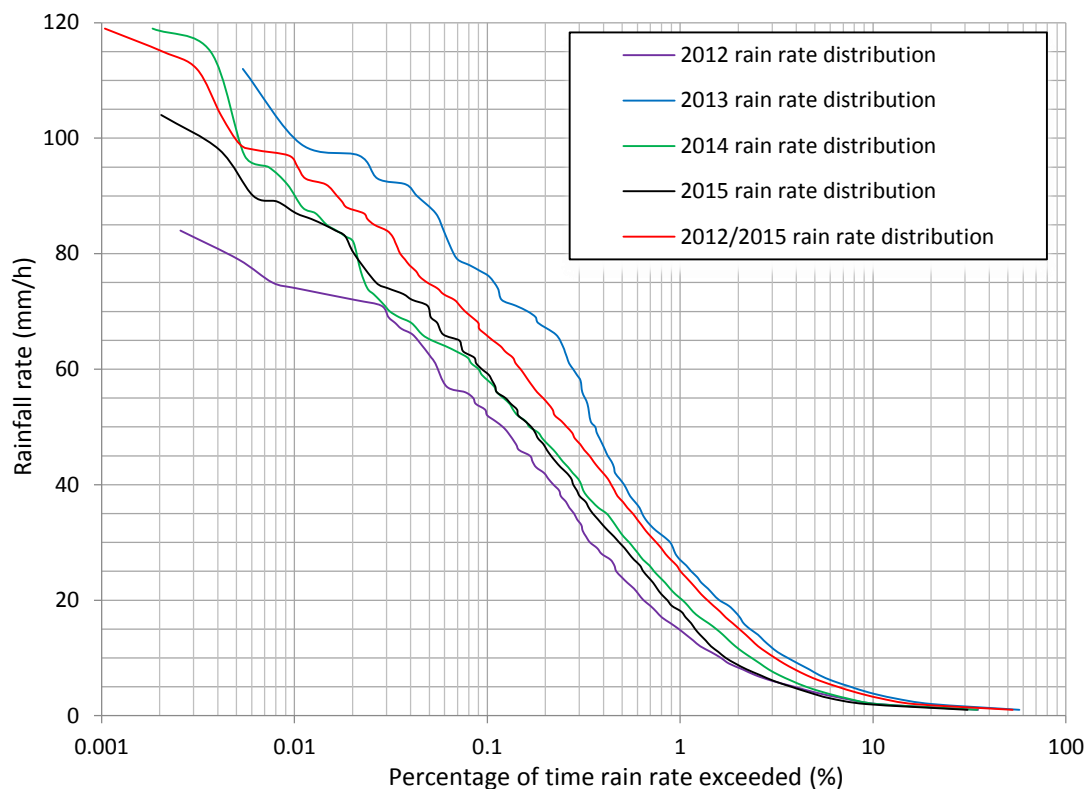


Figure 4-5: Annual cumulative distribution of rainfall rate in Butare, Rwanda between 2012 and 2015.

The annual cumulative distribution of rainfall rate  $R(mm/h)$ , exceeded for different percentages of time using measurements obtained from Butare, Rwanda between 2012 and 2015 is shown in Figure 4-5. From the plots of Figure 4-5, the annual values of  $R_{0.01}$  are obtained as 74 mm/h, 99 mm/h, 92 mm/h, 87 mm/h and 96 mm/h for 2012, 2013, 2014, 2015 and the overall period (2012/2015), respectively. Results show that, the measured value of the rainfall rate exceeded at 0.01% ( $R_{0.01}=96$  mm/h) for the entire period of measurement is much higher than the recommended value from ITU-R P.837 ( $R_{0.01}=70$  mm/h).

#### 4.4 Rainfall Drop Size Distribution Modelling Using Existing Models for Butare, Rwanda.

This section presents rainfall drop size distribution (DSD) modelling and analysis. Different standard DSD models such as Lognormal, Gamma, Marshall-Palmer and Weibull distributions are selected using the method of moment (MoM) technique to compute their corresponding rainfall DSD estimators.

#### 4.4.1 Drop Size Distribution Models with the Method of Moments Estimation Technique

In this section, four different statistical distributions have been developed to represent the rain drop size distribution  $N(D)$  for different rainfall types in Butare, Rwanda. The four distributions are Lognormal [105], Modified gamma [107], Negative exponential (Marshall and Palmer) [72] and Weibull [85] functions. From disdrometer data, the rain DSD is estimated using the following expression [113]:

$$N(D_i) = \frac{n_i}{A \times T \times v(D_i) \Delta D_i} \quad [m^{-3}mm^{-1}] \quad (4.2)$$

Where  $n_i$  represents the number of drops measured in the drop size class  $i$ ,  $A$  is the sampling area,  $T$  is the sampling time,  $v(D_i)$  is the terminal velocity and  $\Delta D_i$  is the diameter interval of the rain drops at the  $i$ th channel of the disdrometer. Generally, the measured rainfall DSD can be estimated by [114]:

$$N(D_i) = N_T f(D_i) \quad (4.3)$$

Where  $N_T$  is the raindrop concentration per unit volume of rainfall drops and  $f(D_i)$  is the probability density function of the raindrop distribution. In this study, the statistical correlation between the measured data and the four distributions is established by using the method of moment technique (MoM) to estimate their corresponding fit parameters.

The method of moments is a technique developed by Pearson in 1895 to construct estimators of parameters for fitting distributions by matching the sample moments with the distribution moments [115-117]. This means that, the sampled and the theoretical moments are equated. However, the method of moments estimation technique is known to produce some preference in the derivation of fitting model parameters [118] and in this study, it is used as it has been applied by previous researchers in the study of attenuation due to rain [25,67,78,85]. In the case of rainfall DSD estimation, the  $n$ th order moment is expressed as [25, 27,69,104-107]:

$$M_n = \sum_{i=1}^N D_i^n N(D_i) \Delta D_i \quad (4.4)$$

Where  $N(D_i)$  is the drop size distribution,  $\Delta D_i$  is the diameter interval,  $D_i$  is the mean drop diameter in the  $i$ th class and  $N$  is the sample size. As indicated by research, the most commonly used moments which are useful for radio and microwave studies are  $M_0$ ,  $M_3$ ,  $M_4$  and  $M_6$  and their expression are given by:

$$M_0 = \sum_{i=1}^N N(D_i) dD_i \quad (4.5a)$$

$$M_3 = \sum_{i=1}^N D_i^3 N(D_i) dD_i \quad (4.5b)$$

$$M_4 = \sum_{i=1}^N D_i^4 N(D_i) dD_i \quad (4.5c)$$

$$M_6 = \sum_{i=1}^N D_i^6 N(D_i) dD_i \quad (4.5d)$$

Where  $M_0$  is rainfall drop concentration,  $M_3$  is the rainfall rate and water liquid content,  $M_4$  is the rainfall specific attenuation and  $M_6$  is the radar reflectivity.

To estimate the rainfall DSD, equation (4.4) can be expressed as [119]:

$$M_n = \sum_{i=1}^N D_i^n \left[ \frac{n_i}{A.T.v(D_i)} \right] \quad (4.6)$$

The method of moment technique is used by equating the statistical moments to the measured moments.

#### 4.4.1.1 Lognormal Rainfall Drop Size Distribution Moments Estimation.

The three parameter Lognormal rainfall DSD model is given in [25] as:

$$N(D_i) = \frac{N_T}{\sigma D_i \sqrt{2\pi}} \exp \left\{ -\frac{1}{2} \left[ \frac{\ln(D_i) - \mu}{\sigma} \right]^2 \right\} \quad [m^{-3}mm^{-1}] \quad (4.7)$$

Where  $N(D_i)$  is the rain drop size distribution,  $N_T$  is the drop concentration (in  $m^{-3}$ ),  $\mu$  is the mean (shape parameter) of  $\ln(D_i)$  and  $\sigma$  is the standard deviation (scale parameter) of the drop sizes.  $D_i$  is the mean drop diameter (in mm) which is obtained directly from rainfall data. The three parameters,  $N_T$ ,  $\mu$  and  $\sigma$  were estimated using the MoM technique. For the Lognormal DSD model, the  $n$ th moment,  $M_n$ , is given as:

$$M_n = N_T \exp \left[ n\mu + \frac{1}{2} (n\sigma)^2 \right] \quad (4.8)$$

Using the third ( $M_3$ ), the fourth ( $M_4$ ) and the sixth ( $M_6$ ) moments and by solving the three simultaneous equations, the Lognormal DSD parameters  $N_T$ ,  $\mu$  and  $\sigma$ , are expressed as [78,105]:

$$N_T = \exp[(24L_3 - 27L_4 + 6L_6)/3] \quad (4.9)$$

$$\mu = (-10L_3 + 13.5L_4 - 3.5L_6)/3 \quad (4.10)$$

$$\sigma^2 = (2L_3 - 3L_4 - L_6)/3 \quad (4.11)$$

Where  $L_3, L_4, L_6$  are the natural logarithms of the measured moments  $M_3, M_4$  and  $M_6$  respectively. Based on equations (4.9) to (4.11), the three lognormal parameters  $N_T, \mu$  and  $\sigma$  are calculated from the observed spectrum for rain event and they are related to rainfall rate,  $R$ , as:

$$N_T = a_0 R^{b_0} \quad (4.12)$$

$$\mu = A_\mu + B_\mu \ln(R) \quad (4.13)$$

$$\sigma^2 = A_\sigma + B_\sigma \ln(R) \quad (4.14)$$

Where  $R$  is the rainfall rate,  $a_0, b_0, A_\mu, B_\mu, A_\sigma,$  and  $B_\sigma$  are regression coefficients

#### 4.4.1.2 Modified Gamma Rainfall Drop Size Distribution Moments Estimation.

The modified Gamma rainfall DSD model is given in [73-74,78,81] as:

$$N(D_i) = N_m (D_i)^\mu \exp(-\Lambda D_i) \quad [m^{-3} mm^{-1}] \quad (4.15)$$

Where  $N(D_i)$  is the rain drop size distribution,  $D_i$  has the same definition as in (4.7),  $N_m$  is the scaling parameter,  $\mu$ , the shape parameter and  $\Lambda$  is the slope parameter of the distribution. The modified Gamma DSD parameters are also estimated using the MoM parameter estimation technique. For the modified Gamma DSD model, the  $n$ th moment,  $M_n$ , is given as:

$$M_n = N_m \frac{\Gamma(\mu + n + 1)}{\Lambda^{\mu+n+1}} \quad (4.16)$$

By considering the third, fourth and sixth moments, the estimated modified Gamma DSD parameters  $N_m, \mu$  and  $\Lambda$ , are obtained from simultaneous equations (4.16) and are expressed as [78,112,120]:

$$\mu = \frac{11F - 8 + \sqrt{F(F + 8)}}{2(1 - F)} \quad \text{with} \quad F = \frac{M_4^3}{M_3^2 M_6} \quad (4.17)$$

$$N_m = \frac{M_3 \Lambda^{\mu+4}}{\Gamma(\mu + 4)} \quad (4.18)$$

$$\Lambda = \frac{M_3(\mu + 4)}{M_4} \quad (4.19)$$

In this study, the shape parameter  $\mu$  is fixed to 2 then,  $\Lambda$  and  $N_m$  are estimated by the third and the fourth moments only. The other remaining parameters  $\Lambda$  and  $N_m$ , are fitted against measured rainfall rate,  $R$  as:

$$N_m = a_m(R)^{b_m} \quad (4.20)$$

$$\Lambda = a_\Lambda(R)^{b_\Lambda} \quad (4.21)$$

Where  $a_m, b_m, a_\Lambda$  and  $b_\Lambda$  are regression coefficients.

#### 4.4.1.3 Negative Exponential Drop Size Distribution Moments Estimation.

A special case of (4.15) occurs when the shape parameter  $\mu=0$  then  $N(D_i)$ , becomes the Negative exponential rainfall DSD model (Marshall-Palmer) given by [72]:

$$N(D_i) = N_0 \exp(-\Lambda D_i) \quad [m^{-3} mm^{-1}] \quad (4.22)$$

Where the inputs parameters for the Negative exponential rainfall DSD model are similar to those of the modified Gamma rainfall DSD model in (4.15). The Negative exponential DSD parameters were estimated using the MoM parameter estimation technique. For this model, the  $n$ th moment,  $M_n$ , is given as:

$$M_n = N_0 \frac{\Gamma(n + 1)}{\Lambda^{n+1}} \quad (4.23)$$

Therefore, using the third, fourth and sixth moments,  $N_0$  and  $\Lambda$  are expressed by the following expressions:

$$N_0 = \frac{M_3 \Lambda^4}{\Gamma(4)} \quad (4.24)$$

$$\Lambda = \frac{4M_3}{M_4} \quad (4.25)$$

The scaling parameter,  $N_0$  and the slope parameter,  $\Lambda$  of the Negative exponential DSD model are also fitted against measured rainfall rate,  $R$  as:

$$N_0 = a_o(R)^{b_o} \quad (4.26)$$

$$\Lambda = a_\Lambda(R)^{b_\Lambda} \quad (4.27)$$

Where  $a_o$ ,  $b_o$ ,  $a_A$  and  $b_A$  are regression coefficients.

#### 4.4.1.4 Weibull Rainfall Drop Size Distribution Moments Estimation.

The Weibull rainfall DSD model is expressed as proposed by Sekine et al. [76,90] by:

$$N(D_i) = N_w \left(\frac{\beta}{\gamma}\right) \left(\frac{D_i}{\gamma}\right)^{\beta-1} \exp\left[-\left(\frac{D_i}{\gamma}\right)^\beta\right] \quad (4.28)$$

Where  $\beta$  is the shape parameter,  $\gamma$  is the scale parameter and  $N_w$ , the modified parameter. The  $n^{\text{th}}$  moment function of Weibull DSD model is given as [85,121]:

$$M_n = N_w \gamma^n \Gamma\left(1 + \frac{\gamma}{\beta}\right) \quad (4.29)$$

The solutions for  $\beta$ ,  $\gamma$  and  $N_w$  from the third, fourth and the sixth moments are expressed in [85] as:

$$\beta = \frac{-0.7067}{\ln(\varphi)} \text{ with } \varphi = \frac{0.9186M_4^2}{M_3^2 M_6} \quad (4.30)$$

$$\gamma = \frac{0.8660 M_4}{M_3} x(0.2867\beta)^{1/\beta} \quad (4.31)$$

$$N_w = \frac{0.2303M_3\beta^{(\beta+6)/2\beta}}{\gamma^3(1.3443)^{1/\beta}} \quad (4.32)$$

The moments  $M_3$ ,  $M_4$ ,  $M_6$  can be obtained from measured data and  $\beta$ ,  $\gamma$  and  $N_w$  are derived by using regression technique with respect to the rainfall rate  $R$  as:

$$N_w = a_w(R)^{b_w} \quad (4.33)$$

$$\beta = a_\beta(R)^{b_\beta} \quad (4.34)$$

$$\gamma = a_\gamma(R)^{b_\gamma} \quad (4.35)$$

Where  $a_w$ ,  $b_w$ ,  $a_\beta$ ,  $b_\beta$ ,  $a_\gamma$  and  $b_\gamma$  are regression coefficients.

#### 4.5 Variability of Drop Size Distribution Modelling for Butare, Rwanda.

In this section, by using the method of moments estimation technique as previously explained, various input parameters for the four different rainfall DSD models applied in this work are estimated and results are presented in Tables 4-5 and 4-6.



By using the estimated parameters in Table 4-6, different drop size distribution models for Butare are developed, and the results are presented in Figures 4-6 to 4-11 at rainfall rates of 1.53 mm/h, 4.95 mm/h, 9.54 mm/h, 26.86 mm/h, 60.08 mm/h and 118.5 mm/h respectively. DSD models are fitted to the rain DSD as spectra observed from the disdrometer at Butare station. The rain drop diameters, the modelled drop size distribution and the measured data are compared for different models. From Figures 4-6 to 4-11, one observes a progressive change in the shape of the DSD as rainfall rate increases. This means that as the rain rate increases, the coverage area (diameter region) of the DSD gets wider.

In figure 4-6 ( $R_{0.01}=1.53$  mm/h), the Lognormal model underestimates the measurement at drop diameter region between 0.359 and 0.913 mm. Comparing with other statistical models, the Weibull model seems to perform better at this low rainfall rate.

At the rainfall rate of 4.95 mm/h, in Figure 4-7, the Lognormal model takes the shape of the measured DSD even though it underestimates it at drop size diameter region less than 1 mm. It is observed that the Gamma and Weibull models seem to coincide with the measured DSD, even though they overestimate it at drop size diameter regions less than 0.656 mm.

Table 4-5. Model parameters for different rainfall DSD statistical models based on annual rainfall analysis in Butare, Rwanda

Lognormal DSD model					
$N_T = a_o R^{b_o}$		$\mu = A_\mu + B_\mu \ln(R)$		$\sigma^2 = A_\sigma + B_\sigma \ln(R)$	
$a_o$	$b_o$	$A_\mu$	$B_\mu$	$A_\sigma$	$B_\sigma$
113.7	0.2057	-0.0753	0.1908	0.0695	0.0695
Modified Gamma DSD Model					
		$N_m = a_m(R)^{b_m}$		$\Lambda = a_\Lambda(R)^{b_\Lambda}$	
$\mu$		$a_m$	$b_m$	$a_\Lambda$	$b_\Lambda$
2		17605	-0.497	5.0726	-0.219
Negative Exponential DSD model (MP)					
		$N_0 = a_o(R)^{b_o}$		$\Lambda = a_\Lambda(R)^{b_\Lambda}$	
$\mu$		$a_o$	$b_o$	$a_\Lambda$	$b_\Lambda$
0		2703	-0.06	3.3817	-0.219
Weibull DSD model					
$\beta = a_\beta(R)^{b_\beta}$		$\gamma = a_\gamma(R)^{b_\gamma}$		$N_w = a_w(R)^{b_w}$	
$a_\beta$	$b_\beta$	$a_\gamma$	$b_\gamma$	$a_w$	$b_w$
2.5873	-0.127	0.8538	-0.1835	179.25	-0.2139

Table 4-6. Model parameters for different rainfall DSD statistical models analysis in Butare, Rwanda based on rainfall regimes.

Input parameter	Lognormal DSD model					
	$N_T = a_0 R^{b_0}$		$\mu = A_\mu + B_\mu \ln(R)$		$\sigma^2 = A_\sigma + B_\sigma \ln(R)$	
	$a_0$	$b_0$	$A_\mu$	$B_\mu$	$A_\sigma$	$B_\sigma$
Drizzle	116.1	0.2144	-0.103	0.1798	0.0778	0.0113
Widespread	143.61	0.0936	-0.2125	0.28	0.1007	-0.017
Shower	209.69	-0.046	-0.2405	0.2874	0.0471	0.0048
Thunderstorm	11.605	0.7502	0.5709	0.0635	0.0475	0.0053
Input parameter	Modified Gamma DSD Model					
	$\mu$	$N_m = a_m(R)^{b_m}$		$\Lambda = a_\Lambda(R)^{b_\Lambda}$		
		$a_m$	$b_m$	$a_\Lambda$	$b_\Lambda$	
Drizzle	2	17066	-0.508	5.0671	-0.219	
Widespread	2	20144	-0.47	5.2187	-0.221	
Shower	2	68953	-0.952	6.357	-0.299	
Thunderstorm	2	167.37	0.6449	2.534	-0.055	
Input parameter	Negative Exponential DSD model (MP)					
	$\mu$	$N_0 = a_0(R)^{b_0}$		$\Lambda = a_\Lambda(R)^{b_\Lambda}$		
		$a_0$	$b_0$	$a_\Lambda$	$b_\Lambda$	
Drizzle	0	2625.9	-0.071	3.378	-0.219	
Widespread	0	2922.1	-0.028	3.4792	-0.221	
Shower	0	6740.8	-0.299	4.238	-0.299	
Thunderstorm	0	102.92	-0.055	1.689	-0.055	
Input parameters	Weibull DSD model					
	$\beta = a_\beta(R)^{b_\beta}$		$\gamma = a_\gamma(R)^{b_\gamma}$		$N_w = a_w(R)^{b_w}$	
	$a_\beta$	$b_\beta$	$a_\gamma$	$b_\gamma$	$a_w$	$b_w$
Drizzle	2.3231	-0.168	0.8181	-0.1668	186.63	-0.2299
Widespread	1.857	0.1595	0.6987	-0.32	248.24	0.0331
Shower	3.0432	0.044	0.7571	-0.2846	300.59	-0.032
Thunderstorm	3.1356	0.062	2.0294	0.0194	10.431	0.8681

Figure 4-8 shows that, at 9.54 mm/h, Weibull, Gamma and the Negative Exponential (Marshall-Palmer) models overestimate the measured DSD in the diameter range of 0.359 to about 1 mm. At this rainfall rate, the Lognormal model performs best because it takes the shape of the measurement data even if it slightly overestimates it between 1.331 and 2.259 mm. At the rainfall rate of 26.86 mm/h as shown on the graph of Figure 4-9, the Lognormal model is seen as a good fit to the measured DSD compared to other models. The Gamma, M-P and Weibull models overestimate the measurement at drop diameter region below 1.665 mm. At high rainfall rates of 60.08 mm/h and 118.5 mm/h, as shown in Figure 4-10 and 4-11 respectively, the Lognormal model takes the shape of the measured DSD but neither it nor other statistical models fits measurements well.

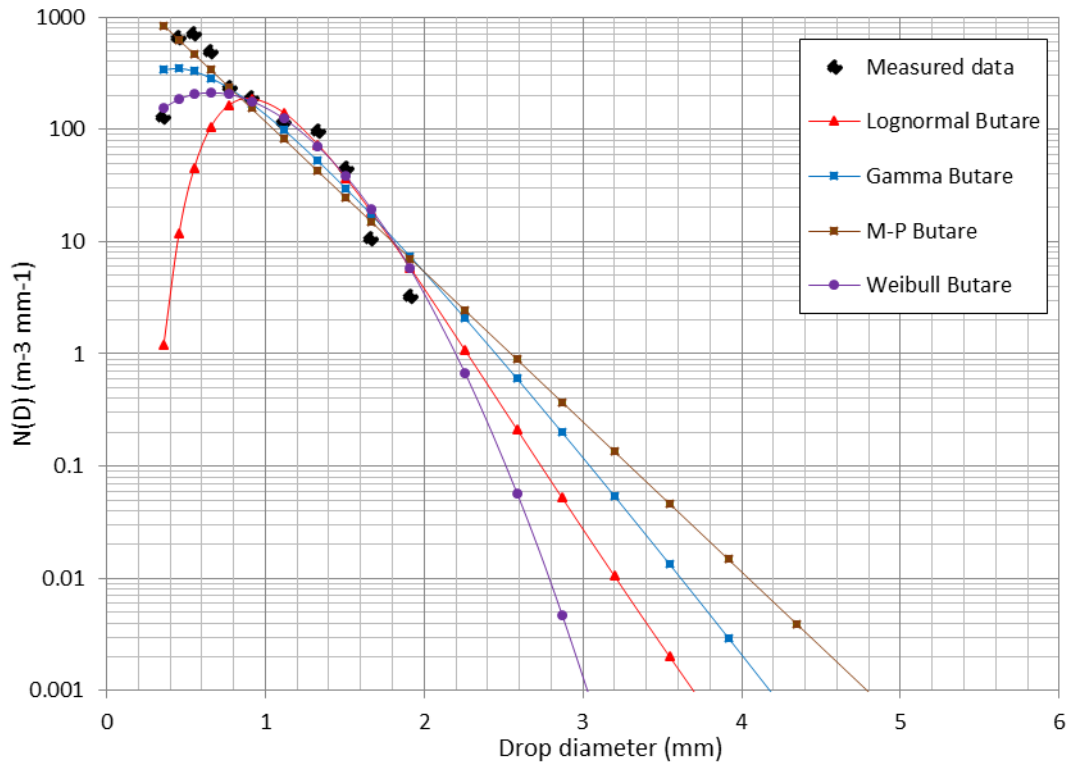


Figure 4-6: Different DSD models for Butare, Rwanda ( $R = 1.53$  mm/h)

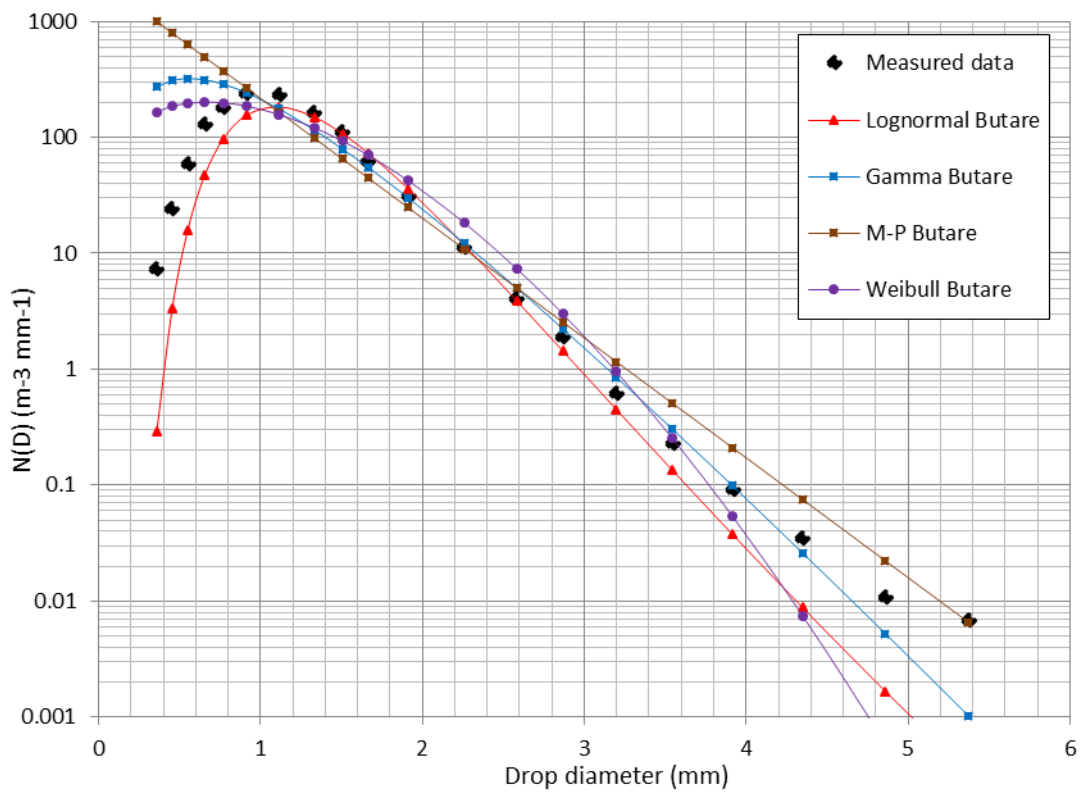


Figure 4-7: Different DSD models for Butare, Rwanda ( $R = 4.95$  mm/h)

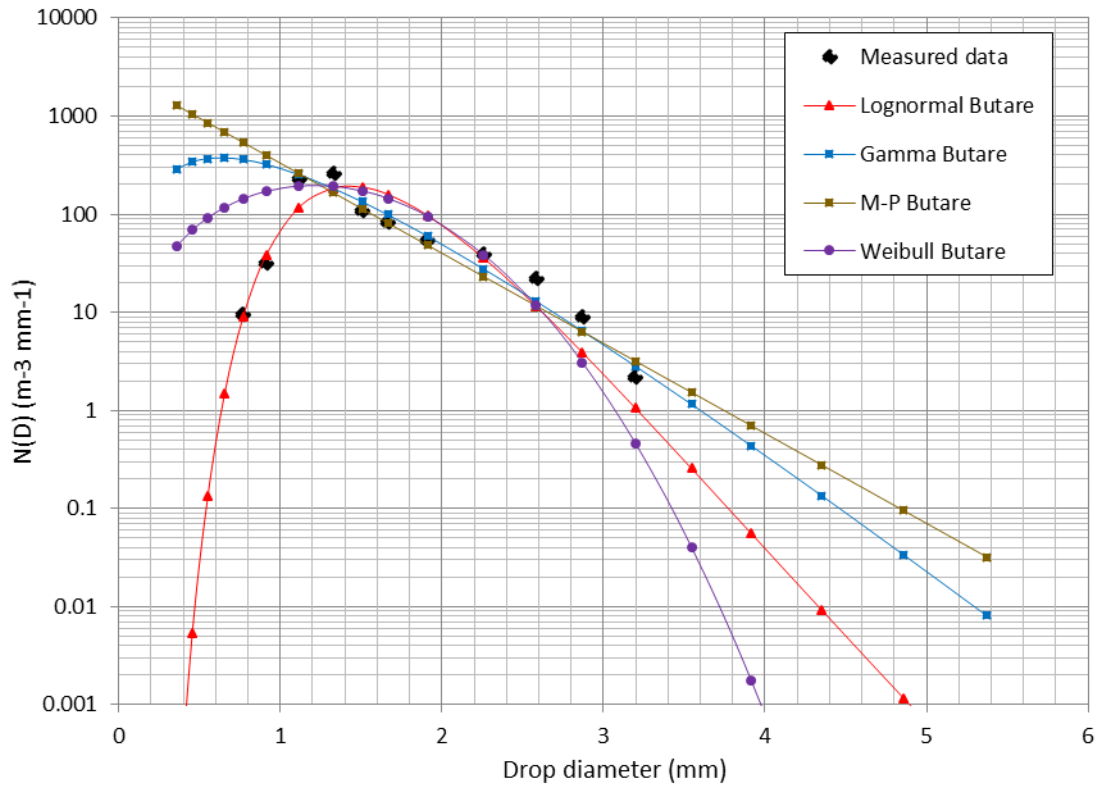


Figure 4.8: Different DSD models for Butare, Rwanda ( $R = 9.54 \text{ mm/h}$ )

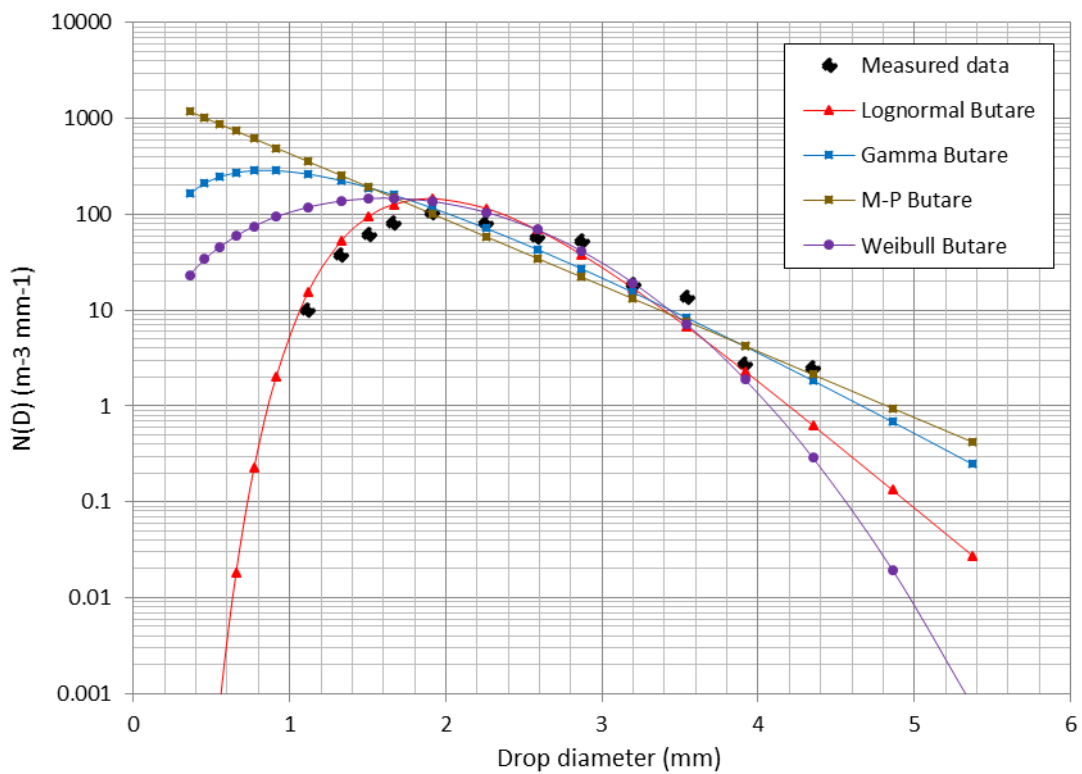


Figure 4.9: Different DSD models for Butare, Rwanda ( $R = 26.86 \text{ mm/h}$ )

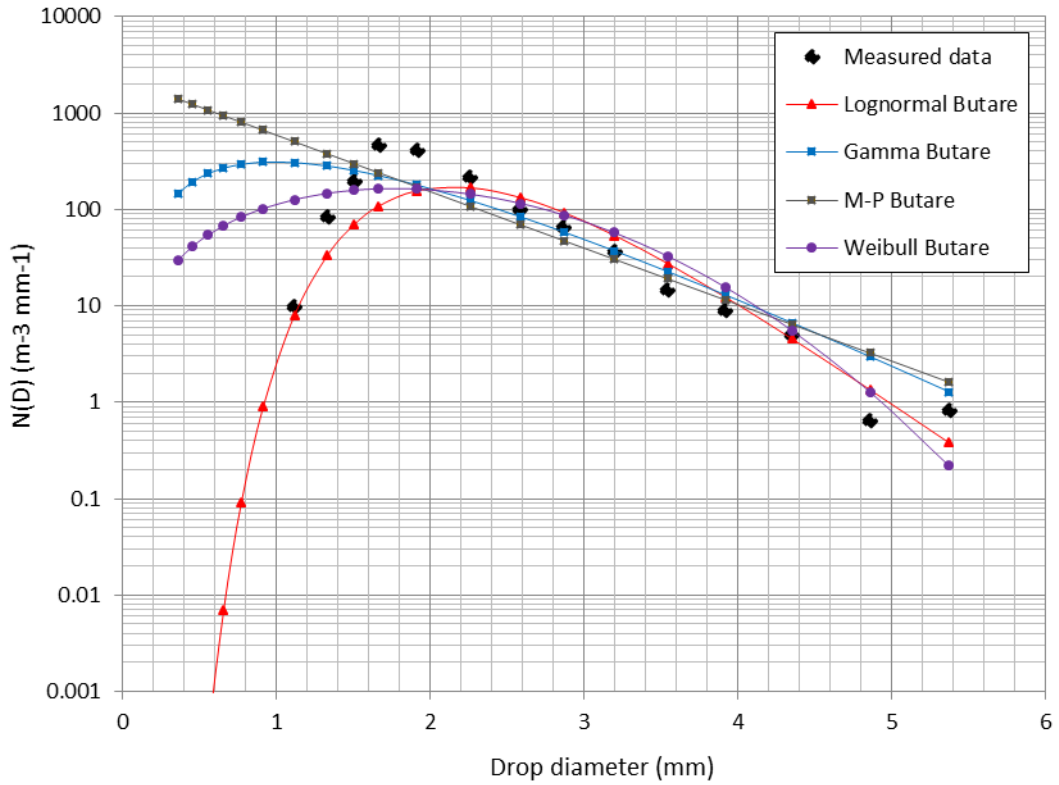


Figure 4-10: Different DSD models for Butare, Rwanda (R = 60.08 mm/h)

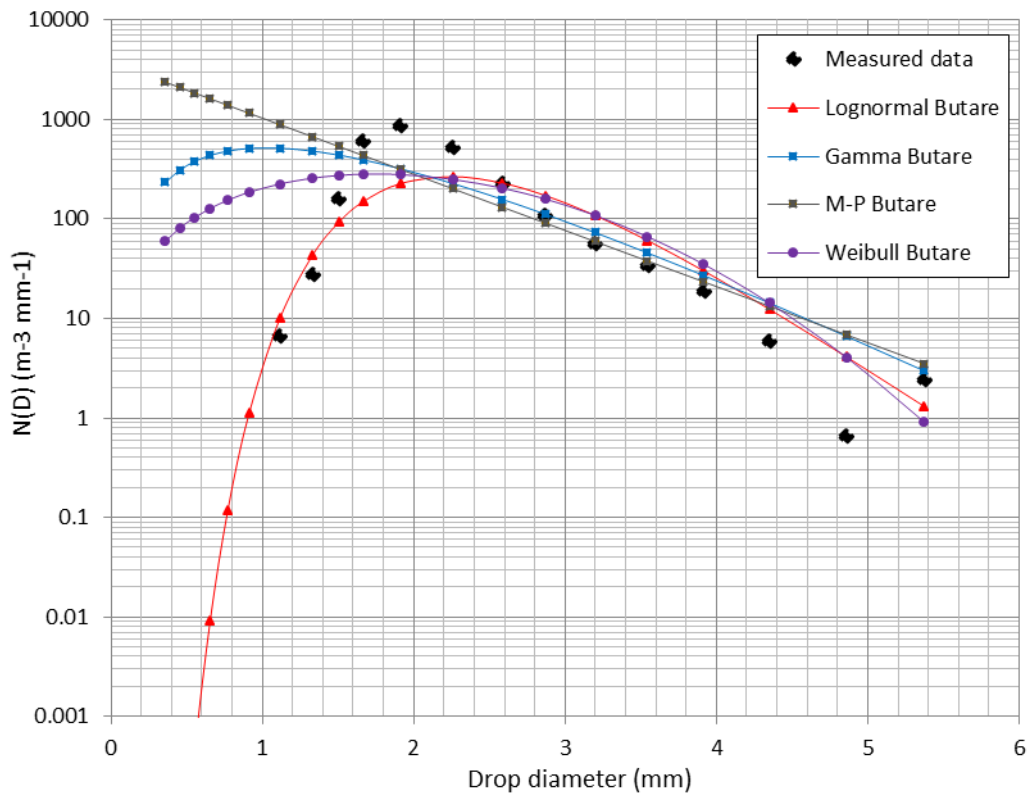


Figure 4-11: Different DSD models for Butare, Rwanda (R = 118.5 mm/h)

From the results, it can be seen that those different models have different performances as the rainfall rate is varied except the M-P which overestimates the measurement for all the rainfall rates considered. Although the Lognormal DSD model tends to give a better fit with the measured DSD particularly at high rainfall rate, it does not match it well, which is why we need to make an improvement by modifying this model to fit our measured DSD especially to those rainfall contributions with high rain intensities that are mostly associated with microwave and millimetre wave attenuation.

#### **4.6 Chapter Summary and Conclusion**

In this chapter, disdrometer data collected in Butare, Rwanda between 2012 and 2015 have been used to develop a suitable model of rain drop size distribution for the region. Four different statistical rainfall DSD models are examined and their corresponding input fit-parameters are determined using the MoM estimation technique for drizzle, widespread, shower and thunderstorm rainfall event. From results, the different models have different performances as the rainfall varies from drizzle to thunderstorm, except the M-P which exhibits consistent inadequacy as a model in the region. It is found that neither the Lognormal nor the Gamma DSD models match properly with the measured DSD, particularly at high rainfall rate. Therefore, a new rainfall DSD model for Central Africa has to be developed to make an improvement on the existing rain drop size distribution models in this region.

The next chapter focuses on the development of a new rainfall drop size distribution model for equatorial Africa.

## Chapter Five

### Proposed Rain Drop Size Distribution Model for Microwave and Millimeter Wave in Central Africa

#### 5.1 Introduction.

In this chapter, the focus is to develop a new rainfall drop size distribution model for equatorial Africa using disdrometer data obtained in Butare, Rwanda. Rainfall data was classified into annual and seasonal as well as rainfall regimes which are drizzle, widespread, shower and thunderstorm based on their rainfall rates. The maximum likelihood estimation technique was applied to construct estimates of input DSD fit parameters of the developed statistical distribution for rainfall DSD in Butare. Thereafter, the newly obtained distribution was compared to the existing rainfall DSD models, namely: Lognormal, Gamma, Marshall- Palmer and Weibull distributions.

#### 5.2 Development of a New Rainfall Drop Size Distribution Model for Rwanda.

From plots of Figures 4-7 to 4-11, it is seen that the diameter rain drop of the DSD gets wider as the rainfall rate increases and the Lognormal model tends to fit the measurement particularly at high rainfall rate. By analysing the results, the drizzle rainfall regime DSD reaches its peak at drop diameter of  $D_p=0.913$  mm, the widespread, shower and the thunderstorm reach their peaks at drop diameters of 1.116 mm, 1.665 mm and 1.912 mm, respectively. When  $D = D_p$ , the measured drop size distribution is at its maximum and its variation with respect to the drop diameter is equal to zero. When  $D \leq D_p$ , the Lognormal model performs better because it takes the shape of the measurements even if it slightly underestimates. When  $D > D_p$ , the Gamma model best coincides with the measured DSD. Therefore, there is need to develop a new rainfall DSD model to improve on the existing ones. From the results, the new model should be an intermediate distribution between Lognormal and Gamma distributions, so that it makes a better fit for rainfall drops with small and larger diameters. By modifying the Lognormal distribution for  $N(D)$ , our new DSD model can be formulated as follow:

$$N(D) = \frac{N_T}{\sigma D \sqrt{2\pi}} \exp \left\{ -\frac{1}{2} \left[ \frac{\ln(D) - \mu}{\sigma} \right]^2 \right\} \{1 + \exp(-(D + D_p))\} \quad [m^{-3}mm^{-1}] \quad (5.1)$$

Where  $N(D)$  is the rain drop size distribution,  $N_T$  is the drop concentration (in  $m^{-3}$ ),  $D_p$  is the peak diameter in (mm),  $D$  is the mean drop diameter (in mm),  $\mu$  is the shape parameter,  $N_T$ , and  $\sigma$  is the scale parameter. Generally, as discussed in section 4.4, the measured rainfall drop size distribution can be estimated by the following expression:

$$N(D) = N_T f(D) \quad (5.2)$$

Where  $f(D)$  is the probability density function (*pdf*) of the proposed model. Therefore,

$$f(D) = \frac{N(D)}{N_T} = \frac{1}{\sigma D \sqrt{2\pi}} \exp \left\{ -\frac{1}{2} \left[ \frac{\ln(D) - \mu}{\sigma} \right]^2 \right\} \{1 + \exp(-(D + D_p))\}$$

$$f(D) = \frac{1}{\sigma D \sqrt{2\pi}} \exp \left\{ -\frac{1}{2} \left[ \frac{\ln(D) - \mu}{\sigma} \right]^2 \right\} (1 + e^{-D} e^{D_p}) \quad (5.3)$$

Let  $e^{D_p} = \alpha$ ; then the equation (5.3) can be rewritten as:

$$f(D) = \frac{1}{\sigma D \sqrt{2\pi}} \exp \left\{ -\frac{1}{2} \left[ \frac{\ln(D) - \mu}{\sigma} \right]^2 \right\} (1 + \alpha e^{-D}) \quad (5.4)$$

$$0 < D < \infty \quad -\infty < \mu < +\infty \quad \sigma > 0 \quad \alpha > 0$$

But according to [122], for  $f(D)$  to be a valid probability density function of a random variable  $D$ , the following two conditions have to be satisfied:

1.  $f(D) \geq 0$ , for all  $D$  (5.5)

2.  $\sum_D f(D) = 1$  or  $\int_{-\infty}^{+\infty} f(D) dD = 1$  (5.6)

From a purely mathematical perspective, any non-negative function with a finite positive integral (sum) can be converted to a legitimate *pdf*. As an example, let the function  $h(x)$  be a non-negative function that is positive on the interval  $L \leq x \leq U$ , zero elsewhere, and  $C$ , a positive constant given by [122]:

$$\int_L^U h(x) dx = C < \infty \quad (5.7)$$

Therefore, the probability density function of a random variable  $x$  taking values on the interval  $L \leq x \leq U$  will be given by:

$$f(x) = \frac{h(x)}{C} \quad (5.8)$$

By applying the approach in (5.7) and (5.8) from [122], the equation (5.4) has to be normalized so as to satisfy the two important conditions stated in (5.5) and (5.6) for a valid pdf. Therefore, the normalized form of (5.4) is given by:



$$f(D) = \frac{1}{C\sigma D\sqrt{2\pi}} \exp\left\{-\frac{1}{2}\left[\frac{\ln(D) - \mu}{\sigma}\right]^2\right\} (1 + \alpha e^{-D}) \quad (5.9)$$

With  $C$  is a normalizing constant given by:

$$C = \int_L^U \frac{1}{\sigma D\sqrt{2\pi}} e^{-\frac{1}{2}\left[\frac{\ln(D) - \mu}{\sigma}\right]^2} (1 + \alpha e^{-D}) dD \quad (5.10)$$

Where  $L$  and  $U$  are the lower and upper diameter ranges of the mean rain drop. Therefore, the mathematical expression of the proposed DSD model will be expressed as:

$$N(D_i) = \frac{N_T}{C\sigma D\sqrt{2\pi}} \exp\left\{-\frac{1}{2}\left[\frac{\ln(D) - \mu}{\sigma}\right]^2\right\} \{1 + \alpha \exp(-D)\} [m^{-3}mm^{-1}] \quad (5.11)$$

Where  $N(D)$  is the rain drop size distribution,  $N_T$  is the drop concentration ( $m^{-3}$ ),  $D$  is the mean drop diameter in ( $mm$ ),  $\mu$  is the shape parameter and  $\sigma$  is the scale parameter for  $L \leq D \leq U$  and zero otherwise.  $-\infty < \mu < \infty$ ,  $\sigma$  and  $\alpha$  are positive constants.

### 5.3 Method of Maximum Likelihood Estimation Technique.

In finding input fit parameters for the new proposed model, the maximum likelihood estimation technique has been used. This method, developed by R.A. Fisher in 1922, is the most popular technique for deriving estimators [123]. Remember that if  $D_1, D_2, D_3 \dots D_n$  are an independent and identically distributed random sample from a population with probability density function  $f$  denoted as  $f(D_1, D_2, D_3 \dots D_n / \mu, \sigma^2, \alpha)$ , the likelihood function is defined by [33, 34]:

$$L(D_1, D_2, D_3 \dots, D_n / \mu, \sigma^2, \alpha) = \prod_{i=1}^n [f(D_i / \mu, \sigma^2, \alpha)] \quad (5.12)$$

The maximum likelihood estimate of parameter  $\hat{\mu}$  ( $\hat{\sigma}^2$  or  $\hat{\alpha}$ ) is that value of  $\mu$  ( $\sigma^2$  or  $\alpha$ ) which maximises the likelihood function in (5.12): it is the value that makes the observed data the ‘‘most probable’’. Substituting (5.9) in (5.12), the likelihood function will be expressed as:

$$L(D_1, D_2, D_3 \dots, D_n / \mu, \sigma^2, \alpha) = \prod_{i=1}^n \left[ \frac{1}{C\sigma D_i\sqrt{2\pi}} e^{-\frac{1}{2}\left[\frac{\ln(D_i) - \mu}{\sigma}\right]^2} (1 + \alpha e^{-D_i}) \right] \quad (5.13)$$

$$L(D_1, D_2, D_3 \dots, D_n / \mu, \sigma^2, \alpha) = \frac{1}{(2\pi\sigma^2 C^2)^{\frac{n}{2}}} \prod_{i=1}^n \left[ D_i^{-1} e^{-\frac{1}{2}\left[\frac{\ln(D_i) - \mu}{\sigma}\right]^2} (1 + \alpha e^{-D_i}) \right]$$

$$\begin{aligned}
L(D_1, D_2, D_3, \dots, D_n / \mu, \sigma^2, \alpha) &= (2\pi\sigma^2 C^2)^{-\frac{n}{2}} \prod_{i=1}^n \left[ D_i^{-1} e^{-\frac{1}{2} \left[ \frac{\ln(D_i) - \mu}{\sigma} \right]^2} (1 + \alpha e^{-D_i}) \right] \\
L(D_1, D_2, D_3, \dots, D_n / \mu, \sigma^2, \alpha) &= (2\pi\sigma^2 C^2)^{-\frac{n}{2}} \prod_{i=1}^n \left[ e^{-\frac{1}{2} \left[ \frac{\ln(D_i) - \mu}{\sigma} \right]^2} \left( \frac{1 + \alpha e^{-D_i}}{D_i} \right) \right] \\
L(D_1, D_2, D_3, \dots, D_n / \mu, \sigma^2, \alpha) &= (2\pi\sigma^2 C^2)^{-\frac{n}{2}} \prod_{i=1}^n \left( e^{-\frac{1}{2} \left[ \frac{\ln(D_i) - \mu}{\sigma} \right]^2} \right) \prod_{i=1}^n \left( \frac{1 + \alpha e^{-D_i}}{D_i} \right) \\
&= (2\pi\sigma^2 C^2)^{-\frac{n}{2}} \left( e^{-\frac{1}{2} \left[ \frac{\ln(D_1) - \mu}{\sigma} \right]^2} e^{-\frac{1}{2} \left[ \frac{\ln(D_2) - \mu}{\sigma} \right]^2} e^{-\frac{1}{2} \left[ \frac{\ln(D_3) - \mu}{\sigma} \right]^2} \dots e^{-\frac{1}{2} \left[ \frac{\ln(D_n) - \mu}{\sigma} \right]^2} \right) \prod_{i=1}^n \left( \frac{1 + \alpha e^{-D_i}}{D_i} \right) \\
&= (2\pi\sigma^2 C^2)^{-\frac{n}{2}} \left( e^{-\frac{1}{2} \left[ \frac{\ln(D_1) - \mu}{\sigma} \right]^2} e^{-\frac{1}{2} \left[ \frac{\ln(D_2) - \mu}{\sigma} \right]^2} e^{-\frac{1}{2} \left[ \frac{\ln(D_3) - \mu}{\sigma} \right]^2} \dots e^{-\frac{1}{2} \left[ \frac{\ln(D_n) - \mu}{\sigma} \right]^2} \right) \prod_{i=1}^n \left( \frac{1 + \alpha e^{-D_i}}{D_i} \right)
\end{aligned}$$

Then,

$$\begin{aligned}
L(D_1, D_2, D_3, \dots, D_n / \mu, \sigma^2, \alpha) &= (2\pi\sigma^2 C^2)^{-\frac{n}{2}} e^{-\frac{1}{2} \sum_{i=1}^n \left( \frac{\ln(D_i) - \mu}{\sigma} \right)^2} \prod_{i=1}^n \left( \frac{1 + \alpha e^{-D_i}}{D_i} \right) \\
L(D_1, \dots, D_n / \mu, \sigma^2, \alpha) &= (2\pi\sigma^2 C^2)^{-\frac{n}{2}} e^{-\frac{1}{2} \sum_{i=1}^n \left( \frac{\ln(D_i) - \mu}{\sigma} \right)^2} \prod_{i=1}^n (D_i^{-1}) \prod_{i=1}^n (1 + \alpha e^{-D_i}) \quad (5.14)
\end{aligned}$$

By finding the natural logarithm of the likelihood function expressed in (5.14), the log likelihood of the probability distribution function is developed and is given by:

$$\ln L = \ln(2\pi\sigma^2 C^2)^{-\frac{n}{2}} - \frac{1}{2} \sum_{i=1}^n \left( \frac{\ln(D_i) - \mu}{\sigma} \right)^2 + \ln \left[ \prod_{i=1}^n (D_i^{-1}) \right] + \ln \left[ \prod_{i=1}^n (1 + \alpha e^{-D_i}) \right] \quad (5.15)$$

Adopting partial differential of equation (5.15) and equating to zero, results in the following maximum likelihood estimation equations:

$$\frac{\partial \ln L}{\partial \mu} = \frac{1}{\sigma^2} \sum_{i=1}^n (\ln(D_i) - \mu) = 0 \quad (5.15)$$

$$\frac{\partial \ln L}{\partial \sigma^2} = -\frac{n}{2} \frac{\partial}{\partial \sigma^2} [\ln(2\pi\sigma^2 C^2)] - \frac{1}{2} \sum_{i=1}^n (\ln(D_i) - \mu)^2 \frac{\partial}{\partial \sigma^2} [\sigma^{-2}] = 0 \quad (5.16)$$

$$\frac{\partial \ln L}{\partial \alpha} = \frac{\partial}{\partial \alpha} \left[ \ln \left[ \prod_{i=1}^n (1 + \alpha e^{-D_i}) \right] \right] = 0 \quad (5.17)$$

Solution of equations (5.15), (5.16) and (5.17) represent the maximum likelihood estimators of the probability distribution function in (5.9).

From equation (5.15), the parameter  $\hat{\mu}$  that maximizes the likelihood function can be determined as follows:

$$\begin{aligned}\frac{\partial \ln L}{\partial \mu} &= \frac{1}{\sigma^2} \sum_{i=1}^n (\ln(D_i) - \mu) = 0 \\ \frac{1}{\sigma^2} \sum_{i=1}^n \ln(D_i) &= \frac{1}{\sigma^2} \sum_{i=1}^n \mu \\ \sum_{i=1}^n \ln(D_i) &= \sum_{i=1}^n \mu \\ \sum_{i=1}^n \ln(D_i) &= n\mu\end{aligned}$$

Therefore,

$$\hat{\mu} = \frac{1}{n} \sum_{i=1}^n \ln(D_i) \quad (5.18)$$

From (5.16) below, the parameter  $\hat{\sigma}^2$ , is obtained as following:

$$\frac{\partial \ln L}{\partial \sigma^2} = -\frac{n}{2} \frac{\partial}{\partial \sigma^2} [\ln(2\pi\sigma^2 C^2)] - \frac{1}{2} \sum_{i=1}^n (\ln(D_i) - \mu)^2 \frac{\partial}{\partial \sigma^2} [\sigma^{-2}] = 0$$

Let  $\sigma^2 = y$ , then, the above expression becomes:

$$\frac{\partial \ln L}{\partial y} = -\frac{n}{2} \frac{\partial}{\partial y} [\ln(2\pi C^2 y)] - \frac{1}{2} \sum_{i=1}^n (\ln(D_i) - \mu)^2 \frac{\partial}{\partial y} [y^{-1}]$$

$$\frac{\partial \ln L}{\partial y} = -\frac{n}{2y} + \frac{1}{2y^2} \sum_{i=1}^n (\ln(D_i) - \mu)^2$$

For  $y = \sigma^2$ , then we have:

$$\frac{\partial \ln L}{\partial \sigma^2} = -\frac{n}{2} \sigma^{-2} + \frac{1}{2\sigma^4} \sum_{i=1}^n (\ln(D_i) - \mu)^2 = 0$$

$$-n + \frac{1}{\sigma^2} \sum_{i=1}^n (\ln(D_i) - \mu)^2 = 0$$

$$n\sigma^2 = \sum_{i=1}^n (\ln(D_i) - \mu)^2$$

Therefore,

$$\hat{\sigma}^2 = \frac{1}{n} \sum_{i=1}^n \left( \ln(D_i) - \frac{1}{n} \sum_{i=1}^n \ln(D_i) \right)^2 = \frac{1}{n} \sum_{i=1}^n (\ln(D_i) - \hat{\mu})^2 \quad (5.19)$$

From (5.17), the parameter that maximizes the likelihood function can be determined as follows:

$$\frac{\partial \ln L}{\partial \alpha} = \frac{\partial}{\partial \alpha} \left[ \ln \left[ \prod_{i=1}^n (1 + \alpha e^{-D_i}) \right] \right] = 0$$

But, for 1, 2, 3...n,

$$\prod_{i=1}^n (1 + \alpha e^{-D_i}) = (1 + \alpha e^{-D_1})(1 + \alpha e^{-D_2}) \dots (1 + \alpha e^{-D_n})$$

Then,

$$\ln \left[ \prod_{i=1}^n (1 + \alpha e^{-D_i}) \right] = \ln(1 + \alpha e^{-D_1}) + \ln(1 + \alpha e^{-D_2}) + \dots + \ln(1 + \alpha e^{-D_n})$$

Thus,

$$\begin{aligned} \frac{\partial \ln L}{\partial \alpha} &= \frac{\partial}{\partial \alpha} \left[ \ln \left[ \prod_{i=1}^n (1 + \alpha e^{-D_i}) \right] \right] \\ &= \frac{\partial}{\partial \alpha} [\ln(1 + \alpha e^{-D_1}) + \ln(1 + \alpha e^{-D_2}) + \dots + \ln(1 + \alpha e^{-D_n})] \\ &= \frac{\partial}{\partial \alpha} \ln(1 + \alpha e^{-D_1}) + \frac{\partial}{\partial \alpha} \ln(1 + \alpha e^{-D_2}) + \dots + \frac{\partial}{\partial \alpha} \ln(1 + \alpha e^{-D_n}) \\ &= \frac{e^{-D_1}}{(1 + \alpha e^{-D_1})} + \frac{e^{-D_2}}{(1 + \alpha e^{-D_2})} + \dots + \frac{e^{-D_n}}{(1 + \alpha e^{-D_n})} \\ &= \frac{1}{e^{D_1}(1 + \alpha e^{-D_1})} + \frac{1}{e^{D_2}(1 + \alpha e^{-D_2})} + \dots + \frac{1}{e^{D_n}(1 + \alpha e^{-D_n})} \\ &= \frac{1}{(\alpha + e^{D_1})} + \frac{1}{(\alpha + e^{D_2})} + \dots + \frac{1}{(\alpha + e^{D_n})} = \sum_{i=1}^n \frac{1}{(\alpha + e^{D_i})} \end{aligned}$$

Therefore

$$\frac{\partial \ln L}{\partial \alpha} = \sum_{i=1}^n \frac{1}{(\alpha + e^{D_i})}$$

For  $\frac{\partial \ln L}{\partial \alpha} = 0$

$$\sum_{i=1}^n \frac{1}{(\alpha + e^{D_i})} = 0$$

$$\sum_{i=1}^n \frac{1}{(\alpha + e^{D_i})} \frac{(\alpha - e^{D_i})}{(\alpha - e^{D_i})} = 0$$

$$\sum_{i=1}^n \frac{(\alpha - e^{D_i})}{(\alpha^2 - e^{-2D_i})} = 0$$

$$\sum_{i=1}^n (\alpha - e^{D_i}) = 0$$

$$n\alpha = \sum_{i=1}^n e^{D_i}$$

Therefore,  $\hat{\alpha}$ , is given by:

$$\hat{\alpha} = \frac{1}{n} \sum_{i=1}^n e^{D_i} \quad (5.20)$$

The method of maximum likelihood estimation technique is thus used to estimate the fit parameters of the developed model in (5.11) and parameters  $\mu$ ,  $\sigma^2$  and  $\alpha$  from measured data are determined using estimators given in equations (5.18), (5.19) and (5.20). The last parameter,  $N_T$  is optimized from the self-consistency rule of rainfall DSD such that:

$$N_{T,opt} = \frac{R}{6\pi \times 10^{-4} \sum_{i=1}^N D^3 f(D_i) v(D_i) \Delta D} \quad (5.21)$$

Where  $R$ , is the rainfall rate,  $f(D_i)$  is the probability density function,  $v(D_i)$  is the terminal velocity and  $\Delta D_i$  is the diameter interval of the rain drops at the  $i$ th channel of the disdrometer.

From (5.18) to (5.20), estimation of fit parameters by the method of maximum likelihood are presented as follows:

$$\mu = A_\mu + B_\mu \ln(R) \quad (5.22)$$

$$\sigma^2 = A_\sigma + B_\sigma \ln(R) \quad (5.23)$$

$$\alpha = a_\alpha(R)^{b_\alpha} \quad (5.24)$$

#### 5.4 Measurement and Data Processing

As indicated before, the rainfall DSD measurement data used in this chapter is obtained from the J-W RD-80 disdrometer installed at the roof of the ICT building, University of Rwanda, Huye Campus, Butare (2°36'53.88"S, 29°44'31.53") at 1769 m of altitude in the southern province of Rwanda for a period of 32 months between 2012 and 2015. This disdrometer is capable of processing rainfall data (rainfall rate and rain drop statistics) into 20 channels via the indoor unit, with each of the channels related to rain drops with diameter,  $D$ , in the range  $0.313 \text{ mm} \leq D \leq 5.373 \text{ mm}$ . In this section, with set up similar to that presented in Figure 4-1, section 4.2, instead of the rainfall rate, the rain drop size distribution is the main parameter of interest in the measurement. The data was sorted and categorized into different rainfall regimes based on rainfall rates, annual and seasonal variations, as presented in Table 5-1. Note that in this context, the term “annual” means the overall data at one-minute integration time, including all seasons. Rwanda experiences four seasons in a yearly cycle, which are determined by the variability of rainfall [124].

Table 5-1. Rainfall DSD measurements over Butare, Rwanda between 2012 and 2015

Category	Number of samples	Total number of Rain drops	Observed maximum number of rain drops per sample	Percentage samples
Annual (overall)	56620	8737205	3643	100
Rainfall regimes				
Drizzle	50920	6640982	3643	89.93
Widespread	2113	868738	1293	4.79
Shower	2536	990540	1870	4.48
Thunderstorm	451	236945	1487	0.8
Seasonal				
Short dry season	9756	1854069	3643	17.23
Long rain season	22407	3389739	2833	39.57
Long dry season	10023	1356077	3570	17.7
Short rain season	14434	2137320	2716	25.5

These seasons include a dual rainy season interspersed between two dry seasons as follows: the Short dry season (From January to February); the Long rainy season (March to the beginning of June); the Long dry season (from June to mid-September); and the Short rainy season (mid-September to December). The maximum number of rain drops per sample in the period of measurement is 3643 drops and the maximum rainfall rate is 118.5 mm/h. Table 5-1 gives the summary of Rainfall DSD measurements recorded in Butare, Rwanda in the entire period of measurement between 2012 and 2015.

### **5.5 Comparison of the new proposed DSD model with other DSD models in Butare, Rwanda.**

Distribution parameters for different rainfall DSD statistical models were estimated using the methods earlier explained in sections 4.4 and 5.3. The Lognormal (LGN), Modified Gamma (MGM), Marshal-Palmer (M-P) and Weibull (WBL) distributions were fitted to the measurement data using the method of moment (MoM) technique. The new DSD model was fitted using maximum likelihood (ML) estimation technique. Therefore, various input model parameters obtained by applying the above techniques (MoM or ML) are expressed as a function of rainfall rate via regression techniques and results are presented in subsections 5.51 to 5.53.

#### **5.5.1 Regime Variation of Rainfall Drop Size Distribution.**

Using the method of moment (MoM) technique and maximum likelihood (ML) estimation technique described in sections 4.4 and 5.3 respectively, various input parameters for different DSD models for Butare were estimated and results are presented in Tables 4-6 and 5-2 for the existing DSD models (LGN, MGM, MP and WBL) and the new DSD model, respectively. Tables 4-6 and 5-2 present the model parameters for different DSD statistical models in Butare based on

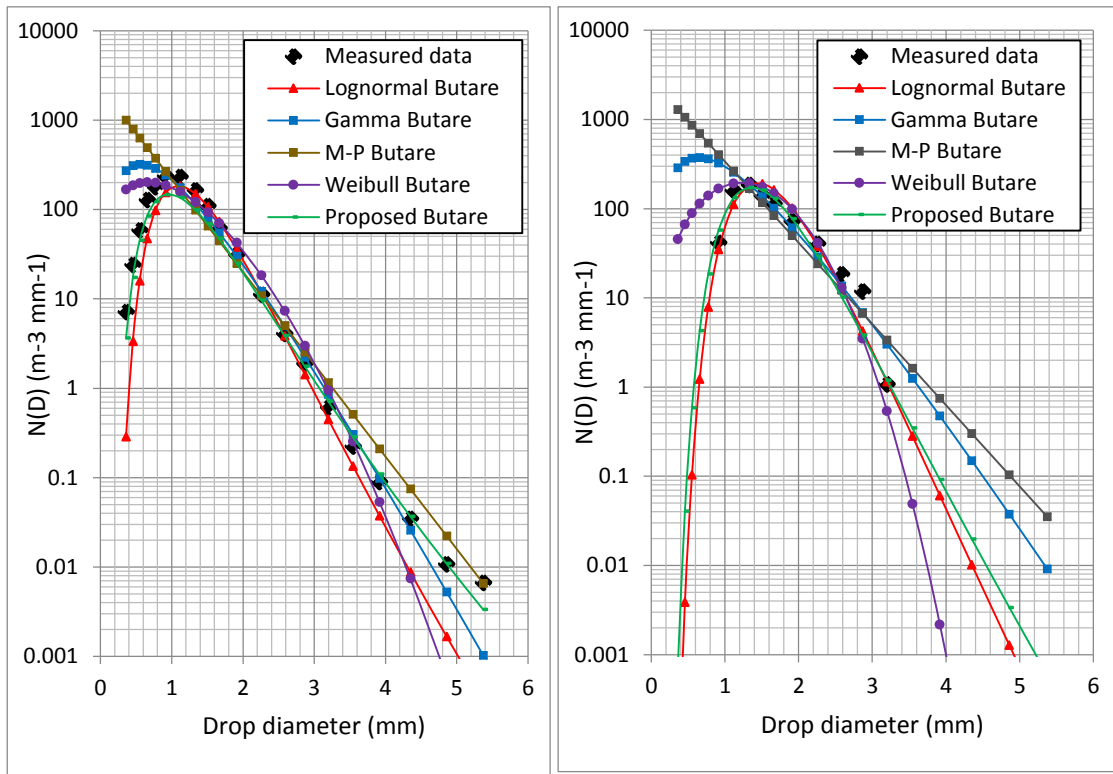
rainfall regimes. The measured data was compared with different DSD models at selected rainfall rates. The comparison is done at rainfall rate of 4.95 mm/h for drizzle; 9.9 mm/h for widespread; 27.7 mm/h for shower; and 75.28 mm/h for thunderstorm regime; and results are shown in Figure 5-1(a)-(d).

In Figure 5-1(a), at rainfall rate of 4.95 mm/h, the LGN model underestimates the measurement at drop diameter region between 0.359 and 0.913 mm. It is seen that, the MGM and WBL models seem to coincide with the measured DSD even though they overestimate it at lower raindrop diameter regions. Compared with other statistical models, the measured DSD is best fitted by the proposed DSD model. In Figure 5-1(b), for widespread at 9.9 mm/h, the WBL, MGM and the M-P models overestimate the measurement in the diameter range up to 1 mm, the LGN model seems to fit the measurement better. In Figure 5-1(c), for shower rainfall at 27.7 mm/h, the proposed DSD model best fits the measured DSD compared to other models. The MGM, M-P and WBL models all overestimate the measurement at drop diameter region less than 1.506 mm. For thunderstorm rain at 75.28 mm/h (as shown in Figure 5-1(d)), the proposed DSD model gives a better fit compared to other DSD models. From the plotted graphs of Figure 5-1, it is observed that the models have different performances as the rainfall rate changes. Therefore, there is need for proper error estimation between the measured DSD and the distribution models at various rainfall rates to establish the best model in the region.

In this regard, the various DSD models were tested using the root mean square error (RMSE) test and the Chi-squared test ( $\chi^2$ ) for confirming the rejection or acceptance of the null hypothesis of each model.

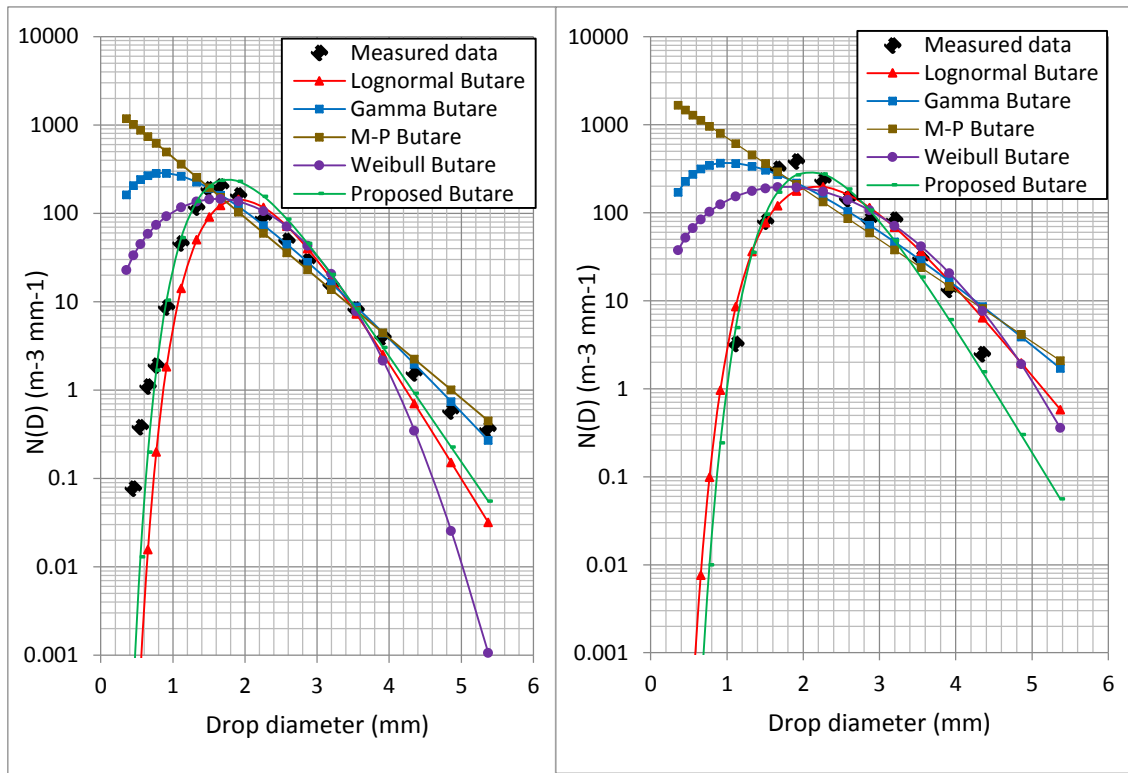
Table 5.2. Model parameters for the new proposed DSD statistical model analysis in Butare, Rwanda based on rainfall regimes.

Input parameters	Rain rate (mm/h)	$N_{T,opt}$	$\mu = A_\mu + B_\mu \ln(R)$		$\sigma^2 = A_\sigma + B_\sigma \ln(R)$		$\alpha = a_\alpha R^{b_\alpha}$	
			$A_\mu$	$B_\mu$	$A_\sigma$	$B_\sigma$	$a_\alpha$	$b_\alpha$
Drizzle	4.95	137.23	-0.1053	0.1754	0.1095	0.0172	2.8875	0.1504
Widespread	9.9	157.53	-0.1785	0.2697	0.1128	-0.017	2.2146	0.4247
Shower	27.7	165.48	-0.232	0.2869	0.0817	-0.002	1.2755	0.6425
Thunderstorm	75.28	293.38	0.6065	0.0599	0.1067	0.008	8.5443	0.1477



(a)

(b)



(c)

(d)

Figure 5-1: Rain size distribution in Butare, Rwanda based on rainfall regimes. (a) Drizzle at 4.95 mm/h (b) Widespread at 9.9 mm/h (c) Shower at 27.7 mm/h (d) Thunderstorm at 75.28 mm/h.



Expressions for these two error tools are given in (5.25) and (5.26) [5, 34]:

$$RMSE = \sqrt{\frac{1}{n} \sum_{i=1}^n [f^*(x_i) - f(x_i)]^2} \quad (5.25)$$

$$\chi^2 = \sum_{i=1}^n \frac{(f^*(x_i) - f(x_i))^2}{f(x_i)} \quad (5.26)$$

Where  $f^*(x_i)$  is the measured data from the disdrometer and  $f(x_i)$  the modelled data, with  $n$  being the sample size.

Using equations (5.25) and (5.26), the results of the error estimation for different rainfall DSD models for Butare based on the four rainfall regimes are presented in Table 5-3. The chi-squared test was done with 19 degree of freedom at the level of significance of 0.01 which corresponds to a chi-squared threshold value of 36.191.

From Table 5-3, a comparison with the chi-squared threshold shows that MGM and M-P drop size distribution models fail the chi-squared test for drizzle and widespread regimes. Thus, they are automatically rejected for those rainfall regimes in Butare. The DSD model giving the lowest RMSE will be the best fit to the measurements; therefore, by combining the information from Figure 5-1 and Table 5-3, the Weibull DSD model best fits the measured data with RMSE of 0.108 and  $\chi^2$  of 3.208 for drizzle rainfall events. The Lognormal best fits the measured data with RMSE of 0.061 and  $\chi^2$  of 0.672 for widespread rainfall events. For the shower rainfall event, both Lognormal and the new DSD models best fit the measurement with RMSE of 0.095 and  $\chi^2$  of 0.878 for Lognormal and the RMSE of 0.096 and  $\chi^2$  of 1.422 for the new DSD model. Finally, the new proposed model best fits the measured data with RMSE of 0.072 and  $\chi^2$  of 0.558 for thunderstorm rainfall regime.

Table 5-3. Error estimation from different rainfall DSD models for Butare based on rainfall regimes.

Regime	TESTS	LGN	MGM	M-P	WBL	Proposed model
Drizzle	RMSE	0.128	0.433	0.417	0.108	0.110
	CHI	0.165	210.521	66.025	3.208	0.463
Widespread	RMSE	0.061	0.398	0.417	0.231	0.078
	CHI	0.672	206.788	92.560	3.479	0.891
Shower	RMSE	0.095	0.325	0.384	0.170	0.096
	CHI	0.878	32.783	35.234	3.596	1.422
Thunderstorm	RMSE	0.111	0.292	0.387	0.213	0.072
	CHI	0.662	28.313	33.610	2.828	0.558

### 5.5.2 Annual Variation of Rainfall Drop Size Distribution.

Estimation of annual fit parameters for different rainfall DSD statistical models was carried out using the MoM and ML techniques as earlier explained. The LGN, MGM, M-P and WBL drop size distribution models were fitted to the measured DSD by the MoM technique and results are presented in Table 4-5 in section 4.5. For the proposed DSD model given in (5.11) and maximum likelihood estimators given in (5.18) to (5.20), the model parameters for the prediction of annual drop size distribution in Butare for rainfall rates between 0.0029 and 118.516 mm/h are given by:

$$\hat{\mu} = -0.073 + 0.1881 \ln(R) \quad (5.27)$$

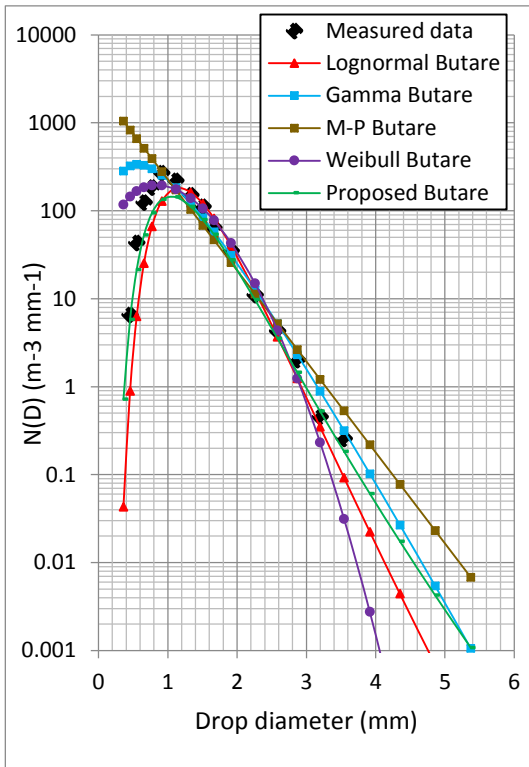
$$\hat{\sigma}^2 = 0.0941 + 0.0112 \ln(R) \quad (5.28)$$

$$\hat{\alpha} = 3.1897(R)^{0.1899} \quad (5.29)$$

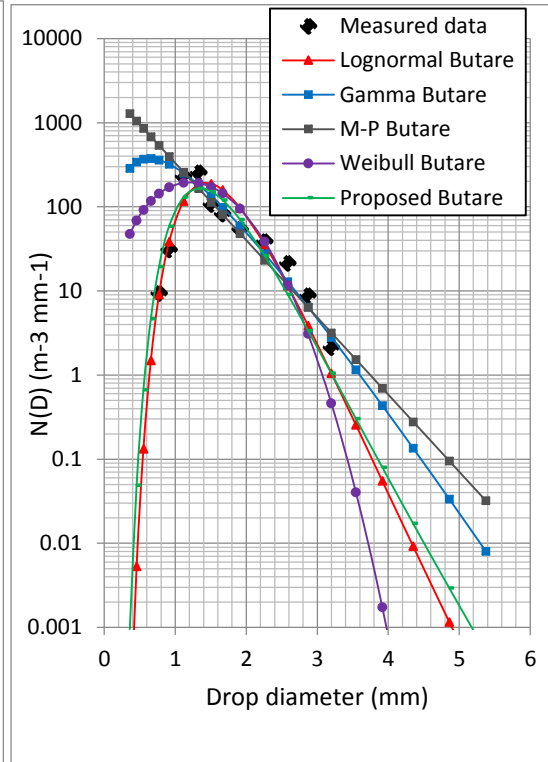
The measured data was compared with the different DSD models at selected rainfall rates. The selected rainfall rates are 4.97 mm/h for drizzle, 9.9 mm/h for widespread, 25.55 mm/h for shower and 60.08 mm/h for thunderstorm rainfall regimes, and results are shown in Figure 5-2. From the plotted graphs of Figure 5-2, it is observed that those different models have different performances as the rainfall rate is varied. That is why there is need for quantitative analysis between the measured DSD and the distribution models so as to determine the suitable annual DSD model. Using equations (5.25), the results of the error estimation are presented in Table 5-4. From Table 5-4, the annual RMSE values show that the WBL DSD model best fits the measurement with rainfall rate less than 5 mm/h. As the rainfall rate increases, results show that between 5 mm/h and 40 mm/h, the LGN DSD model best fits the measurement.

Table 5-4. Error estimation from different annual rainfall DSD models in Butare.

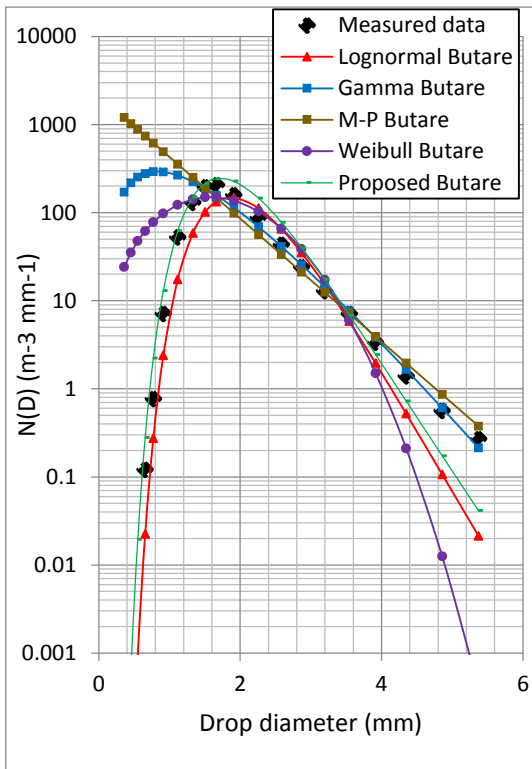
Rain rate (mm/h)	LGN	MGM	M-P	WBL	Proposed model
3	0.217	0.490	0.456	0.204	0.205
5	0.121	0.438	0.423	0.153	0.127
10	0.029	0.406	0.421	0.317	0.104
20	0.074	0.364	0.403	0.322	0.078
40	0.096	0.286	0.375	0.173	0.123
50	0.075	0.266	0.364	0.180	0.068
60	0.095	0.269	0.367	0.185	0.073
80	0.151	0.301	0.394	0.214	0.081
90	0.190	0.250	0.358	0.205	0.129
100	0.185	0.228	0.345	0.203	0.146
110	0.192	0.227	0.344	0.201	0.161
118	0.171	0.320	0.412	0.244	0.123
Average	0.133	0.3204	0.3885	0.2167	0.116



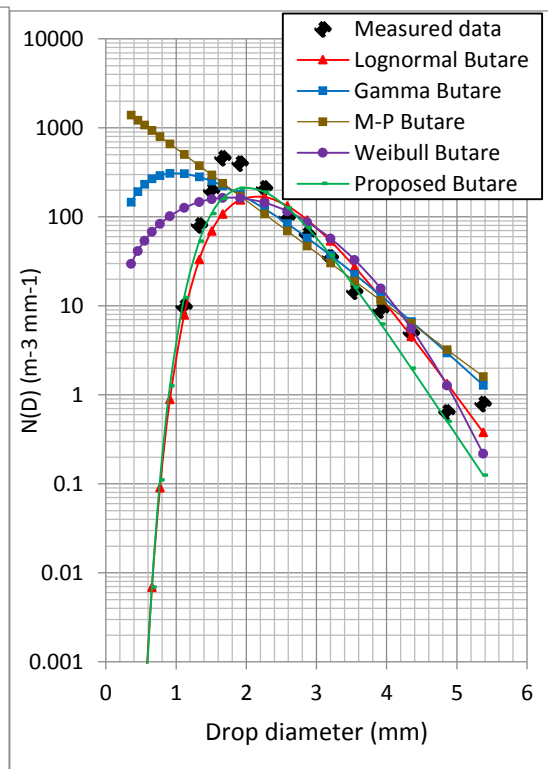
(a)



(b)



(c)



(d)

Figure 5-2: Annual Rain drop size distribution in Butare, Rwanda (a) Drizzle at 4.97 mm/h (b) Widespread at 9.9 mm/h (c) Shower at 25.55 mm/h (d) Thunderstorm at 60.08 mm/h.

Finally beyond 50 mm/h, the proposed model is seen to be the best as it gives the lowest RMSE values compared to other distributions and therefore it can be considered as the best annual model for Butare because it best fits the measured DSD at high rain rates that are mostly associated with microwave and millimetre wave attenuation.

### **5.5.3 Seasonal Variation of Rainfall Drop Size Distribution.**

Estimation of seasonal fit parameters for different rainfall DSD statistical models was carried out using the MoM and ML techniques as done in previous subsections, and results are presented in Tables 5-5 to 5-8. The measured seasonal data was compared with different DSD models at selected rainfall rate of 3.9 mm/h for drizzle, and 9.9 mm/h for widespread, 38.7 mm/h for shower and the corresponding seasonal point rainfall rate  $R_{0.01}$  value for thunderstorm rainfall regime. The results are shown in Figure 5-3 to 5-6.

The plots in Figure 5-3(a)-(d) show the results for the seasonal variation of rainfall DSDs for drizzle rains in Butare. The Short dry season DSD plots at 3.91 mm/h are presented in 5(a) where the new DSD model appears to perform well compared to the other DSD models. In Figure 5.3(b) for the Long rainy season with rainfall rate of 3.88 mm/h, the M-P and MGM overestimate the measurement at low raindrop diameter less than 0.771 mm, while the LGN and the proposed DSD model seem to fit better the measurement in this low raindrop diameter-range. Beyond 0.913 mm, the LGN Model overestimates the measured DSD while, MGM and the new Model best fit the measured DSD. In Figure 5-3(c) for the Long dry season with rainfall rate of 3.92 mm/h, the WBL model is seen to match well the measured DSD beyond 0.505 mm compared to other DSD models. In Figure 5-3(d), compared with other DSD models in the Short rainy season at 3.88 mm/h, the measured DSD data is best fitted by the new proposed DSD Model.

Figure 5-4(a)-(d) plots present the results for the seasonal variation of rainfall DSDs for widespread rains in Butare. Comparing with other DSD models for this rainfall regimes at 9.93 mm/h for the Short dry season in Figure 5-4(a), 9.99 mm/h for the Long rainy season in Figure 5-4(b), and at 9.94 mm/h for the Short rainy season in Figure 5-4(d), the LGN and the new DSD model are seen to compare well with the measurement. For the Long dry season at 9.97 mm/h as shown in Figure 5.4(c), the new DSD model gives a better fit compared to other DSD models.

Figure 5-5(a)-(d) plots present the results for the seasonal variation of rainfall DSDs for shower regime rains in Butare. For this rainfall regime, the estimated DSD for the Short dry season in Figure 5-5(a) at 38.7 mm/h, Long rainy season in Figure 5-5(b) at 38.73 mm/h, Long and the Short rainy season at 38.58 mm/h peak their drop number density at drop diameter about 2.259 mm while the estimated DSD for the Long dry season in Figure 5-5(c) at 37.44 mm/h reaches its

maximum drop density in the drop diameter range close to 2 mm. From the plots of Figure 5-3(a)-(d) to 5.5(a)-(d) in all seasons, compared to other DSD models, it is observed that, the LGN model and the new DSD model tend to better match the measured DSD as the rainfall regime varies (rainfall rate increases). From the results, the LGN and the new DSD model are seen to give better fits to the shower rain size data in all the four seasons in Butare, Rwanda.

Table 5-5: Model parameters for different rainfall DSD statistical models for Short dry season analysis in Butare, Rwanda

Lognormal DSD model								
Input parameters	$N_T = a_0 R^{b_0}$		$\mu = A_\mu + B_\mu \ln(R)$		$\sigma^2 = A_\sigma + B_\sigma \ln(R)$			
	$a_0$	$b_0$	$A_\mu$	$B_\mu$	$A_\sigma$		$B_\sigma$	
Drizzle	152.66	0.2269	-0.1669	0.177	0.0759		0.0109	
Widespread	86.14	0.2653	-0.0054	0.2021	0.0668		-0.001	
Shower	192.02	-0.045	-0.2242	0.2888	0.052		0.0042	
Thunderstorm	2.221	1.1415	1.0074	-0.04	0.0886		-0.004	
Modified Gamma DSD Model								
Input parameters	$\mu$	$N_m = a_m(R)^{b_m}$		$\Lambda = a_\Lambda(R)^{b_\Lambda}$				
		$a_m$	$b_m$	$a_\Lambda$		$b_\Lambda$		
Drizzle	2	28604	-0.468	5.4624		-0.213		
Widespread	2	11894	-0.341	4.8192		-0.202		
Shower	2	55135	-1.022	6.1539		-0.31		
Thunderstorm	2	9.7417	1.3327	1.6066		0.055		
Negative Exponential DSD model (MP)								
Input parameters	$\mu$	$N_0 = a_0(R)^{b_0}$		$\Lambda = a_\Lambda(R)^{b_\Lambda}$				
		$a_0$	$b_0$	$a_\Lambda$		$b_\Lambda$		
Drizzle	0	3787	-0.043	3.6416		-0.213		
Widespread	0	2023.3	0.0625	3.2128		-0.202		
Shower	0	5751.7	-0.401	4.1026		-0.31		
Thunderstorm	0	14.91	1.2227	1.0711		0.055		
Weibull DSD model								
Input parameters	$\beta = a_\beta(R)^{b_\beta}$		$\gamma = a_\gamma(R)^{b_\gamma}$		$N_w = a_w(R)^{b_w}$			
	$a_\beta$	$b_\beta$	$a_\gamma$	$b_\gamma$	$a_w$		$b_w$	
Drizzle	2.4044	-0.167	0.7625	-0.1625	247.496		-0.2505	
Widespread	2.5331	0.0072	0.9115	0.2097	138.67		0.2508	
Shower	3.3601	-0.087	0.8108	0.2777	249.34		-0.036	
Thunderstorm	2.3442	0.0073	2.3187	-0.014	3.9311		1.1072	
New DSD model								
Input parameters	Rain rate (mm/h)	$N_{T,opt}$	$\mu = A_\mu + B_\mu \ln(R)$		$\sigma^2 = A_\sigma + B_\sigma \ln(R)$		$\alpha = a_\alpha R^{b_\alpha}$	
			$A_\mu$	$B_\mu$	$A_\sigma$	$B_\sigma$	$a_\alpha$	$b_\alpha$
Drizzle	3.91	171.981	-0.1737	0.1693	0.1076	0.0175	2.7316	0.1432
Widespread	9.93	143.401	-0.069	0.2322	0.1326	-0.025	2.8082	0.3436
Shower	38.7	140.309	-0.1956	0.2909	0.0837	-0.003	1.3004	0.3436
Thunderstorm	89.2	402.235	0.8944	-0.011	0.1402	-0.017	38.109	-0.212

Table 5-6: Model parameters for different rainfall DSD statistical models for Long rainy season analysis in Butare, Rwanda

Lognormal DSD model								
Input parameters	$N_T = a_0 R^{b_0}$		$\mu = A_\mu + B_\mu \ln(R)$		$\sigma^2 = A_\sigma + B_\sigma \ln(R)$			
	$a_0$	$b_0$	$A_\mu$	$B_\mu$	$A_\sigma$		$B_\sigma$	
Drizzle	117.03	0.1847	-0.1004	0.1844	0.0755		0.0126	
Widespread	192.1	-0.053	-0.3142	0.3287	0.1136		-0.022	
Shower	175.03	0.0154	-0.2085	0.2772	0.0578		0.0008	
Thunderstorm	6.1033	0.8857	0.6825	0.043	0.0952		-0.007	
Modified Gamma DSD Model								
Input parameters	$\mu$	$N_m = a_m(R)^{b_m}$		$\Lambda = a_\Lambda(R)^{b_\Lambda}$				
		$a_m$	$b_m$	$a_\Lambda$		$b_\Lambda$		
Drizzle	2	17694	-0.576	5.0931		-0.228		
Widespread	2	29420	-0.677	5.4201		-0.252		
Shower	2	60868	-0.896	6.2375		-0.29		
Thunderstorm	2	63.703	-0.8645	2.1732		-0.02		
Negative Exponential DSD model (MP)								
Input parameters	$\mu$	$N_0 = a_0(R)^{b_0}$		$\Lambda = a_\Lambda(R)^{b_\Lambda}$				
		$a_0$	$b_0$	$a_\Lambda$		$b_\Lambda$		
Drizzle	0	2694.7	-0.119	3.3954		-0.228		
Widespread	0	3814.2	-0.173	3.6801		-0.252		
Shower	0	6180.6	-0.316	4.1583		-0.29		
Thunderstorm	0	53.288	0.9047	1.4488		-0.02		
Weibull DSD model								
Input parameters	$\beta = a_\beta(R)^{b_\beta}$		$\gamma = a_\gamma(R)^{b_\gamma}$		$N_w = a_w(R)^{b_w}$			
	$a_\beta$	$b_\beta$	$a_\gamma$	$b_\gamma$	$a_w$		$b_w$	
Drizzle	2.3827	-0.192	0.8257	0.1719	186.4		0.1976	
Widespread	1.6479	0.2056	0.6011	0.3915	353.83		-0.14	
Shower	2.7051	-8E-05	0.7369	0.2939	303.54		-0.031	
Thunderstorm	1.9429	0.057	1.7272	0.0627	10.407		0.8575	
New DSD model								
Input parameters	Rain rate (mm/h)	$N_{T,opt}$	$\mu = A_\mu + B_\mu \ln(R)$		$\sigma^2 = A_\sigma + B_\sigma \ln(R)$		$\alpha = a_\alpha R^{b_\alpha}$	
			$A_\mu$	$B_\mu$	$A_\sigma$	$B_\sigma$	$a_\alpha$	$b_\alpha$
Drizzle	3.8	125.2	-0.0984	0.1823	0.1036	0.0179	2.8971	0.1532
Widespread	9.9	149.989	-0.2346	0.2963	0.1039	-0.011	2.0395	0.4668
Shower	38.7	172.272	-0.2459	0.2897	0.0937	-0.007	1.2621	0.6433
Thunderstorm	94.3	331.151	0.612	0.0596	0.1328	-0.014	11.277	0.0853

Figure 5-6(a)-(d) plots present the results for the seasonal variation of rainfall DSDs for thunderstorm rains in Butare. The measured DSD is compared with DSD models at the corresponding point rainfall rate  $R_{0.01}$  value for each season. The Short dry season at  $R_{0.01}=89$  mm/h in 5.6(a), the Long rainy season at  $R_{0.01}=94$  mm/h in 5-6(b), the Long dry season at  $R_{0.01}=70$  mm/h in 5-6(c) and lastly, the Short rainy season at  $R_{0.01}=114$  mm/h in 5-6(d). From the plotted graphs of Figure 5-6(a)-(d) for all seasons, it is observed that the Marshall-Palmer, Gamma and the Weibull DSD models all overestimate the measured DSD at drop diameter regions lower than

1.506 mm, while the DSD measurements agree with the DSD models for diameters above 2 mm. Thus for thunderstorm regime, as observed in all the four seasons in Butare, the new DSD model is found to give a better fit to the DSD measurement compared to all the existing DSD models.

Table 5-7: Model parameters for different rainfall DSD statistical models for long dry season analysis in Butare, Rwanda

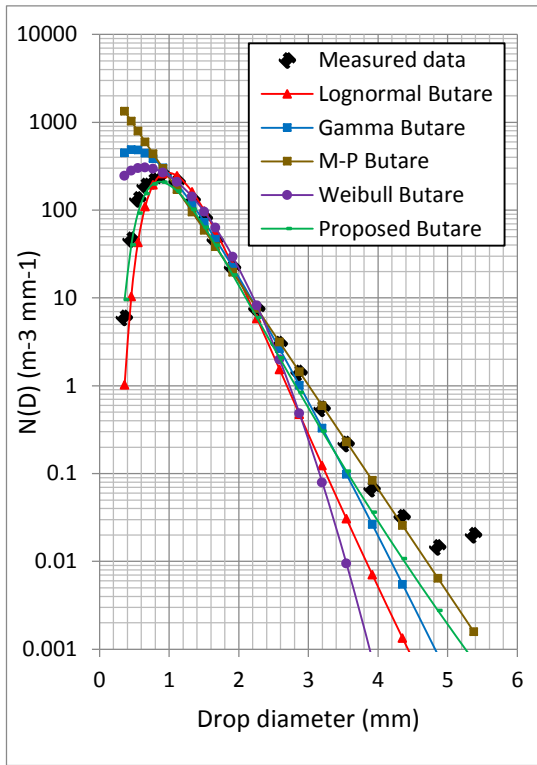
Lognormal DSD model								
Input parameters	$N_T = a_0 R^{b_0}$		$\mu = A_\mu + B_\mu \ln(R)$		$\sigma^2 = A_\sigma + B_\sigma \ln(R)$			
	$a_0$	$b_0$	$A_\mu$	$B_\mu$	$A_\sigma$		$B_\sigma$	
Drizzle	100.49	0.2177	-0.0679	0.1797	0.0791		0.0109	
Widespread	107.72	0.2437	-0.1245	0.2369	0.0936		-0.015	
Shower	269.77	-0.137	-0.3236	0.3157	0.0556		0.0028	
Thunderstorm	63.199	0.3367	0.191	0.1553	-0.0216		0.0227	
Modified Gamma DSD Model								
Input parameters	$\mu$	$N_m = a_m(R)^{b_m}$		$\Lambda = a_\Lambda(R)^{b_\Lambda}$				
		$a_m$	$b_m$	$a_\Lambda$		$b_\Lambda$		
Drizzle	2	12987	-0.502	4.8691		-0.218		
Widespread	2	12754	-0.21	4.8788		-0.183		
Shower	2	113569	-1.149	6.8654		-0.329		
Thunderstorm	2	19792	-0.504	5.3464		-0.235		
Negative Exponential DSD model (MP)								
Input parameters	$\mu$	$N_0 = a_0(R)^{b_0}$		$\Lambda = a_\Lambda(R)^{b_\Lambda}$				
		$a_0$	$b_0$	$a_\Lambda$		$b_\Lambda$		
Drizzle	0	2164	-0.066	3.2461		-0.218		
Widespread	0	2116.8	0.1552	3.2526		-0.183		
Shower	0	9519	-0.491	4.5769		-0.329		
Thunderstorm	0	2735.5	-0.034	3.5643		-0.235		
Weibull DSD model								
Input parameters	$\beta = a_\beta(R)^{b_\beta}$		$\gamma = a_\gamma(R)^{b_\gamma}$		$N_w = a_w(R)^{b_w}$			
	$a_\beta$	$b_\beta$	$a_\gamma$	$b_\gamma$	$a_w$		$b_w$	
Drizzle	2.2761	-0.168	0.8451	0.1662	161.8		0.2325	
Widespread	1.8329	0.1775	0.7645	0.2788	186.56		0.1822	
Shower	3.4213	-0.084	0.7419	0.2966	358.23		-0.107	
Thunderstorm	6.2227	-0.235	1.4095	0.1031	70.197		0.4158	
New DSD model								
Input parameters	Rain rate (mm/h)	$N_{T,opt}$	$\mu = A_\mu + B_\mu \ln(R)$		$\sigma^2 = A_\sigma + B_\sigma \ln(R)$		$\alpha = a_\alpha R^{b_\alpha}$	
			$A_\mu$	$B_\mu$	$A_\sigma$	$B_\sigma$	$a_\alpha$	$b_\alpha$
Drizzle	3.92	149.4	-0.072	0.1762	0.075	0.0116	2.9893	0.153
Widespread	9.97	164.08	-0.1035	0.2311	0.098	-0.01	2.3419	0.3912
Shower	37.44	161.76	-0.2725	0.3054	0.066	0.0017	1.1076	0.6996
Thunderstorm	70	255.53	0.1678	0.175	0.0245	0.007	1.479	0.566

Table 5-8: Model parameters for different rainfall DSD statistical models for Short rainy season analysis in Butare, Rwanda

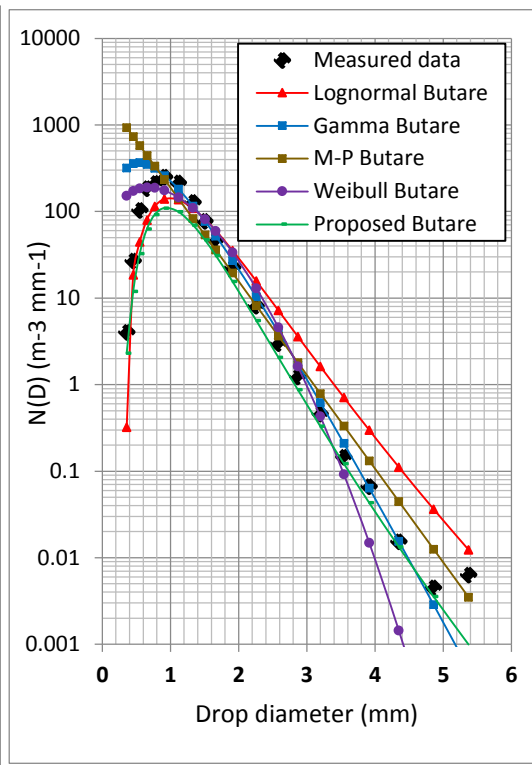
Lognormal DSD model								
Input parameters	$N_T = a_o R^{b_o}$		$\mu = A_\mu + B_\mu \ln(R)$		$\sigma^2 = A_\sigma + B_\sigma \ln(R)$			
	$a_o$	$b_o$	$A_\mu$	$B_\mu$	$A_\sigma$		$B_\sigma$	
Drizzle	107.51	0.2815	-0.088	0.1718	0.0803		0.0074	
Widespread	190.85	-0.006	-0.3133	0.3195	0.1141		-0.024	
Shower	166.47	0.0641	-0.1849	0.259	0.0537		0.002	
Thunderstorm	7.8759	0.8265	0.7507	0.0248	0.0041		0.0161	
Modified Gamma DSD Model								
Input parameters	$\mu$	$N_m = a_m(R)^{b_m}$			$\Lambda = a_\Lambda(R)^{b_\Lambda}$			
		$a_m$	$b_m$		$a_\Lambda$		$b_\Lambda$	
Drizzle	2	14342	-0.37		4.9409		-0.2	
Widespread	2	21105	-0.418		5.2547		-0.213	
Shower	2	63196	-0.851		6.2653		-0.283	
Thunderstorm	2	301.2	0.4867		2.7923		-0.4867	
Negative Exponential DSD model (MP)								
Input parameters	$\mu$	$N_o = a_o(R)^{b_o}$			$\Lambda = a_\Lambda(R)^{b_\Lambda}$			
		$a_o$	$b_o$		$a_\Lambda$		$b_\Lambda$	
Drizzle	0	2320.9	0.0288		3.294		-0.2	
Widespread	0	3019.6	0.0079		3.5032		-0.213	
Shower	0	6360.2	-0.286		4.1768		-0.283	
Thunderstorm	0	152.62	0.6489		1.8615		-0.081	
Weibull DSD model								
Input parameters	$\beta = a_\beta(R)^{b_\beta}$		$\gamma = a_\gamma(R)^{b_\gamma}$		$N_w = a_w(R)^{b_w}$			
	$a_\beta$	$b_\beta$	$a_\gamma$	$b_\gamma$	$a_w$		$b_w$	
Drizzle	2.2494	-0.108	0.8257	0.1596	173.57		0.2926	
Widespread	1.8015	0.1821	0.6834	0.3269	261.86		0.1821	
Shower	3.0313	-0.042	0.7614	0.2719	291.54		0.0163	
Thunderstorm	4.3234	-0.141	2.4346	-0.024	9.1063		0.8952	
New DSD model								
Input parameters	Rain rate (mm/h)	$N_{T,opt}$	$\mu = A_\mu + B_\mu \ln(R)$		$\sigma^2 = A_\sigma + B_\sigma \ln(R)$		$\alpha = a_\alpha R^{b_\alpha}$	
			$A_\mu$	$B_\mu$	$A_\sigma$	$B_\sigma$	$a_\alpha$	$b_\alpha$
Drizzle	3.88	128.5	-0.0948	0.1644	0.1162	0.0143	2.9143	0.15
Widespread	9.94	168.3	-0.2171	0.2817	0.1269	-0.025	2.9143	0.15
Shower	38.58	194.6	-0.209	0.2706	0.077	-0.003	1.3898	0.5862
Thunderstorm	114	397.82	0.5782	0.0694	0.1007	-0.0098	6.2232	0.232

The error estimation from different seasonal rainfall DSD models for Butare are computed using equation (5.25) as done in previous subsections, and results are presented in Table 5-9(a) for the Short dry and Long rainy seasons and Table 5-9(b) for the Long dry and Short rainy seasons at different rainfall rates. The DSD model with the least RMSE would be the best fit to the DSD measurements; Thus the Short dry season is best estimated by the new DSD model as it has the least average RMSE value of 0.122 for all the considered rainfall rate compared to the average RMSE value of 0.157 for LGN, 0.329 for MGM, 0.395 for MP and 0.228 for WBL DSD model.

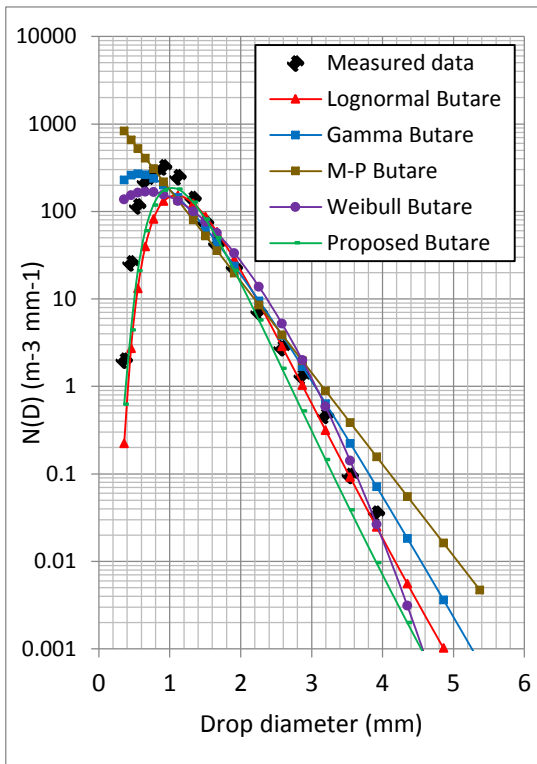




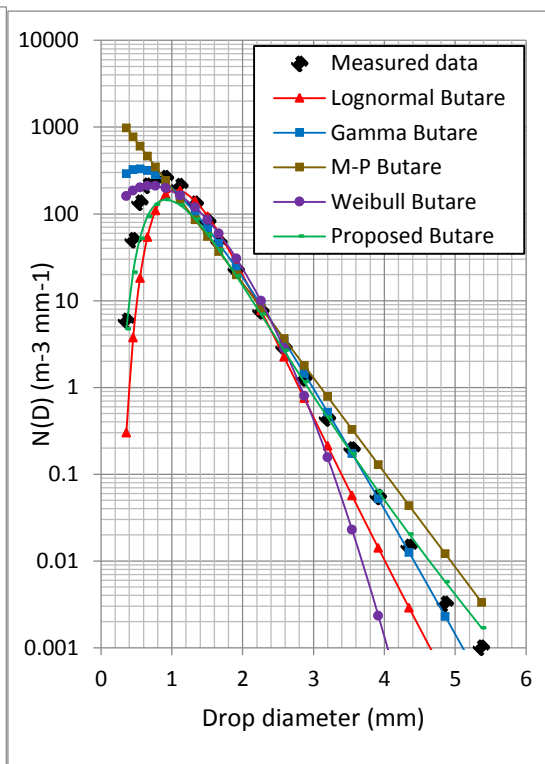
(a)



(b)

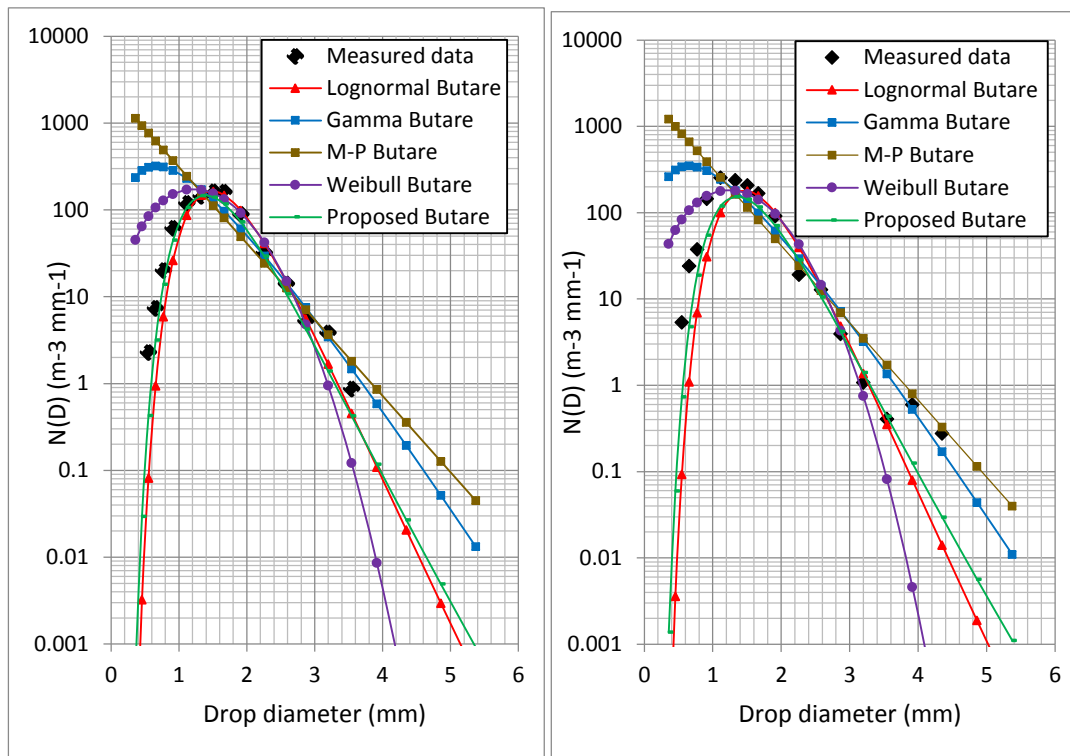


(c)



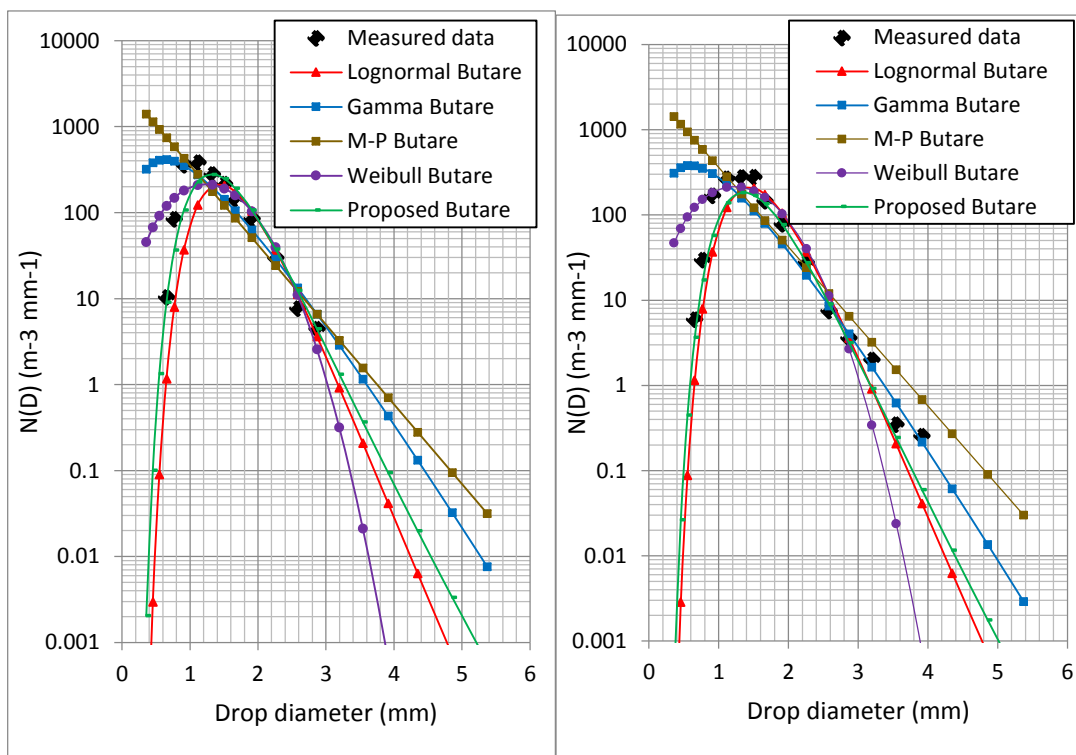
(d)

Figure 5-3: Seasonal rainfall DSDs for drizzle rains in Butare, Rwanda. (a) Short dry season at 3.91 mm/h (b) Long rainy season at 3.88 mm/h (c) Long dry season at 3.92 mm/h (d) Short rainy season at 3.88 mm/h.



(a)

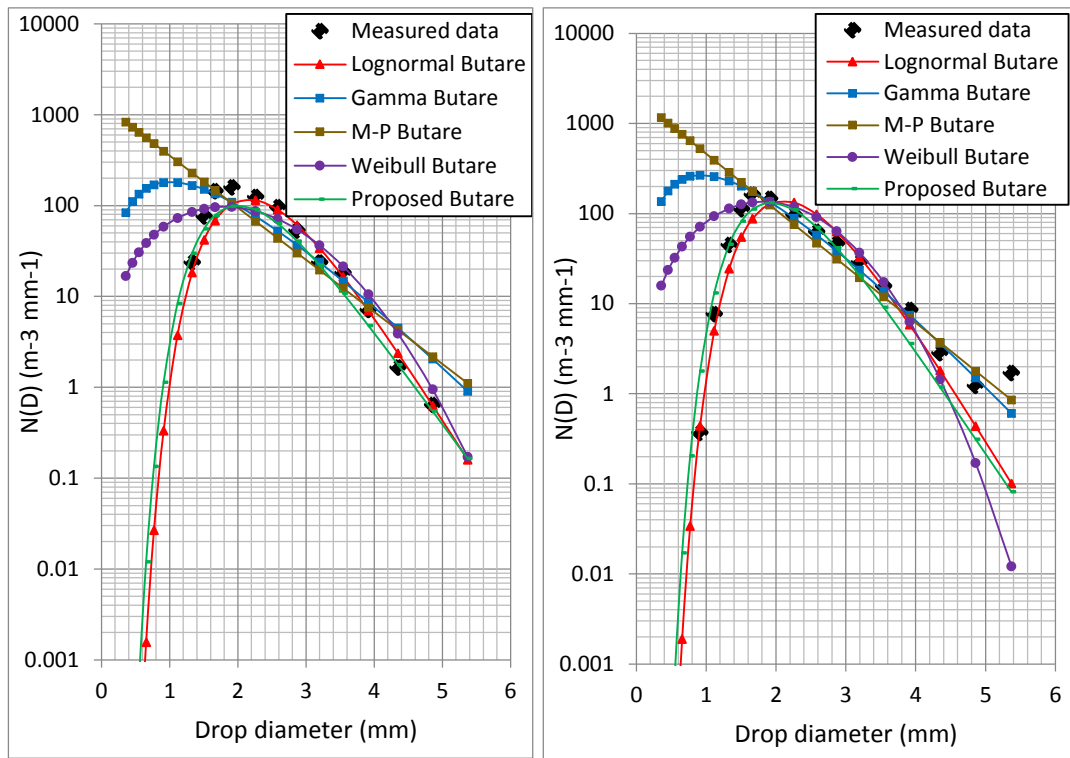
(b)



(c)

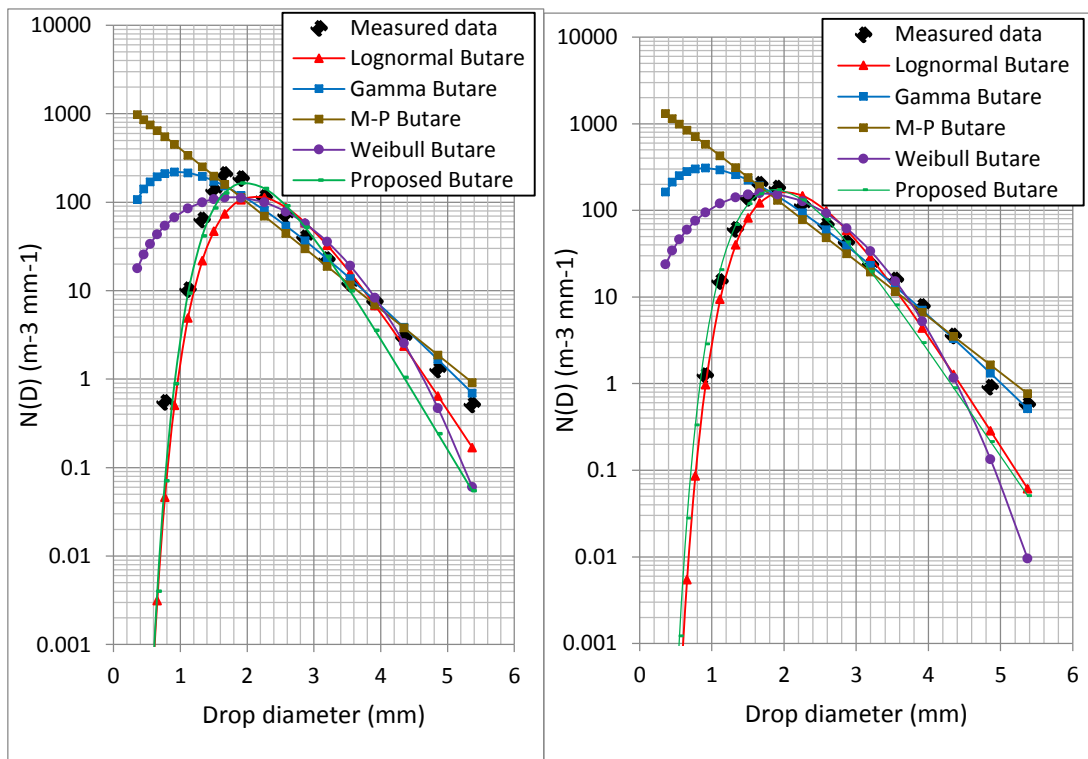
(d)

Figure 5-4: Seasonal rainfall DSDs for widespread rains in Butare, Rwanda. (a) Short dry season at 9.93 mm/h (b) Long rainy season at 9.99 mm/h (c) Long dry season at 9.97 mm/h (d) Short rainy season at 9.94 mm/h.



(a)

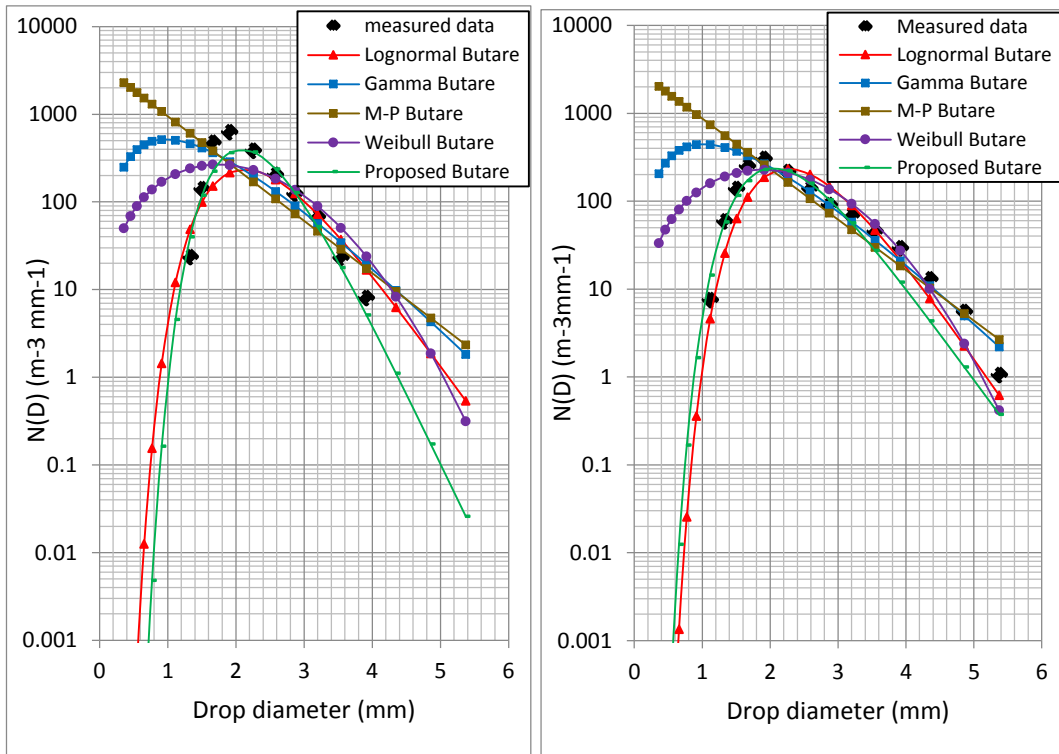
(b)



(c)

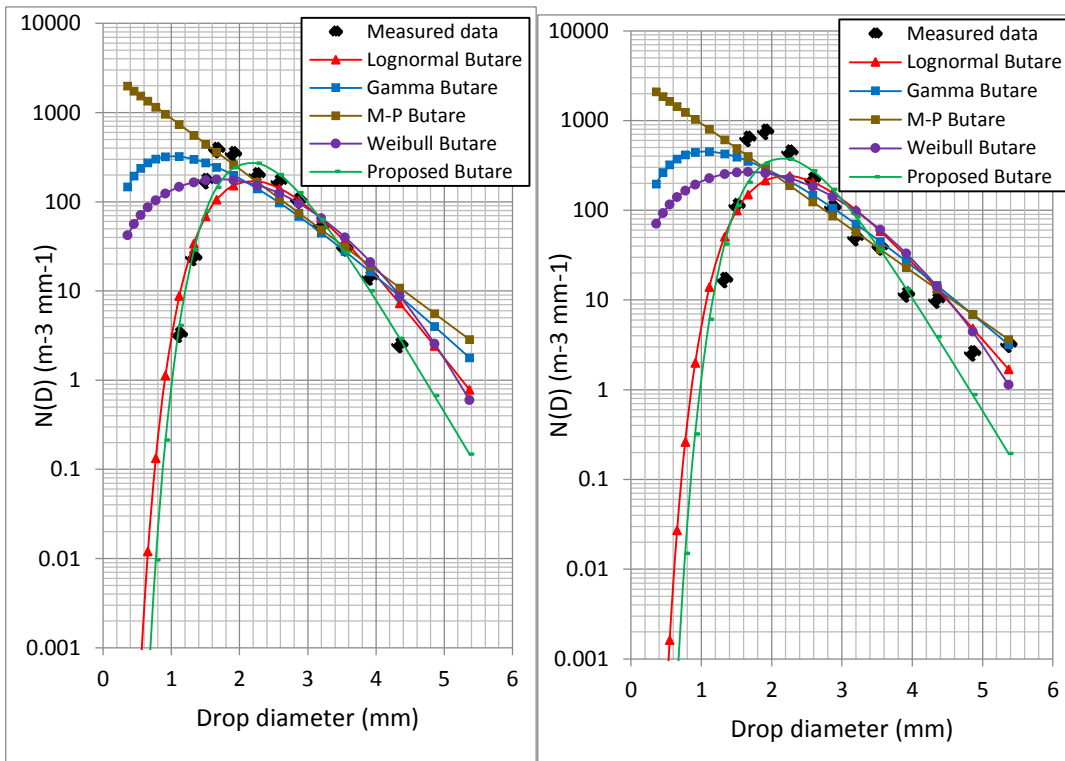
(d)

Figure 5.5: Seasonal rainfall DSDs for Shower rains in Butare, Rwanda. (a) Short dry season at 38.7 mm/h (b) Long rainy season at 38.73 mm/h (c) Long dry season at 37.44 mm/h (d) Short rainy season at 38.58 mm/h.



(a)

(b)



(c)

(d)

Figure 5.6: Seasonal rainfall DSDs for Thunderstorm rains in Butare, Rwanda. (a) Short dry season at  $R_{0.01}=89$  mm/h (b) Long rainy season at  $R_{0.01}=94$  mm/h (c) Long dry season at  $R_{0.01}=70$  mm/h (d) Short rainy season at  $R_{0.01}=114$  mm/h.

Table 5-9: Error estimation from different seasonal rainfall DSD models in Butare, Rwanda. (a) Short dry and Long rainy season. (b) Long dry and Short rainy season.

(a)

Rainfall rate (mm/h)	Short dry season					Long rainy season				
	LGN	MGM	MP	WBL	Proposed	LGN	MGM	MP	WBL	Proposed
3	0.347	0.427	0.424	0.432	0.339	0.297	0.454	0.430	0.282	0.203
5	0.280	0.377	0.385	0.271	0.181	0.117	0.419	0.416	0.212	0.134
10	0.197	0.535	0.551	0.344	0.220	0.199	0.415	0.427	0.191	0.039
20	0.096	0.318	0.368	0.141	0.051	0.141	0.374	0.412	0.135	0.044
30	0.085	0.290	0.372	0.167	0.043	0.086	0.318	0.382	0.167	0.033
40	0.101	0.276	0.376	0.176	0.062	0.087	0.286	0.379	0.188	0.076
50	0.103	0.265	0.366	0.187	0.101	0.094	0.272	0.370	0.177	0.063
60	0.189	0.287	0.381	0.191	0.082	0.079	0.260	0.363	0.188	0.077
70	0.124	0.269	0.366	0.181	0.088	0.084	0.265	0.367	0.175	0.066
80	0.097	0.281	0.374	0.201	0.086	0.084	0.249	0.356	0.166	0.069
90	0.105	0.295	0.384	0.214	0.090	0.080	0.246	0.355	0.177	0.091
100						0.082	0.229	0.344	0.183	0.117

(b)

Rainfall rate (mm/h)	Long dry season					Short rainy season				
	LGN	MGM	MP	WBL	Proposed	LGN	MGM	MP	WBL	Proposed
3	0.137	0.482	0.464	0.134	0.112	0.261	0.498	0.461	0.225	0.235
5	0.121	0.436	0.432	0.255	0.111	0.199	0.451	0.436	0.211	0.126
10	0.077	0.472	0.484	0.245	0.100	0.081	0.408	0.421	0.109	0.077
20	0.101	0.363	0.406	0.188	0.124	0.045	0.349	0.390	0.194	0.076
30	0.086	0.300	0.375	0.200	0.095	0.063	0.333	0.388	0.183	0.054
40	0.066	0.289	0.368	0.189	0.078	0.091	0.264	0.362	0.158	0.064
50	0.098	0.286	0.372	0.200	0.085	0.096	0.269	0.366	0.178	0.076
60	0.081	0.264	0.362	0.186	0.065	0.114	0.281	0.377	0.193	0.077
70						0.084	0.263	0.367	0.191	0.063
80						0.079	0.251	0.360	0.199	0.077
90						0.187	0.329	0.419	0.255	0.150
100						0.062	0.242	0.358	0.214	0.060
110						0.091	0.225	0.347	0.214	0.088
118						0.170	0.318	0.414	0.257	0.140

For the Long rainy season, the new DSD model is again seen to be adequate for this season, with an average RMSE value of 0.084 followed by the LGN with average RMSE value of 0.119, then the WBL, MGM and the MP model with average RMSE values of 0.187, 0.316 and 0.383, respectively. For the Long dry season, both LGN and the new models are found to give best fits to the DSD measurements, as they both have the same least average RMSE value of 0.096 for all the considered rainfall rates compared to the average RMSE value of 0.362 for MGM, 0.408 for MP and 0.200 for WBL DSD model. Finally, the Short rainy season is again best fitted by the new

DSD model as it has the least average RMSE value of 0.097, followed by the LGN, WBL, MGM and the PM DSD models with average RMSE values of 0.116, 0.199, 0.320 and 0.390 respectively.

## **5.6 Chapter Summary and Conclusion**

In this chapter, the new rainfall drop size distribution model for equatorial Africa has been developed using disdrometer data collected in Butare, Rwanda, and the method of maximum likelihood estimation technique has been used to determine its corresponding input fit-parameters. The Lognormal, Gamma, Marshall- Palmer, Weibull and the new proposed DSD models were used to generate rainfall distributions for various data classes (annual, seasonal and regime variation of rainfall DSD). From results, the derived drop size distribution models have different performances as the rainfall rate increases. The error analysis reveals that, the new DSD model for Central Africa has been determined to give a better fit to the DSD measurement compared to the existing DSD models particularly for those rainfall contributions with high rainfall rates that are mostly associated with microwave and millimetre wave attenuation.

The next chapter focuses on the estimation of rainfall attenuation over Butare, using derived drop size distribution models in this chapter and the Mie scattering technique.

## Chapter Six

### Specific Rainfall Attenuation Patterns over Butare, Rwanda

#### 6.1 Introduction

While the International Telecommunication Union (ITU-R) recommends the power law model approximation to calculate the rainfall attenuation, this chapter derives the power law coefficients from the Lognormal, Gamma, Marshall- Palmer, Weibull and the new proposed DSD models for Butare, Rwanda based on the Mie scattering theory. The derived values of  $k$  and  $\alpha$  are presented both in tabular as well as graphical format, and compared against the corresponding ITU-R P.838-3 parameters. Then, the derived power law coefficients are used for the estimation of rainfall attenuation in the region of Central Africa. Finally, The International Telecommunication Union Recommendation (ITU-R) model and the Synthetic Storm Techniques (SST) are applied for comparison with other rainfall attenuation models in this region.

#### 6.2 Specific Rain Attenuation over Butare.

In this chapter, we use the Mie theory for electromagnetic scattering using spherical rain drops to calculate the rainfall attenuation using Joss-Waldvogel disdrometer data measurements at the University of Rwanda, Huye Campus, Butare in the southern province of Rwanda. We assume that the raindrops, illuminated by a plane wave, are uniformly distributed in a rain-filled medium and the distance between raindrops is sufficiently large to avoid multiple scattering [125]. The polarisation independent specific attenuation  $A_S$  (dB/Km) due to rainfall drops is given by [76,126-128]:

$$A_S [dB/Km] = 4.343 \times 10^{-3} \int_0^{\infty} Q_{ext}(D)N(D)dD \quad (6.1)$$

Where  $A_S$  is the specific attenuation,  $N(D)$  is the drop size distribution,  $dD$ , the diameter interval and  $Q_{ext}$  is the extinction cross-section (ECS) in  $mm^2$ .

The extinction cross-section is a hypothetical area of interaction between an electromagnetic wave and a rain drop which describes a possibility of energy being scattered by raindrops.  $Q_{ext}$  depends on the complex refractive index of water,  $m$ , the wavelength,  $\lambda$ , the shape and the size of the rainfall drop and can be computed by the following expression [129-130]:

$$Q_{ext}(D) = \frac{4\pi}{k^2} Re\{S(0)\} \quad (6.2)$$

Where,  $k = \frac{2\pi}{\lambda}$  is the wave number and  $Re\{S(0)\}$  is the real part of the forward scattering amplitude for spherical raindrops which is the greater portion of the extinction cross-section coefficient. The forward scattering amplitude for spherical rain drops is expressed by [129-130]:

$$S(0) = \frac{1}{2} \sum_{n=1}^{\infty} (2n+1)[a_n(m, \alpha) + b_n(m, \alpha)] \quad (6.3)$$

Where  $S(0)$  represents the forward scattering amplitude,  $a_n(m, \alpha)$  and  $b_n(m, \alpha)$  are the Mie scattering coefficients which are functions of rain drop diameter, wavelength, and complex refractive index of water. Parameters  $m$  and  $\alpha$  depends on the ambient temperature and the frequency of droplet [131]. The index  $n$  runs from one to infinity but the infinity series can be truncated after  $n_{max}$  terms [132-133]:

$$n_{max} = \alpha + 4\alpha^{\frac{1}{3}} + 2 \quad (6.4)$$

Where  $\alpha = k\bar{a}$  is the particle size for all wavelengths ( $\lambda$ ) of the rain drops,  $k$  is the wave number and  $\bar{a}$  is the radius of the assumed spherical droplets. The Mie scattering coefficients  $a_n(m, \alpha)$  and  $b_n(m, \alpha)$  can be given by [124,129,133,134]:

$$a_n(m, \alpha) = \frac{m^2 j_n(m\alpha)[\alpha j_n(\alpha)]' - j_n(\alpha)[m\alpha j_n(m\alpha)]'}{m^2 j_n(m\alpha)[\alpha h_n^{(1)}(\alpha)]' - h_n^{(1)}(\alpha)[m\alpha j_n(m\alpha)]'} \quad (6.5)$$

$$b_n(m, \alpha) = \frac{j_n(\alpha)[m\alpha j_n(m\alpha)]' - j_n(m\alpha)[\alpha j_n(\alpha)]'}{h_n^{(1)}(\alpha)[m\alpha j_n(m\alpha)]' - j_n(m\alpha)[\alpha h_n^{(1)}(\alpha)]'} \quad (6.6)$$

Where  $j_n(\alpha)$  and  $h_n^{(1)}(\alpha)$  are spherical Bessel and Hankel function of the first kind and are given by [135]:

$$j_n(\alpha) = \sqrt{\frac{\pi}{2\alpha}} j_{n+\frac{1}{2}}(\alpha) \quad (6.7)$$

$$h_n^{(1)}(\alpha) = \sqrt{\frac{\pi}{2\alpha}} H_{n+\frac{1}{2}}(\alpha) \quad (6.8)$$

Where  $j_{n+\frac{1}{2}}(\alpha)$  and  $H_{n+\frac{1}{2}}(\alpha)$  are half-integral order Bessel and Hankel functions respectively.

In this study, we use the Liebe model [136] of complex refractive index of water to obtain the Mie coefficients. The temperature of the rainy medium is assumed to be 20°C as the average annual temperature in Rwanda turns around 20°C with no significant differences [137]. The



complex permittivity of pure water is expressed by single and double Debye models for the frequency below and beyond 100 GHz, respectively.

The complex permittivity of pure water expressed by the single Debye model [136]:

$$\epsilon_D(f, T) = \frac{(\epsilon_0 - \epsilon_\infty)}{1 - i(f/\gamma_D)} + \epsilon_\infty \quad (6.9)$$

Where

$$\epsilon_0(T) = 77.66 - 103.3\theta \quad (6.9a)$$

$$\theta = 1 - \frac{300}{T + 273.15} \quad (6.9b)$$

$$\epsilon_\infty = 0.066 \epsilon_0 \quad (6.9c)$$

$$\gamma_D(T) = 20.27 + 146.5\theta + 314\theta^2 \quad (6.9d)$$

Where  $i$  is the complex number operator,  $\epsilon_0$  is the static dielectric of pure water,  $\epsilon_\infty$  and  $\gamma_D$  are the high frequency constant and the relaxation frequency respectively.

For frequencies beyond 100 GHz, the complex permittivity of pure water is expressed by the double Debye model [136]:

$$\epsilon_w(f, T) = \epsilon_0 - f \left[ \frac{(\epsilon_0 - \epsilon_1)}{(f + i\gamma_1)} + \frac{(\epsilon_1 - \epsilon_2)}{(f + i\gamma_1)} \right] \quad (6.10)$$

The static and high frequency permittivities are given by [136]:

$$\epsilon_0 = 77.66 - 103.3(\theta - 1) \quad (6.10a)$$

$$\epsilon_1 = 0.0671 \epsilon_0 \quad (6.10b)$$

$$\epsilon_2 = 3.52 \quad (6.10c)$$

The two relaxation frequencies are expressed as [136]:

$$\gamma_1 = 20.20 + 146.5(\theta - 1) + 314(\theta - 1)^2 \quad (6.10d)$$

$$\gamma_2 = 39.8 \gamma_1 \quad (6.10e)$$

With  $\theta$  given in equation (6.9b) as:

$$\theta = 1 - \frac{300}{T + 273.15}$$

Where  $T$  is the temperature in °C and  $f$  is the frequency in GHz.

Table 6-1: Extinction cross section power-law coefficients at 20°C using Mie scattering technique

Frequency (GHz)	Complex Refractive Index	$k_{ext}$	$\zeta_{ext}$
2	8.9014 + 0.4843i	0.0027	3.2737
4	8.7763 + 0.9442i	0.0191	3.7875
6	8.5830 + 1.3599i	0.0851	4.3988
8	8.3396 + 1.7196i	0.217	4.5805
10	8.0649 + 2.0188i	0.3857	4.5272
12	7.7755 + 2.2594i	0.5866	4.4443
15	7.3405 + 2.5234i	0.955	4.3453
16	7.1994 + 2.5892i	1.0939	4.3164
18	6.9272 + 2.6934i	1.3883	4.2576
20	6.6705 + 2.7667i	1.6936	4.194
23	6.3171 + 2.8321i	2.1474	4.0885
25	6.1026 + 2.8532i	2.4567	4.0186
28	5.8107 + 2.8603i	2.8544	3.9035
30	5.6345 + 2.8530i	3.1204	3.8323
35	5.2500 + 2.8072i	3.7452	3.6639
40	4.9322 + 2.7383i	4.3106	3.5077
45	4.6668 + 2.6586i	4.8223	3.3646
50	4.4428 + 2.5752i	5.2855	3.2353
60	4.0869 + 2.4099i	6.0493	3.0094
70	3.8182 + 2.2560i	6.625	2.8209
90	3.4421 + 1.9907i	7.4097	2.5284
100	3.3061 + 1.8778i	7.6874	2.4156
150	2.9154 + 1.5083i	8.3061	2.0691
200	2.7103 + 1.2655i	8.3464	1.9293
250	2.5871 + 1.1051i	8.2291	1.8785
300	2.5029 + 0.9932i	8.0777	1.8672
400	2.3882 + 0.8493i	7.8144	1.875
500	2.3067 + 0.7597i	7.6315	1.8812

The complex refractive index of water can be calculated using the following relationship [25]:

$$m(f, T) = \sqrt{\epsilon_w(f, T)} \quad (6.11)$$

Based on equations (6.3) to (6.11), with the help of the Matlab program developed by Mätzler in [135,139,140], the forward scattering amplitude for spherical raindrops,  $S(0)$  were calculated from the Mie computations. Therefore, the extinction cross section,  $Q_{ext}$  can be estimated as in equation (6.2). But many researchers such as: Rogers and Olsen [94] and Odedina and Afullo

[125] have shown that the extinction cross section expressed in equation (6.2) can be reduced to a power law relation as a function of raindrop diameter,  $D$ , as follows:

$$Q_{ext}(D) = k_{ext} \bar{a}^{\zeta_{ext}} \quad (6.12)$$

Where  $\bar{a} = D/2$ , is the radius of the assumed spherical droplet in millimetres,  $k_{ext}$  and  $\zeta_{ext}$  are constants at a given frequency and temperature. Using the spherical method, the power law coefficients values  $k_{ext}$  and  $\zeta_{ext}$  are derived for frequencies from 2 to 500 GHz and results are shown in Table 6-1.

Based on the Joss-Waldvogel disdrometer channels, equation (6.1) can be reduced to the following expression:

$$A_S[dB/Km] = 4.343 \times 10^{-3} \sum_{i=1}^{20} k_{ext} \bar{a}^{\zeta_{ext}} N(D_i) \Delta D_i \quad (6.13)$$

Where  $N(D_i) \Delta D_i$  is the number density of the droplet with equivalent diameter  $D_i$  in the diameter interval  $\Delta D_i$ .

In the computation of the specific attenuation due to rain in Butare, equation (6.13) has been used and this estimation is based on raindrop size distribution models developed in chapters four and five.

### 6.2.1 Seasonal Variation of Specific Attenuation.

The values of  $R_{0.01}$  for the Short dry season (89.26 mm/h), Long rainy season (97.82 mm/h), Long dry season (70.8 mm/h) and the Short rainy season (114.01 mm/h) as determined in chapter four are used to estimate the seasonal specific attenuation due to rain over Butare, Rwanda. From seasonal data, through equation (6.13), the specific attenuation was estimated using various developed theoretical DSD models and results are presented in Figures 6-1 to 6-4. From results, it is shown that the Weibull DSD model has a higher specific rain attenuation for all the four seasons in Butare except in the Short rainy season where the new DSD model gives the highest estimate above 40 GHz. The Short rainy season (mid-September to December) and the Long rainy season (March to the beginning of June) both give higher specific rain attenuation values compared to the two dry seasons at selected frequencies and their respective value of  $R_{0.01}$ . The lowest specific rain attenuation is recorded in the Long dry season.

For example, at 8 GHz: the Short dry season estimates ranges from 0.997 dB/km to 1.868 dB/km; the Long rainy season from 1.059 dB/km to 2.067 dB/km; the Long dry season from 0.808 dB/km to 1.483 dB/km and the Short rainy season from 1.080 dB/km to 1.190 dB/km.

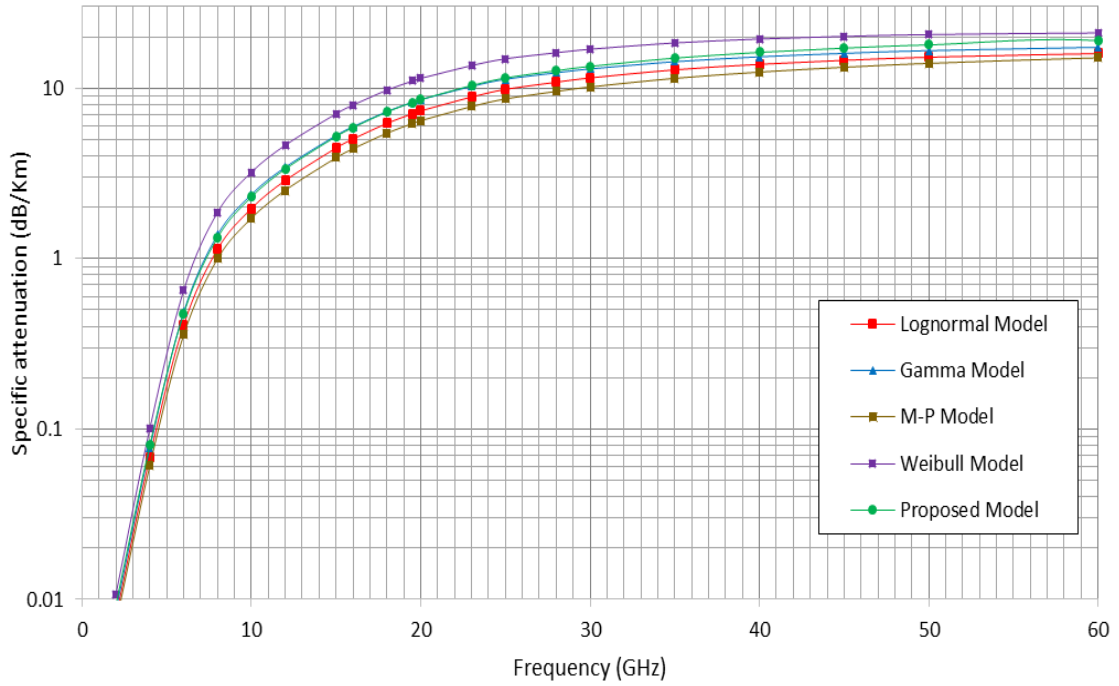


Figure 6-1: Specific rain attenuation estimation in Short dry season in Butare, Rwanda for  $R_{0.01}=89.26$  mm/h

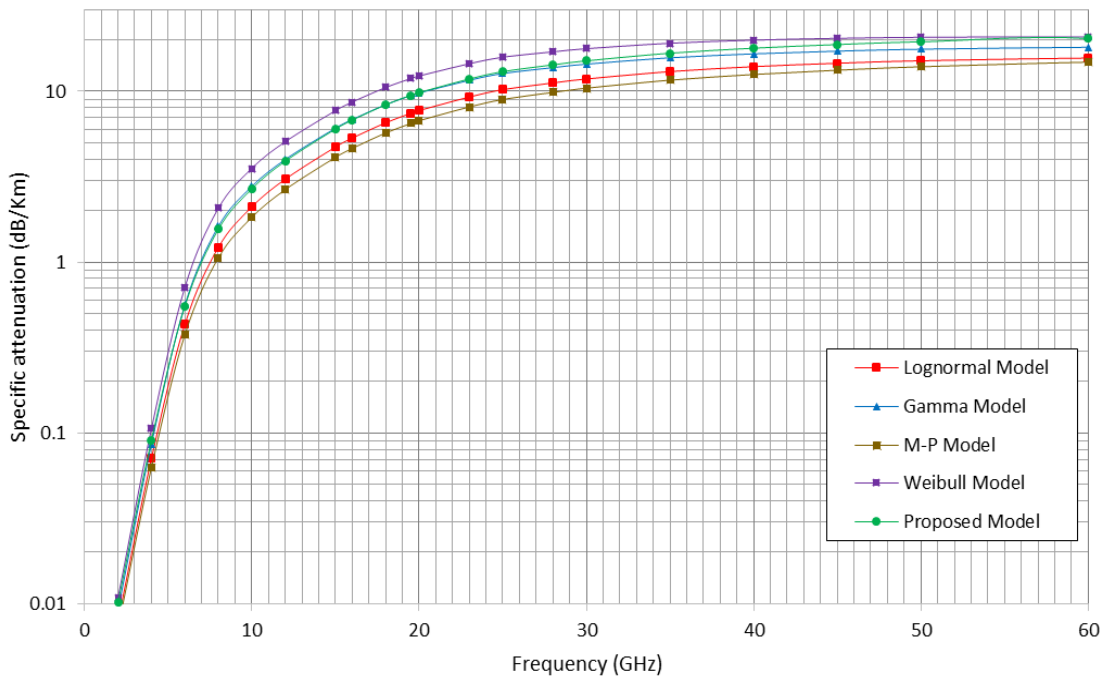


Figure 6-2: Specific rain attenuation estimation in Long rain season in Butare, Rwanda for  $R_{0.01}=97.82$  mm/h

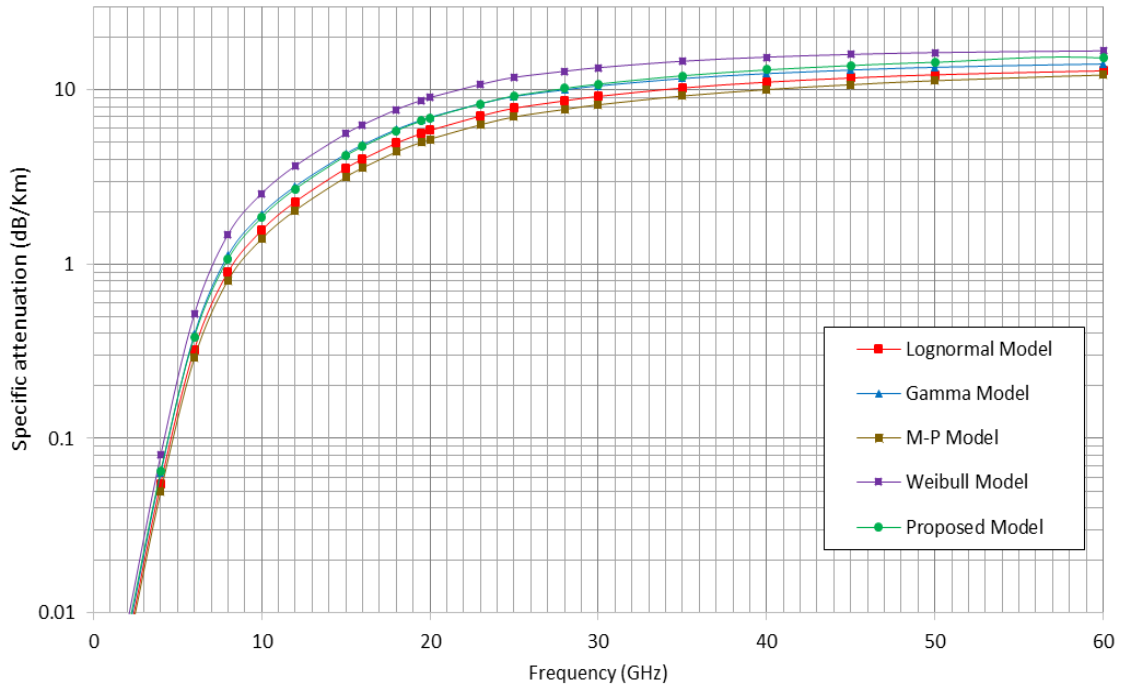


Figure 6-3: Specific rain attenuation estimation in Long dry season in Butare, Rwanda for  $R_{0.01}=70.8$  mm/h

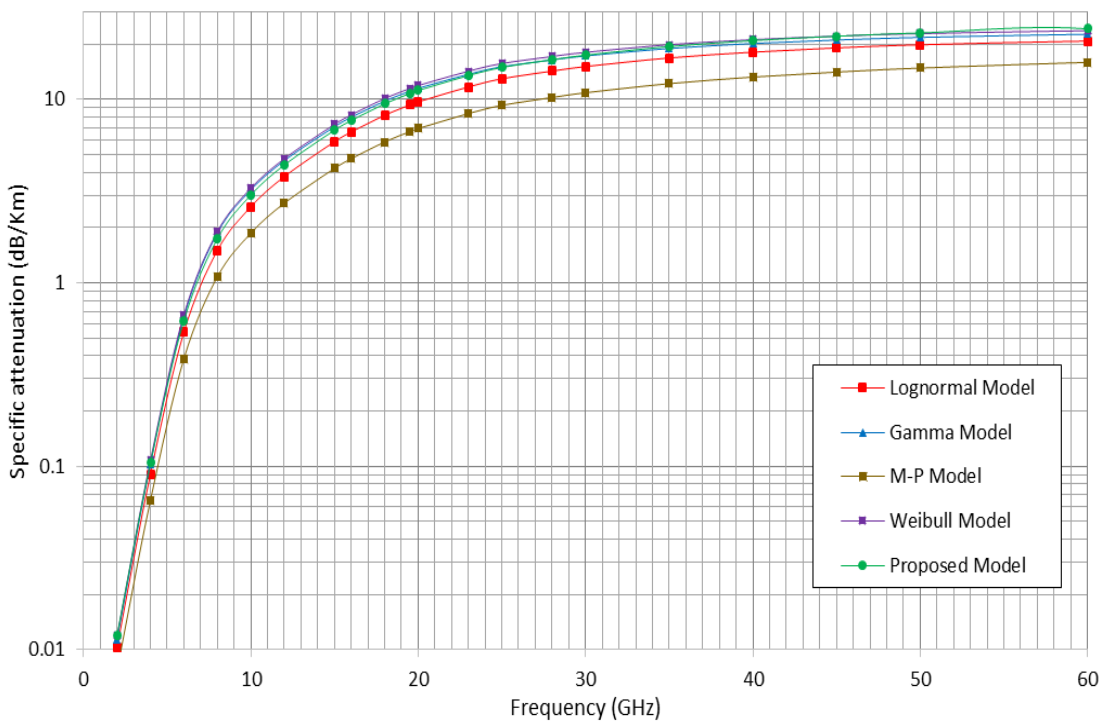


Figure 6-4: Specific rain attenuation estimation in Short rain season in Butare, Rwanda for  $R_{0.01}=114.01$  mm/h

At 12 GHz: the Short dry season estimates ranges from 2.516 dB/km to 4.625 dB/km; the Long rainy season from 2.657 dB/km to 5.07 dB/km; the Long dry season from 2.040 dB/km to 3.672 dB/km and the Short rainy season from 2.721 dB/km to 4.756 dB/km.

At 18 GHz: Short dry season estimates ranges from 5.440 dB/km to 9.725 dB/km; Long rainy season from 5.701 dB/km to 10.537 dB/km; Long dry season from 4.410 dB/km to 7.726 dB/km; Short rainy season from 5.868 dB/km to 10.123 dB/km.

At 25 GHz: Short dry season estimates ranges from 8.639 dB/km to 14.86 dB/km; Long rainy season from 8.958 dB/km to 15.84 dB/km; Long dry season from 7.003 dB/km to 11.812 dB/km; Short rainy season from 9.289 dB/km to 15.709 dB/km.

At 30 GHz: Short dry season estimates ranges from 10.151 dB/km to 16.898 dB/km; Long rainy season from 10.433 dB/km to 17.778 dB/km; Long dry season from 8.336 dB/km to 13.438 dB/km; Short rainy season from 10.88 dB/km to 18.079 dB/km.

At 50 GHz: Short dry season estimates ranges from 13.967 dB/km to 20.60 dB/km; Long rainy season from 13.99 dB/km to 20.727 dB/km; Long dry season from 11.314 dB/km to 16.405 dB/km; Short rainy season from 14.83 dB/km to 23.069 dB/km.

At 60 GHz: Short dry season estimates ranges from 15.057 dB/km to 21.06 dB/km; Long rainy season from 14.826 dB/km to 20.80 dB/km; Long dry season from 12.194 dB/km to 16.777 dB/km; Short rainy season from 15.93 dB/km to 24.29 dB/km.

### **6.2.2 Regime Variation of Specific Attenuation.**

By using the expression given in (6.13), the specific rain attenuation for the four rainfall regimes are estimated over frequencies from 2 GHz to 60 GHz at 20 °C in Butare, Rwanda, and the results are presented in Figures 6-5 to 6-8. These plots show comparisons between the specific rain attenuation for drizzle at 4.9 mm/h, widespread at 9.9 mm/h, shower at 39.1 mm/h, and thunderstorm at 96.02 mm/h using various DSD models including the ITU-R estimation for both horizontal and vertical polarization [138]. From the results, it is seen that the specific attenuation due to rain increases as the frequency increases where the lowest and highest values of rain attenuation are recorded in the drizzle and thunderstorm rainfall regimes, respectively.

In Figure 6-5, for drizzle at 4.9 mm/h, the ITU-R models (horizontal and vertical polarization) underestimate the measurement for frequencies less than 10 GHz, while they overestimate beyond this frequency. In this regime, the other remaining models appear to match the measurement at all considered frequencies.

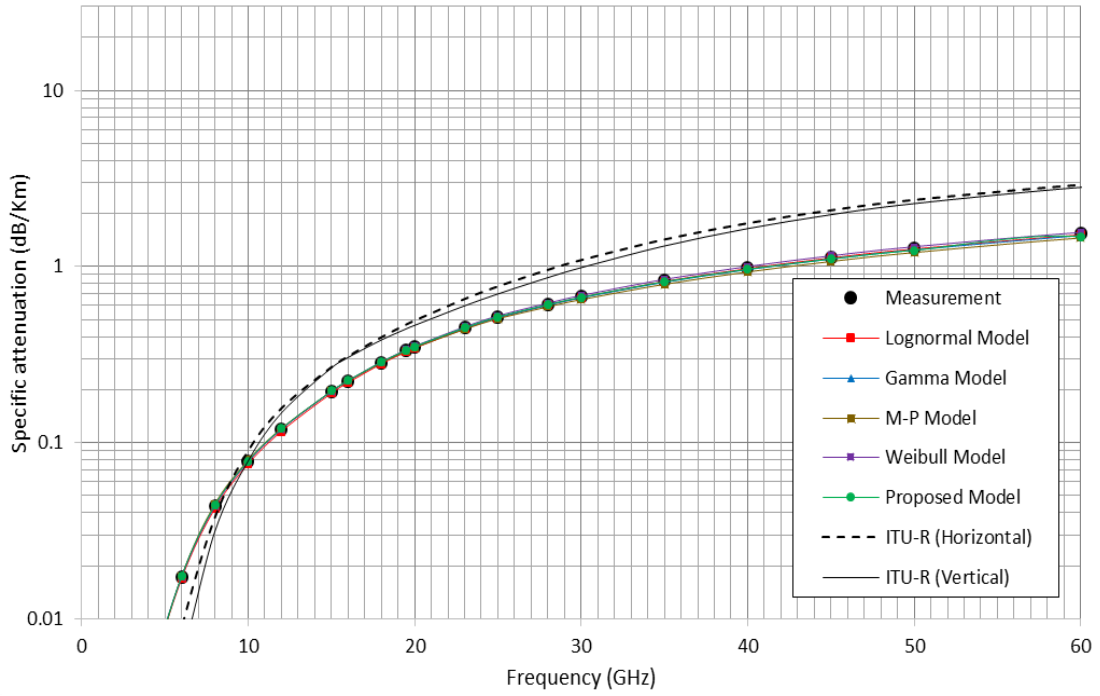


Figure 6-5: Comparison of Specific rain attenuation for various models in Butare, Rwanda for drizzle rainfall regime at 4.9 mm/h.

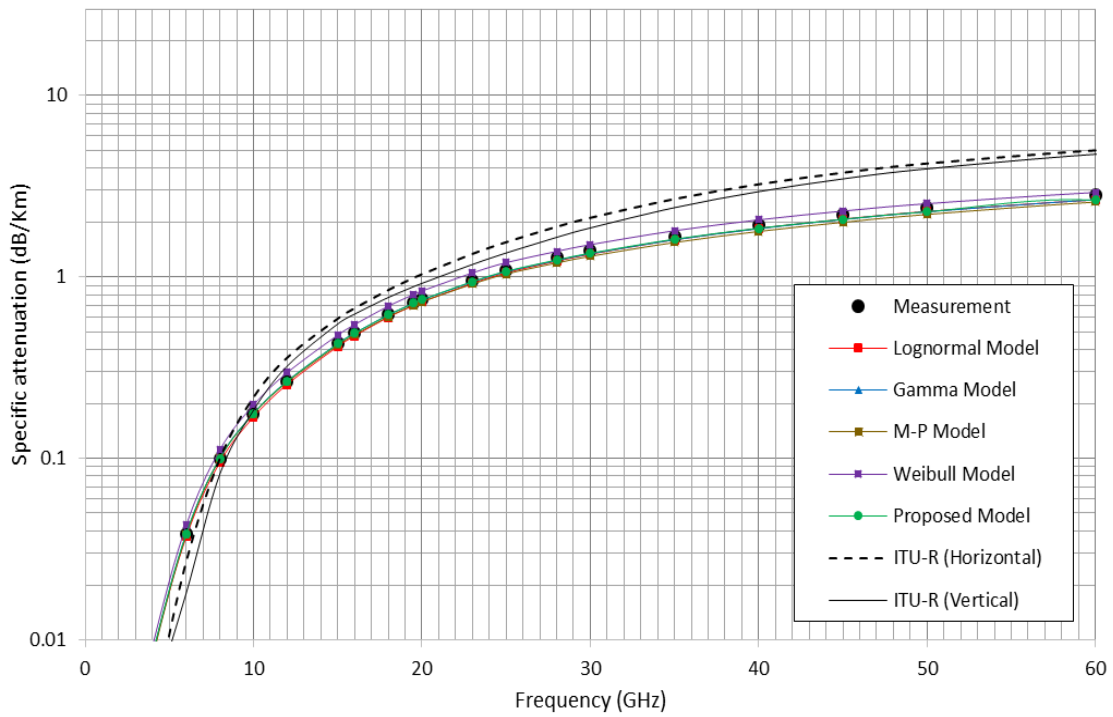


Figure 6-6: Comparison of Specific rain attenuation for various models in Butare, Rwanda for widespread rainfall regime at 9.9 mm/h.

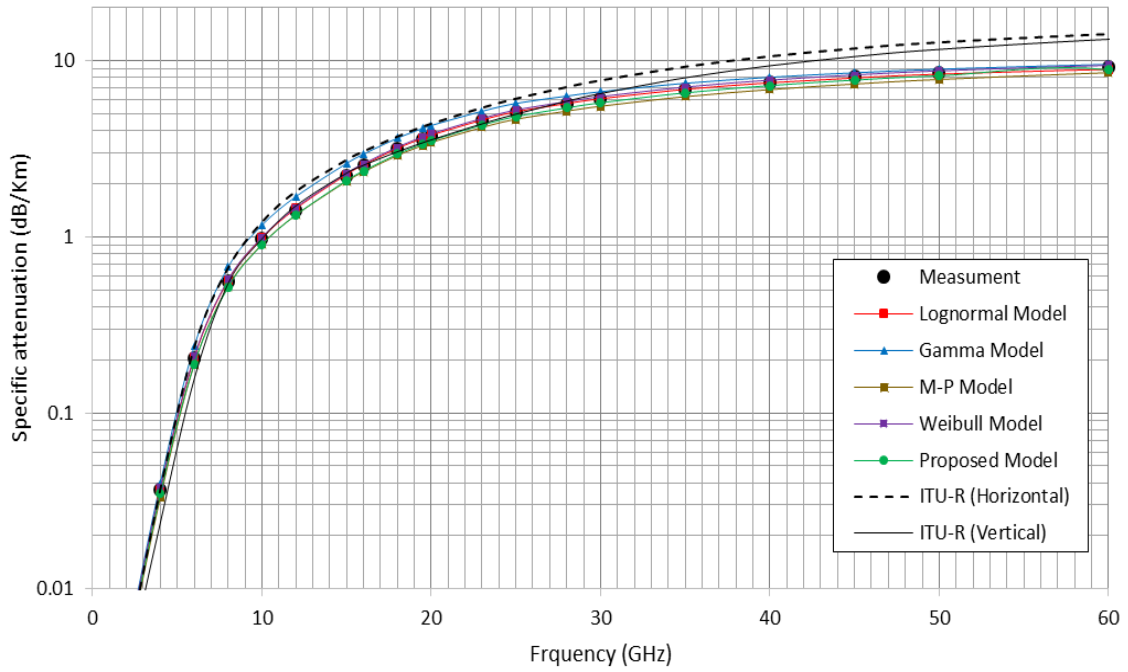


Figure 6-7: Comparison of Specific rain attenuation for various models in Butare, Rwanda for shower rainfall regime at 39.1 mm/h.

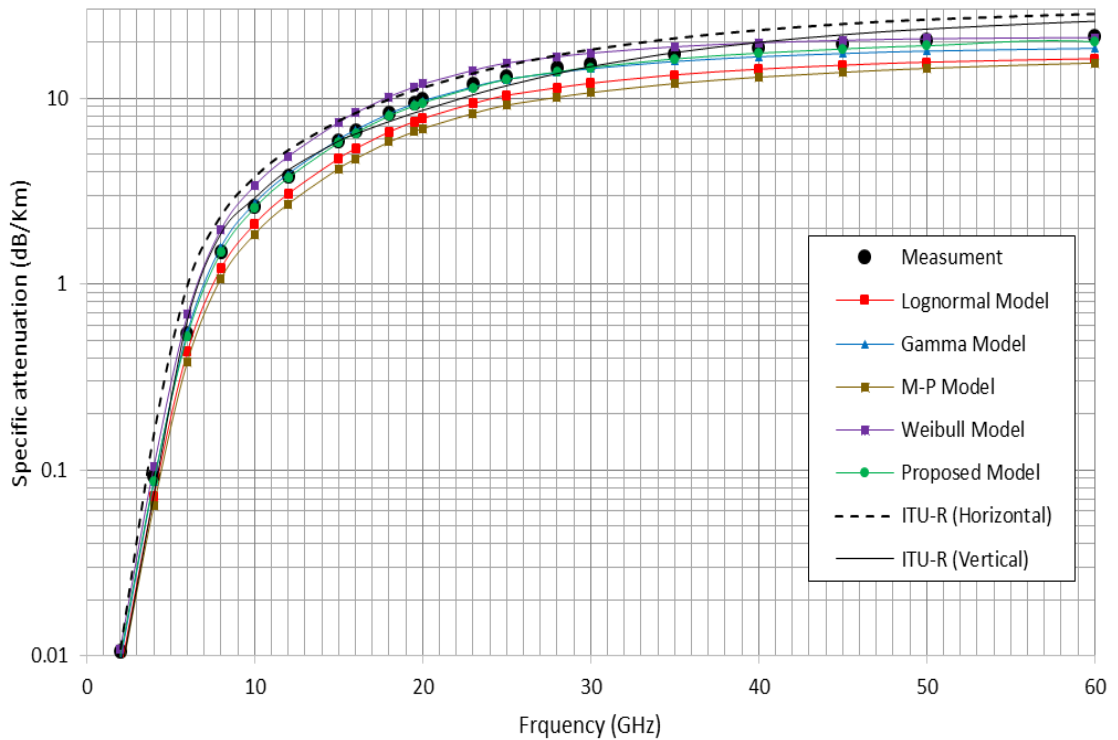


Figure 6-8: Comparison of Specific rain attenuation for various models in Butare, Rwanda for thunderstorm rainfall regime at 96.02 mm/h.



In Figure 6-6, for widespread at 9.9 mm/h, the Lognormal, Gamma and the new Model give the best fit to the measurement compared to other models.

For shower rainfall regime at 39.1 mm/h shown in Figure 6-7, the ITU-R model for horizontal polarization and Gamma models are seen to match the measurement for frequencies up to 8 GHz, while they overestimate the measurement for frequencies above 8 GHz. It is also observed that, the Marshall-Palmer model underestimates the measurement in this rainfall regime for all the frequency ranges, while the ITU-R for vertical polarization coincides with the measurement for frequencies up to 33 GHz, and then overestimates it beyond this frequency. In this regime, the Lognormal, Weibull and the new proposed models give better fits compared to other models.

For thunderstorm at 96.02 mm/h as shown in Figure 6-8, the ITU-R model for horizontal polarization overestimates the measurement, while the Marshall-Palmer model underestimates them. The ITU-R model for vertical polarization overestimates the measurement between 6 GHz and 10 GHz, then closely follows the measurement up to 45 GHz. The Weibull model predicts well for frequencies above 35 GHz. In this rainfall regime as seen on plot of Figure 6-8, the new model gives a better fit to the measurement compared to other models.

### 6.3 Specific Attenuation Constants

According to Olsen et al. [94], the specific rain attenuation at any location can be determined by the following power law expression as given in (3.5) as:

$$A_S = kR^\alpha \quad [dB/Km] \quad (6.14)$$

Where  $k$  and  $\alpha$  are the power-law coefficients related to the frequency of transmission for a given radio link. In deriving the power law coefficients ( $k$  and  $\alpha$ ) from each drop size distribution model for rainfall range of 0 mm/h  $<R \leq$  120 mm/h at selected frequency between 2 GHz and 500 GHz, a regression technique is applied as suggested by different researchers [94,138,139]. The correlation coefficients obtained for each case was at least 0.9898. Evidently this validates the power law relationship which exists between the specific rain attenuation and the rainfall rate. The results for the power law coefficients are presented in Table 6-2 and Figures 6-9 to 6-10 alongside those of the ITU-R P.838-3 values (Appendix B-1).

From the plots of Figure 6-9, the coefficient  $k$  increases as the frequency increases. It is also observed that this coefficient overlaps all over the frequency range for both ITU-R models. The coefficient  $k$  for the ITU-R model is lower in the frequency range below 10 GHz compared to other DSD models, while above 10 GHz, the coefficient  $k$  for ITU-R model is notably higher than other models'  $k$  coefficients.

Table 6-2: Regression coefficients  $k$  and  $\alpha$  for various models for Butare, Rwanda at 20°C

Frequency (GHz)	LGN Model		GM Model		M-P Model		WBL Model		Proposed Model	
	$k_{LGN}$	$\alpha_{LGN}$	$k_{GM}$	$\alpha_{GM}$	$k_{M-P}$	$\alpha_{M-P}$	$k_{WBL}$	$\alpha_{WBL}$	$k_{Pr}$	$\alpha_{Pr}$
2	0.0001	0.9353	0.0001	0.9614	0.0001	0.9213	0.0001	0.9405	0.0002	0.9115
4	0.0008	1.0402	0.0008	1.0735	0.0008	1.0735	0.0008	1.0461	0.0009	1.0002
6	0.0027	1.1635	0.0026	1.2054	0.003	1.1149	0.0027	1.1709	0.0031	1.1017
8	0.0064	1.1998	0.0063	1.2456	0.0073	1.1447	0.0064	1.2078	0.0075	1.1311
10	0.0116	1.1892	0.0114	1.2342	0.0132	1.136	0.0117	1.197	0.0136	1.1225
12	0.0183	1.1726	0.0179	1.2163	0.0204	1.1224	0.0184	1.1802	0.0212	1.1091
15	0.0311	1.1528	0.0302	1.1949	0.0339	1.1061	0.0313	1.16	0.0356	1.093
18	0.0469	1.1352	0.0453	1.1759	0.0504	1.0915	0.0473	1.1422	0.0532	1.0789
25	0.0922	1.087	0.0883	1.1239	0.0955	1.0511	0.0934	1.0934	0.1024	1.0391
28	0.1129	1.0638	0.1078	1.0988	0.1152	1.0315	0.1145	1.0699	0.1241	1.0198
30	0.1276	1.0493	0.1216	1.0833	0.1291	1.0192	0.1296	1.0553	0.1394	1.0077
40	0.206	0.9832	0.196	1.0125	0.2025	0.9627	0.2105	0.9887	0.2195	0.9522
50	0.29	0.9274	0.2774	0.9531	0.2815	0.9145	0.298	0.9326	0.3032	0.9047
70	0.4537	0.8418	0.443	0.863	0.4424	0.8402	0.4717	0.8467	0.3089	0.7551
90	0.5987	0.781	0.5987	0.7998	0.5961	0.7875	0.6291	0.7859	0.3403	0.7384
100	0.6634	0.7574	0.6709	0.7756	0.6685	0.7672	0.7004	0.7623	0.3729	0.7169
150	0.8835	0.6846	0.9324	0.7018	0.9374	0.7052	0.9491	0.6898	0.4814	0.6496
200	0.9689	0.6551	1.0438	0.6723	1.0561	0.6804	1.0495	0.6605	0.5218	0.6221
250	0.9865	0.6444	1.0713	0.6617	1.0869	0.6715	1.072	0.6498	0.5292	0.612
300	0.9753	0.642	1.0611	0.6593	1.0772	0.6695	1.0607	0.6474	0.5227	0.6098
400	0.9389	0.6436	1.0201	0.6609	1.0352	0.6709	1.0205	0.649	0.5035	0.6113
500	0.9133	0.6449	0.9913	0.6622	1.0057	0.672	0.9923	0.6504	0.49	0.6125

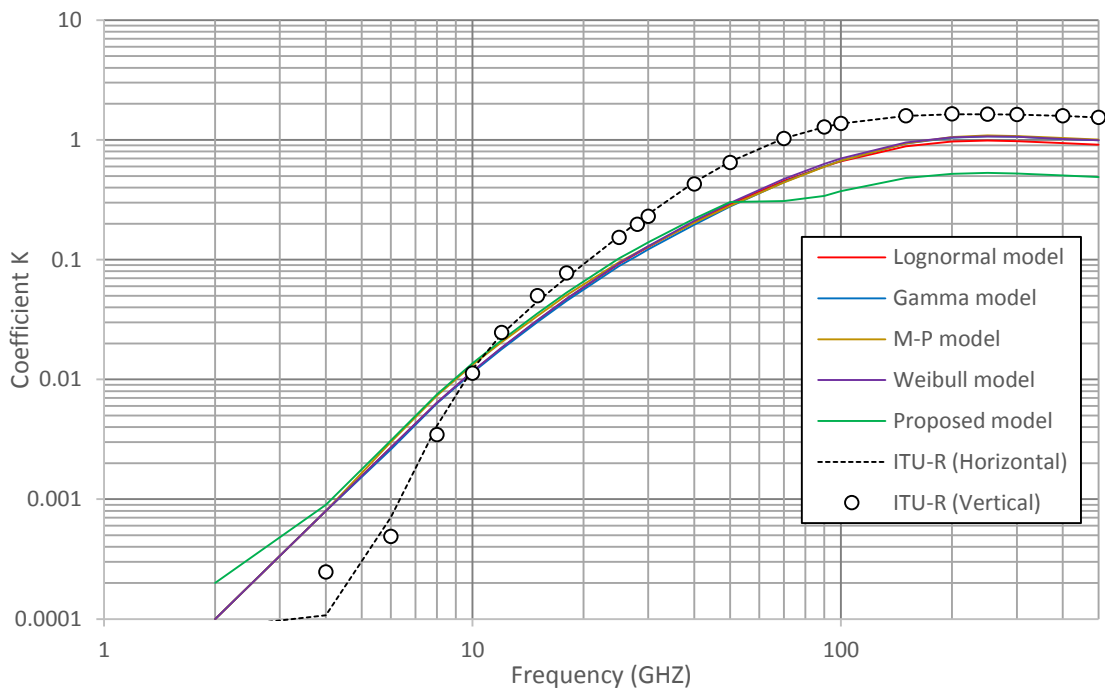


Figure 6-9: Variation of coefficient  $k$  with frequency over Butare, Rwanda at 20°C

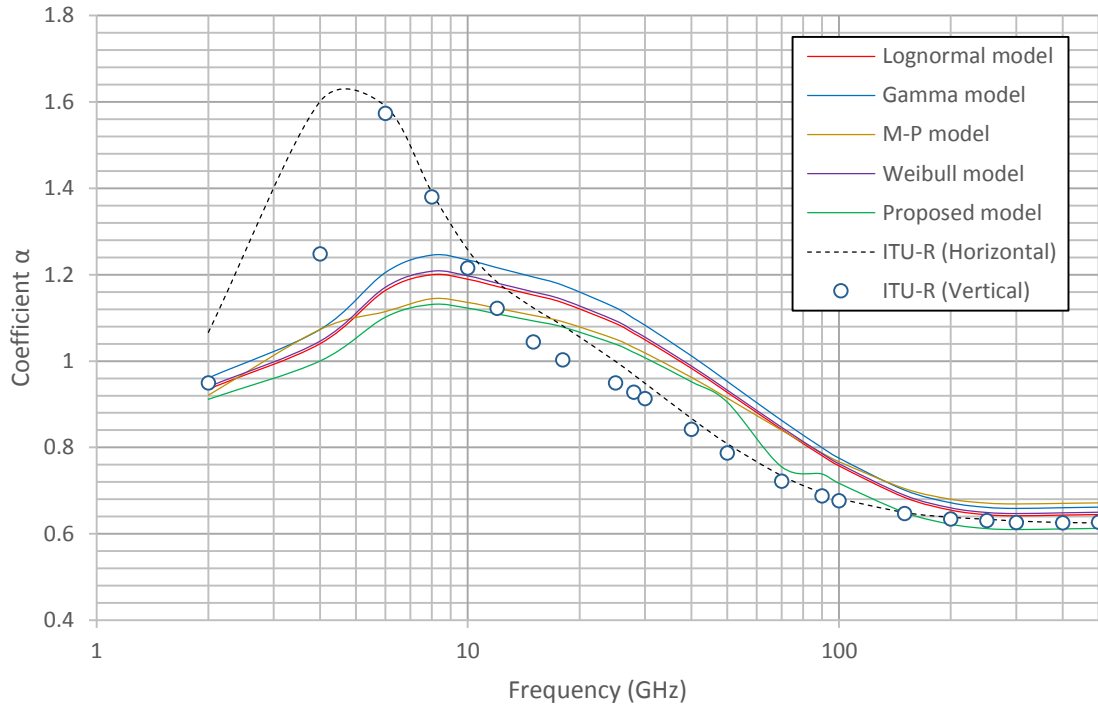


Figure 6-10: Variation of coefficient  $\alpha$  with frequency over Butare, Rwanda at 20°C

In Figure 6-10, the coefficient  $\alpha$  increases sharply for frequencies 2 GHz to 8 GHz, followed by a slow decrease with increasing frequency for all models except for the ITU-R models which reach their peaks earlier (3.5 GHz and 6 GHz for vertical and horizontal polarization, respectively) than other models but their graphs fall off rapidly and reach the lowest values of  $\alpha$  in the frequencies above 18 GHz.

## 6.4 Attenuation Prediction Models

In this section, different raindrop size distribution models developed in chapter four and five are used for formulating the rain attenuation models used in this study. In addition, the International Telecommunication Union (ITU-R) model and the Synthetic Storm Techniques (SST) are applied for comparison with the formulated rainfall attenuation models.

### 6.4.1 ITU-R Rain Attenuation Model

The ITU-R P.530-16 provides a simple method for estimating the statistical attenuation due to rain in terrestrial links. The path attenuation for 0.01 % of the time is given by [3]:

$$A_{0.01} = A_s \cdot d_{eff} \text{ [dB]} \quad (6.15)$$

Where  $A_S = kR^\alpha$  is the specific attenuation due to rain,  $d_{eff}$  is the effective path length which is the product of the actual path length  $d$  and the distance factor  $r$  and is given by the following expression:

$$d_{eff} = r \cdot d \quad (6.16)$$

The distance factor  $r$  is estimated as given by [3]:

$$r = \frac{1}{0.477 d^{0.633} R_{0.01}^{0.073 \cdot \alpha} f^{0.123} - 10.579 (1 - \exp(-0.024 d))} \quad (6.17)$$

Where  $f$  is the frequency of transmission expressed in GHz,  $\alpha$  is the exponent in the specific rain attenuation model. The maximum recommended value of the distance factor  $r$  is 2.5.

The attenuation exceeded for another percentage of time  $p$  between 0.001–1 percent can be deduced from the power law given by the following expression [3]:

$$\frac{A_p}{A_{0.01}} = C_1 p^{-(C_2 + C_3 \log_{10} p)} \quad (6.18)$$

With:

$$C_1 = (0.07^{C_o}) [0.12^{(1-C_o)}] \quad (6.18a)$$

$$C_2 = 0.855 C_o + 0.546 (1 - C_o) \quad (6.18b)$$

$$C_3 = 0.139 C_o + 0.043 - C_o \quad (6.18c)$$

Where:

$$C_o = \begin{cases} 0.12 + 0.4 \left[ \log_{10} \left( \frac{f}{10} \right)^{0.8} \right] & f \geq 10 \text{ GHz} \\ 0.12 & f < 10 \text{ GHz} \end{cases} \quad (6.19)$$

The prediction procedure outlined above is considered to be valid in all parts of the world at least for frequencies up to 100 GHz and path lengths up to 60 km.

#### 6.4.2 Synthetic Storm Techniques Rain Attenuation Model

The Synthetic Storm Technique (SST) has been successfully used to predict rain attenuation in terrestrial line of sight radio links [140-141]. It is a physical- mathematical radio propagation approach that can be used to convert a rain rate time series measured by a rain gauge or a disdrometer at a given location into a rain attenuation time series [142]. This process of generating reliable rain attenuation time series requires the knowledge about the length of the signal path through the rain cell, the rain cell speed ( $v$ ) and the rainfall rate ( $R$ ) at the location under

investigation [142]. Therefore, the generated signal attenuation time series can be used to investigate the rain attenuation characteristics in the absence of real attenuation measurements [143].

Assuming that the location under consideration is at a specific point on the  $x_0$ -axis (the projection of the link on the ground) and that a rainfall rate,  $R$  (mm/h) , is measured at that point on the ground with specific attenuation (dB/km) given by:

$$A_S(x_0) = k R^\alpha(x_0) \quad (6.20)$$

Where  $k$  and  $\alpha$  are two constants given in [138] which depend on the frequency and the polarisation of the signal crossing the rain cell. The attenuation due to rain on terrestrial path of length (Km) along the horizontal  $x$  axis is given by following expression at 20°C [144]:

$$A(x_0) = k \int_{x_0 - \frac{L}{2}}^{x_0 + \frac{L}{2}} R^\alpha(x) dx \quad (6.21)$$

The variation of signal attenuation with time can be simulated by changing  $x_0$  according to the storm speed,  $v$ , of the rain cell at the rate of:

$$x_0 = vt \quad (6.22)$$

As the path of the signal in the atmosphere and the motion of the storm are supposed to be on the same plane, mathematically, this can be described as the convolution between a rectangular pulse of unit amplitude and length  $L$ . Then, the signal attenuation at  $x_0$  is given by:

$$A(x_0) = k \int_{-\infty}^{+\infty} R^\alpha(x_0 - x) \text{rect}\left(\frac{x}{L}\right) dx = k \int_{-\infty}^{+\infty} R^\alpha(x) \text{rect}\left(\frac{x_0 - x}{L}\right) dx \quad (6.23)$$

Equation (6.23) represents the principle of the Synthetic Storm Techniques.

### 6.4.3 Lognormal Rain Attenuation Model

To formulate the Lognormal attenuation model, the lognormal DSD model as given by Ajayi-Olsen and Ajay-Ademula [25,80] for all rainfall regimes is used. The rain attenuation on a line of sight (LOS) path can be expressed as:

$$A(\text{dB}) = A_S \cdot d_{eff} \quad (6.24)$$

Where  $A_S$  and  $d_{eff}$  have the same definition as in equation (6.15). Therefore, by substituting (6.13) in (6.24), the expression of the rain attenuation on a LOS path will be given by:

$$A(\text{dB}) = \left[ 4.343 \times 10^{-3} \sum_{i=1}^{20} k_{ext} \bar{a}^{\zeta_{ext}} N(D_i) \Delta D_i \right] \cdot d_{eff} \quad (6.25)$$

Where  $N(D_i)$  is the drop size distribution model. The lognormal rainfall DSD model as given in (4.7) can be written as:

$$N(D_i) = \frac{N_T}{\sigma D_i \sqrt{2\pi}} \exp \left\{ -\frac{1}{2} \left[ \frac{\ln(D_i) - \mu}{\sigma} \right]^2 \right\} \quad (6.26)$$

Substitution of (6.26) into (6.25), we have

$$A(dB) = \left[ 4.343 \times 10^{-3} \sum_{i=1}^{20} k_{ext} \bar{a}^{\zeta_{ext}} \cdot \frac{N_T}{\sigma D_i \sqrt{2\pi}} \exp \left\{ -\frac{1}{2} \left[ \frac{\ln(D_i) - \mu}{\sigma} \right]^2 \right\} \Delta D_i \right] \cdot d_{eff} \quad (6.27)$$

Where the expression in bracket of equation (6.27) represents the lognormal specific rain attenuation that can be represented by the power law expression as following:

$$A_S = 4.343 \times 10^{-3} \sum_{i=1}^{20} k_{ext} \bar{a}^{\zeta_{ext}} \cdot \frac{N_T}{\sigma D_i \sqrt{2\pi}} \exp \left\{ -\frac{1}{2} \left[ \frac{\ln(D_i) - \mu}{\sigma} \right]^2 \right\} \Delta D_i = k_{LGN} R^{\alpha_{LGN}} \quad (6.28)$$

Substitution of (6.28) into (6.27), the rain attenuation on a LOS path with a lognormal distribution will be gives as:

$$A(dB) = k_{LGN} R^{\alpha_{LGN}} \cdot d_{eff} \quad (6.29)$$

Where  $R$  is the rainfall rate,  $d_{eff}$  is the effective path length as define in equation (6.16),  $k_{LGN}$  and  $\alpha_{LGN}$  are lognormal frequency dependent regression coefficients given in Table 6-2.

#### 6.4.4 Modified Gamma Rain Attenuation Model

The modified gamma rain attenuation is formulated from the modified gamma DSD model as discussed in section 4.4.1.2. The modified gamma drop size distribution model as given in (4.15) can be written as:

$$N(D_i) = N_m(D_i)^\mu \exp(-\Lambda D_i) \quad (6.30)$$

Substitution of equation (6.30) into (6.25), we have:

$$A(dB) = \left[ 4.343 \times 10^{-3} \sum_{i=1}^{20} k_{ext} \bar{a}^{\zeta_{ext}} \cdot N_m(D_i)^\mu \exp(-\Lambda D_i) \Delta D_i \right] \cdot d_{eff} \quad (6.31)$$

Where the expression in bracket of equation (6.31) represents the modified gamma specific rain attenuation that can be represented by the power law expression as following:

$$A_S = 4.343 \times 10^{-3} \sum_{i=1}^{20} k_{ext} \bar{a}^{\zeta_{ext}} \cdot N_m(D_i)^\mu \exp(-\Lambda D_i) \Delta D_i = k_{GM} R^{\alpha_{GM}} \quad (6.32)$$

Substitution of (6.32) into (6.31), the rain attenuation on a LOS path with a modified gamma distribution will be gives as:

$$A(dB) = k_{GM} R^{\alpha_{GM}} \cdot d_{eff} \quad (6.33)$$

Where  $R$  is the rainfall rate,  $d_{eff}$  is the effective path length as define in (6.16),  $k_{GM}$  and  $\alpha_{GM}$  are modified gamma frequency dependent regression coefficients given in Table 6-2.

#### 6.4.5 Negative Exponential Rain Attenuation Model

The negative exponential rain attenuation model is formulated from the negative exponential DSD model as given by Marshall and Palmer (M-P) for all rainfall regimes [117]. The negative exponential drop size distribution as given in (4.22) can be written as:

$$N(D_i) = N_0 \exp(-\Lambda D_i) \quad (6.34)$$

Substitution of equation (6.34) into (6.25), we have:

$$A(dB) = \left[ 4.343 \times 10^{-3} \sum_{i=1}^{20} k_{ext} \bar{a}^{\zeta_{ext}} \cdot N_0 \exp(-\Lambda D_i) \Delta D_i \right] \cdot d_{eff} \quad (6.35)$$

Where the expression in bracket of equation (6.35) represents the negative exponential specific rain attenuation that can be represented by the power law expression as following:

$$A_S = 4.343 \times 10^{-3} \sum_{i=1}^{20} k_{ext} \bar{a}^{\zeta_{ext}} \cdot N_0 \exp(-\Lambda D_i) \Delta D_i = k_{M-P} R^{\alpha_{M-P}} \quad (6.36)$$

Substitution of equation (6.36) into (6.35), the rain attenuation on a LOS path with a negative exponential distribution will be gives as:

$$A(dB) = k_{M-P} R^{\alpha_{M-P}} \cdot d_{eff} \quad (6.37)$$

Where  $R$  is the rainfall rate,  $d_{eff}$  is the effective path length as define in (6.16),  $k_{M-P}$  and  $\alpha_{M-P}$  are negative exponential frequency dependent regression coefficients given in Table 6-2.

#### 6.4.6 Weibull Rain Attenuation Model

The Weibull rain attenuation model is formulated based on the Weibull DSD model as given by Sekine et al. [75-76]. The Weibull rainfall DSD model as given in (4.8) can be written as:

$$N(D_i) = N_w \left( \frac{\beta}{\gamma} \right) \left( \frac{D_i}{\gamma} \right)^{\beta-1} \exp \left[ - \left( \frac{D_i}{\gamma} \right)^\beta \right] \quad (6.38)$$

Substitution of equation (6.38) into (6.25), we have:

$$A(dB) = \left[ 4.343 \times 10^{-3} \sum_{i=1}^{20} k_{ext} \bar{a}^{\zeta_{ext}} \cdot N_w \left( \frac{\beta}{\gamma} \right) \left( \frac{D_i}{\gamma} \right)^{\beta-1} \exp \left[ - \left( \frac{D_i}{\gamma} \right)^{\beta} \right] \Delta D_i \right] \cdot d_{eff} \quad (6.39)$$

Where the expression in bracket of equation (6.39) represents the Weibull specific rain attenuation that can be represented by the power law expression as following:

$$A_S = 4.343 \times 10^{-3} \sum_{i=1}^{20} k_{ext} \bar{a}^{\zeta_{ext}} \cdot N_w \left( \frac{\beta}{\gamma} \right) \left( \frac{D_i}{\gamma} \right)^{\beta-1} \exp \left[ - \left( \frac{D_i}{\gamma} \right)^{\beta} \right] \Delta D_i = k_{WBL} R^{\alpha_{WBL}} \quad (6.40)$$

Substitution of equation (6.40) into (6.39), the rain attenuation on a LOS path with a Weibull distribution will be gives as:

$$A(dB) = k_{WBL} R^{\alpha_{WBL}} \cdot d_{eff} \quad (6.41)$$

Where R is the rainfall rate,  $d_{eff}$  is the effective path length as define in (6.16),  $k_{WBL}$  and  $\alpha_{WBL}$  are Weibull frequency dependent regression coefficients given in Table 6-2.

#### 6.4.7 Proposed Rain Attenuation Model

The proposed rain attenuation model is formulated from the new rainfall drop size distribution model for Rwanda developed in chapter five of this thesis. This DSD model as give in equation (5.11) can be written as:

$$N(D_i) = \frac{N_T}{C \sigma D_i \sqrt{2\pi}} \exp \left\{ - \frac{1}{2} \left[ \frac{\ln(D_i) - \mu}{\sigma} \right]^2 \right\} \{ 1 + \alpha \exp(-D_i) \} \quad (6.42)$$

Substitution of equation (6.42) into (6.25), we have:

$$A(dB) = \left[ 4.343 \times 10^{-3} \sum_{i=1}^{20} k_{ext} \bar{a}^{\zeta_{ext}} \frac{N_T}{C \sigma D_i \sqrt{2\pi}} \exp \left\{ - \frac{1}{2} \left[ \frac{\ln(D_i) - \mu}{\sigma} \right]^2 \right\} \{ 1 + \alpha \exp(-D_i) \} \Delta D_i \right] \cdot d_{eff} \quad (6.43)$$

Where the expression in bracket of equation (6.43) represents the specific rain attenuation that can be represented by the power law expression as following:

$$4.343 \times 10^{-3} \sum_{i=1}^{20} k_{ext} \bar{a}^{\zeta_{ext}} \frac{N_T}{C \sigma D_i \sqrt{2\pi}} \exp \left\{ - \frac{1}{2} \left[ \frac{\ln(D_i) - \mu}{\sigma} \right]^2 \right\} \{ 1 + \alpha \exp(-D_i) \} \Delta D_i = k_{pr} R^{\alpha_{pr}} \quad (6.44)$$

Substitution of equation (6.44) into (6.43), the rain attenuation on a LOS path with the new proposed DSD model will be gives as:

$$A(dB) = k_{pr} R^{\alpha_{pr}} \cdot d_{eff} \quad (6.45)$$



Where  $R$  is the rainfall rate,  $d_{eff}$  is the effective path length as define in (6.16),  $k_{pr}$  and  $\alpha_{pr}$  are regression coefficients given in Table 6-2.

### **6.5 Calculation of rain attenuation statistics**

Four years of rainfall measurements obtained from the J-W RD-80 disdrometer installed at the roof of ICT building, University of Rwanda, Huye Campus, Butare at latitude 2°36'53.88"South and longitude 29°44'31.53" East at 1769 m of altitude in the Southern province of Rwanda between 2012 and 2015 is used to compute the rain attenuation statistics. At one-minute integration time, the maximum number of rain drops per sample in the period of measurement is 3643 drops and the maximum rainfall rate is 118.5 mm/h as earlier explained in section 5.4. During the period of measurement, all rain events have been observed and recorded. Then, some of the recorded rainfall events with high rainfall intensity have been converted to rain attenuation time series using the synthetic storm technique and other rain attenuation models given in section 6.4. The rain attenuation prediction models presented in section 6.4 enable us to compute the attenuation due to rain for a given transmission frequency and path length. By considering these prediction models used for estimating the attenuation due to rain, a comparison is done between them and results from the synthesized rain attenuation converted by the synthetic storm technique model. Note that this study is using 8 GHz, 12 GHz and 19 GHz as the microwave frequencies of operation in Rwanda as obtained from the Rwanda Utilities Regulatory Authority (RURA). The rain advection velocity (storm speed) is assumed to be  $v=5\text{m/s}$  as obtained from meteorological measurement in Butare, Rwanda.

Figures 6-11 to 6-13 present examples of three rain rate time series measurements for three different rain events taken on 06/12/2013, 01/10/2014 and 18/05/2015 in Butare, Rwanda. From these rain rate time series measurements, the rain attenuation time series are generated using the synthetic storm technique model and compared with other rain attenuation prediction models for the same rain event, and results are shown in Figures 6-14 to 6-37. From the results, it is observed that, the rain rate time series and the predicted rain attenuation time series show strong correlation during the rainy event as the generated rain attenuation time series and the corresponding rain rate time series are observed to follow a pattern but SST plots look much smoother because of windowing.

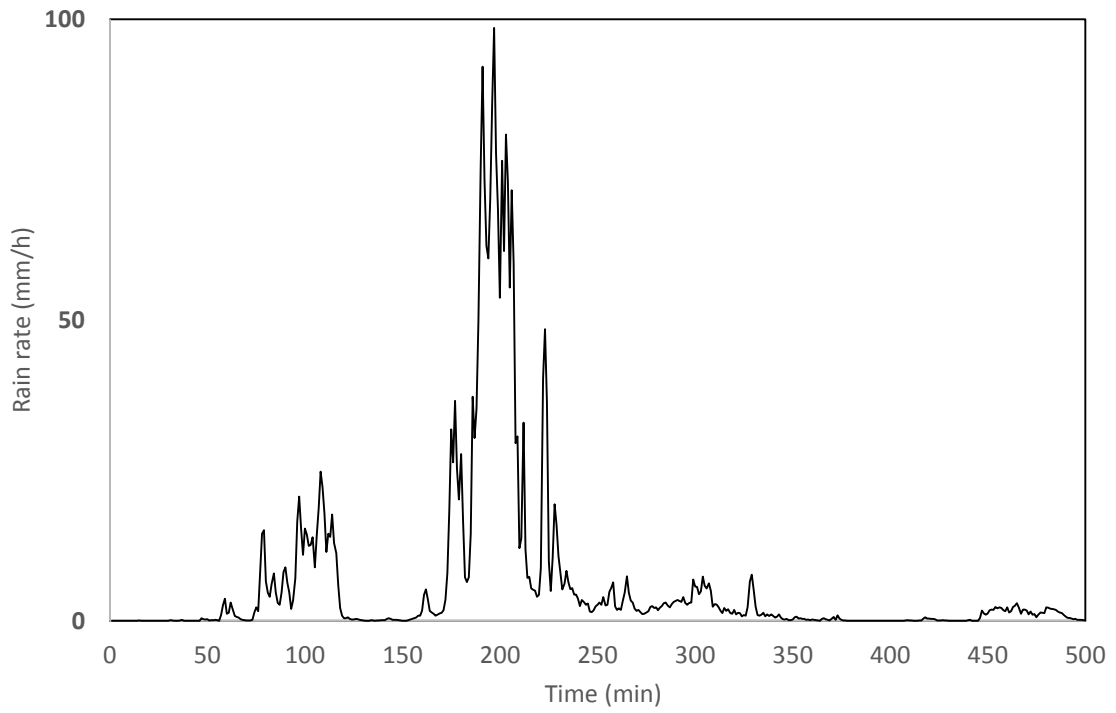


Figure 6-11: Rain rate time series measurements during the rain event of 06/12/2013 in Butare, Rwanda

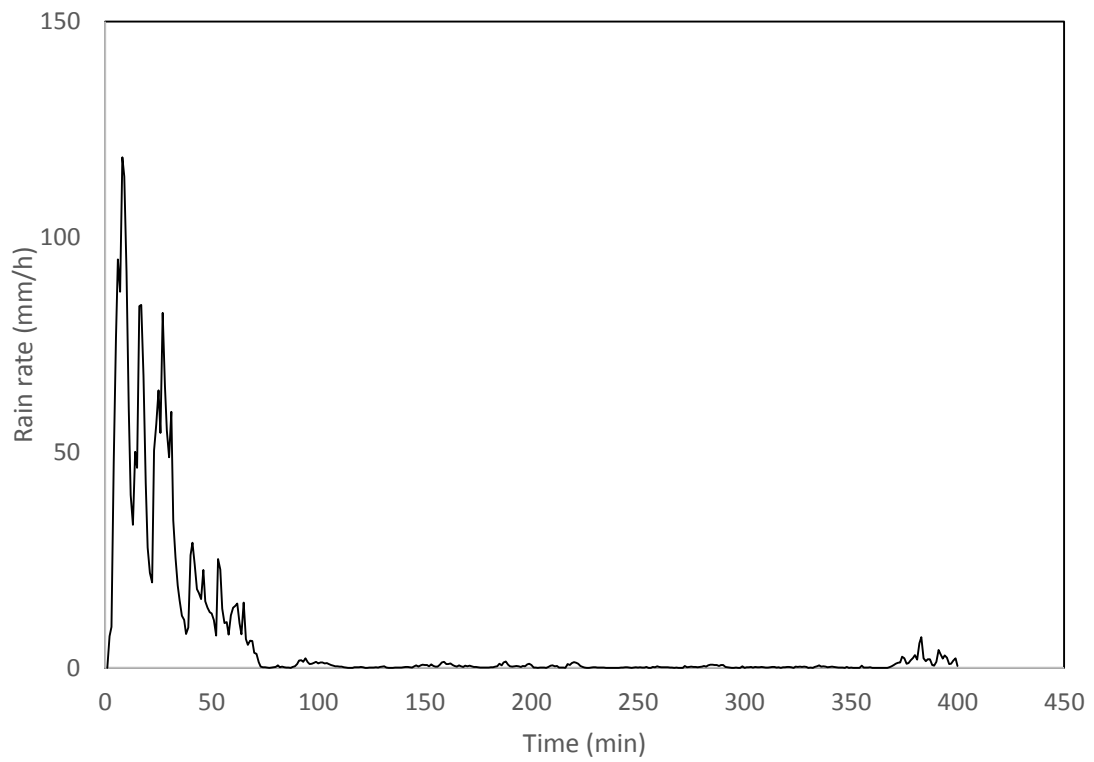


Figure 6-12: Rain rate time series measurements during the rain event of 01/10/2014 in Butare, Rwanda

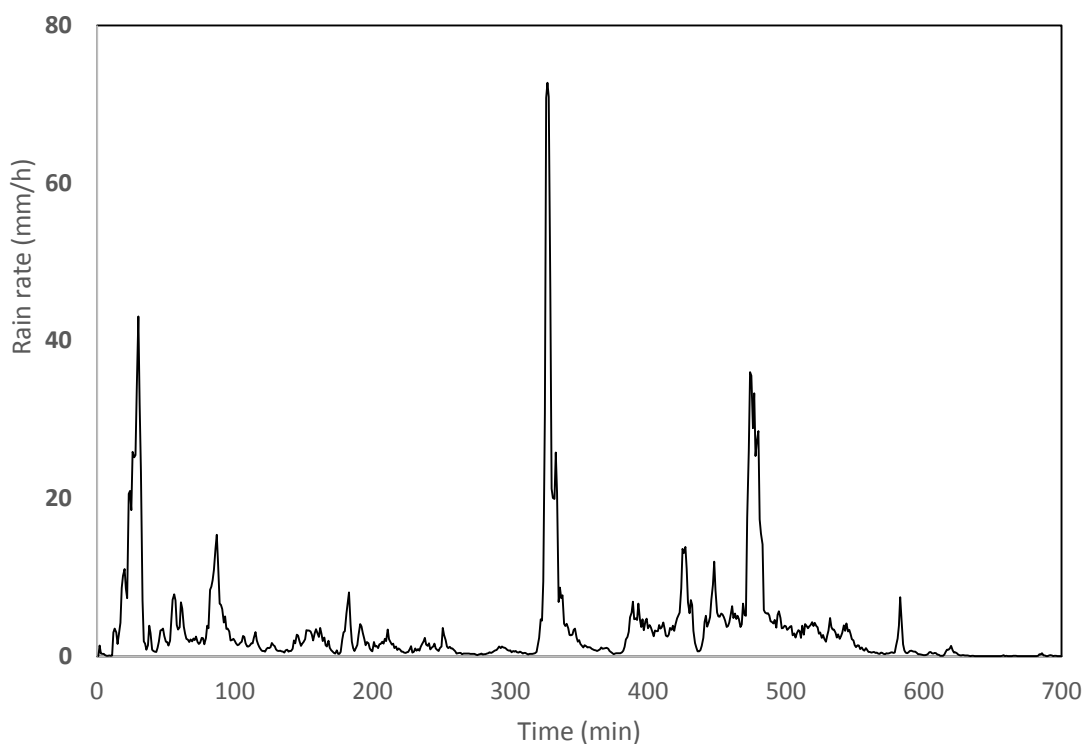


Figure 6-13: Rain rate time series measurements during the rain event of 18/05/2015 in Butare, Rwanda

Figures 6-14 to 6-16 present the comparison between the generated rain attenuation time series using SST model and other rain attenuation models for the rain event on 06/12/2013 at frequency of 8 GHz and path lengths of 1 km, 5 km and 8 km respectively. There are several peaks, but the highest peak of rain attenuation value occurs when the corresponding rain rate is at its maximum value as shown on the plots.

In Figure 6-14, at a frequency of 8 GHz and path length of 1 km, when the rain rate is close to 100 mm/h, the highest peak of rain attenuation value is close to 1.37dB using SST model and 1.57 dB, 1.91 dB, 1.4 dB, 1.64 dB, 1.35 dB, 2.44 dB, 1.94 dB for Lognormal, Modified Gamma, Negative exponential, Weibull, Proposed model, ITU-R (H) and ITU-R (V) models, respectively. In Figure 6.15, at a frequency of 8 GHz and path length of 5 km, the peak value of rain attenuation is close to 6.8 dB using SST model, and 7.89 dB, 9.58 dB, 6.99 dB, 8.19 dB, 6.75 dB, 12.18 dB, 9.71dB for Lognormal, Modified Gamma, Negative exponential, Weibull, Proposed model, ITU-R (H) and ITU-R (V) models, respectively.

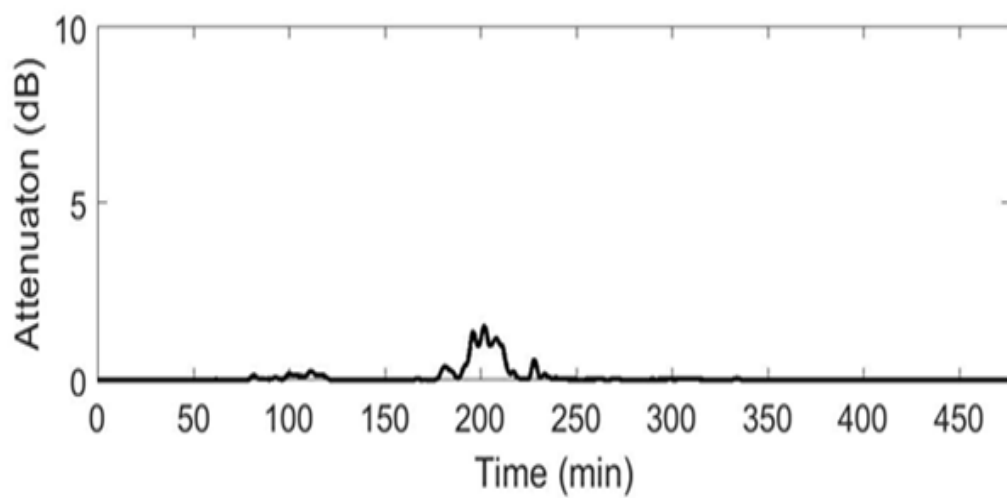
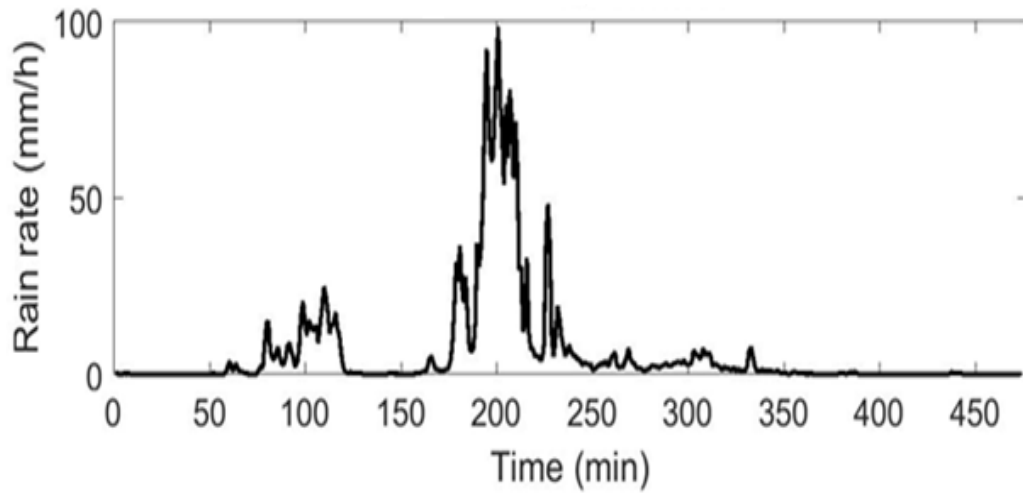
In Figure 6-16, at a frequency of 8 GHz and path length of 8 km, the highest peak value of rain attenuation is close to 52 dB using the SST model, and 50.5 dB, 58.3 dB, 43.5 dB, 51.4 dB, 43 dB, 62.2 dB, 48.3dB for Lognormal, Modified Gamma, Negative exponential, Weibull, Proposed model, ITU-R (H) and ITU-R (V) models, respectively.

Figures 6-17 to 6-19 show the comparison between the generated rain attenuation time series using the SST model and other rain attenuation models for a rainy event on 06/12/2013 at frequency of 12 GHz and path lengths of 2 km, 5 km and 8 km respectively.

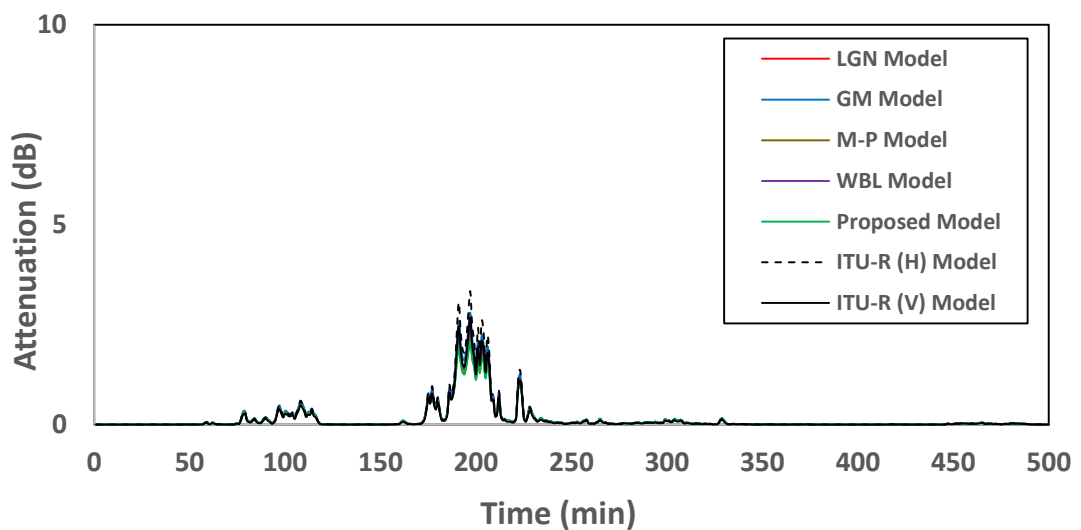
In Figure 6-17, at a frequency of 12 GHz and path length of 2 km, the highest peak of rain attenuation is about 7.5 dB using SST model and 7.97 dB, 9.52 dB, 7.05 dB, 8.29 dB, 7.29 dB, 10.87 dB, 8.46dB for Lognormal, Modified Gamma, Negative exponential, Weibull, Proposed model, ITU-R (H) and ITU-R (V) models, respectively. In Figure 6.18, at a frequency of 12 GHz and path length of 5 km, the peak value of rain attenuation is close to 17.4 dB using SST model, and 19.92 dB, 23.8 dB, 17.6 dB, 20.73 dB, 17.23 dB, 27.2 dB, 21.14 dB for Lognormal, Modified Gamma, Negative exponential, Weibull, Proposed model, ITU-R (H) and ITU-R (V) models, respectively. In Figure 6-19, at a frequency of 12 GHz and path length of 8 km, the highest value of rain attenuation is close to 28.5 dB using the SST model, and 31.87 dB, 38.09 dB, 28.21 dB, 33.2 dB, 27.58 dB, 43.5 dB, 33.8 dB for Lognormal, Modified Gamma, Negative exponential, Weibull, Proposed model, ITU-R (H) and ITU-R (V) models, respectively.

Figures 6-20 to 6-22 present the comparison between the generated rain attenuation time series using SST model and other rain attenuation models for a rainy event on 06/12/2013 at a frequency of 19 GHz and path lengths of 2 km, 5 km and 8 km respectively.

In Figure 6-20 at frequency of 19 GHz and path length of 2 km, the peak value of rain attenuation is about 15.1 dB using SST model, and 17.29 dB, 20.01 dB, 15.22 dB, 17.9 dB, 15.06 dB, 20.31 dB, 15.37dB for Lognormal, Gamma, Negative exponential, Weibull, Proposed model, ITU-R (H) and ITU-R (V) models, respectively. In Figure 6-21, at a frequency of 19 GHz and path length of 5 km, the peak value of rain attenuation is close to 37.5 dB using the SST model, and 42.99 dB, 50.06 dB, 37.80 dB, 44.78 dB, 37.66 dB, 50.78 dB, 38.42dB for Lognormal, Gamma, Negative exponential, Weibull, Proposed model, ITU-R (H) and ITU-R (V) models, respectively. In Figure 6-22, at a frequency of 19 GHz and path length of 8 km, the peak value of rain attenuation is close to 55.5 dB using SST model, and 68.79 dB, 80.09 dB, 60.49 dB, 71.64 dB, 60.25 dB, 81.24 dB, 61.48 dB for Lognormal, Gamma, Negative exponential, Weibull, Proposed model, ITU-R (H) and ITU-R (V) models, respectively.

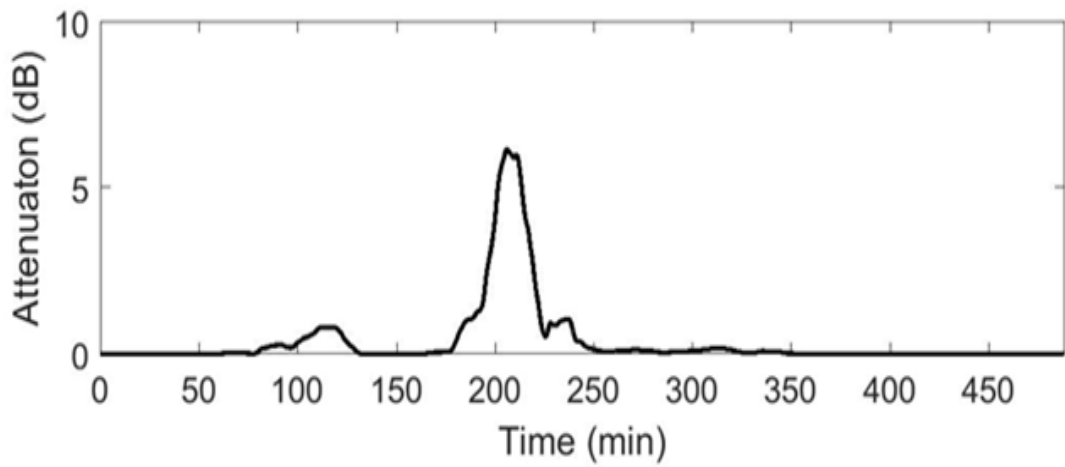
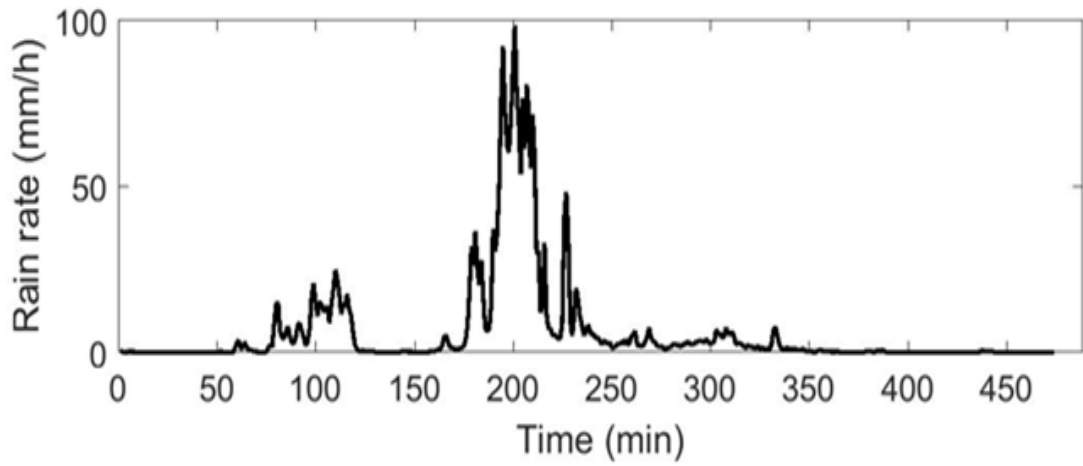


(a)

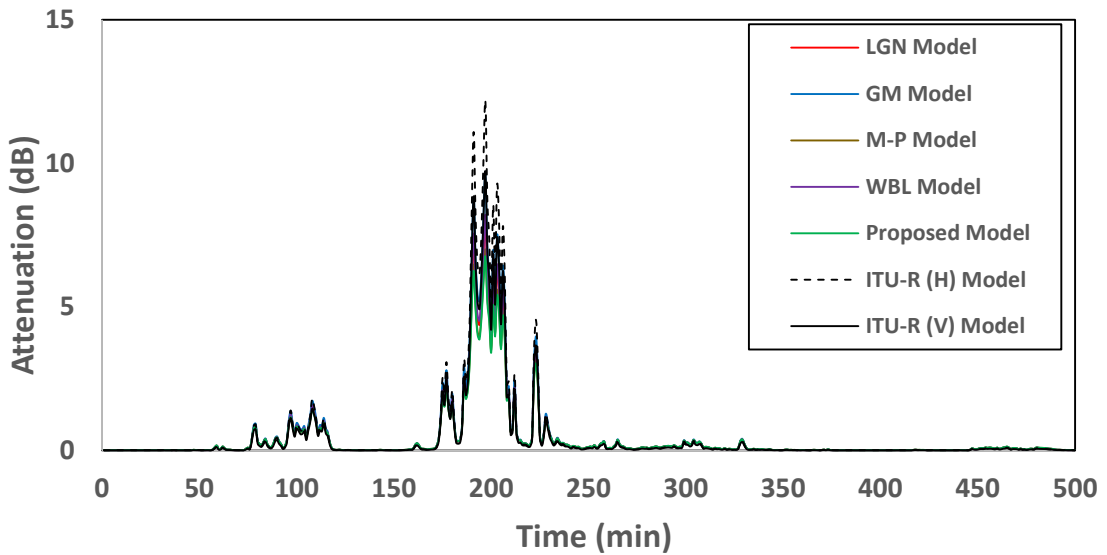


(b)

Figure 6-14: Rain rate and rain attenuation time series converted by: (a) SST (b) various models for a measured rainy event on 06/12/2013 at frequency  $f=8$  GHz and path length  $L=1$  km

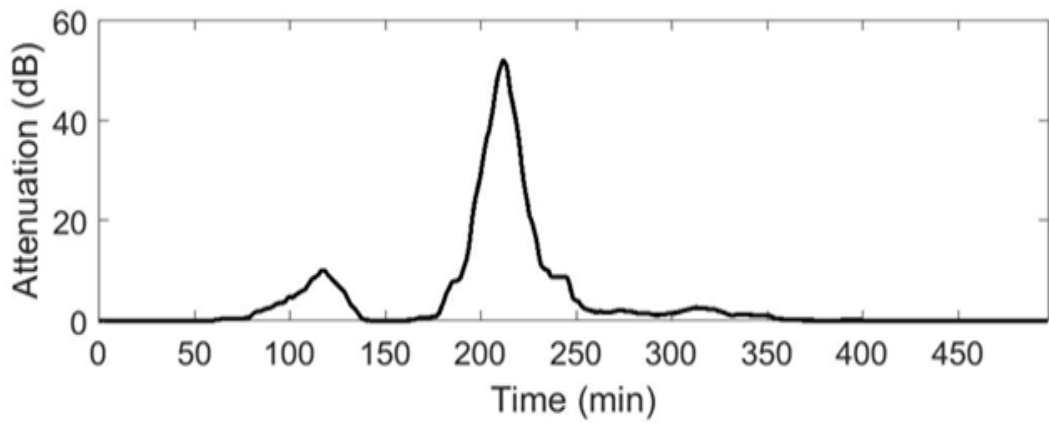
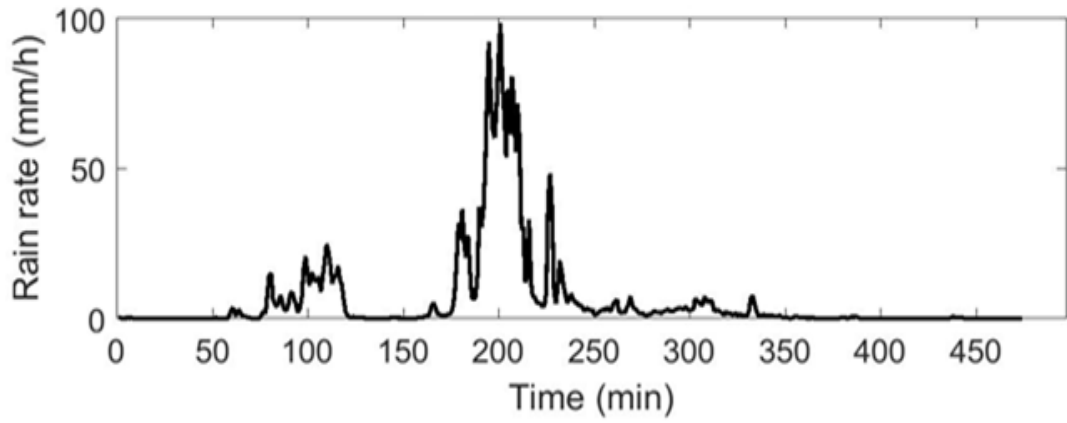


(a)

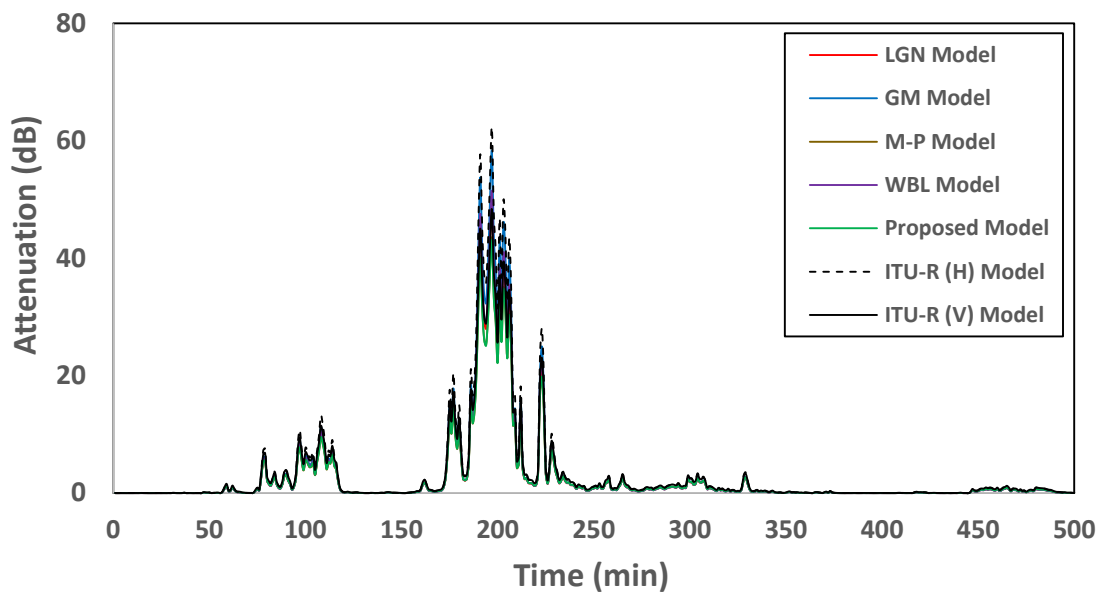


(b)

Figure 6-15: Rain rate and rain attenuation time series converted by: (a) SST (b) various models for a measured rainy event on 06/12/2013 at frequency  $f=8$  GHz and path length  $L=5$  km



(a)



(b)

Figure 6-16: Rain rate and rain attenuation time series converted by: (a) SST (b) various models for a measured rainy event on 06/12/2013 at frequency  $f=8$  GHz and path length  $L=8$  km

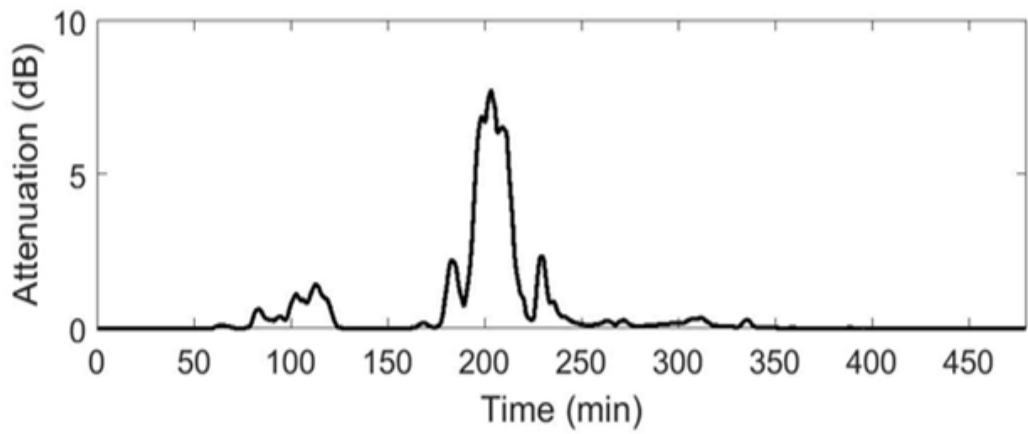
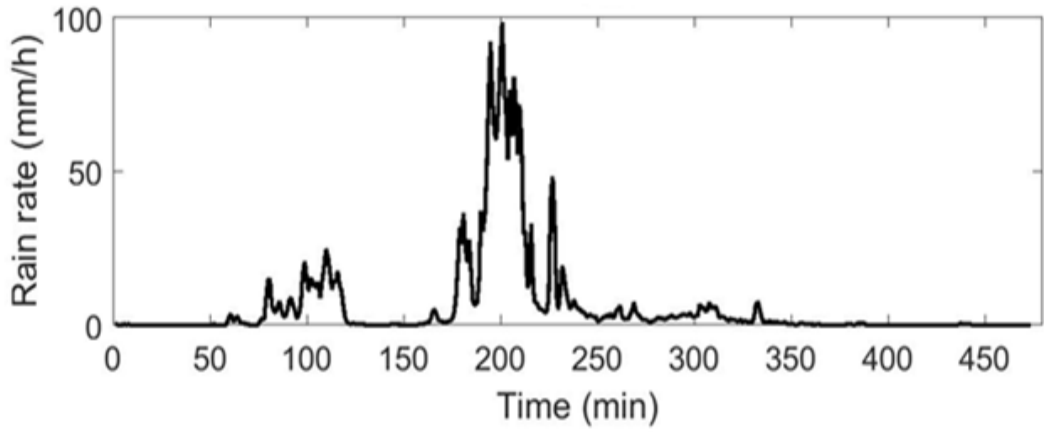
Figures 6-23 to 6-25 present the comparison between the generated rain attenuation time series using SST model and other rain attenuation models for the rain event on 01/10/2014 at a frequency of 8 GHz and path lengths of 1 km, 5 km and 8 km respectively. In this rainy event, there are several peaks, but the highest peak of rain attenuation value occurs when the corresponding rain rate is at its maximum value as shown on the plots. The highest peak of rainfall rate of this event corresponds to the maximum rain rate value attained for the entire period of measurement between 2012 and 2015.

In Figure 6-23, at a frequency of 8 GHz and path length of 1 km, when the rain rate is 118.516 mm/h, the peak value of rain attenuation is close to 1.6 dB using SST model, and 1.88 dB, 2.3 dB, 1.65 dB, 1.95 dB, 1.59 dB, 2.98 dB, 2.38 dB for Lognormal, Modified Gamma, Negative exponential, Weibull, Proposed model, ITU-R (H) and ITU-R (V) models, respectively. In Figure 6-24, at a frequency of 8 GHz and path length of 5 km, the highest peak value of rain attenuation is close to 6.5 dB using the SST model, and 7.88 dB, 9.65 dB, 6.60 dB, 7.81 dB, 6.65 dB, 12.59 dB, 9.90 dB for Lognormal, Modified Gamma, Negative exponential, Weibull, Proposed model, ITU-R (H) and ITU-R (V) models, respectively. In Figure 6-25, at a frequency of 8 GHz and path length of 8 km, the peak value of rain attenuation is close to 49 dB using SST model, and 58.49 dB, 72.61 dB, 51.11 dB, 60.9 dB, 50.44 dB, 73.29 dB, 56.26 dB, 49 dB for Lognormal, Modified Gamma, Negative exponential, Weibull, Proposed model, ITU-R (H) and ITU-R (V) models, respectively.

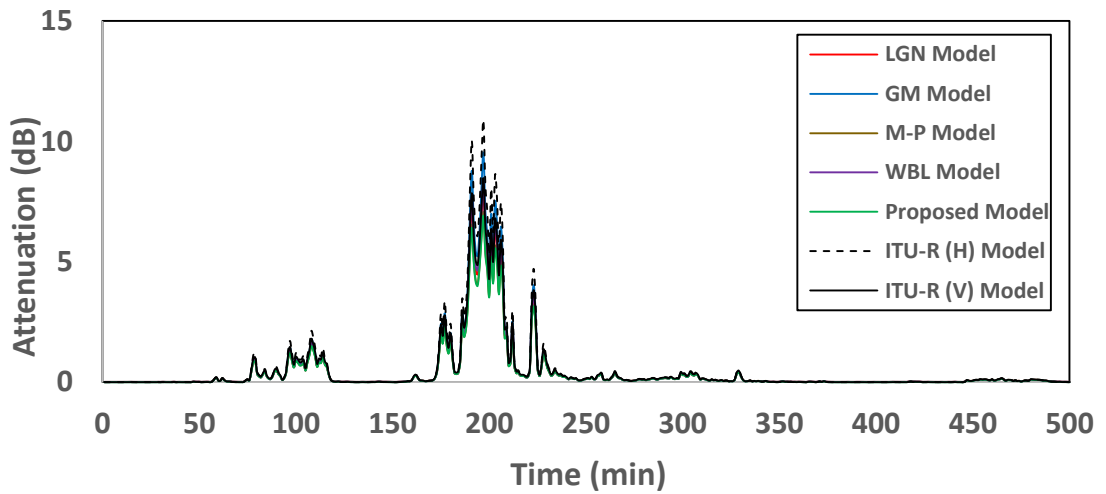
Figures 6-26 to 6-28 present the comparison between the generated rain attenuation time series using SST model and other rain attenuation models for a rainy event on 01/10/2014 at frequency of 12 GHz and path length of 2 km, 5 km and 8 km respectively.

In Figure 6-26, at a frequency of 12 GHz and path length of 2 km, the peak value of rain attenuation is about 10 dB using the SST model; and 9.45 dB, 11.37 dB, 8.67 dB, 9.85 dB, 8.46 dB, 12.91 dB, 9.96 dB for Lognormal, Modified Gamma, Negative exponential, Weibull, Proposed model, ITU-R (H) and ITU-R (V) models, respectively. In Figure 6-27, at a frequency of 12 GHz and path length of 5 km, the peak value of rain attenuation is close to 17 dB using the SST model; and 19.78 dB, 23.84 dB, 17.34 dB, 20.62 dB, 16.92 dB, 27.03 dB, 20.79 dB for Lognormal, Modified Gamma, Negative exponential, Weibull, Proposed model, ITU-R (H) and ITU-R (V) models, respectively. In Figure 6-28, at a frequency of 12 GHz and a path length of 8 km, the peak value of rain attenuation is about 25 dB using SST model; and 29.67 dB, 35.75 dB, 26.02 dB, 30.93 dB, 25.38 dB, 40.56 dB, 31.2 dB for Lognormal, Modified Gamma, Negative exponential, Weibull, Proposed model, ITU-R (H) and ITU-R (V) models, respectively.



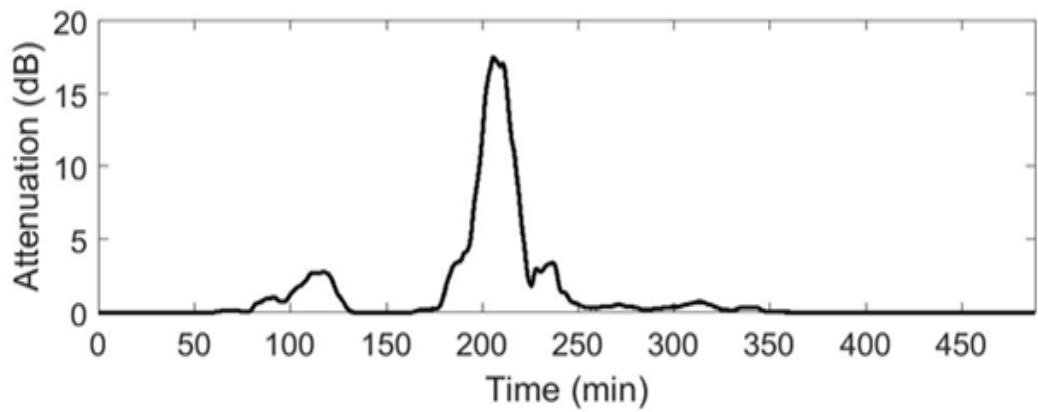
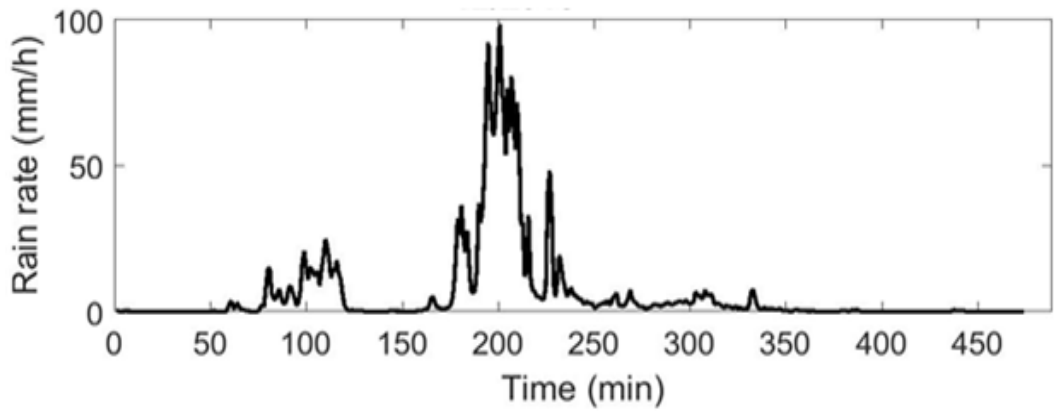


(a)

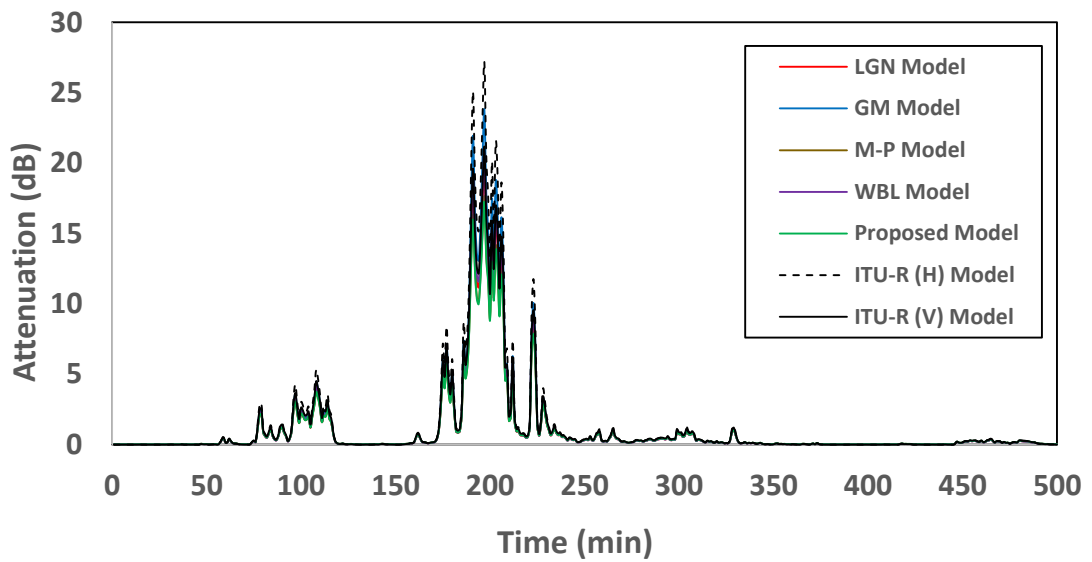


(b)

Figure 6-17: Rain rate and rain attenuation time series converted by: (a) SST (b) various models for a measured rainy event on 06/12/2013 at frequency  $f=12$  GHz and path length  $L=2$  km

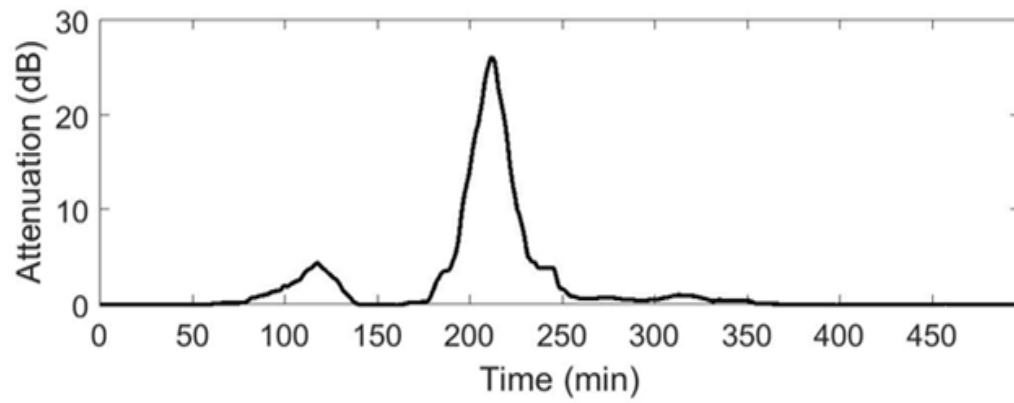
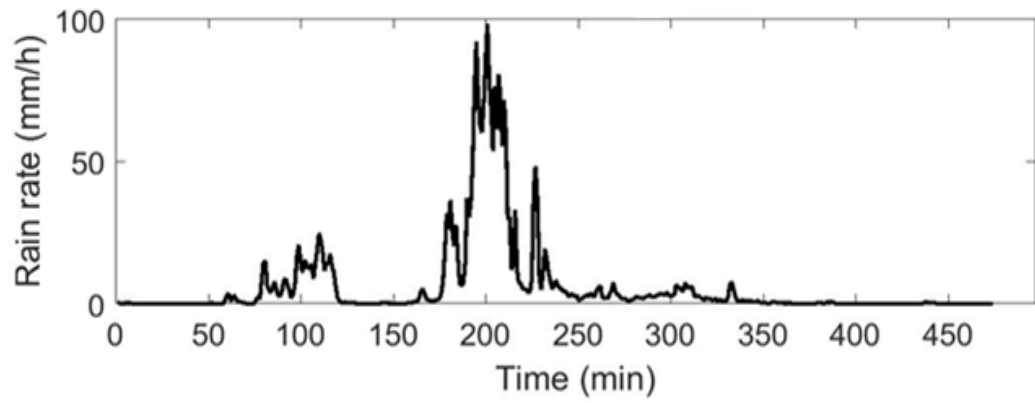


(a)

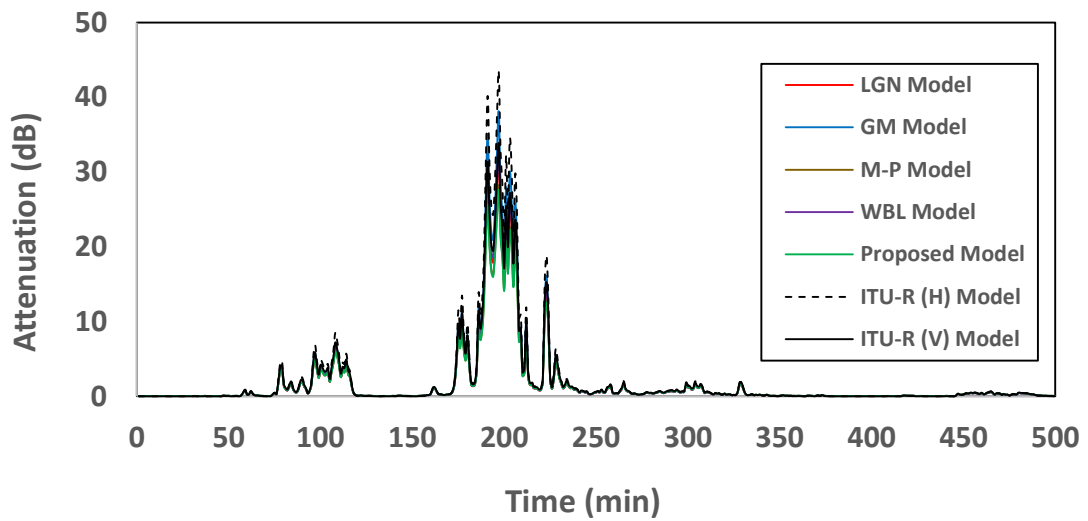


(b)

Figure 6-18: Rain rate and rain attenuation time series converted by: (a) SST (b) various models for a measured rainy event on 06/12/2013 at frequency  $f=12$  GHz and path length  $L=5$  km

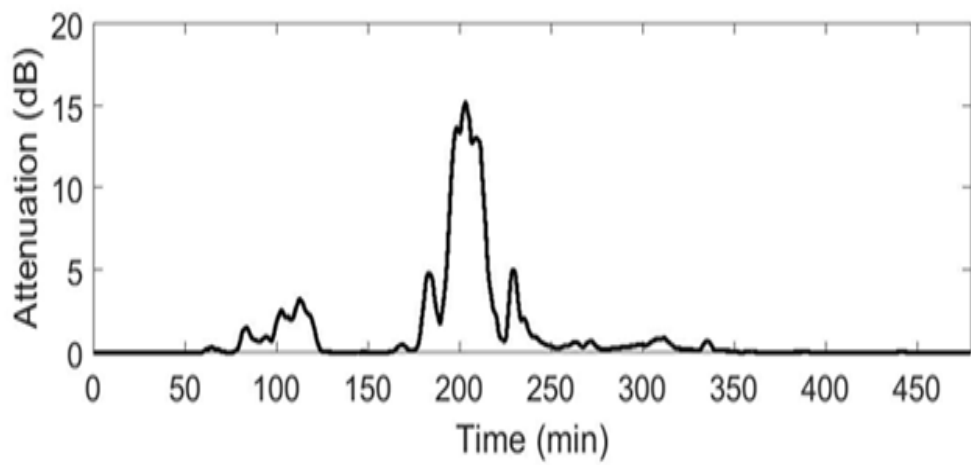
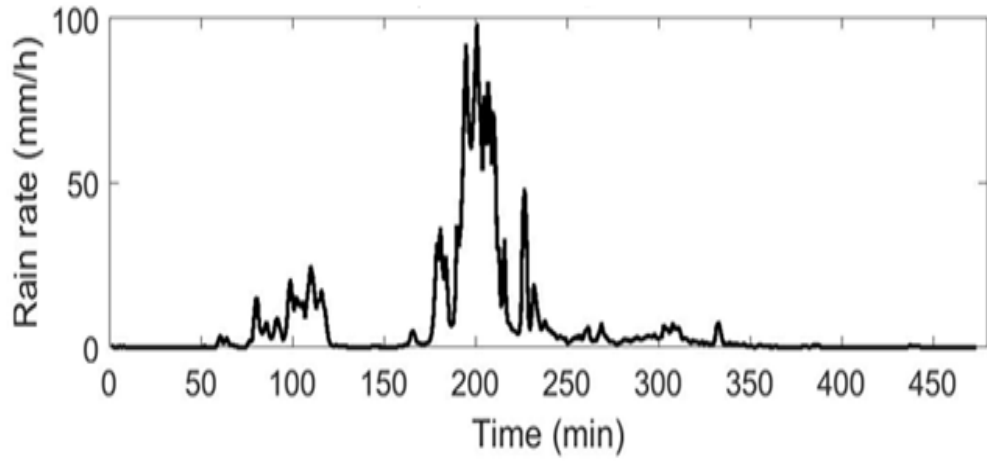


(a)

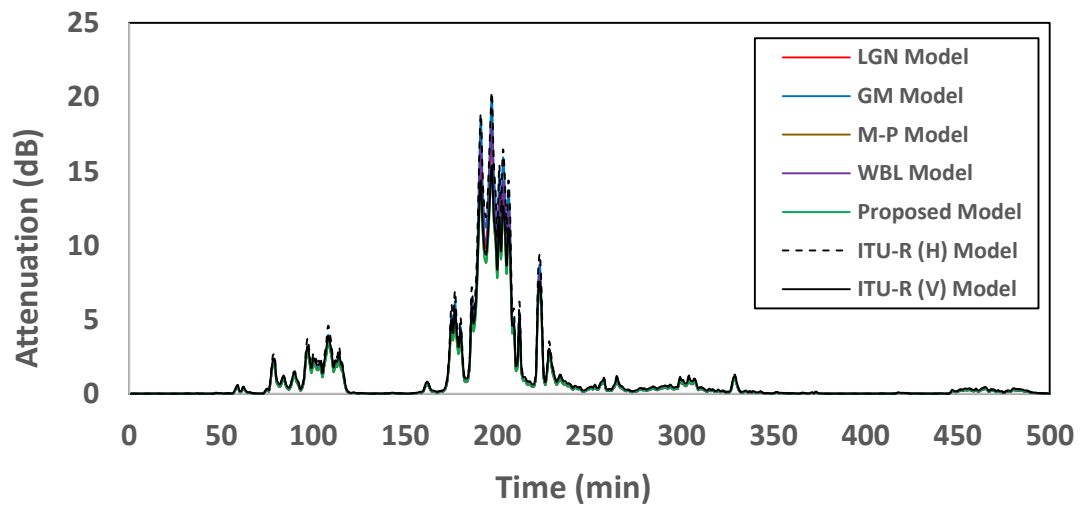


(b)

Figure 6-19: Rain rate and rain attenuation time series converted by: (a) SST (b) various models for a measured rainy event on 06/12/2013 at frequency  $f=12$  GHz and path length  $L=8$  km

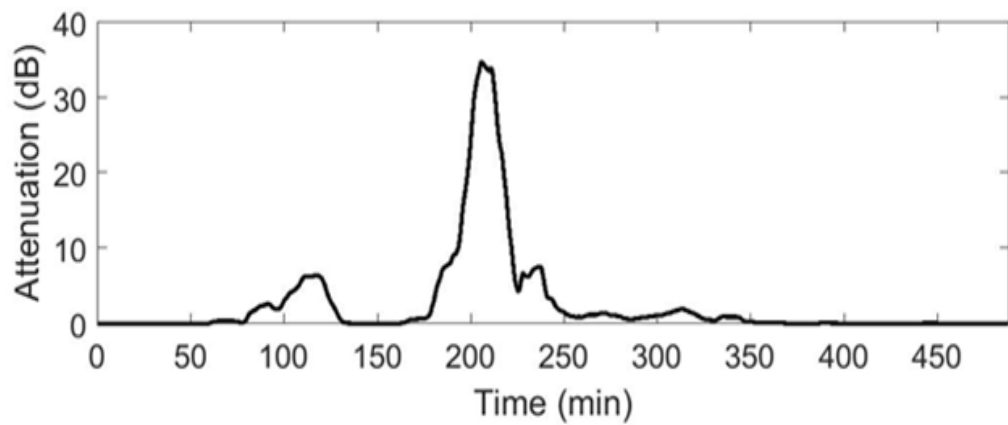
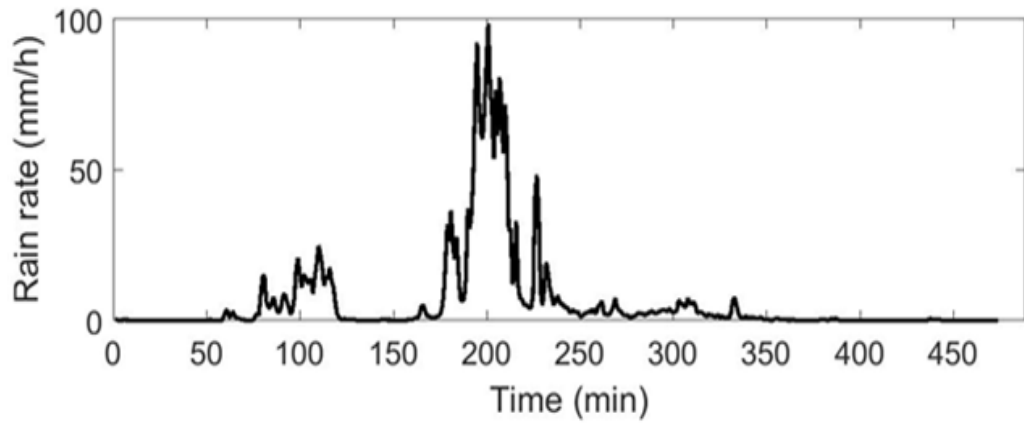


(a)

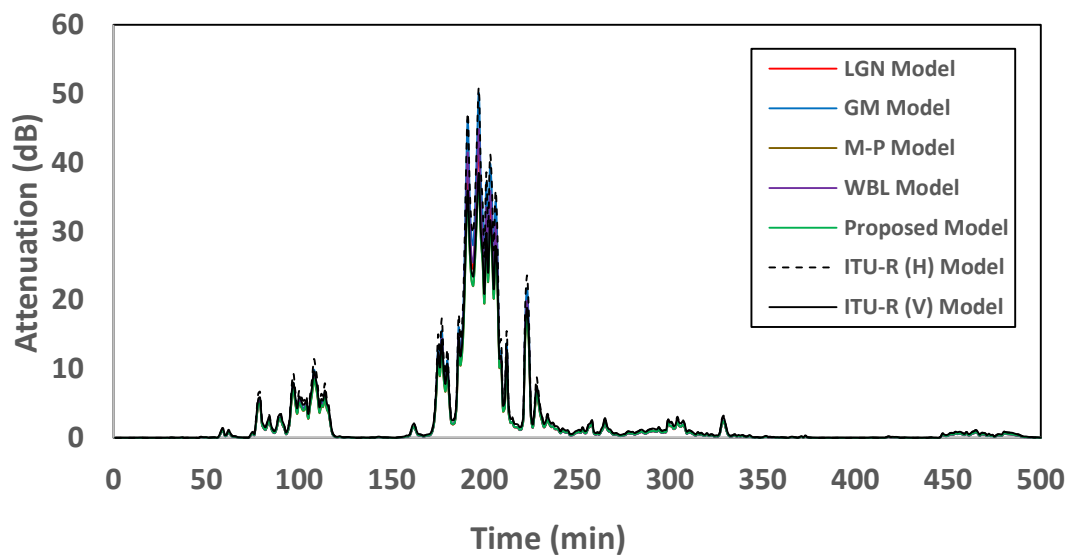


(b)

Figure 6-20: Rain rate and rain attenuation time series converted by: (a) SST (b) various models for a measured rainy event on 06/12/2013 at frequency  $f=19$  GHz and path length  $L=2$  km

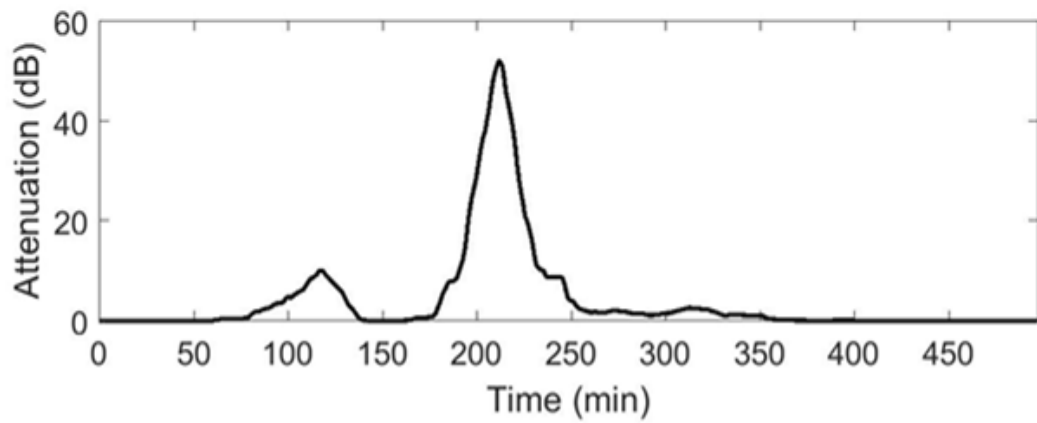
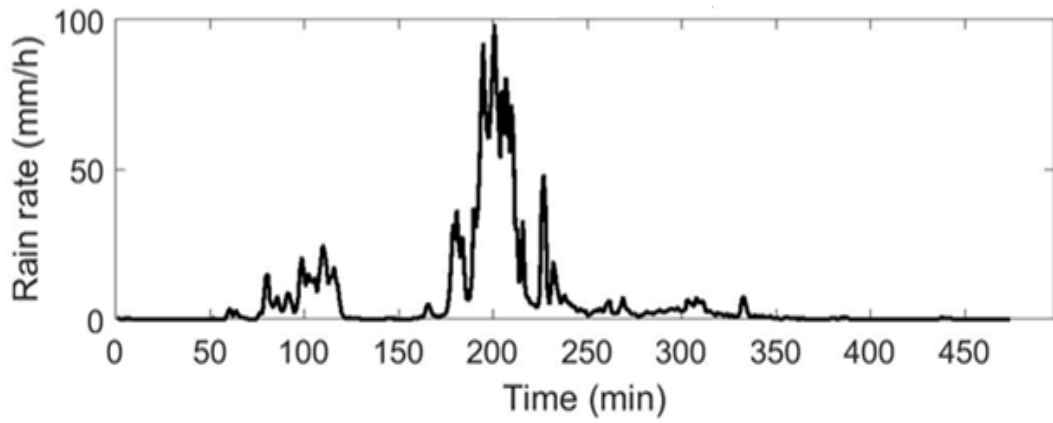


(a)

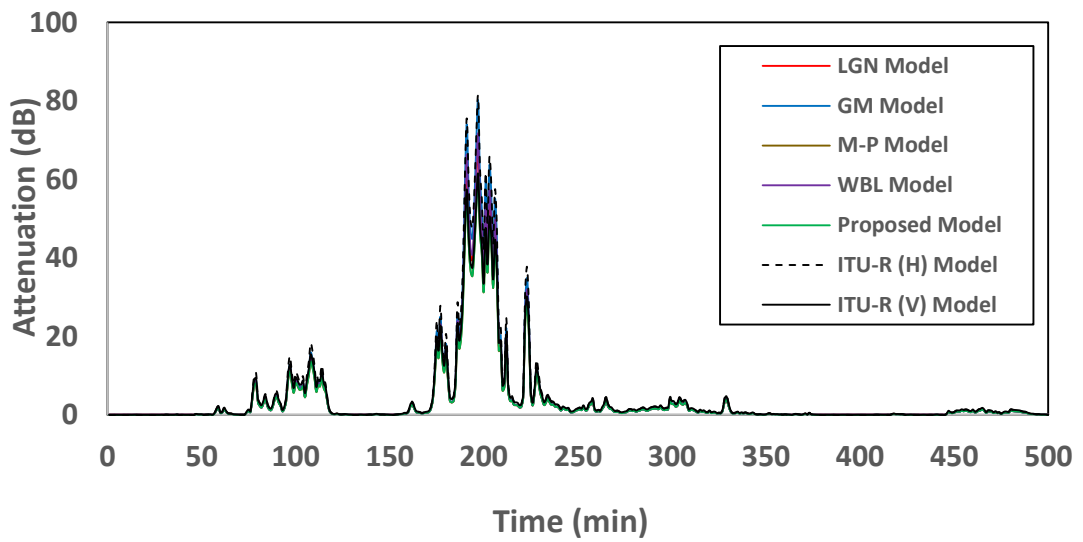


(b)

Figure 6-21: Rain rate and rain attenuation time series converted by: (a) SST (b) various models for a measured rainy event on 06/12/2013 at frequency  $f=19$  GHz and path length  $L=5$  km



(a)



(b)

Figure 6-22: Rain rate and rain attenuation time series converted by: (a) SST (b) various models for a measured rainy event on 06/12/2013 at frequency  $f=19$  GHz and path length  $L=8$  km

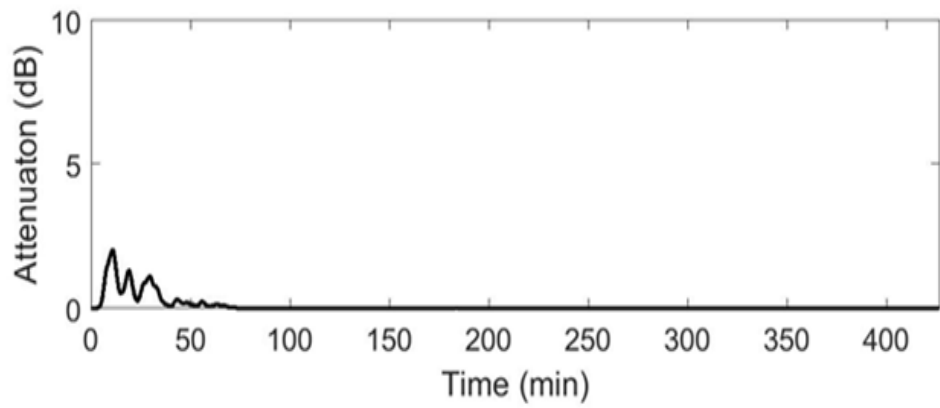
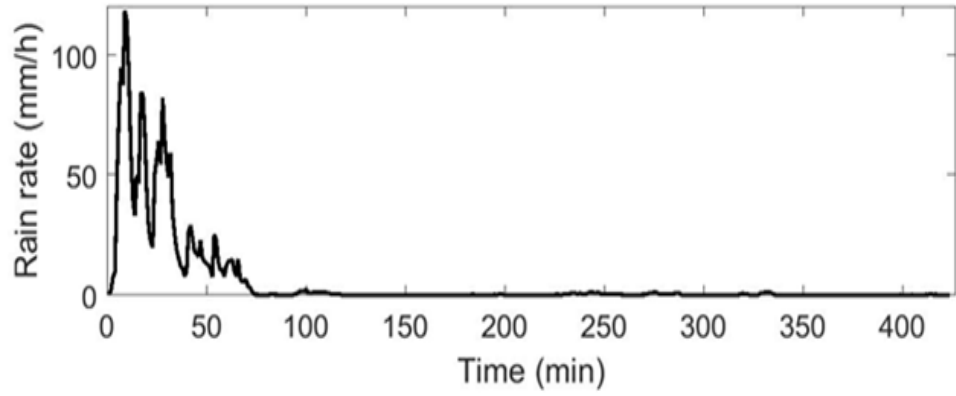
Figures 6-29 to 6-31 present the comparison between the generated rain attenuation time series using the SST model and other rain attenuation models for a rainy event on 01/10/2014 at frequency of 19 GHz and path lengths of 2 km, 5 km and 8 km respectively.

In Figure 6-29, at a frequency of 19 GHz and path length of 2 km, the highest peak value of rain attenuation is about 19 dB using SST model; and 21.20 dB, 24.87 dB, 19.50 dB, 22.11 dB, 18.90 dB, 24.79 dB, 19.02 dB for Lognormal, Modified Gamma, Negative exponential, Weibull, Proposed model, ITU-R (H) and ITU-R (V) models, respectively. In Figure 6-30, at a frequency of 19 GHz and path length of 5 km, the peak value of rain attenuation is close to 35 dB using SST model; and 42.40 dB, 49.74 dB, 36.98 dB, 44.22 dB, 36.76 dB, 49.59 dB, 36.98 dB for Lognormal, Modified Gamma, Negative exponential, Weibull, Proposed model, ITU-R (H) and ITU-R (V) models, respectively. In Figure 6-31, at a frequency of 19 GHz and path length of 8 km, the peak value of rain attenuation is about 50 dB using the SST model; and 74.20 dB, 87.05 dB, 64.72 dB, 77.38 dB, 64.33 dB, 86.78 dB, 64.71 dB for Lognormal, Modified Gamma, Negative exponential, Weibull, Proposed model, ITU-R (H) and ITU-R (V) models, respectively.

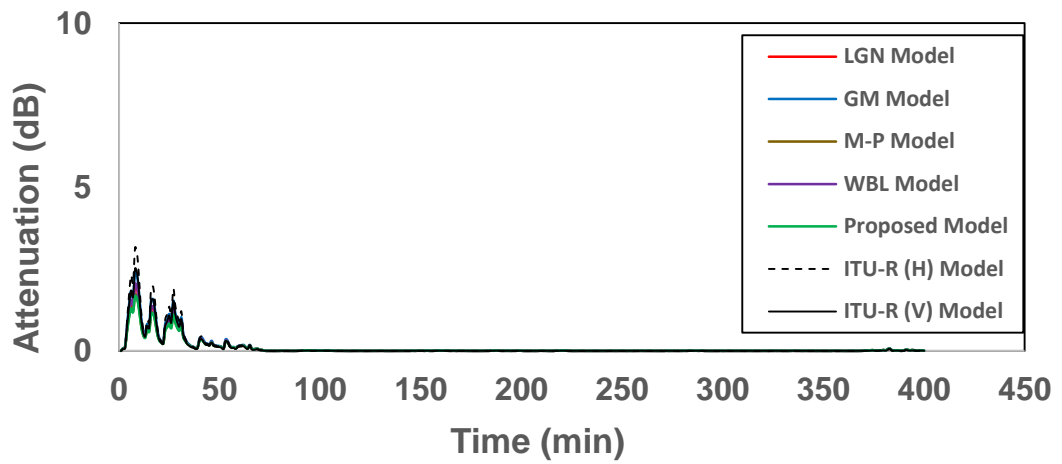
Figures 6-32 to 6-34 present the comparison between the generated rain attenuation time series using SST model and other rain attenuation models for a rainy event on 18/05/20115 at a frequency of 8 GHz and path length of 1 km, 5 km and 8 km, respectively. In this rainy event, there are several peaks but the highest peak of rain attenuation value occurs when the corresponding rain rate is at its maximum value (72.69 mm/h) as shown on the plots.

In Figure 6-32, at a frequency of 8 GHz and path length of 1 km, the first peak is at 43.09mm/h and its corresponding predicted rain attenuation values is about 0.5dB using the SST model; and 0.59 dB, 0.68 dB, 0.54 dB, 0.60 dB, 0.53 dB, 0.77 dB, 0.62 dB for Lognormal, Modified Gamma, Negative exponential, Weibull, Proposed model, ITU-R (H) and ITU-R (V) models, respectively. The highest peak values of rain attenuation are about 1 dB using the SST model; and 1.09 dB, 1.31 dB, 0.99 dB, 1.13 dB, 0.96 dB, 1.59 dB, 1.28 dB for Lognormal, Modified Gamma, Negative exponential, Weibull, Proposed model, ITU-R (H) and ITU-R (V) models, respectively.

In Figure 6-33, at a frequency of 8 GHz and path length of 5 km, the first peak of the predicted rain attenuation values is 2 dB using the SST model; and 2.92 dB, 3.42 dB, 2.71 dB, 3.01 dB, 2.65 dB, 3.85 dB, 3.10 dB for Lognormal, Modified Gamma, Negative exponential, Weibull, Proposed model, ITU-R (H) and ITU-R (V) models, respectively.



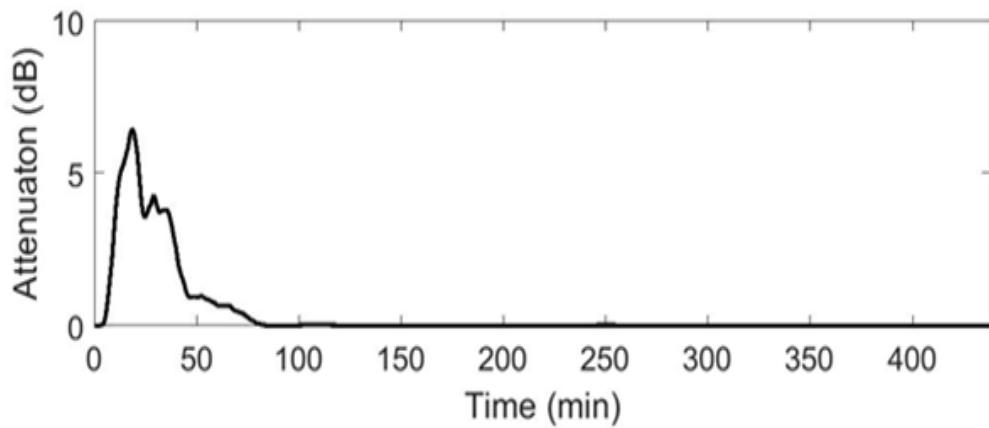
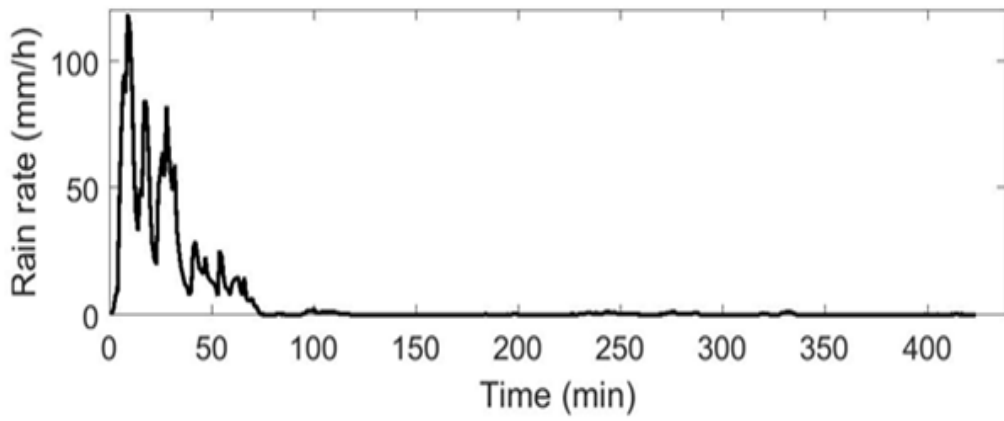
(a)



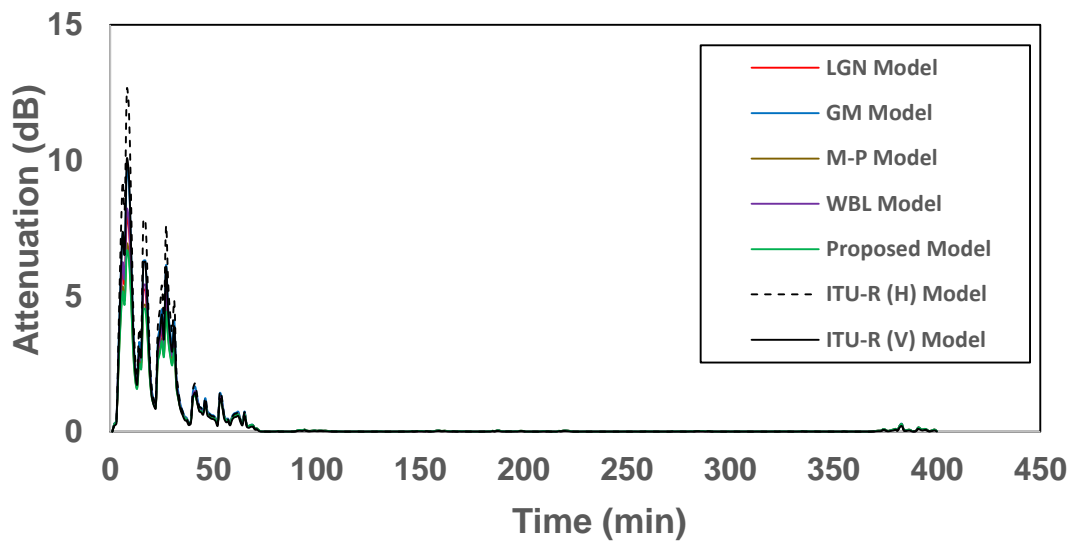
(b)

Figure 6-23: Rain rate and rain attenuation time series converted by: (a) SST (b) various models for a measured rainy event on 01/10/2014 at frequency  $f=8$  GHz and path length  $L=1$  km



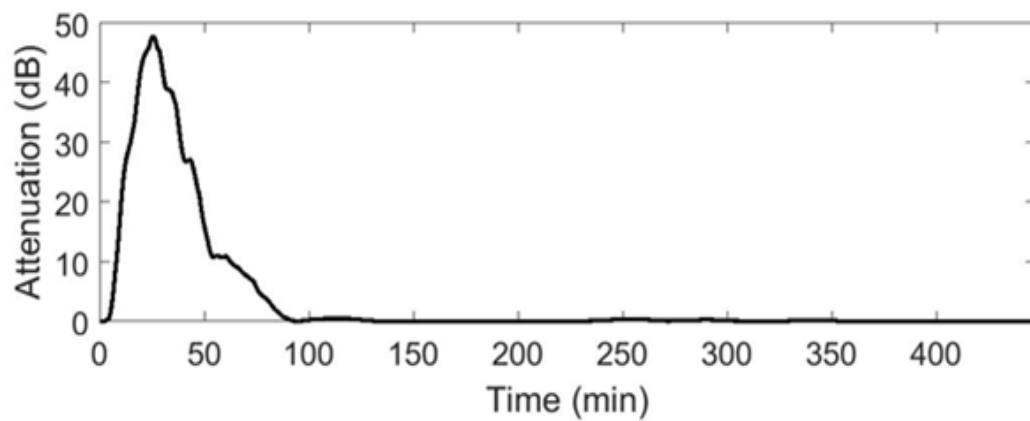
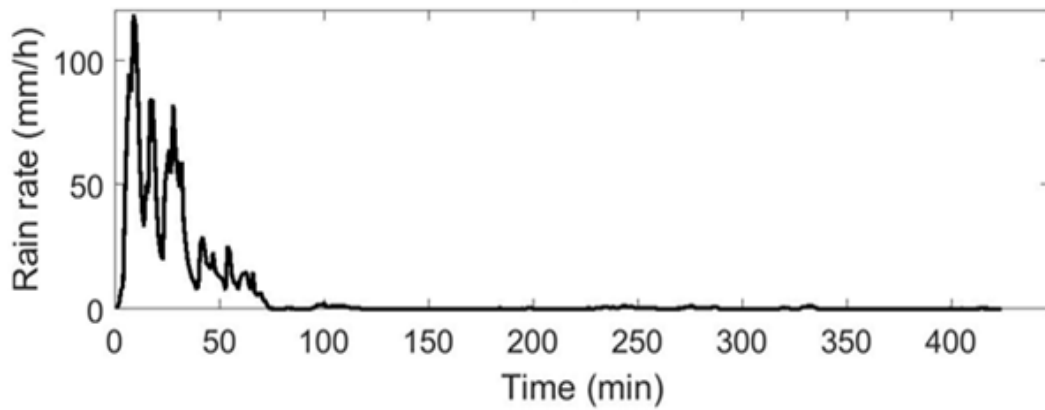


(a)

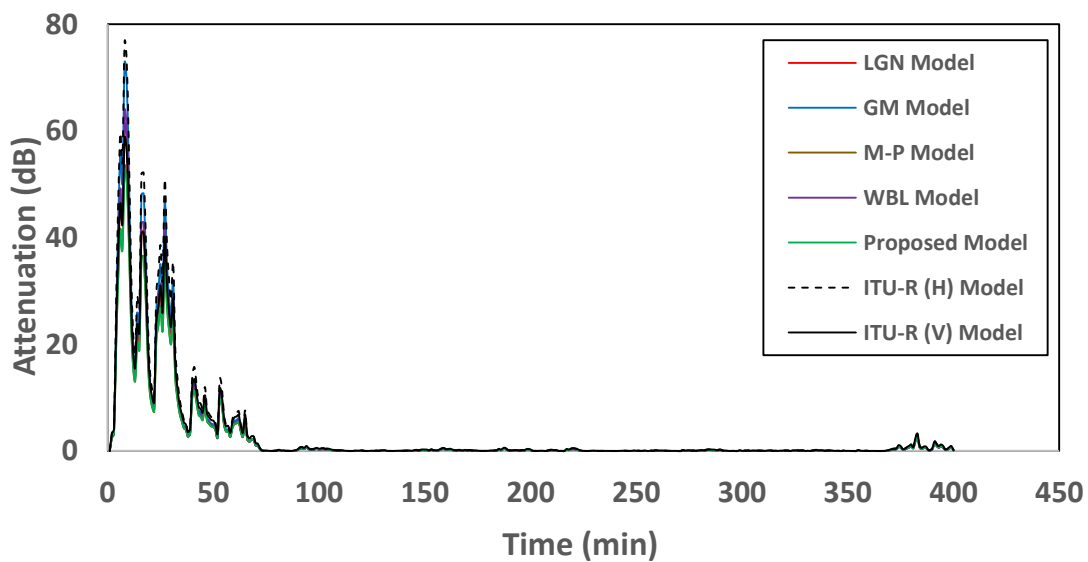


(b)

Figure 6-24: Rain rate and rain attenuation time series converted by: (a) SST (b) various models for a measured rainy event on 01/10/2014 at frequency  $f=8$  GHz and path length  $L=5$  km

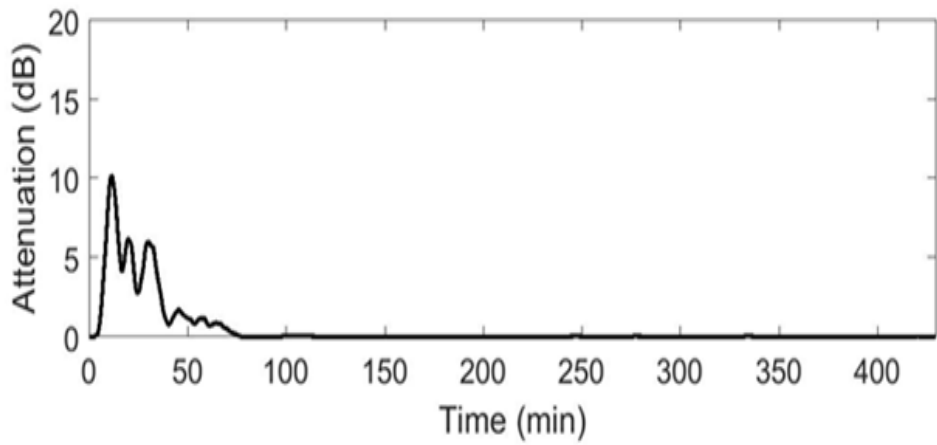
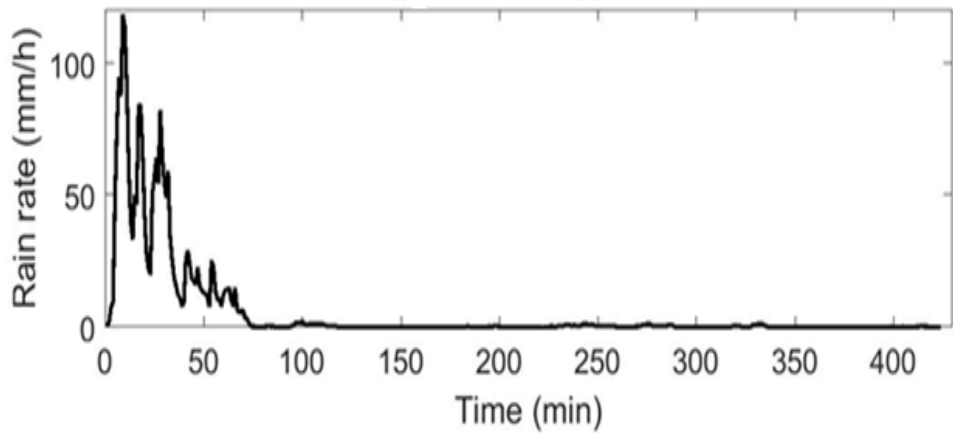


(a)

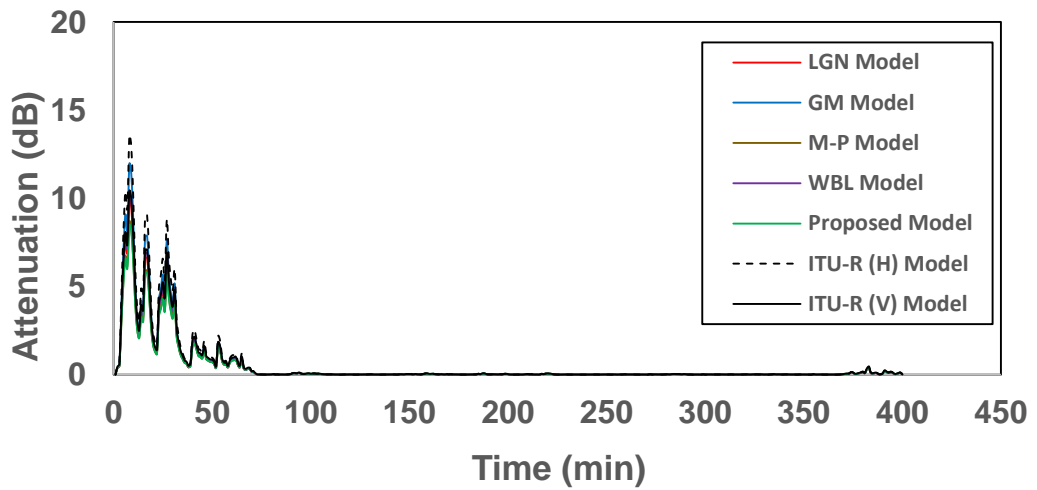


(b)

Figure 6-25: Rain rate and rain attenuation time series converted by: (a) SST (b) various models for a measured rainy event on 01/10/2014 at frequency  $f=8$  GHz and path length  $L=8$  km

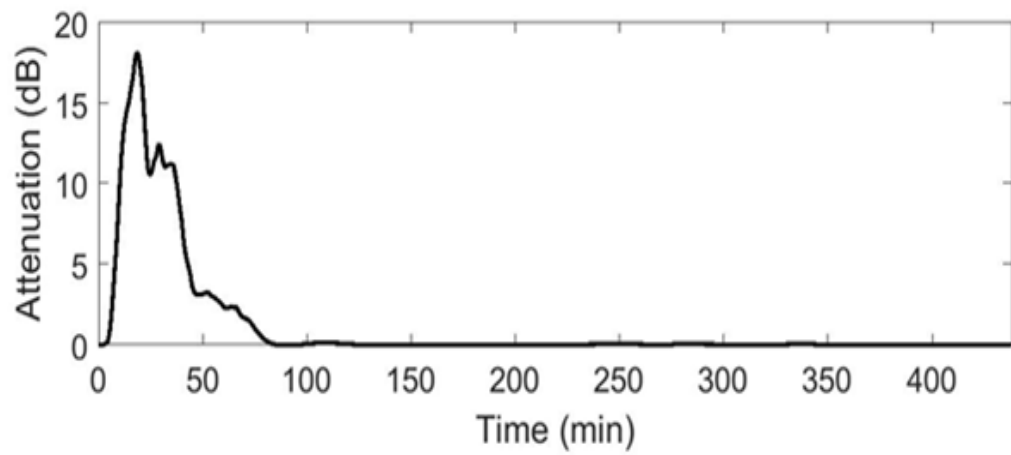
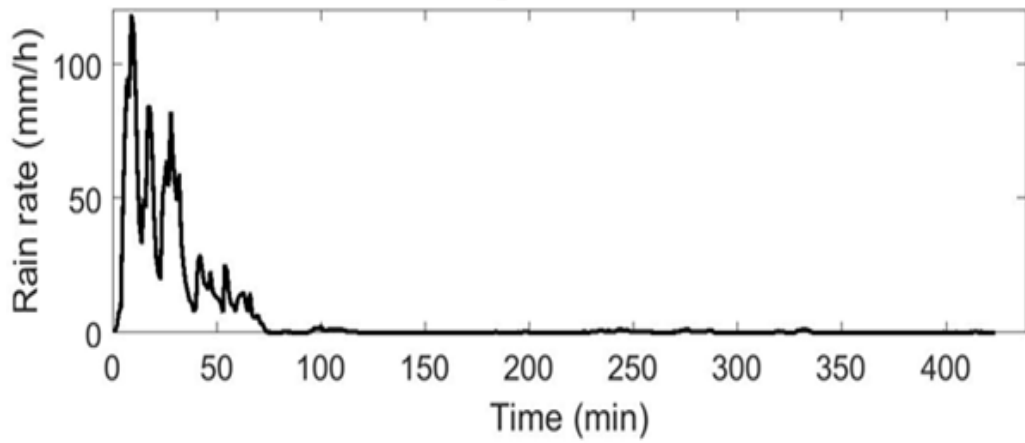


(a)

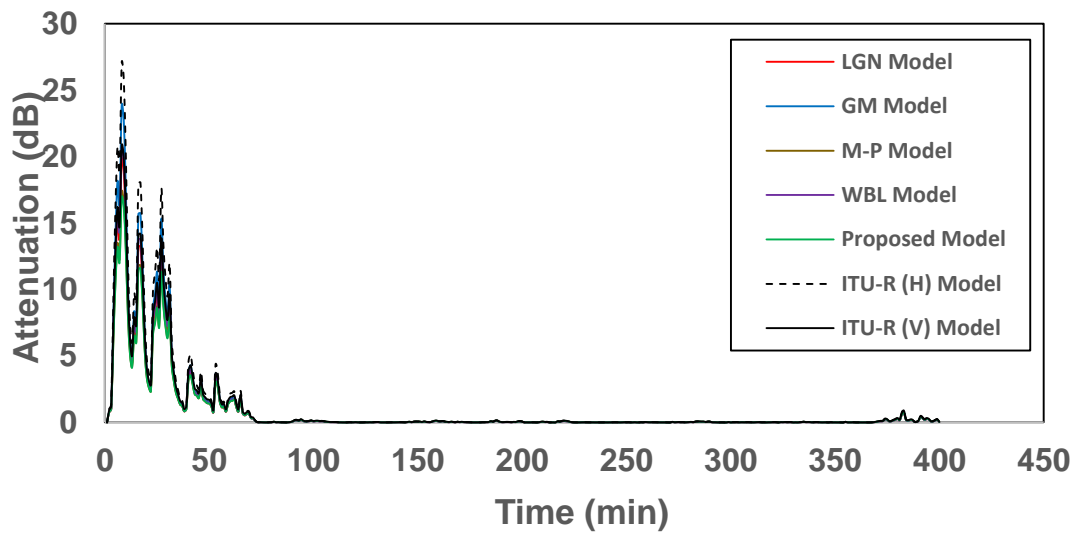


(b)

Figure 6-26: Rain rate and rain attenuation time series converted by: (a) SST (b) various models for a measured rainy event on 01/10/2014 at frequency  $f=12$  GHz and path length  $L=2$  km

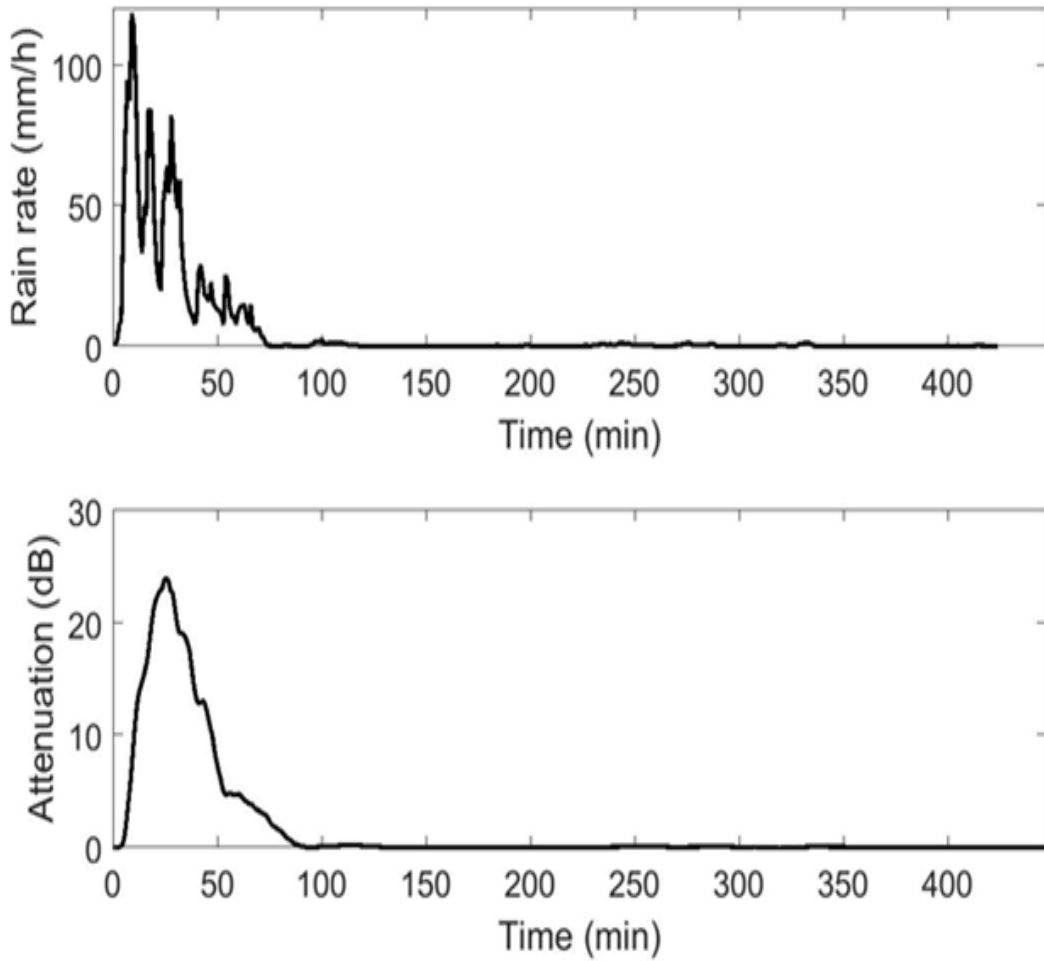


(a)

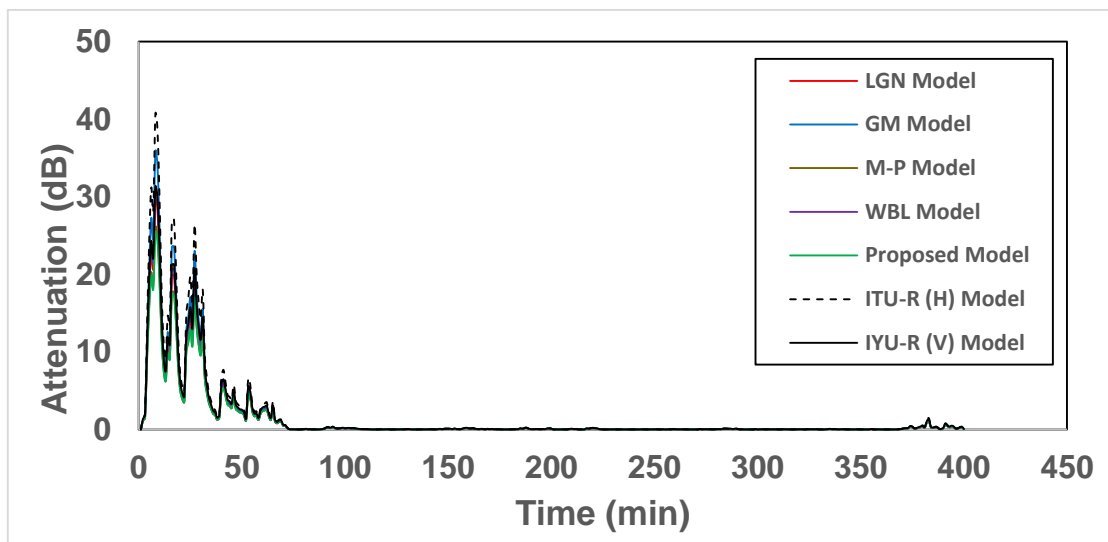


(b)

Figure 6-27: Rain rate and rain attenuation time series converted by: (a) SST (b) various models for a measured rainy event on 01/10/2014 at frequency  $f=12$  GHz and path length  $L=5$  km



(a)



(b)

Figure 6-28: Rain rate and rain attenuation time series converted by: (a) SST (b) various models for a measured rainy event on 01/10/2014 at frequency  $f=12$  GHz and path length  $L=8$  km

The highest peak values of rain attenuation are about 2.5 dB using SST model; and 5.47 dB, 6.56 dB, 4.93 dB, 5.66 dB, 4.78 dB, 7.98 dB, 6.38 dB for Lognormal, Modified Gamma, Negative exponential, Weibull, Proposed model, ITU-R (H) and ITU-R (V) models, respectively.

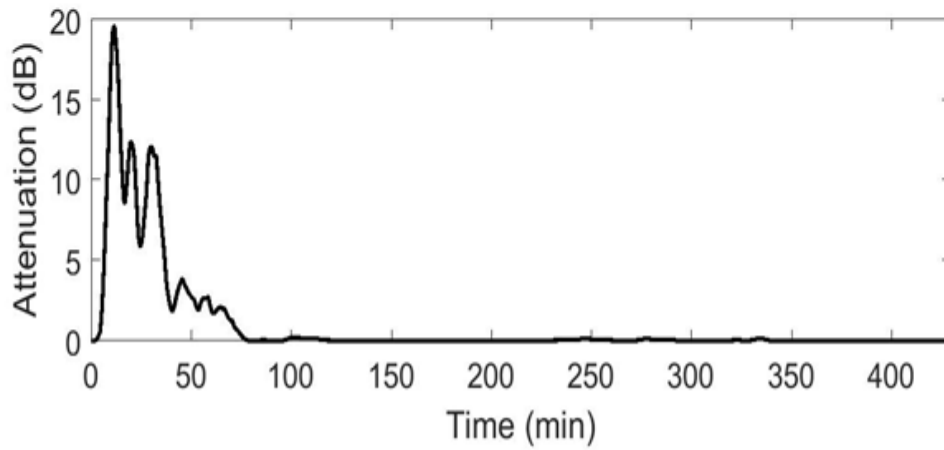
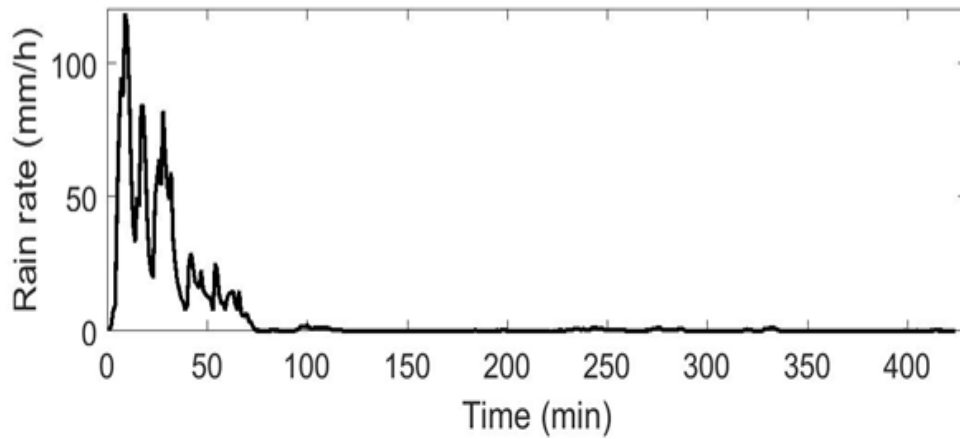
In Figure 6-34, at a frequency of 8 GHz and path length of 8 km, the first peak of the predicted rain attenuation values is close to 2.2 dB using SST model; and 4.67 dB, 5.47 dB, 4.34 dB, 4.82 dB, 4.23 dB, 6.16 dB, 4.96 dB for Lognormal, Modified Gamma, Negative exponential, Weibull, Proposed model, ITU-R (H) and ITU-R (V) models, respectively. The highest peak value of rain attenuation is about 3 dB using SST model; and 8.76 dB, 10.50 dB, 7.89 dB, 9.07 dB, 7.65 dB, 12.76 dB, 10.22 dB for Lognormal, Modified Gamma, Negative exponential, Weibull, Proposed model, ITU-R (H) and ITU-R (V) models, respectively.

Figures 6-35 to 6-37 present the comparison between the generated rain attenuation time series using SST model and other rain attenuation models for a rainy event on 18/05/20115 at frequency of 19 GHz and path lengths of 2 km, 5 km and 8 km respectively.

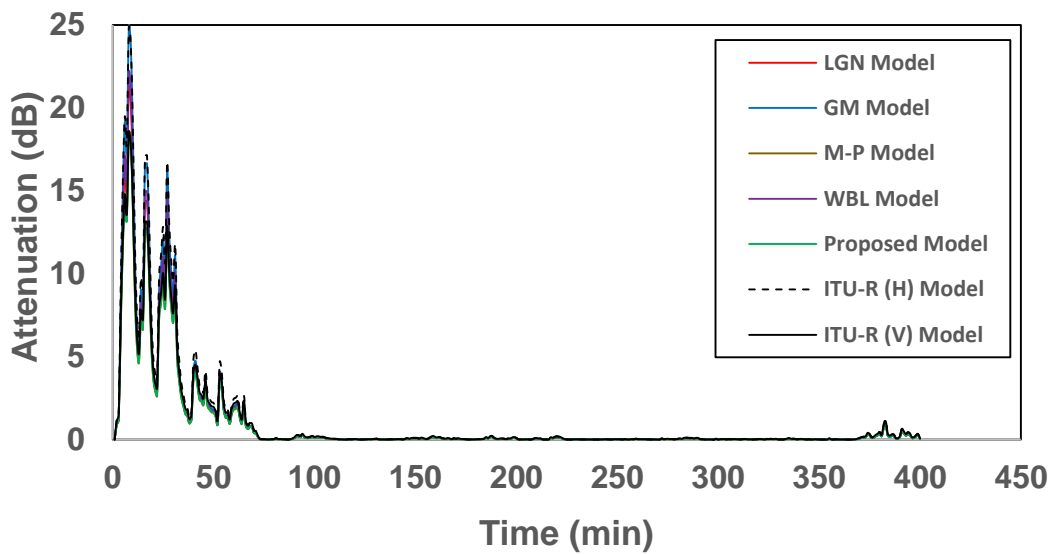
In Figure 6-35, at a frequency of 19 GHz and path length of 2 km, the first peak of the predicted rain attenuation value is 6 dB using SST model, and 6.72 dB, 7.57 dB, 6.13 dB, 6.96 dB, 6.17 dB, 8.29 dB, 6.71 dB for Lognormal, Modified Gamma, Negative exponential, Weibull, Proposed model, ITU-R (H) and ITU-R (V) models, respectively. The highest peak value of rain attenuation is 11dB using SST model, and 12.17 dB, 13.99 dB, 10.85 dB, 12.65 dB, 10.85 dB, 14.61 dB, 11.32 dB for Lognormal, Modified Gamma, Negative exponential, Weibull, Proposed model, ITU-R (H) and ITU-R (V), models, respectively.

In Figure 6-36, at a frequency of 19 GHz and path length of 5 km, the first peak of the predicted rain attenuation value is 10 dB using SST model; and 16.81 dB, 18.92 dB, 15.32 dB, 17.40 dB, 15.42 dB, 20.74 dB, 16.76 dB for Lognormal, Modified Gamma, Negative exponential, Weibull, Proposed model, ITU-R (H) and ITU-R (V) models, respectively. The highest peak values of rain attenuation are about 16 dB using the SST model; and 30.43 dB, 34.99 dB, 27.11 dB, 31.63 dB, 27.12 dB, 36.52 dB, 28.32 dB for Lognormal, Modified Gamma, Negative exponential, Weibull, Proposed model, ITU-R (H) and ITU-R (V) models, respectively.

In Figure 6-37, at a frequency of 19 GHz and path length of 8 km, the first peak value of the predicted rain attenuation is 12 dB using SST model; and 26.89 dB, 30.27 dB, 24.52 dB, 27.85 dB, 24.68 dB, 33.20 dB, 26.82 dB for Lognormal, Modified Gamma, Negative exponential, Weibull, Proposed model, ITU-R (H) and ITU-R (V) models, respectively. The highest peak values of rain attenuation are about 17,5dB using the SST model; and 48.69 dB, 55.99 dB, 43.39 dB, 50.60 dB, 43.30 dB, 58.45 dB, 45.31 dB for Lognormal, Modified Gamma, Negative exponential, Weibull, Proposed model, ITU-R (H) and ITU-R (V) models, respectively.

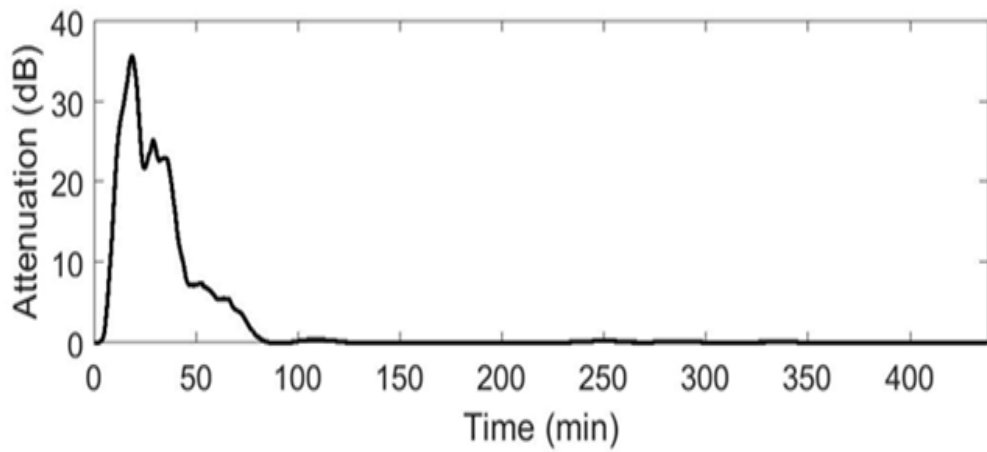
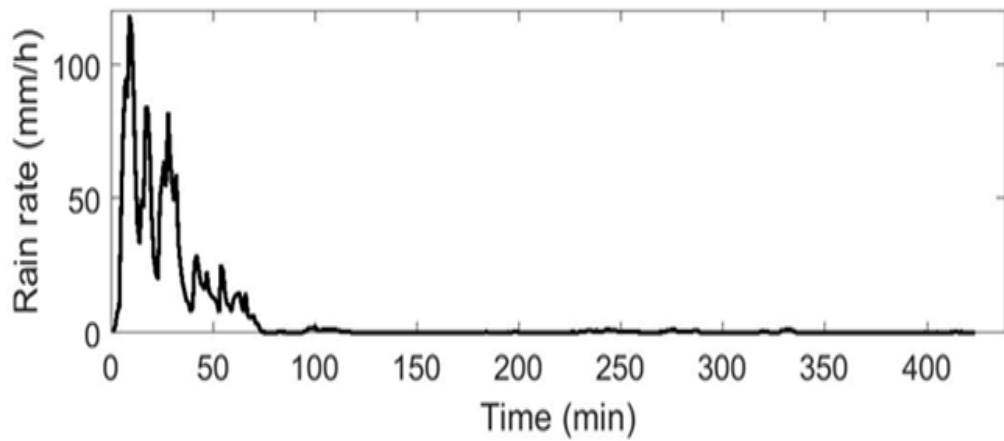


(a)

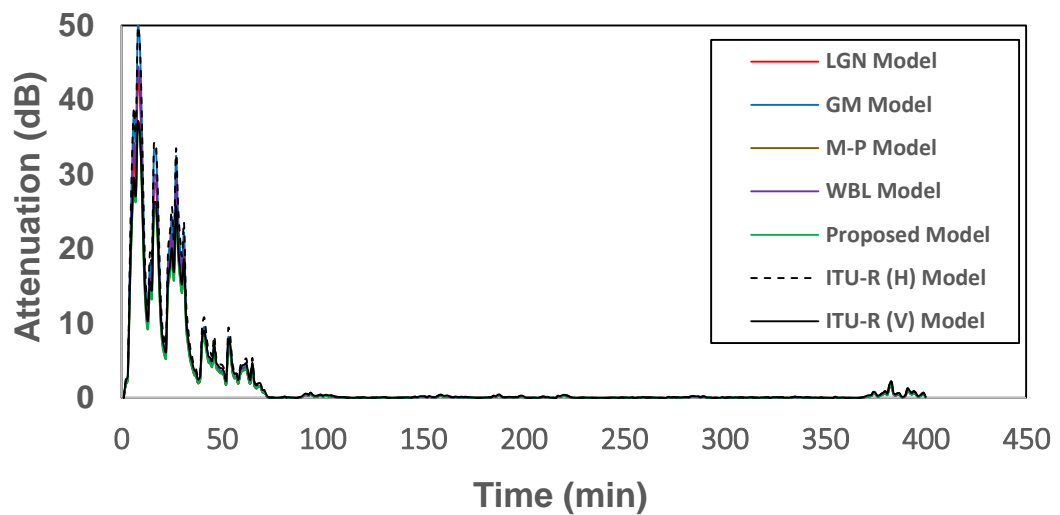


(b)

Figure 6-29: Rain rate and rain attenuation time series converted by: (a) SST (b) various models for a measured rainy event on 01/10/2014 at frequency  $f=19$  GHz and path length  $L=2$  km



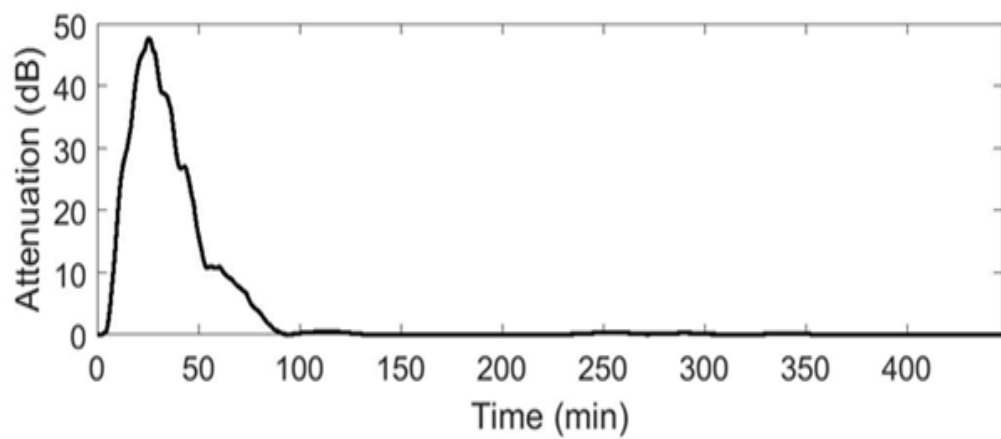
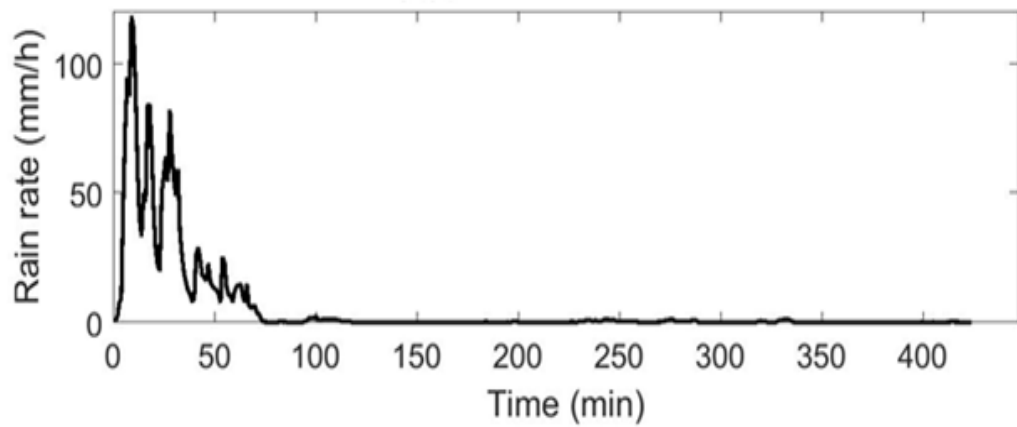
(a)



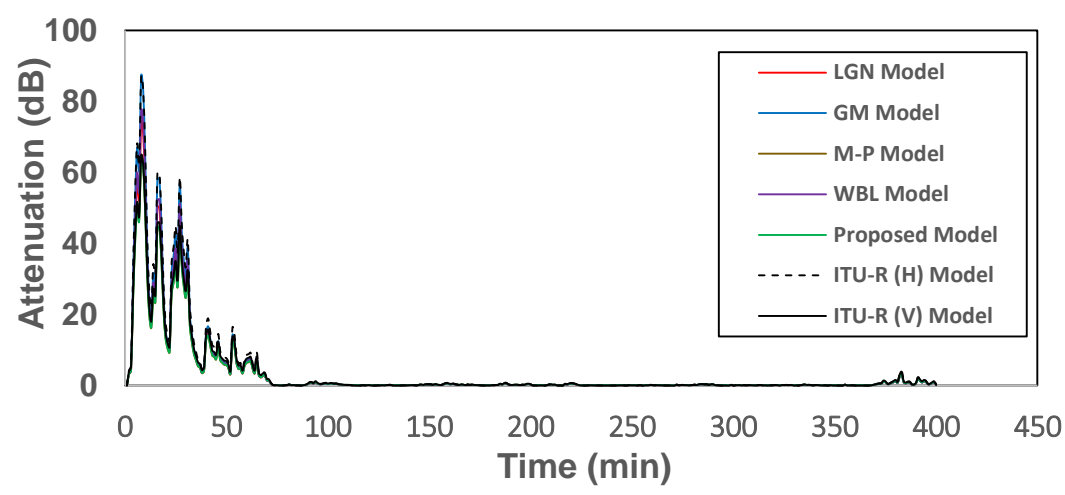
(b)

Figure 6-30: Rain rate and rain attenuation time series converted by: (a) SST (b) various models for a measured rainy event on 01/10/2014 at frequency  $f=19$  GHz and path length  $L=5$  km



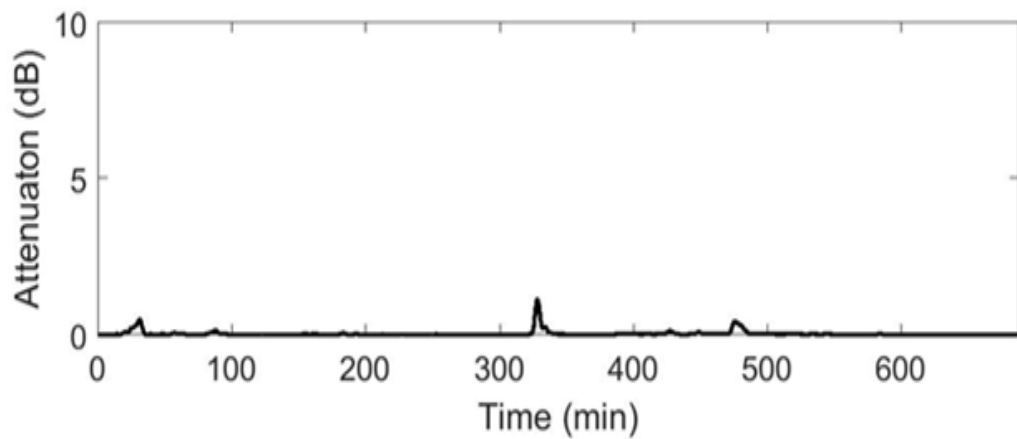
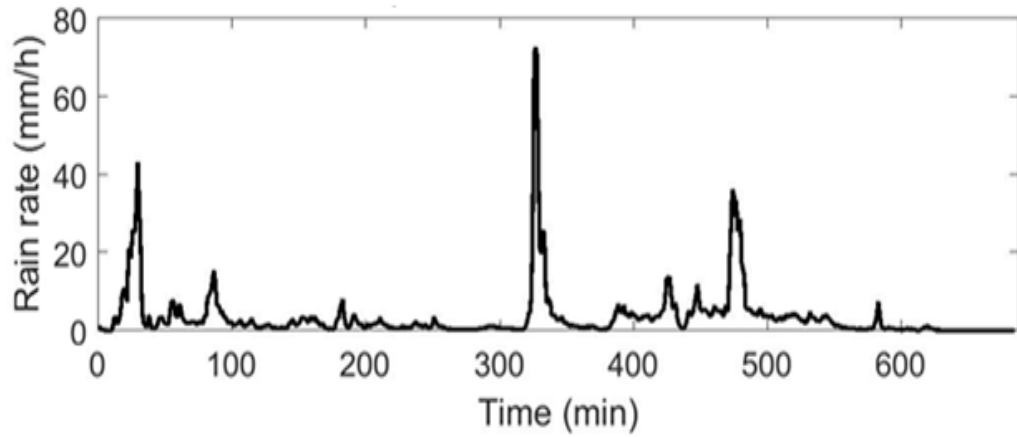


(a)

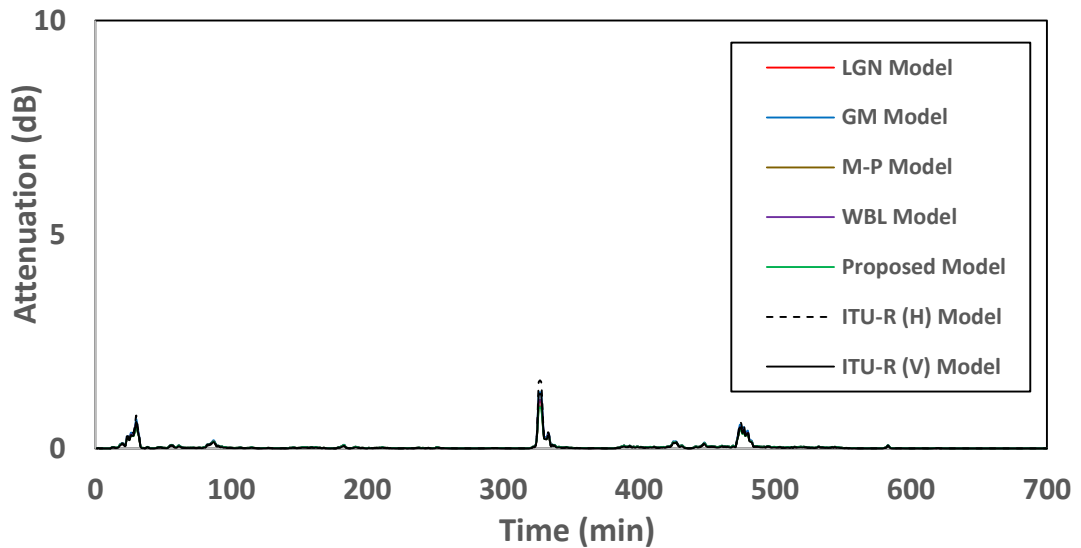


(b)

Figure 6-31: Rain rate and rain attenuation time series converted by: (a) SST (b) various models for a measured rainy event on 01/10/2014 at frequency  $f=19$  GHz and path length  $L=8$  km

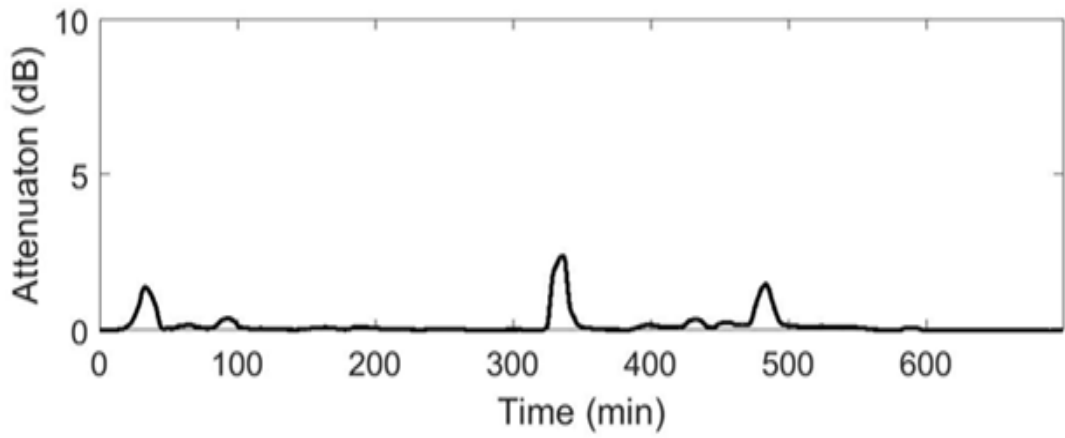
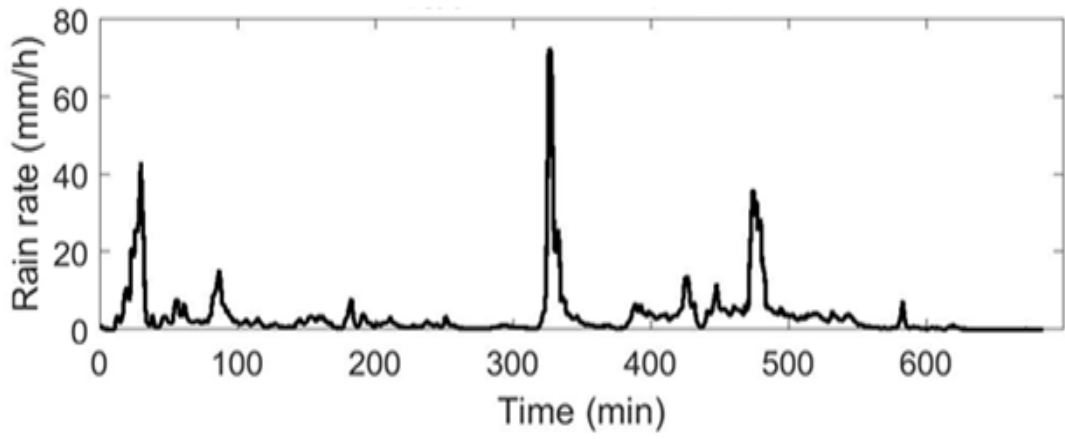


(a)

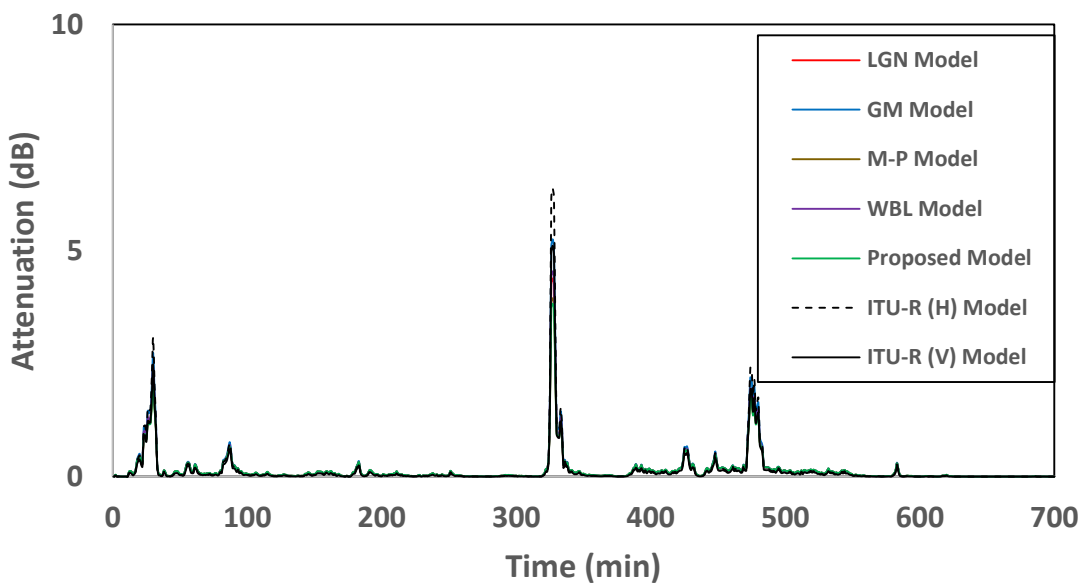


(b)

Figure 6-32: Rain rate and rain attenuation time series converted by: (a) SST (b) various models for a measured rainy event on 18/05/2015 at frequency  $f=8$  GHz and path length  $L=1$  km



(a)



(b)

Figure 6-33: Rain rate and rain attenuation time series converted by: (a) SST (b) various models for a measured rainy event on 18/05/2015 at frequency  $f=8$  GHz and path length  $L=5$  km

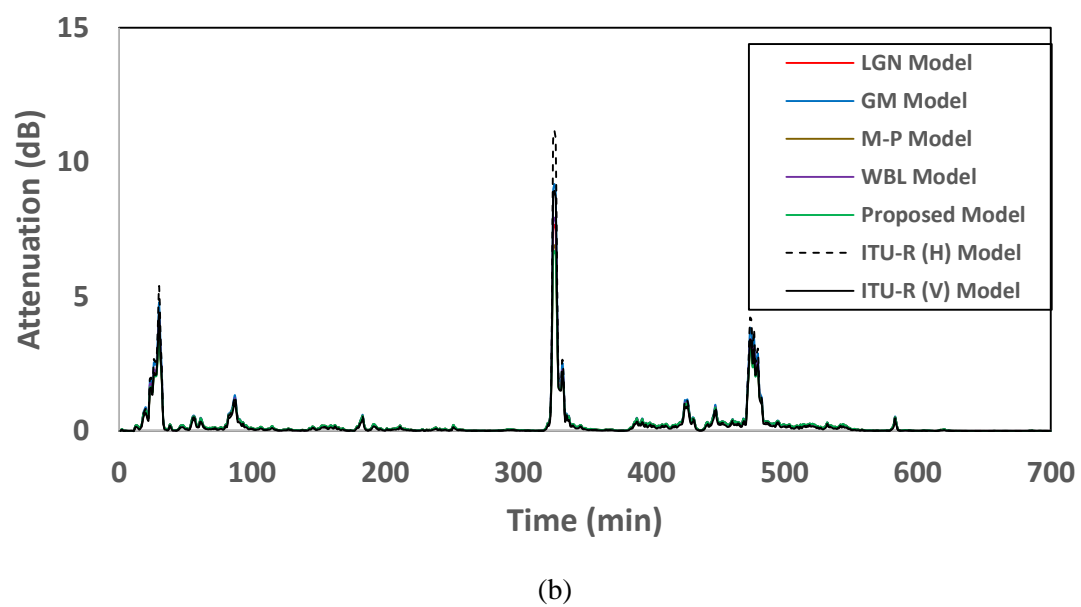
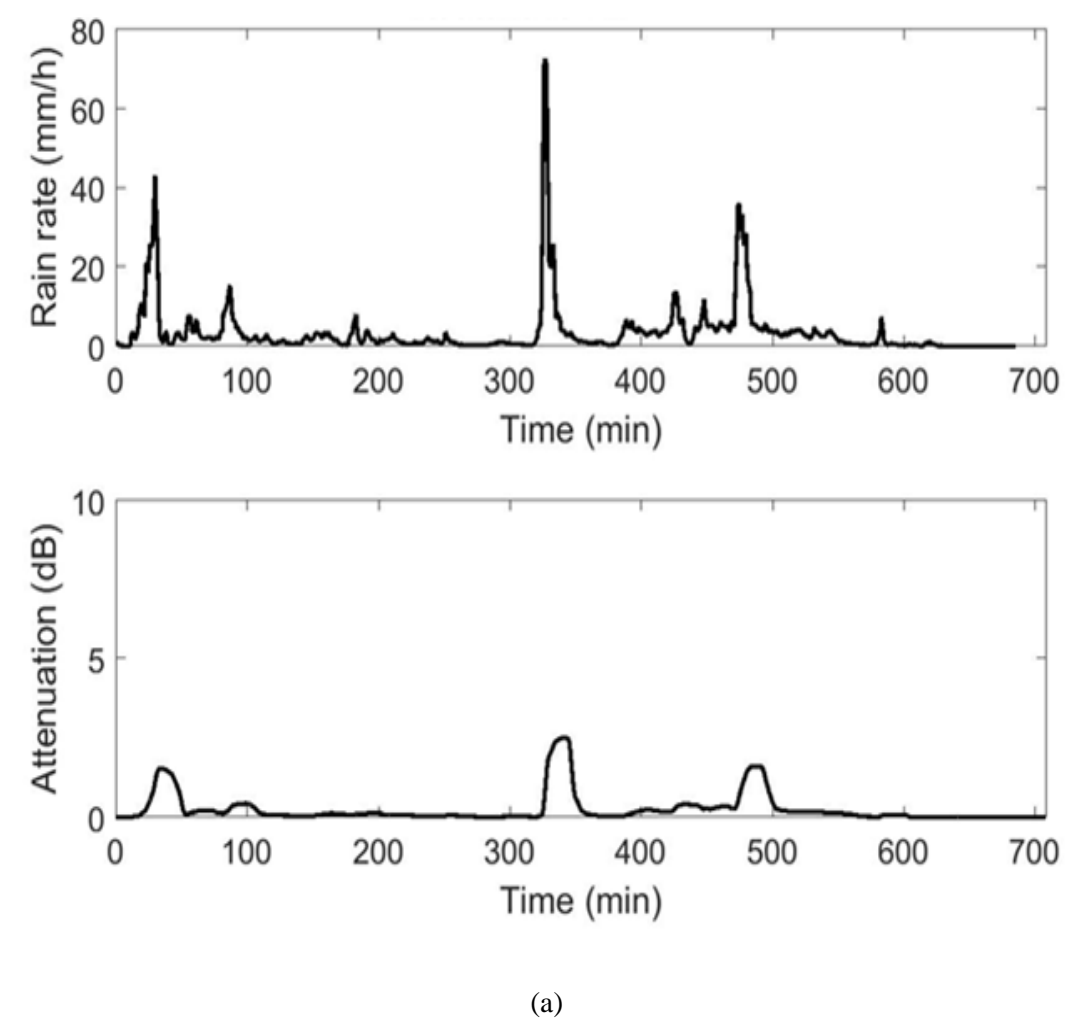


Figure 6-34: Rain rate and rain attenuation time series converted by: (a) SST (b) various models for a measured rainy event on 18/05/2015 at frequency  $f=8$  GHz and path length  $L=8$  km

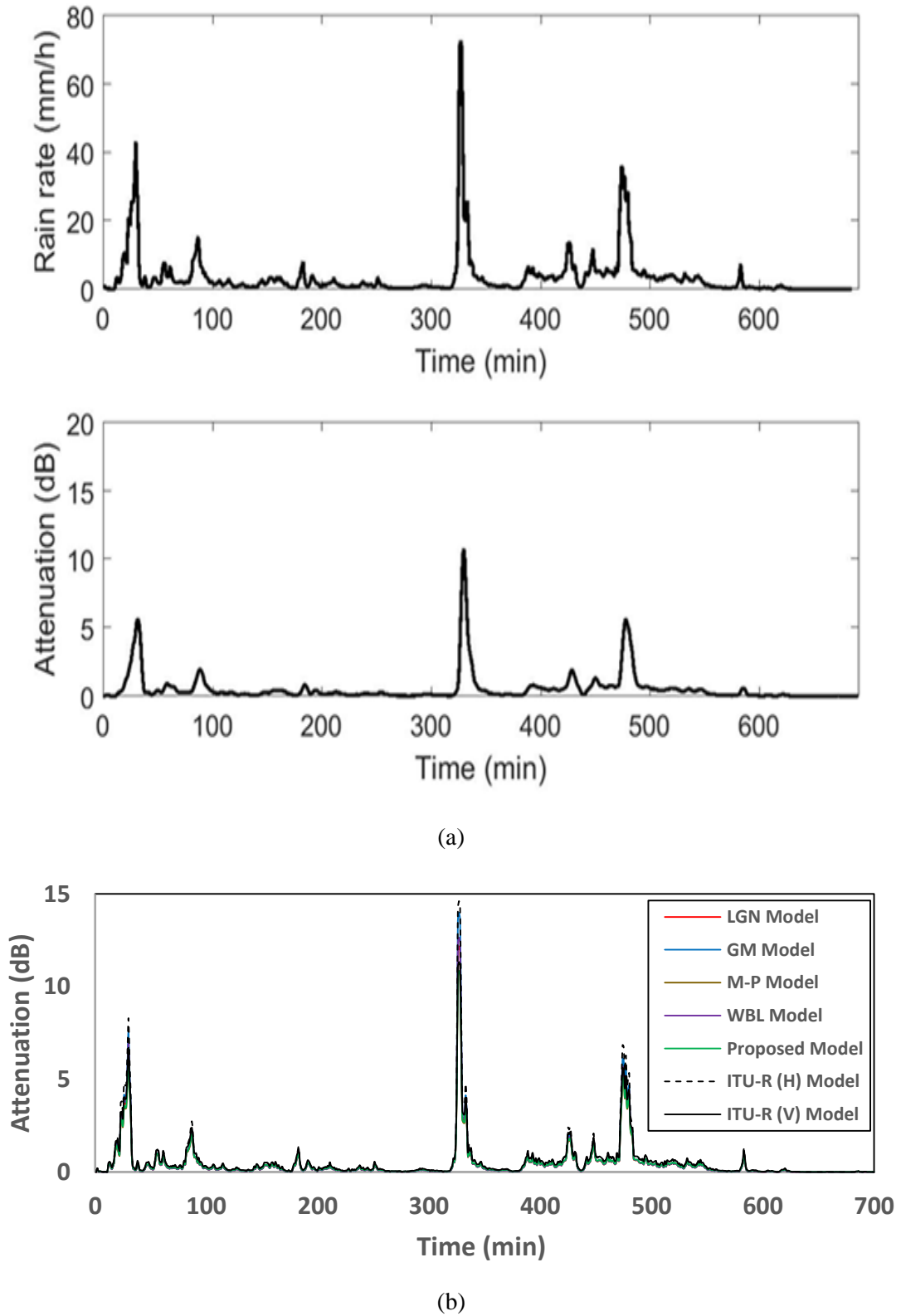
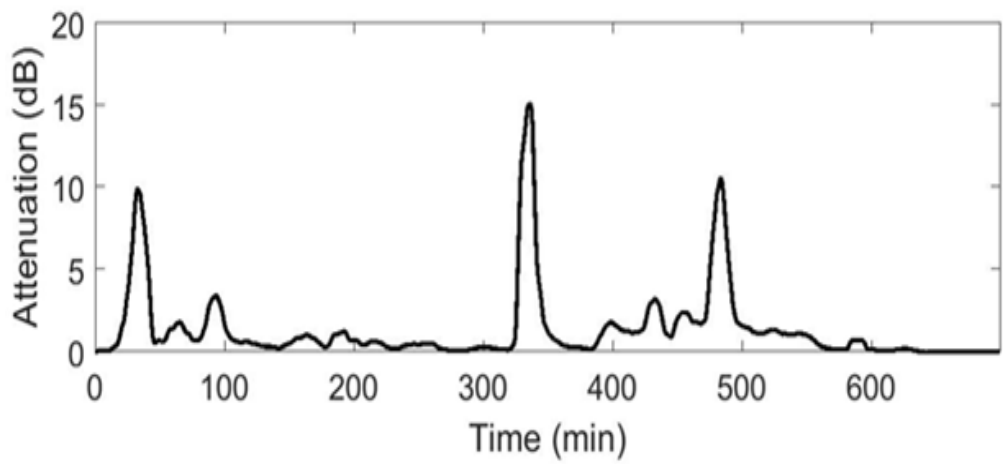
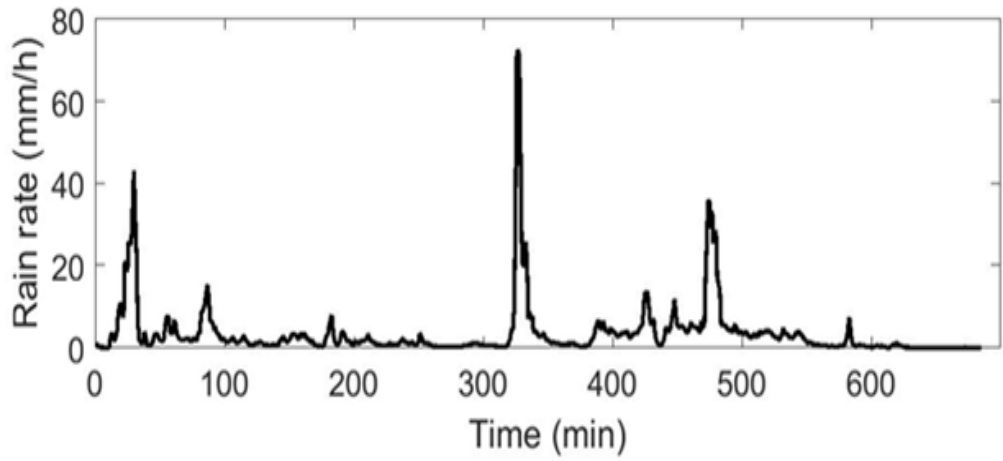
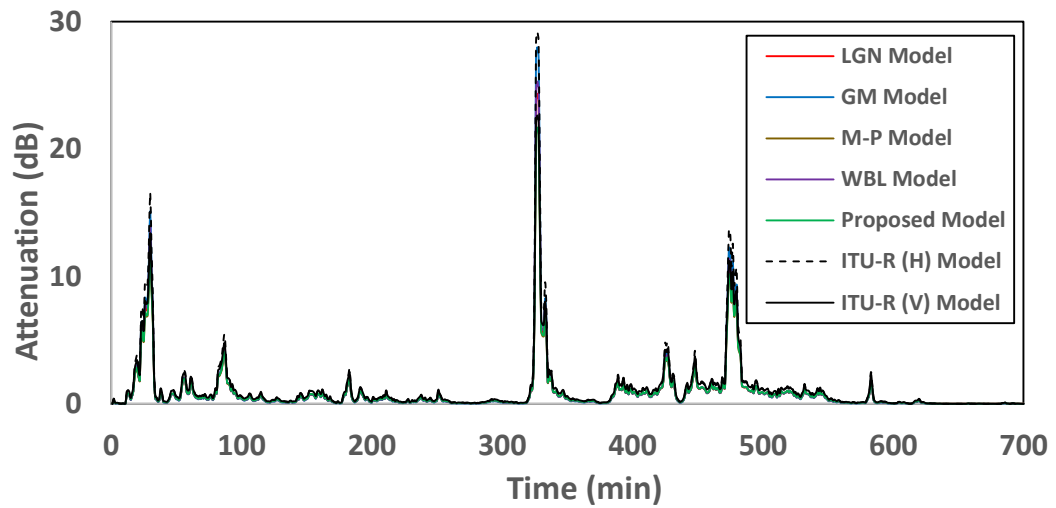


Figure 6-35: Rain rate and rain attenuation time series converted by: (a) SST (b) various models for a measured rainy event on 18/05/2015 at frequency  $f=19$  GHz and path length  $L=2$  km

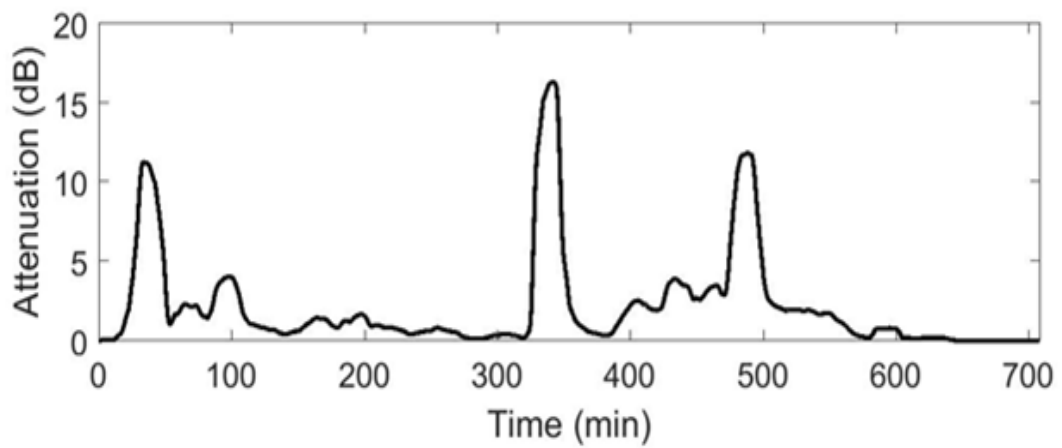
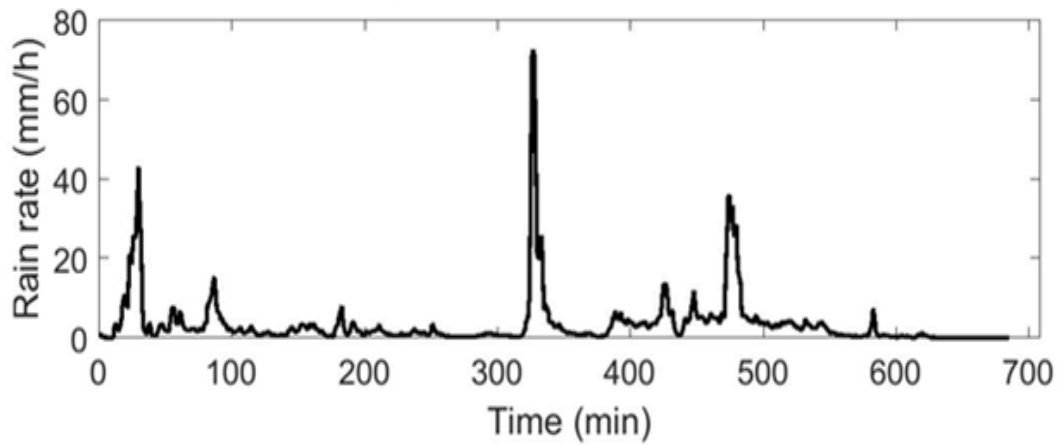


(a)

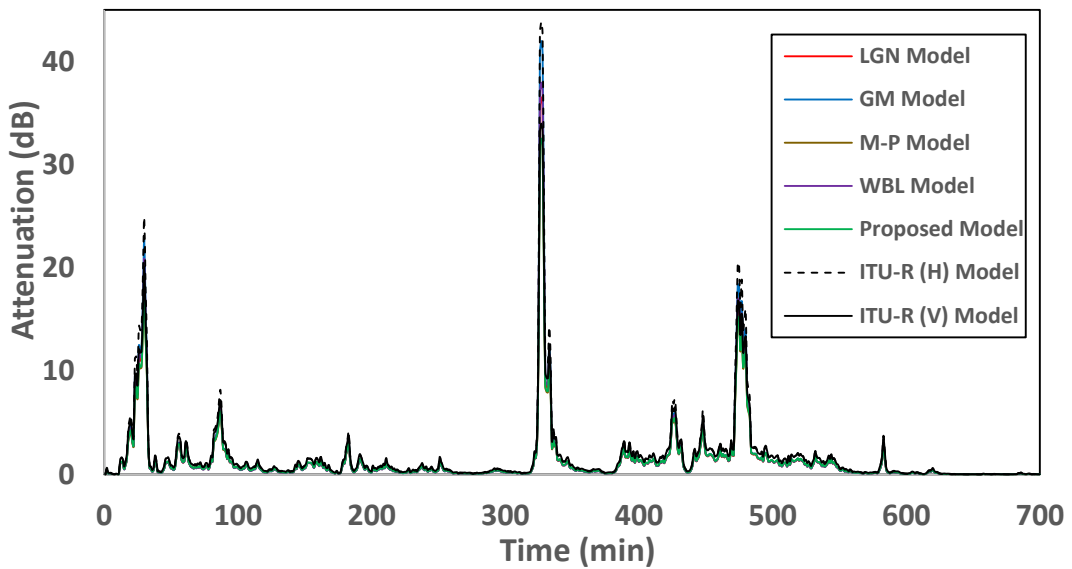


(b)

Figure 6-36: Rain rate and rain attenuation time series converted by: (a) SST (b) various models for a measured rainy event on 18/05/2015 at frequency  $f=19$  GHz and path length  $L=5$  km



(a)



(b)

Figure 6-37: Rain rate and rain attenuation time series converted by: (a) SST (b) various models for a measured rainy event on 18/05/2015 at frequency  $f=19$  GHz and path length  $L=8$  km

The annual cumulative distribution of rainfall rate exceeded for different percentages of time using rainfall measurements obtained in Butare, Rwanda is plotted in Figure 6-38. While designing a microwave link, it is recommended by ITU-R to get 99.99% of system availability; therefore the rainfall rate ( $R_{0.01}$ ) exceeded for 0.01% of the time in the region of interest has to be determined. From the plots of Figure 6-38, the annual values of  $R_{0.01}$  are obtained as 74 mm/h, 92 mm/h and 87 mm/h for 2012, 2014 and 2015 respectively. (Note that there was not enough data for 2013).

The cumulative distribution of rain attenuation converted by SST and other rain attenuation models for different frequencies and path length are plotted in Figures 6-39 to 6-56. From the plots of Figure 6-39 to 6-56, it is shown that the ITU-R (H) model gives highest attenuation while the SST model gives the lowest attenuation.

In Figure 6-39 at frequency of 8 GHz and path length of 1 km over Butare, Rwanda in 2012, the estimated

fade margin to be implemented as recommended by ITU-R to get 99.99% of link availability is between 0.94 dB and 1.635 dB, where SST model prediction gives 0.94 dB, while we have 1.119 dB, 1.342 dB, 1.007 dB, 1.158 dB, 0.976 dB, 1.635 dB, 1.309 dB for Lognormal, Modified Gamma, Marshall-Palmer, ITU-R (H) and ITU-R (V) models, respectively.

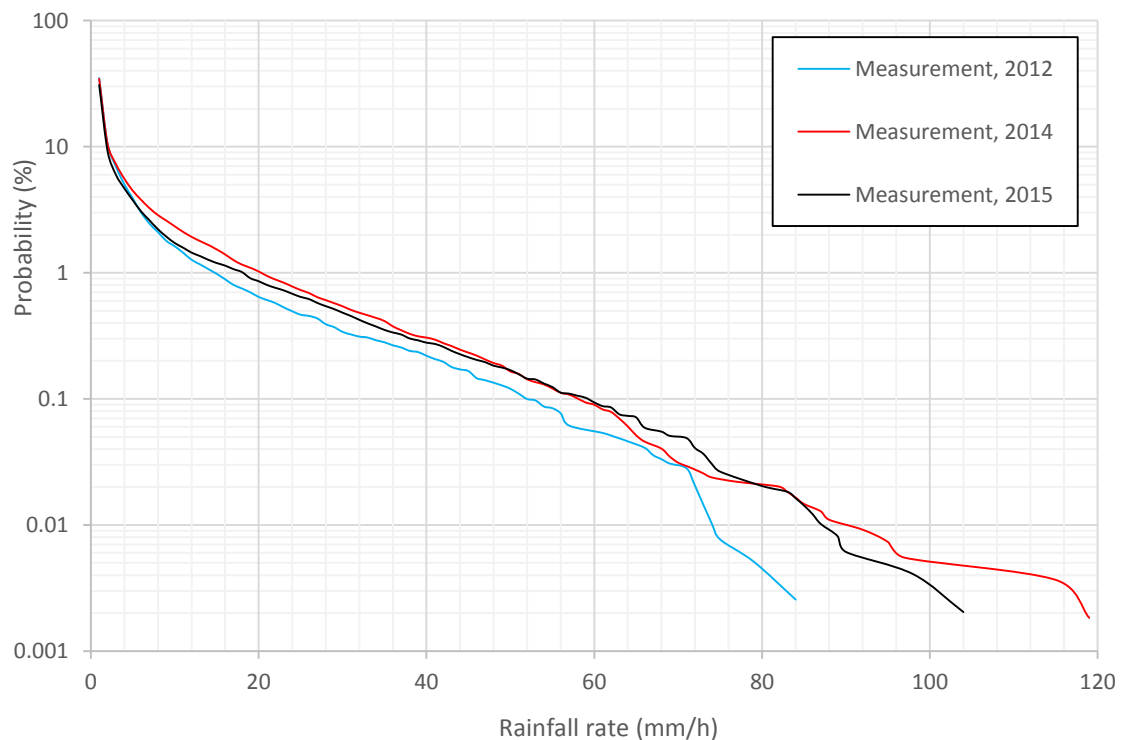


Figure 6-38: Annual rainfall rate distribution in Butare, Rwanda in 2012, 2014 and 2015



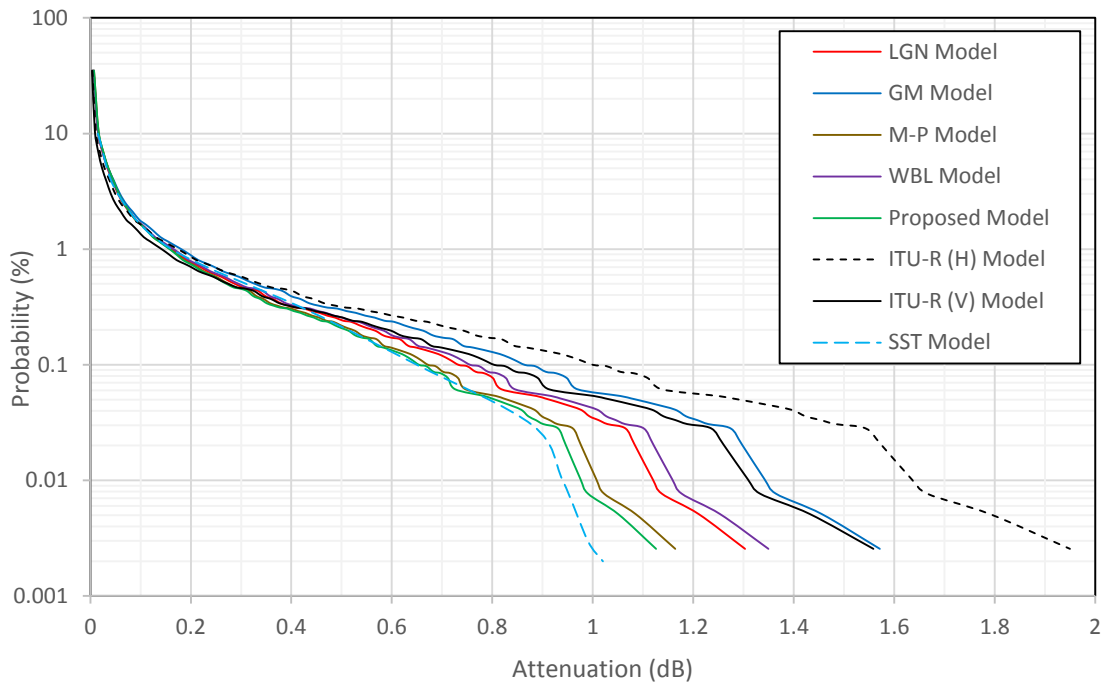


Figure 6-39: Comparison between synthesized rain attenuation converted by SST and other rain attenuation models at frequency  $f=8$  GHz and path length  $L=1$  km over Butare, Rwanda in 2012.

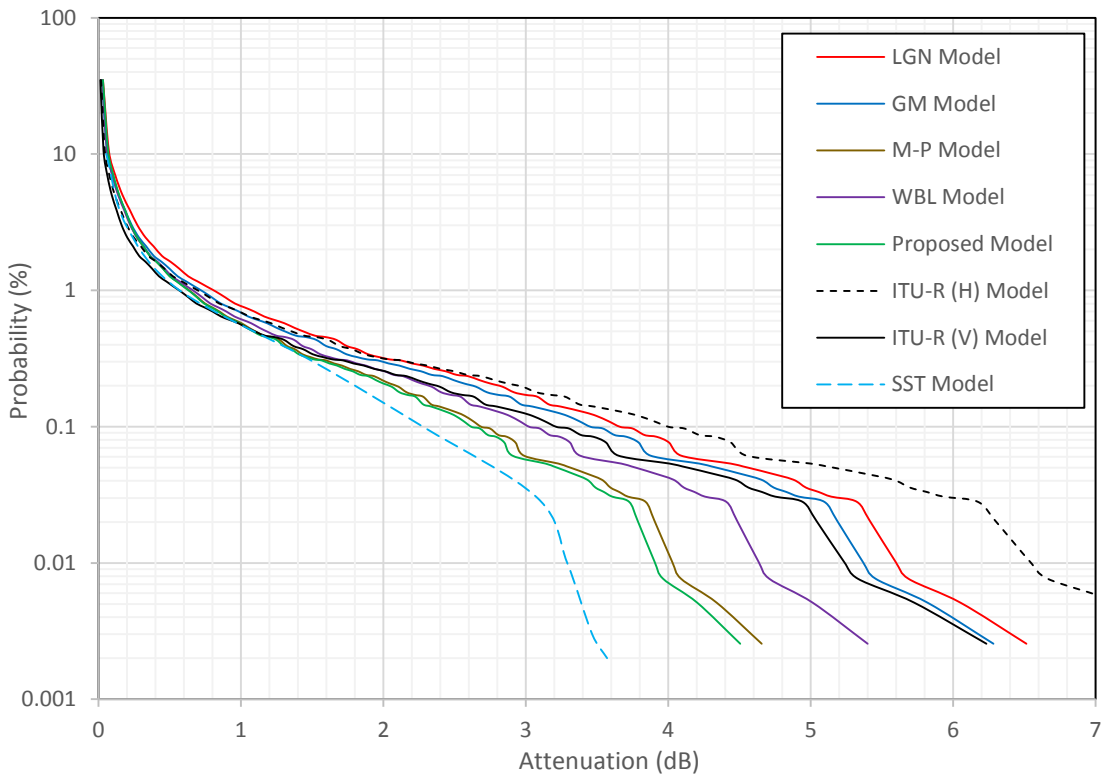


Figure 6-40: Comparison between synthesized rain attenuation converted by SST and other rain attenuation models at frequency  $f=8$  GHz and path length  $L=5$  km over Butare, Rwanda in 2012.

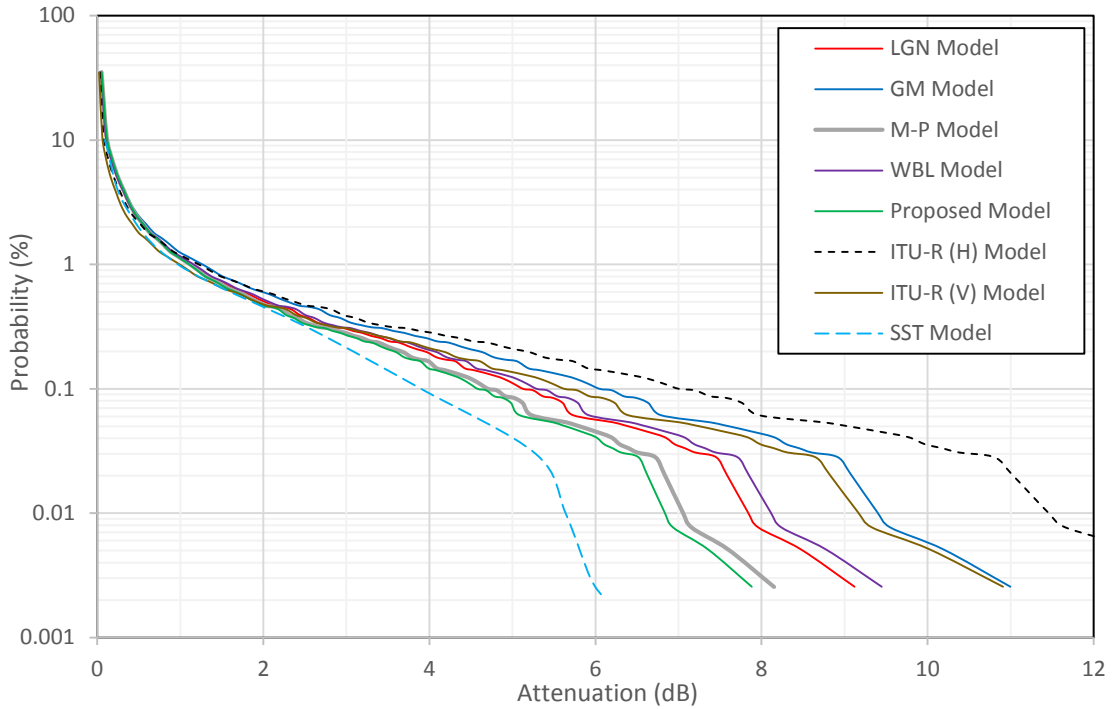


Figure 6-41: Comparison between synthesized rain attenuation converted by SST and other rain attenuation models at frequency  $f=8$  GHz and path length  $L=8$  km over Butare, Rwanda in 2012.

In Figure 6-40 at 8 GHz and path length of 5 km, for 99.99% link availability, the estimated fade margin varies between 3.29 dB and 6.54 dB, where the SST model prediction gives 3.29 dB and we get 5.596 dB, 5.367 dB, 4.028 dB, 4.633 dB, 3.903 dB, 6.540 dB, 5.235 dB for Lognormal, Modified Gamma, Marshall-Palmer, Weibull, Proposed model, ITU-R (H) and ITU-R (V) models, respectively. In Figure 6-41 at 8 GHz and path length of 8 km, for 99.99% link availability, the estimated fade margin varies between 5.64 dB and 11.446 dB, with the SST model prediction giving 5.64 dB, while we have 7.834 dB, 9.392 dB, 7.049 dB, 8.108 dB, 6.830 dB, 11.446 dB, and 9.160 dB for the Lognormal, Modified Gamma, Marshall-Palmer, Weibull, Proposed model, ITU-R (H) and ITU-R (V) models, respectively.

Figures 6-42 to 6-44 present the cumulative distribution of the rain attenuation using SST model and other rain attenuation models at 19 GHz for path length of 2 km, 5 km and 8 km respectively. From the plots, it is shown that the ITU-R (H) model gives highest attenuation while the SST model gives the lowest attenuation.

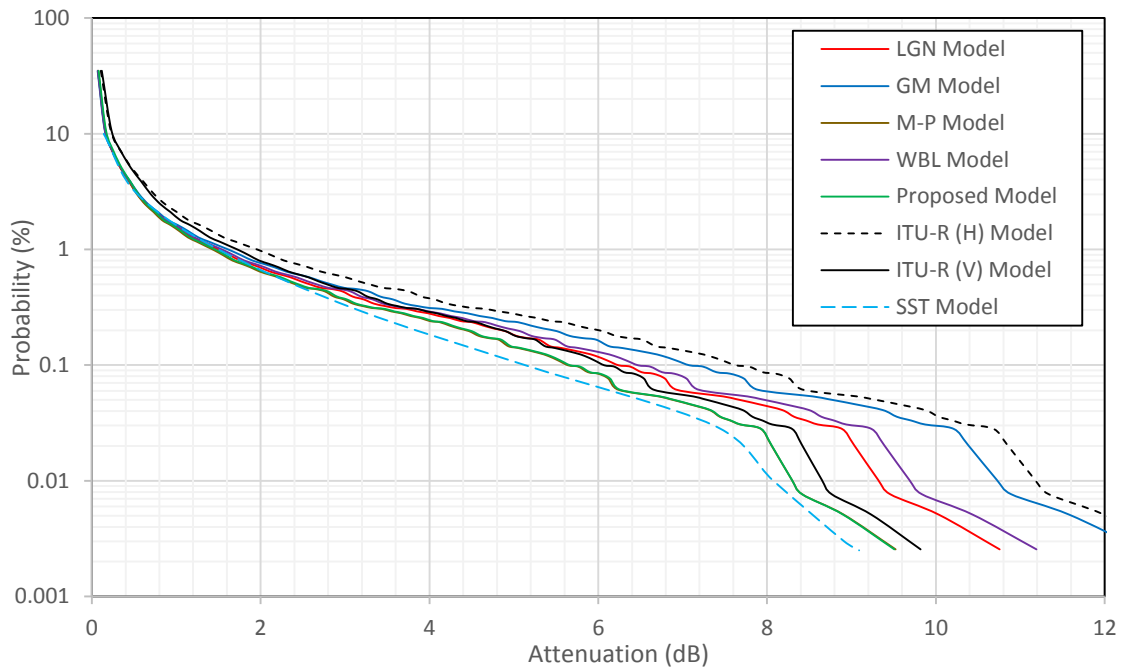


Figure 6-42: Comparison between synthesized rain attenuation converted by SST and other rain attenuation models at frequency  $f=19$  GHz and path length  $L=2$  km over Butare, Rwanda in 2012.

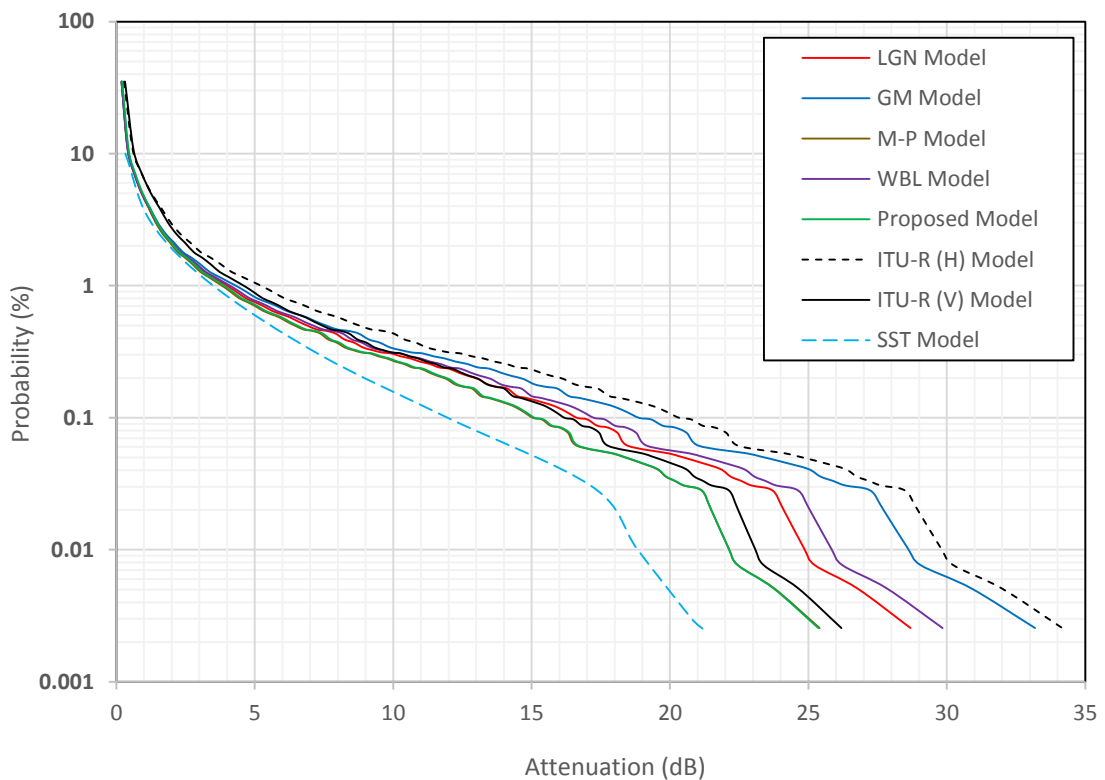


Figure 6-43: Comparison between synthesized rain attenuation converted by SST and other rain attenuation models at frequency  $f=19$  GHz and path length  $L=5$  km over Butare, Rwanda in 2012.

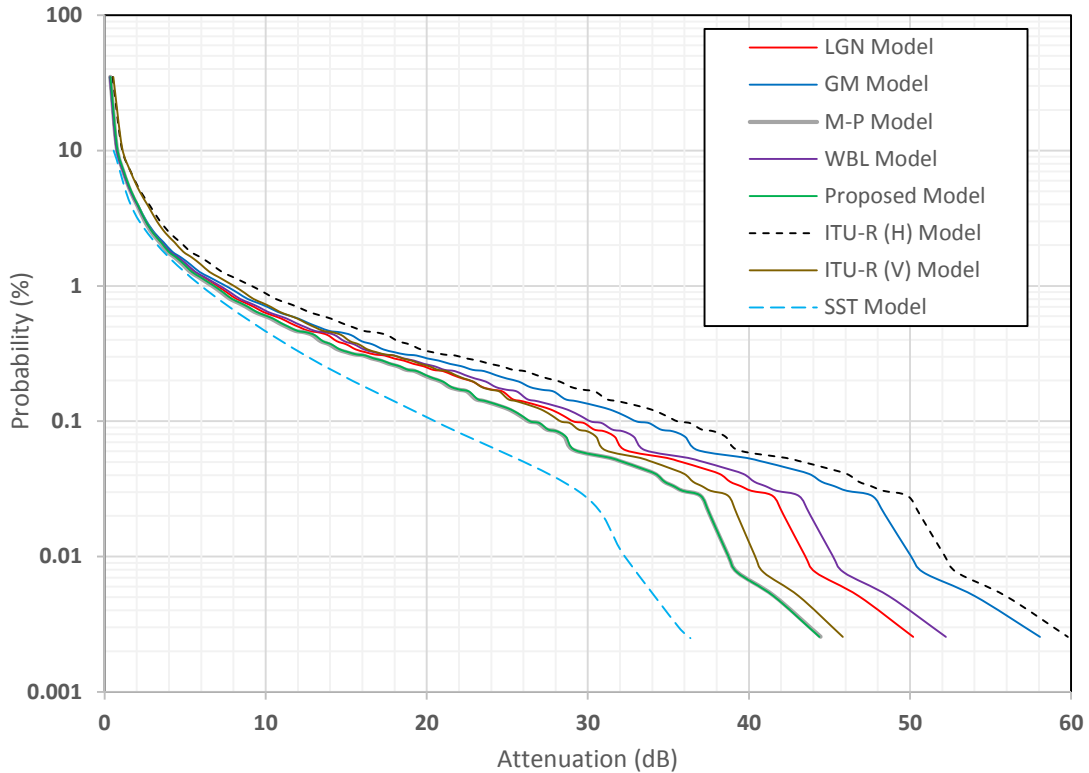


Figure 6-44: Comparison between synthesized rain attenuation converted by SST and other rain attenuation models at frequency  $f=19$  GHz and path length  $L=8$  km over Butare, Rwanda in 2012.

In Figure 6-42 at 19 GHz and path length of 2 km in 2012, the estimated rain attenuation exceedance values at 0.01% of the time (99.99% of link availability) are between 8.073 dB and 11.172 dB, where the SST model prediction gives 8.073 dB, while the other values are 9.316 dB, 10.72 dB, 8.294 dB, 9.682 dB, 8.293 dB, 11.172 dB, 8.648 dB for the Lognormal, Modified Gamma, Marshall-Palmer, Weibull, Proposed model, ITU-R (H) and ITU-R (V) models, respectively.

In Figure 6-43 at 19 GHz and path length of 5 km over Butare in 2012, the corresponding attenuation values for 99.99% of link availability are between 18.837 dB and 29.7924 dB, with the SST model prediction giving 18.83 dB, while we have 24.84 dB, 28.58 dB, 22.12 dB, 25.82 dB, 22.11 dB, 29.79 dB, and 23.06 dB for the Lognormal, Modified Gamma, Marshall-Palmer, Weibull, Proposed model, ITU-R (H) and ITU-R (V) models, respectively.

In Figure 6-44 at 19 GHz and path length of 8 km for 99.99% of link availability, the estimated fade margin varies between 32.29 dB and 52.14 dB, with the SST model giving 32.29 dB, while we get 43.47 dB, 50.03 dB, 38.71 dB, 45.19 dB, 30.7 dB, 52.14 dB, and 40.35 dB for the Lognormal, Modified Gamma, Marshall-Palmer, Weibull, Proposed model, ITU-R (H) and ITU-R (V) models, respectively.

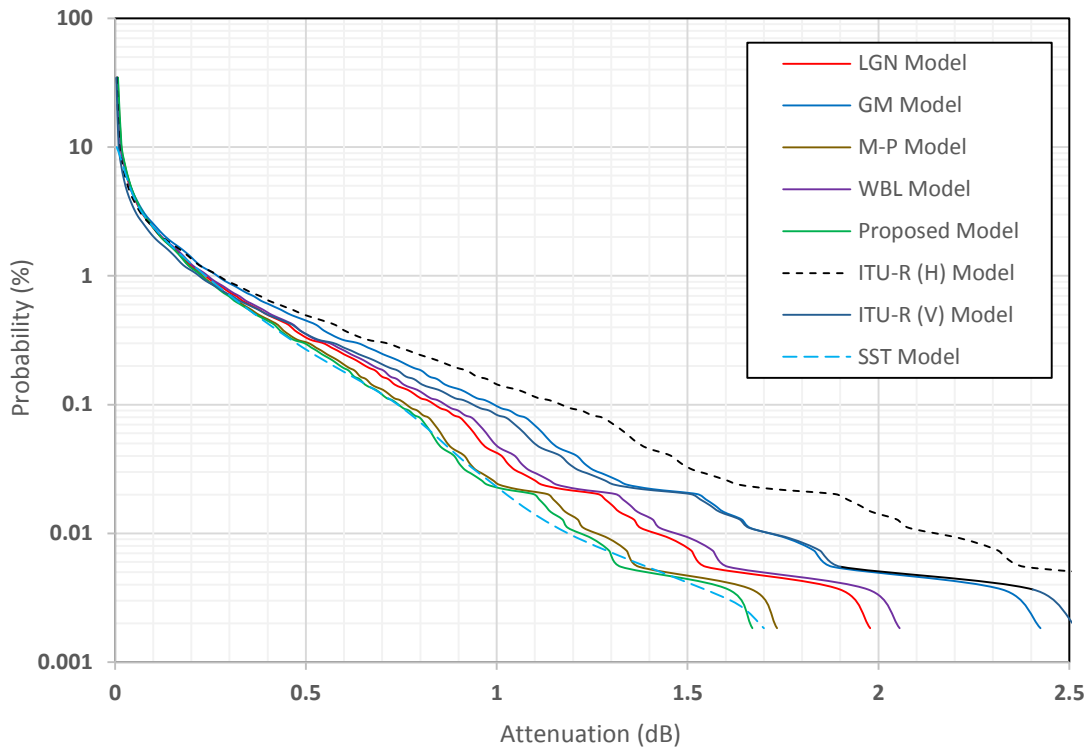


Figure 6-45: Comparison between synthesized rain attenuation converted by SST and other rain attenuation models at frequency  $f=8$  GHz and path length  $L=1$  km over Butare, Rwanda in 2014.

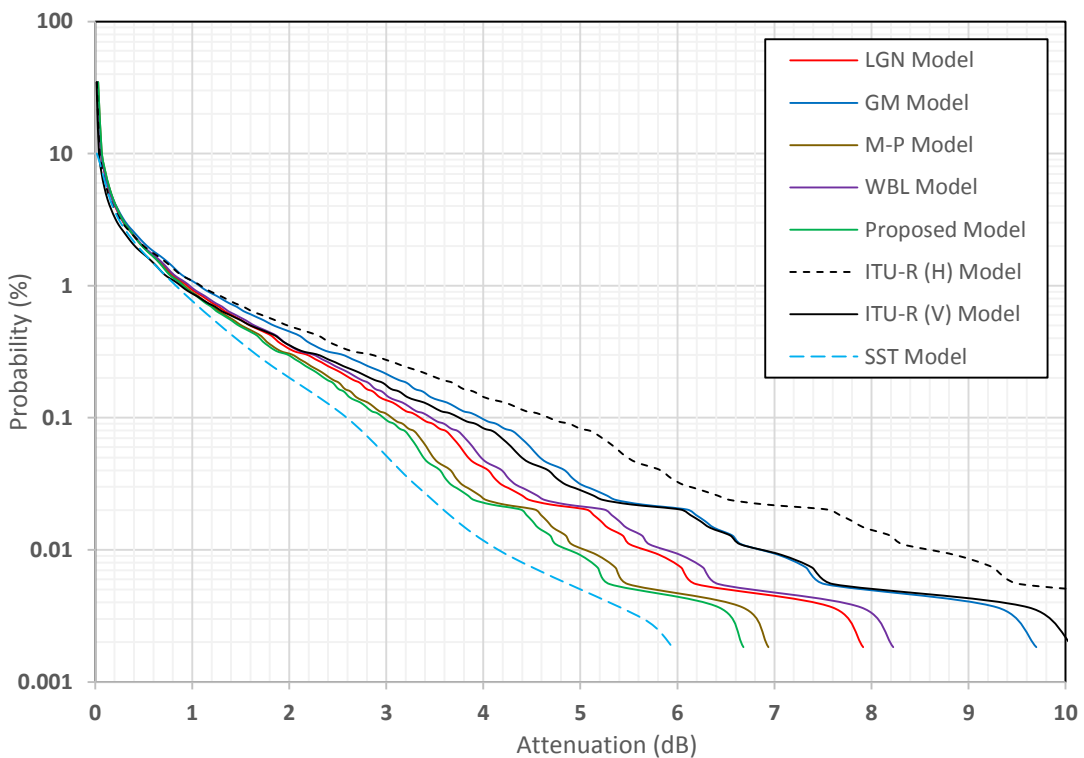


Figure 6-46: Comparison between synthesized rain attenuation converted by SST and other rain attenuation models at frequency  $f= 8$  GHz and path length  $L=5$  km over Butare, Rwanda in 2014.

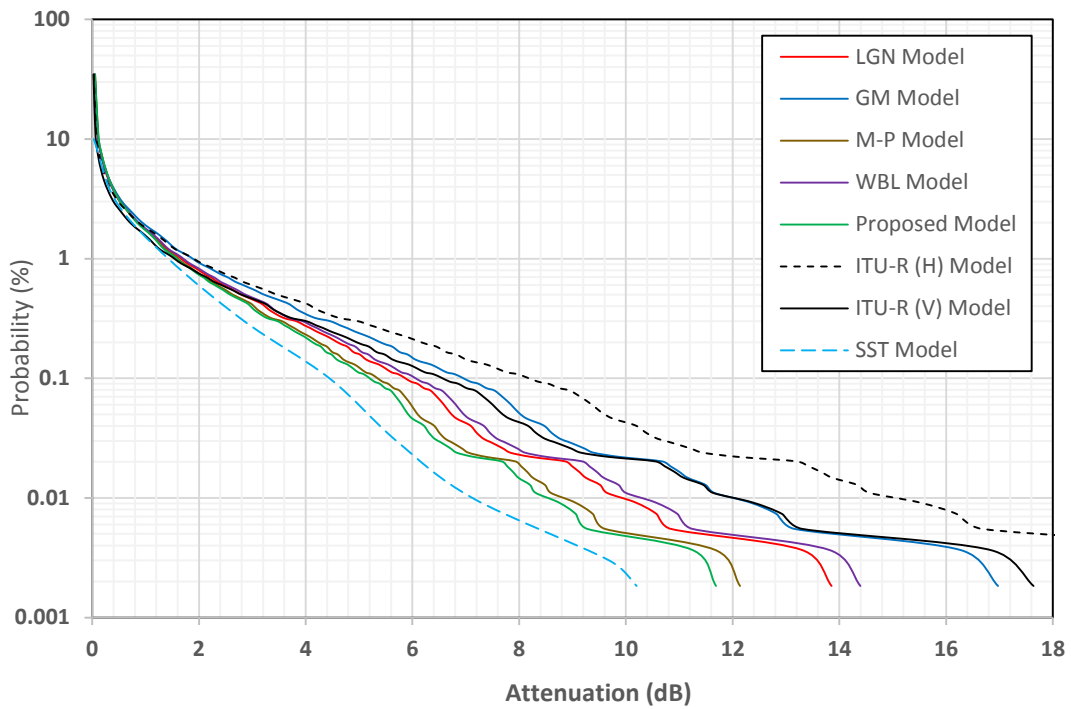


Figure 6-47: Comparison between synthesized rain attenuation converted by SST and other rain attenuation models at frequency  $f=8$  GHz and path length  $L=8$  km over Butare, Rwanda in 2014

Figures 6-45 to 6-47 present the cumulative distribution of the rain attenuation using SST model and other rain attenuation models at 8 GHz and path lengths of 1 km, 5 km and 8 km respectively. From the plots, it is again shown that the ITU-R (H) model gives highest attenuation while the SST model gives the lowest attenuation.

In Figure 6-45 at 8 GHz and path length of 1 km in 2014, the estimated model values for 99.99% link availability, the attenuation due to rain exceeded is between 1.188 dB and 2.081 dB, with SST model prediction giving 1.19 dB while we get 1.67 dB, 1.23 dB, 1.43 dB, 1.19 dB, 2.08 dB, 1.66 dB, 8.648 dB for Lognormal, Modified Gamma, Marshall-Palmer, Weibull, Proposed model, ITU-R (H) and ITU-R (V) models, respectively.

In Figure 6-46 at 8 GHz and path length of 5 km in 2014, the estimated rain attenuation exceedance values at 0.01% of the time are between 4.16 dB and 8.32 dB, where the SST model prediction gives 4.16 dB, while the other values are 5.51 dB, 6.66 dB, 4.91 dB, 5.71 dB, 4.75 dB, 8.32 dB, 6.65 dB for the Lognormal, Modified Gamma, Marshall-Palmer, Weibull, Proposed model, ITU-R (H) and ITU-R (V) models, respectively.

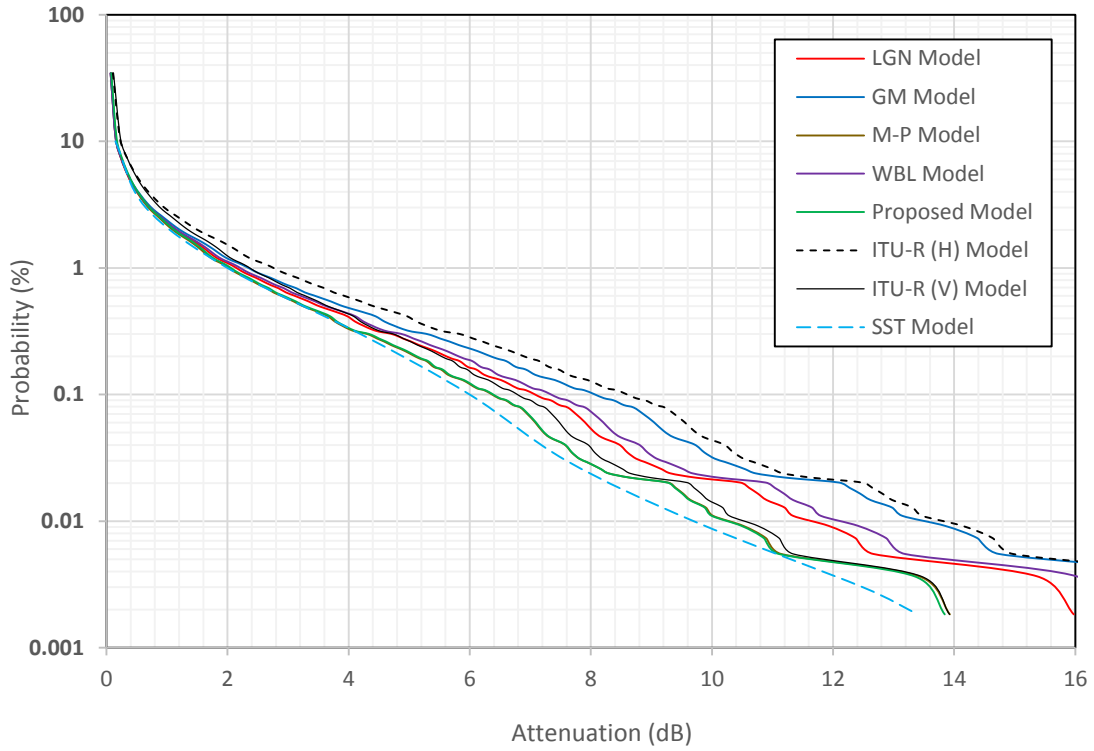


Figure 6-48: Comparison between synthesized rain attenuation converted by SST and other rain attenuation models at frequency  $f=19$  GHz and path length  $L=2$  km over Butare, Rwanda in 2014.

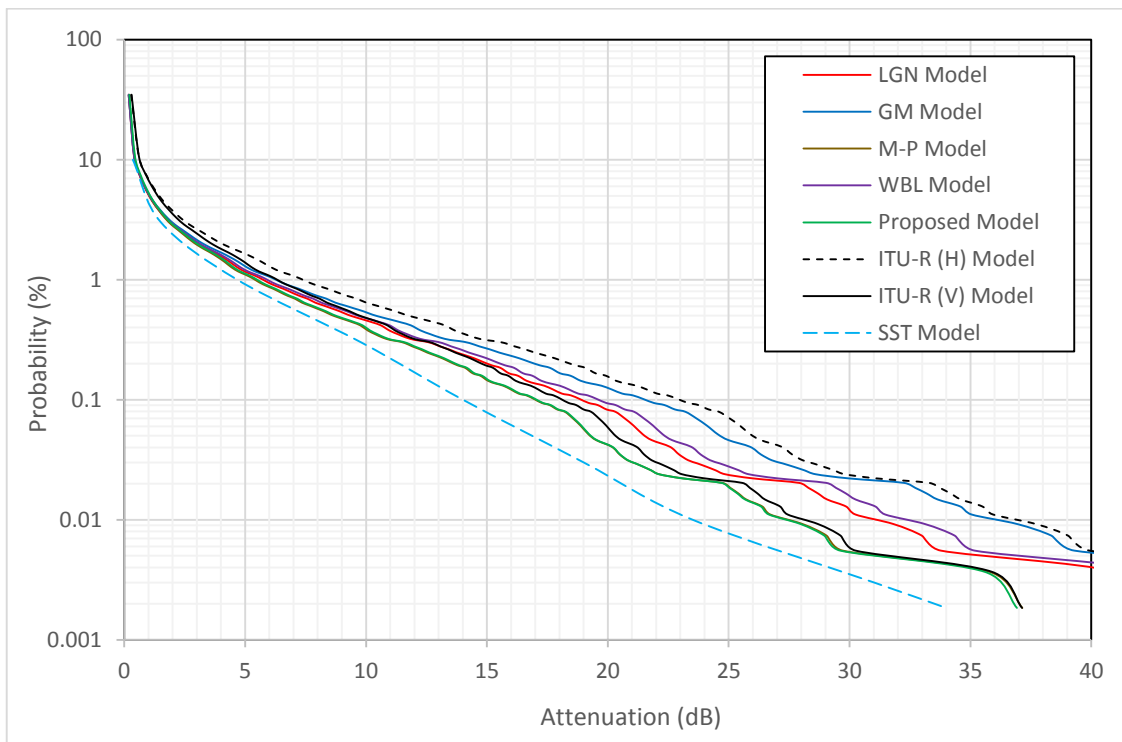


Figure 6-49: Comparison between synthesized rain attenuation converted by SST and other rain attenuation models at frequency  $f=19$  GHz and path length  $L=5$  km over Butare, Rwanda in 2014.

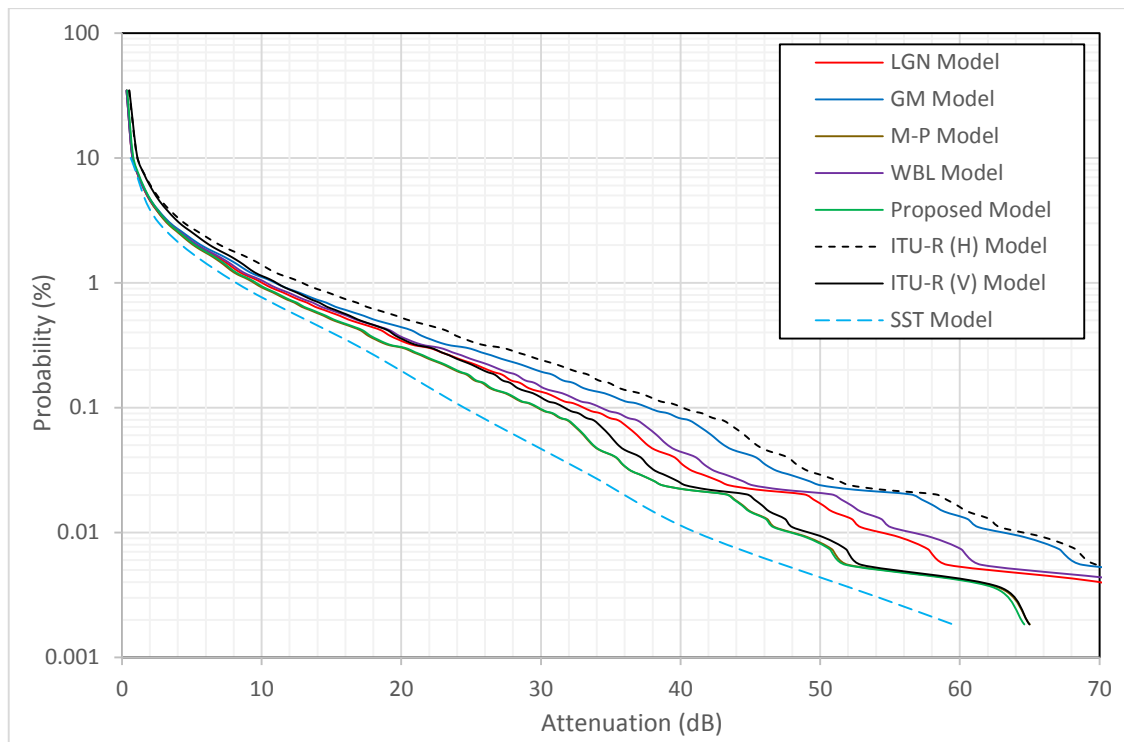


Figure 6-50: Comparison between synthesized rain attenuation converted by SST and other rain attenuation models at frequency  $f=19$  GHz and path length  $L=8$  km over Butare, Rwanda in 2014

In Figure 6-47 at 8 GHz and path length of 8 km in 2014, the corresponding attenuation values for 99.99% of link availability are between 7.13 dB and 14.56 dB, with the SST model prediction giving 7.13 dB, while we have 9.64 dB, 11.65 dB, 8.6 dB, 10.0 dB, 8.31 dB, 14.56 dB, and 11.63 dB for the Lognormal, Modified Gamma, Marshall-Palmer, Weibull, Proposed model, ITU-R (H) and ITU-R (V) models, respectively

Figures 6-48 to 6-50 present the cumulative distribution of the rain attenuation using SST model and other rain attenuation models at 19 GHz and path lengths of 2 km, 5 km and 8 km, respectively. From the plots, it is again shown that the ITU-R (H) model gives highest attenuation while the SST model gives the lowest attenuation.

In Figure 6-48 at 19 GHz and path length of 2 km in 2014, the estimated rain attenuation exceedance values at 0.01% of the time (99.99% of link availability) are between 9.7 dB and 13.47 dB, where the SST model prediction gives 9.7dB, while the other values are 11.34 dB, 13.14 dB, 10.02 dB, 11.80 dB, 9.99 dB, 13.47 dB, 10.29 dB for the Lognormal, Modified Gamma, Marshall-Palmer, Weibull, Proposed model, ITU-R (H) and ITU-R (V) models, respectively.



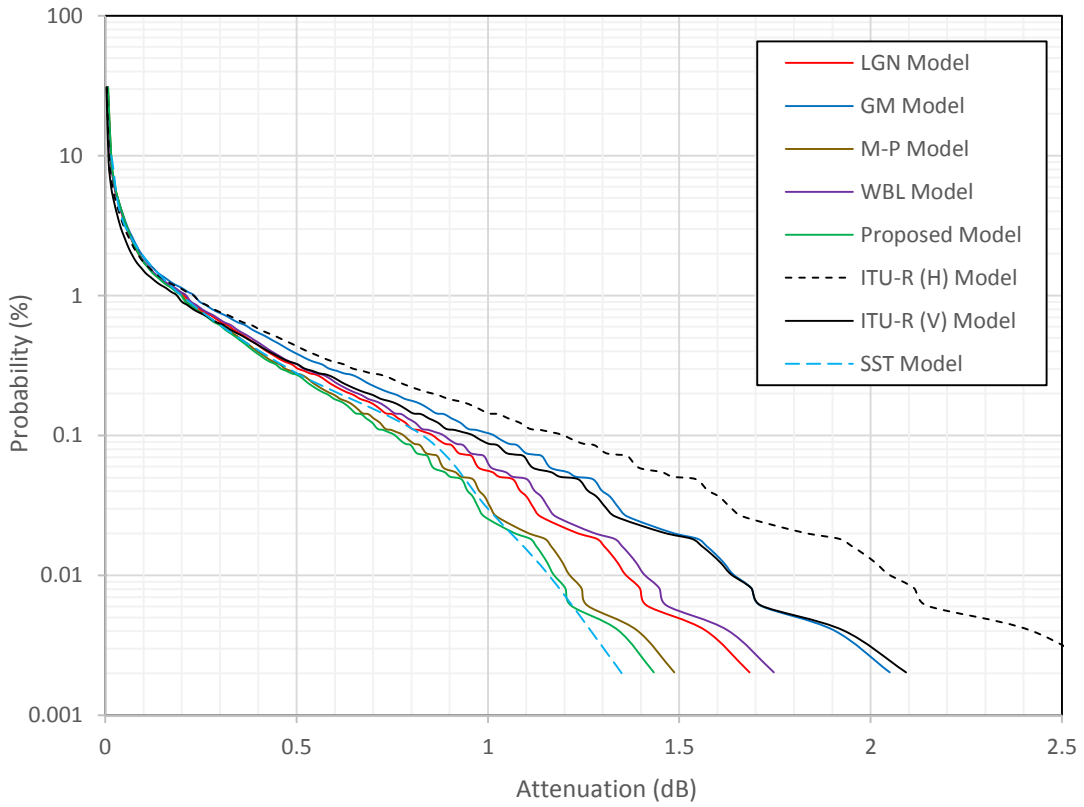


Figure 6-51: Comparison between synthesized rain attenuation converted by SST (a) and other rain attenuation models (b) at frequency  $f=8$  GHz and path length  $L=1$  km over Butare, Rwanda in 2015.

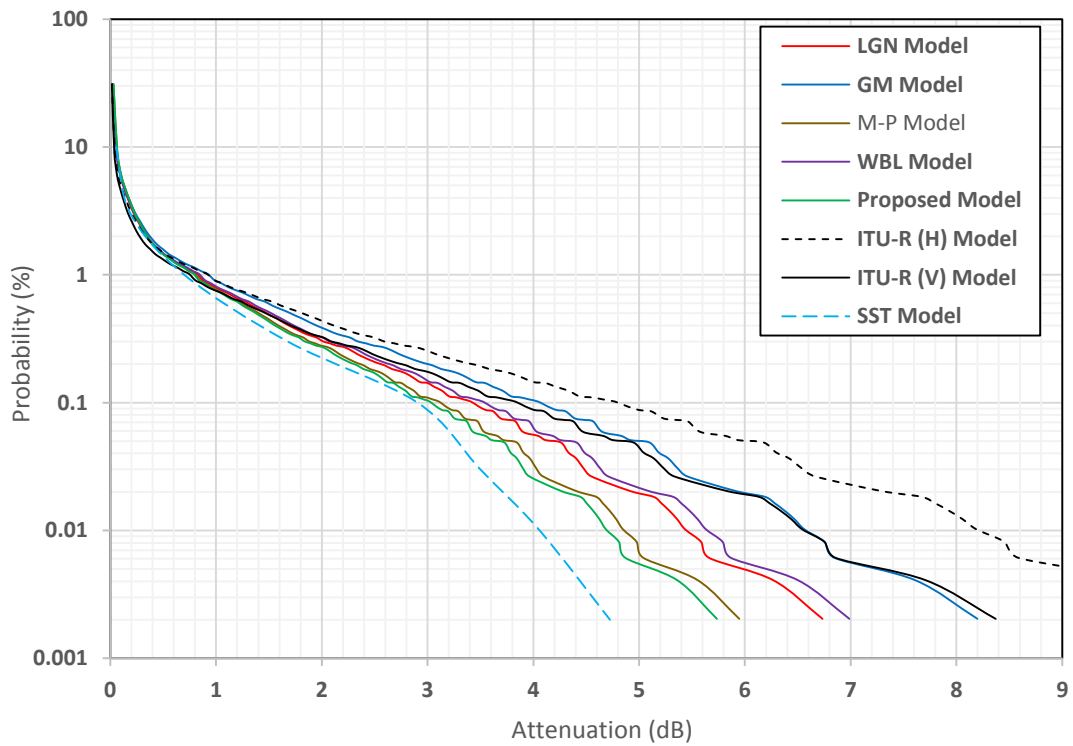


Figure 6-52: Comparison between synthesized rain attenuation converted by SST and other rain attenuation models at frequency  $f=8$  GHz and path length  $L=5$  km over Butare, Rwanda in 2015.

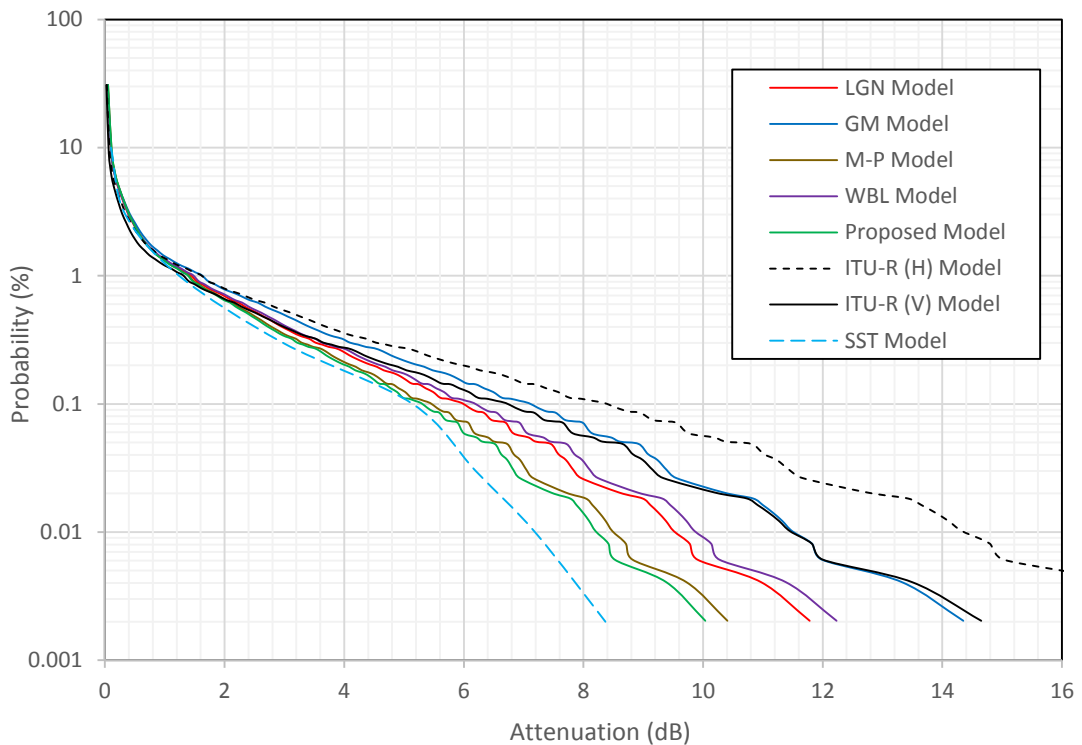


Figure 6-53: Comparison between synthesized rain attenuation converted by SST and other rain attenuation models at frequency  $f=8$  GHz and path length  $L=8$  km over Butare, Rwanda in 2015

In Figure 6-49 at 19 GHz and path length of 5 km over Butare in 2014, the corresponding attenuation values for 99.99% of link availability are between 22.63 dB and 35.93 dB, with the SST model prediction giving 22.63 dB, while we have 30.24 dB, 35.05 dB, 26.72 dB, 31.47 dB, 26.66 dB, 35.93 dB, and 27.44 dB for the Lognormal, Modified Gamma, Marshall-Palmer, Weibull, Proposed model, ITU-R (H) and ITU-R (V) models, respectively.

In Figure 6-50 at 19 GHz and path length of 8 km for 99.99% of link availability, the estimated fade margin varies between 41.13 dB and 62.88 dB, with the SST model giving 41.12 dB, while we get 52.92 dB, 61.33 dB, 46.77 dB, 55.07 dB, 46.66 dB, 62.88 dB, and 48.02 dB for the Lognormal, Modified Gamma, Marshall-Palmer, Weibull, Proposed model, ITU-R (H) and ITU-R (V) models, respectively.

Figures 6-51 to 6-53 present the cumulative distribution of the rain attenuation using SST model and other rain attenuation models at 8 GHz for path lengths of 1 km, 5 km and 8 km respectively.

From the plots, it is shown that the ITU-R (H) model gives highest attenuation while the SST model gives the lowest attenuation.

In Figure 6-51 at 8 GHz and path length of 1 km in 2015, the estimated rain attenuation exceedance values at 0.01% of the time (99.99% of link availability) are between 1.16 dB and 2.04dB, where the SST model prediction gives 1.16 dB, while the other values are 1.35 dB, 1.64 dB, 1.21 dB, 1.41 dB, 1.17 dB, 2.04 dB, 1.64 dB for the Lognormal, Modified Gamma, Marshall-Palmer, Weibull, Proposed model, ITU-R (H) and ITU-R (V) models, respectively.

In Figure 6-52 at 8GHz and path length of 5 km over Butare in 2015, the corresponding attenuation values for 99.99% of link availability are between 4.06 dB and 8.19 dB, with the SST model prediction giving 4.06 dB, while we have 5.43 dB, 6.56 dB, 4.85 dB, 5.63 dB, 4.68 dB, 8.19 dB, and 6.54 dB for the Lognormal, Modified Gamma, Marshall-Palmer, Weibull, Proposed model, ITU-R (H) and ITU-R (V) models, respectively.

In Figure 6-53 at 8 GHz and path length of 8Km for 99.99% of link availability, the estimated fade margin varies between 7.19 dB and 14.33 dB, with the SST model giving 7.19 dB, while we get 9.51 dB, 11.49 dB, 8.48 dB, 9.85 dB, 8.20 dB, 14.33 dB, and 11.45 dB for the Lognormal, Modified Gamma, Marshall-Palmer, Weibull, Proposed model, ITU-R (H) and ITU-R (V) models, respectively

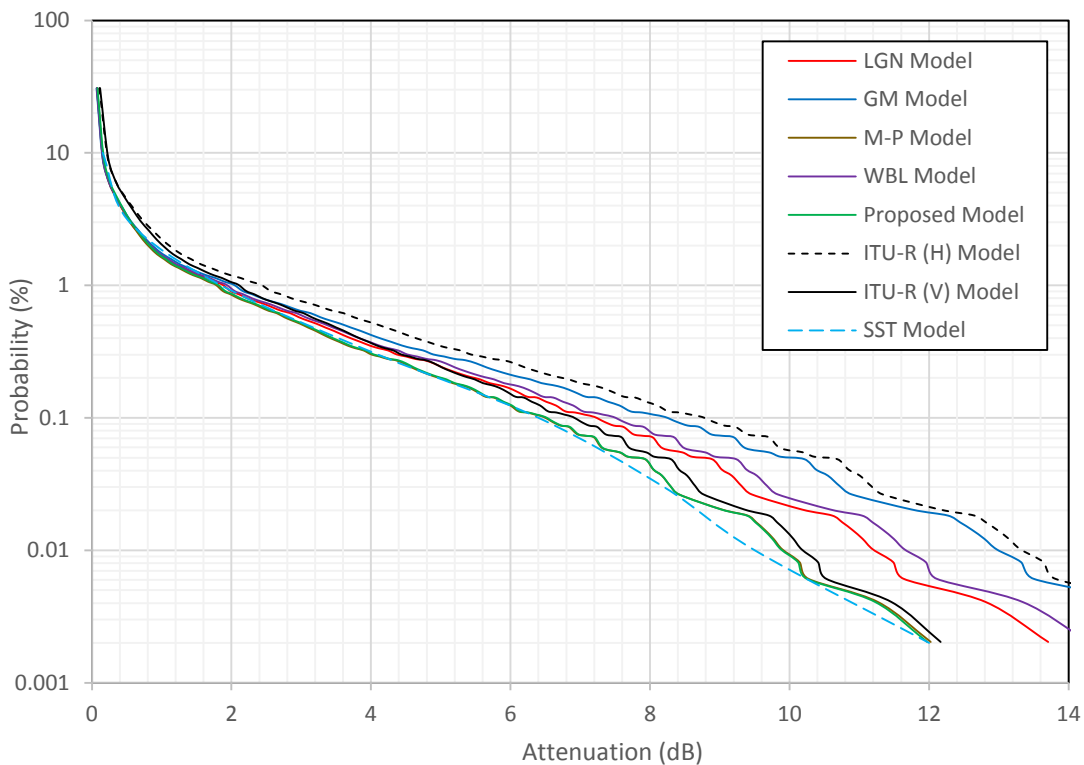


Figure 6-54: Comparison between synthesized rain attenuation converted by SST and other rain attenuation models at frequency  $f=19$  GHz and path length  $L=2$  km over Butare, Rwanda in 2015.

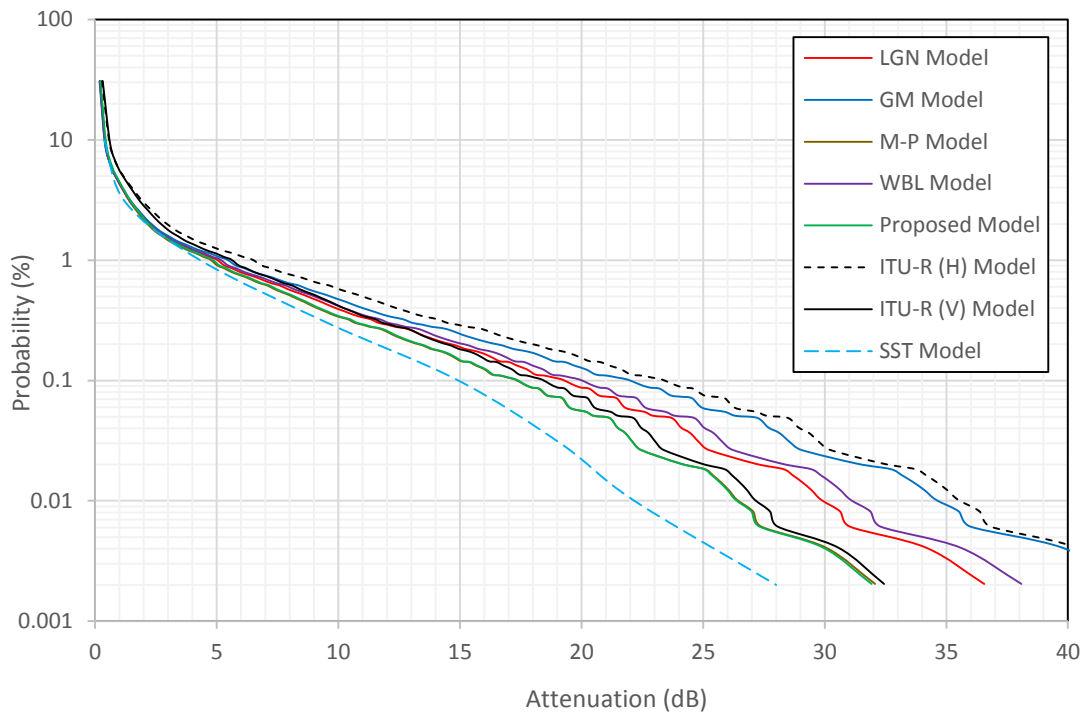


Figure 6-55: Comparison between synthesized rain attenuation converted by SST (a) and other rain attenuation models (b) at frequency  $f=19$  GHz and path length  $L=5$  km over Butare, Rwanda in 2015.

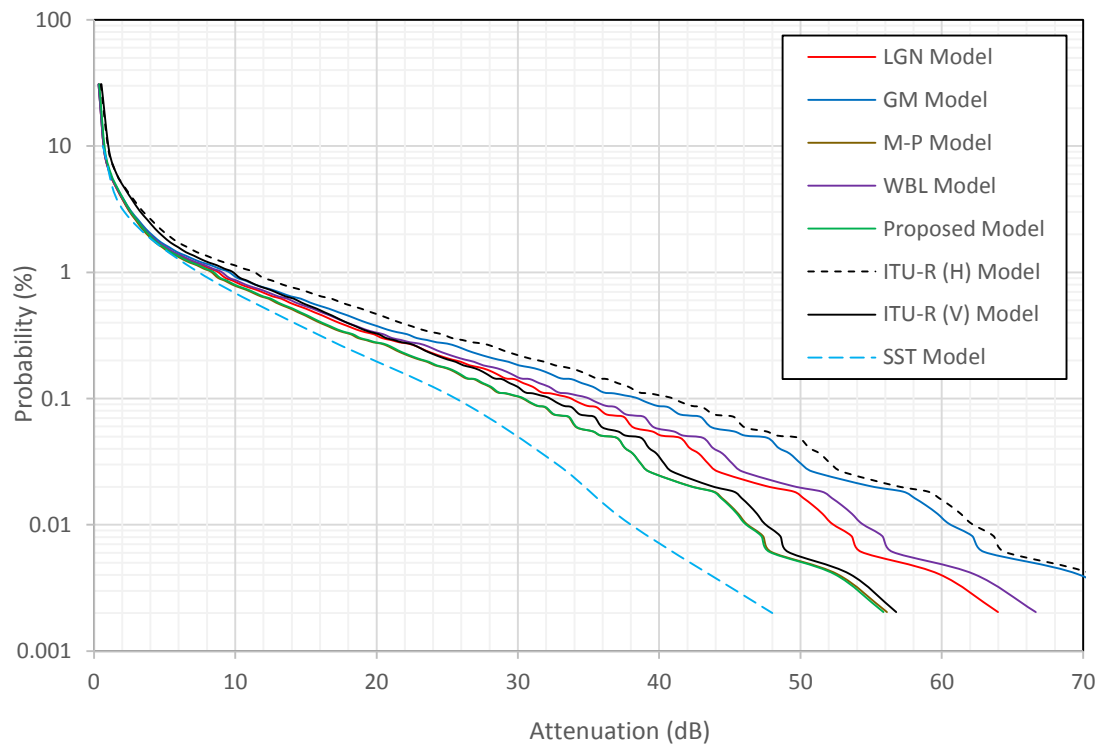


Figure 6-56: Comparison between synthesized rain attenuation converted by SST and other rain attenuation models at frequency  $f=19$  GHz and path length  $L=8$  km over Butare, Rwanda in 2015.

Figures 6-54 to 6-56 present the cumulative distribution of the rain attenuation using SST model and other rain attenuation models at 19 GHz and path lengths of 2 km, 5 km and 8 km, respectively. From the plots, it is again shown that the ITU-R (H) model gives highest attenuation while the SST model gives the lowest attenuation.

In Figure 6-54 at 19 GHz and path length of 2 km in 2015, the estimated rain attenuation exceedance values at 0.01% of the time (99.99% of link availability) are between 9.5 dB and 13.31 dB, where the SST model prediction gives 9.5 dB, while the other values are 11.19 dB, 12.97 dB, 9.90 dB, 11.64 dB, 9.87 dB, 13.30 dB, 10.17 dB for the Lognormal, Modified Gamma, Marshall-Palmer, Weibull, Proposed model, ITU-R (H) and ITU-R (V) models, respectively.

In Figure 6-55 at 19 GHz and path length of 1 km in 2015, the estimated model values for 99.99% link availability, the attenuation due to rain exceeded is between 22.17 dB and 35.49 dB, with SST model prediction giving 22.17 dB while we get 29.85 dB, 34.5 dB, 26.40 dB, 35.49 dB, 27.13 dB, 8.19 dB, 6.54 dB for Lognormal, Modified Gamma, Marshall-Palmer, Weibull, Proposed model, ITU-R (H) and ITU-R (V) models, respectively.

In Figure 6-56 at 19 GHz and path length of 8 km over Butare in 2015, the corresponding attenuation values for 99.99% of link availability are between 38 dB and 62.11 dB, with the SST model prediction giving 38 dB, while we have 52.24 dB, 60.51 dB, 46.18 dB, 54.36 dB, 46.08 dB, 62.11 dB, and 47.47 dB for the Lognormal, Modified Gamma, Marshall-Palmer, Weibull, Proposed model, ITU-R (H) and ITU-R (V) models, respectively.

## 6.6 Chapter Summary and Conclusion

In this chapter, the rainfall specific attenuation where obtained from various developed DSD models such as: Lognormal, Gamma, Marshall- Palmer, Weibull and the new proposed DSD models over Butare, Rwanda in the microwave and millimetre frequency band. The Short rainy season (mid-September to December) and the Long rainy season (March to the beginning of June) both give higher specific rain attenuation compared to two dry seasons at selected frequencies and their respective value of  $R_{0.01}$ . The lowest specific rain attenuation is recorded in the Long dry season. Comparing to other distribution models, both Lognormal and the new proposed model give a better prediction as the rainfall varies from drizzle, widespread to shower rainfall regime while later at high rainfall rate (thunderstorm regime), the new proposed model gives a better fit to the measurement and found to be an improvement over the existing models.

Using various developed drop size distribution models for Butare, the parameters ( $k$  and  $\alpha$ ) for the power law relationship between the rainfall specific attenuation and the rainfall rate have been

derived for frequency range between 2 GHz and 500 GHz. The derived values of  $k$  and  $\alpha$  are both presented in tabular as well as graphical format, and compared against the corresponding ITU-R P.838-3 parameters. Then, the derived parameters  $k$  and  $\alpha$  for each of the developed rain attenuation model have been applied in the prediction of rainfall attenuation on terrestrial line-of-sight links in the region of Central Africa.

Finally, for a given transmission frequency and propagation path length, the ITU-R and the SST models have been applied for comparison with other rainfall attenuation models in this region. It is found that the ITU-R (H) model gives the highest rain attenuation values while the SST model gives the lowest values of the rain attenuation compared to other models at different frequencies of transmission and path lengths. It is also found that, the SST method and the new proposed model for Butare are seen to provide closer results when comparing with other rain attenuation models.

In the next chapter, the conclusion of the study will be presented, together with recommendations for future work.

## **Chapter Seven**

### **Conclusions and Recommendations**

#### **7.1 Introduction**

This chapter presents brief outlines of the conclusions that can be drawn from the results presented in each of the previous chapters as well as some recommendations for applying the results and for further work to validate and expand the results presented.

#### **7.2. Chapter Three: Rainfall zoning and rain attenuation mapping for microwave and millimetric applications in Central Africa**

The results and analyses of rain measurements presented in this chapter from 60 locations in Rwanda clearly indicate that the traditional ITU-R methods of estimating rain intensity and attenuation statistics for system planning may amount to fairly serious underestimations.  $R_{0.01}$  estimates, which are extremely important, are shown to be much higher when obtained from 1-minute integration time conversions of the measured data. It is recommended that the contour maps presented in this chapter be utilized as a quick estimate of rainfall and rain attenuation parameters for all system planning in Rwanda and other Central African locations having similar Koppen weather classifications. The results presented in this chapter can be validated with further long-term measurements as well as measurements in the surrounding countries of Burundi, Democratic Republic of Congo, Uganda and Tanzania.

#### **7.3 Chapter Four: Comparison of Rainfall Drop-Size Distribution Models for Microwave and Millimetric radio propagation in Butare.**

From a few years of disdrometer measurements in Butare, Rwanda, the drop size distribution for various rain regimes was obtained and presented in this chapter. On extensive comparison with four well-established DSD models across four rain regimes, it can be concluded that the Marshall and Palmer (M-P) model is the only model that proved consistently unreliable for the location and/or region. The other models exhibit varying levels of fit at varying rain regimes. However, neither the Lognormal nor the Gamma DSD models – which are traditionally accepted as good fits for tropical rainfall – were consistent enough for modelling the higher rainfall rate regimes of shower and thunderstorm as captured in Butare. This suggests the need for a new model fitted for the region.

#### **7.4 Chapter Five: Proposed Rain Drop Size Distribution Model for Microwave and Millimeter Wave in Central Africa**

Using the method of maximum likelihood estimation, a new model for a DSD that best fits disdrometer data collected at Butare, Rwanda was developed and the parameters of the model are presented in this chapter. Error analysis as well as seasonal and annual comparisons with other models was carried out which showed that the proposed model is a slightly better representation of the rainfall DSD in the region than any of the earlier models. It can be concluded from the results that as rainfall rate increases, the proposed model will prove to be the best prediction model for DSD in Central Africa and other locations having similar climate and similar ranges of maximum rain rate. The Lognormal, Gamma and Weibull models give very mixed performances over the seasons and rain regimes while the proposed model gives a more consistent performance when compared to measured data.

#### **7.5 Chapter Six: Specific Rainfall Attenuation patterns over Butare, Rwanda**

Results of specific attenuation estimates by Mie Scattering method, which involves adopting a DSD model are presented in this chapter. The DSD model developed for the Butare data was used as well as other standard models. The results show conclusively that specific attenuation resulting from the proposed DSD model offers a greater fit to measured data than the other models and also performs slightly better than the ITU model for specific attenuation. In addition, the Synthetic Storm technique (SST) was also applied for estimating path attenuation and compared with the Mie Scattering results. The SST results and the results from the proposed DSD model both give better results than the other models.

#### **7.6 Recommendations for Future Work**

Further validation of the results presented in this thesis by applying long term data is recommended. An extensive deployment of rain measurement stations by disdrometer over Central Africa will be essential for such validation. Disdrometers offer higher accuracy than rain gauges and can be programmed to capture rain rate at one-minute integration time, making conversion between integration times unnecessary.

The wider region of Central Africa having climate similar to Rwanda will offer a more complete picture of actual DSD and attenuation modelling that fits the Central Africa equatorial region. Data from multiple locations in Uganda, Burundi, Tanzania and the Democratic Republic of Congo are essential for developing models that correctly represent the region.



## References

- [1] M.O. Fashuyi, P.A. Owolawi, T.J.O.Afullo, "Rainfall rate modelling for LOS radio systems in South Africa," *Transactions of the SAIEE*, Vol., 97, no. 1, pp. 74-81, March 2006.
- [2] S. P. Shih, "A study of prediction effect on tropospheric electromagnetic wave propagation at frequency 19.5 GHz," *Terr. Atmos. Ocean. Sei*, Vol. 19, no. 3, pp. 309-319, June 2008.
- [3] ITU-R, "Propagation Data and Prediction Methods Required for the Design of Terrestrial Line-of-Sight Systems," in *ITU-R P.530-16*, Geneva, 2015.
- [4] Q. Abbasi, M. Khan, S. Liaqat, M. Kamran, Y. Saleem, "A Novel Path loss Model for Angular and Spatial Dependency of Ultra Wideband Off-Body Radio Channels," *International Journal on Communications Antenna and Propagation (IRECAP)*, Vol. 3, no 4, pp. 206-209, 2013.
- [5] D. Čoko, I. Marinović, I., "Experimental Verification of a Deterministic UWB Channel Model for Single Room Propagation Scenarios," *International Journal on Communications Antenna and Propagation (IRECAP)*, Vol. 4, no. 2, pp. 37-43, 2004.
- [6] P. Elechi, P. Otasowie, "Comparison of Empirical Path Loss Propagation Models with Building Penetration Path Loss Model," *International Journal on Communications Antenna and Propagation (IRECAP)*, Vol. 6, no. 2, pp. 116-123, 2016.
- [7] A.A. Alonge, T.J. Afullo, "Rainfall Microstructural Analysis for Microwave Link Networks: Comparison at Equatorial and Subtropical Africa," *Progress in Electromagnetics Research B*, Vol. 59, pp. 45-58, 2014.
- [8] R. K. Crane, *Electromagnetic Wave Propagation through Rain*. John Wiley, New York, pp. 1-40, 1996.
- [9] S. J. Malinga, P. A. Owolawi, T.J.O.Afullo, "Estimation of Terrestrial Rain Attenuation at Microwave and Millimeter Wave Signals in South Africa Using the ITU-R Model," *PIERS Proceeding*, Kuala Lumpur, Malaysia, pp.952-962, March 27-30, 2012.
- [10] S. Malinga, P. Owolawi, T. Afullo, "Determination of Specific Rain Attenuation Using Different Total Cross Section Models for Southern Africa," *SAIEE Africa Research Journal*, Vol. 105, no. 1, pp.20-30, March 2014.
- [11] S. J. Malinga, P. A. Owolawi, T.J.O.Afullo, "Computation of Rain Attenuation through Scattering at Microwave and Millimeter Bands in South Africa," *Progress in Electromagnetics Research Symposium Proceedings*, Taipei, pp. 959- 971, March 25-28, 2013.
- [12] ITU-R, "Characteristics of Precipitation for propagation modelling," ITU-R P.837-6, vol.6, Geneva, 2012.
- [13] O. M. Fashuyi, "A Study of Rain Attenuation on Terrestrial Paths at Millimetric Wavelengths in South Africa," MSc. dissertation, University of KwaZulu-Natal, Durban, 2006.
- [14] M.O. Odedina, T.J. Afullo, "Seasonal Variation of Rain Attenuation on Radio Propagation Paths in South Africa," *Proceedings of the XXIX General Assembly of the International Union of Radio Science*, Chicago, Illinois, USA, 2008.

- [15] Y. S. Meng; Y. H. Lee, B. C. Ng, “Empirical Near Ground Path Loss Modeling in a Forest at VHF and UHF Bands,” *IEEE Transactions on antennas and propagation*, Vol. 57, no. 5, pp. 1461 – 1468, May 2009.
- [16] E. T.Salonen, J.P.V Poiares-Baptista, “A new global rainfall rate model, *proceeding of the 10th international conference on Antenna and propagation*,” Vol. 2, pp. 182-185, Pub N 14-174-436, April 1997.
- [17] K. L. Bashar, Mohammad, M. Rashid, “Performance Analysis of rain fades on Microwave Earth-to-Satellite links in Bangladesh,” *International Journal of Engineering and Technology*, Vol. 4 No. 7, pp. 430-432, July, UK 2014.
- [18] A. A. Alonge, T.J.O. Afullo, “Rainfall Microstructures for Microwave and Millimeter Wave link budget at Tropical and Subtropical sites,” *IEEE Africon*, Le Merdien-Ile Maurice, pp. 1-5, Mauritius ,09 Sep-12 Sep 2013.
- [19] P. A. Owolawi, “Characteristics of rain at microwave and millimetric bands for terrestrial and satellite links attenuation in South Africa and surrounding Islands,” PhD. Dissertation, in Electronic Engineering at the University of KwaZulu-Natal, Durban 2010.
- [20] ITU-R, “Characteristics of precipitation for propagation modelling,” *ITU-R P.837-1*, Geneva 2012.
- [21] R. K. Crane, *Electromagnetic Wave Propagation through Rain*. John Wiley, New York, pp. 1-40, 1996.
- [22] G.O Ajayi, S. Feng, S. M. Radicella, B. M. Reddy (Ed), *Handbook on Radiopropagation Related to Satellite communications in Tropical and Subtropical Countries (ICTP, Trieste, Italy 1996)*.
- [23] National Research Council. *Handbook of Frequency Allocations and Spectrum Protection for Scientific Uses*. National Academies Press, 2007.
- [24] A.A. Alonge, T.J. Afullo, “Rainfall time series synthesis from queue scheduling of rain event fractals over radio links,” *Radio Science*, Vol. 50. pp. 1209–1224, 2015
- [25] G. O. Ajayi, and R. L. Olsen, “Modelling of a raindrop size distribution for microwave and millimetre wave applications,” *Radio Science*, Vol. 20, No. 2, 193–202, 1985.
- [26] O. Adetan and T.J. Afullo, “Comparison of Two Methods to Evaluate the Lognormal Raindrop Size Distribution Model in Durban,” *In the Proceedings of the Southern Africa Telecommunications Networks Applications Conference, (SATNAC 2012)*, Fancourt, George, South Africa, September 2012.
- [27] Afullo, T. J. O., 2011, “Raindrop size distribution modelling for radio link design along the eastern coast of South Africa,” *Progress In Electromagnetics Research B*, Vol. 34, pp. 345-366.
- [28] M. O. Ajewole, M. O, “Scattering and attenuation of centimetre and millimeter radio signals by tropical rainfall,” Ph.D. Thesis, Dept. of Physics, Fed. Uni. of Tech., Akure, Nigeria, September 1997.

- [29] F. D. Diba, T. J. O. Afullo. and A.A. Alonge,” Rainfall rate and attenuation performance analysis at microwave and millimeter bands for the design of terrestrial line-of-sight radio links in Ethiopia,” *SAIEE Africa Research Journal*, Vol. 107, no. 3, pp. 177-186, 2016.
- [30] A.T.Adediji, M.O.Ajewole, S.E. Falodum and O.R. Oladosu. “Radio Refractivity Measurement at 150m altitude on TV tower in Akure, South-West Nigeria” *Journal of Engineering and Applied Science*, Nigeria 2007.
- [31] Willis, Michael; Bacon, David; Craig, Ken; Rudd, Richard; “ A wide Range Propagation Model,” *IEEE Conferences*, 2000, pp.1-5.
- [32] Yu Song Meng; Yee Hui Lee; Boon Chong Ng;” Empirical Near Ground Path Loss Modeling in a Forest at VHF and UHF Bands,” *IEEE Journals*, vol.57, no. 5,2009, pp. 1461 – 1468.
- [33] P.K. Odedina and T.J. Afullo, “Use of Spatial Interpolation Technique for the Determination of the Geo-climatic Factor and Fade Depth Calculation for Southern Africa,” *Proceedings of IEEE AFRICON conference*, September 26 – 28, 2007, Namibia.
- [34] T. Tjelta, R.L. Olsen and A.L Martin, “Systematic Development of New Multivariable Techniques for Predicting the Distribution of Multipath Fading on Terrestrial Microwave Links,” *IEEE Transactions on Antennas and Propagation*, Vol. 38, pp. 1650-1665 October 1990.
- [35] R.L. Olsen and T.Tjelta, “Worldwide Techniques for Predicting the Multipath Fading Distribution on Terrestrial L.O.S. Links: Background and Results of Tests,” *IEEE Transactions on Antennas and Propagation*, Vol. 47, January 1999, pp. 157-170.
- [36] R.L. Olsen and B. Segal, “New Techniques for Predicting the Multipath Fading Distribution on VHF/ UHF/SHF Terrestrial Line-of-Sight Links in Canada,” *Canada Journal of Elec. And Comp. Engineering*, Vol. 17, No 1. 1992, pp.11-23.
- [37] A. Martin, “Key Radio Meteorological Parameters for Designing Line of- Sight Links in Multipath Fading Environment,” *Martin Communications Pty Ltd, 87 Peters Av, Mulgrave VIC 3170*, Australia.
- [38] V. Antti, Räisänen and L. Arto, “Radio Engineering for Wireless Communication and Sensor Applications”, Artech House Inc., 2003.
- [39] G.P. Brasseur, John J. Orlordo and G.S Tyndall, *Atmospheric Chemistry and Global Change*, New York, Oxford University Press, 1999.
- [40] Trevor Manning, *Microwave Radio Transmission Design Guide*, 2nd edition, Artech House, Canton Street, 2009.
- [41] G. Barry and J. R. Chorly J.R.: *Atmosphere, Weather and Climate*, 5th Edition, Chapman and Hall Inc, New York, 1987.
- [42] M.P.M. Hall, L.W. Barclay and M.T Hewitt: *Propagation of Radio waves*, IEEE, London, United Kingdom, 1996.
- [43] P. Planter, *Communication Systems Design: Line-of-sight and Troposcatter Systems*. Mc. Graw-Hill Inc., New York, 1972.

- [44] Edward A.W., "Electronic communications technology", Prentice-hall, London, 1989.
- [45] A.S. Dabideen, M. Gopichund, and T.J. Afullo, "Radio Refractivity Distribution and Duct and Fading Occurrence Measurements In Kwazulu-Natal," *Transactions of South African Institute of Electrical Engineers (SAIEE)*, Vol. 96, no.2, pp121-132, June 2005.
- [46] E.Valma, M.Tmosiunarte, S.Tamosiunas, M. Zilinkas, "Variation of Radio refractivity with height above ground" *Electrical and Electronics Engineering*, 2011 N0 5(111).
- [47] ITU, "Propagation Data and Prediction Methods Required for the Design of Terrestrial Line of Sight Systems," ITU-R P. 530 –16; Geneva, July 2015.
- [48] D. Sumbiri, T. J. O. Afullo and A. Alonge, "Geoclimatic Factor estimation for Central Africa" Southern Africa Telecommunication Networks and Applications Conference (SATNAC) 2016, At Fancourt, George, South Africa.
- [49] M. O. Asiyoy and T. J. O. Afullo, "Statistical Estimation of Fade Depth and Outage Probability Due To Multipath Propagation in Southern Africa," *Progress In Electromagnetics Research B*, vol. 46, 2013.
- [50] Trevor Manning, "Microwave Radio Transmission Design Guide, Second Edition", Artech House, LONDON, 2009.
- [51] ITU-R, "The radio refractive index: its formula and refractivity data," in Recommendation ITU-R P.453 - 9, Windhoek, Namibia, 2009.
- [52] Gérard Barué,"*Microwave Engineering Land & Space Radiocommunications*", Canada, A JOHN WILEY & SONS, INC., PUBLICATION, 2008.
- [53] H. Sizun, "*Radio Wave Propagation for Telecommunication Applications*", New York, Springer-Verlag Berlin Heidelberg, 2005.
- [54] F. Dushimimana, "Effective earth radius distribution for Central Africa: Rwanda and north-western Tanzania," M.Sc. Thesis, National University of Rwanda, August 2012.
- [55] T.J. Afullo and P.K. Odedina, "On the k-factor distribution and diffraction fading for southern Africa", *Publication in SAIEE Transactions*, Vol. 97, no. 2, June 2006.
- [56] J. S. Ojo, M. O. Ajewole, "Rain rate and rain attenuation prediction for satellite communication in ku and ka bands over Nigeria", *Progress In Electromagnetics Research B*, Vol. 5, 2008.
- [57] R. Houze, "Stratiform precipitation in regions of convection: A meteorological paradox" *Bulletin of the American Meteorological Society*, vol. 78, no. 10, pp. 2179 –2196, 1997.
- [58] F. Moupfouma, "More about rainfall rates and their prediction for radio systems engineering," *IEE Proc.*, vol. 134, no. 6, pp. 527 – 537, 1987.
- [59] Rice, P.L. and N.R. Holmberg (1973), "Cumulative Time Statistics of Surface-Point Rainfall Rates," *IEEE Transactions on Communications*, Vol. COM-21, No. 10, 1131-1136.

- [60] E. J. Dutton and H.T. Dougherty, "A Second Modeling Approach to Year-to-Year Rainfall Variability in the U.S.A. for Microwave/Millimeter Wave Applications," *IEEE Trans. Comm.*, Vol. COM-32, no. 10, pp. 1145-1148, 1984.
- [61] E. J. Dutton, H.T. Dougherty and R.F. Martin, Jr. (1974), "Prediction of European Rainfall and Link Performance Coefficients at 8 to 30 GHz," Off. Telecom. , Dept. of Commerce, NTIS No. AD/A-000804, Springfield, Va.
- [62] F. Moupfouma, and S. Martins, "Modelling of the rainfall rate cumulative distribution for design of satellite and terrestrial communication systems," *International Journal of Satellite Communication*, Vol. 3, no. 2, pp. 105-115, 1995.
- [63] M.A Douglas and A.L Sims, "Climatology of Instantaneous Rainfall Rates," *J. of Applied Mateo*, Vol. 17, no. 8, pp. 1135-1140, 1978.
- [64] C. Ito and Y. Hosoya, "Worldwide 1 min Rain Rate Distribution Prediction Method which uses Thunderstorm Ratio as Regional Climatic Parameter," *Electronic Letters*, Vol.35, No.18, pp.1585-1587, September 1999.
- [65] R.K. Crane, "Evaluation of Global and CCIR models for estimation of rain rate statistics," *Radio Science*, Vol.20, No.4, pp. 865-879, 1985.
- [66] R. K. Crane, Propagation Handbook for Wireless Communication System Design. CRC Press, New York 1985.
- [67] R. K. Crane "Prediction of Attenuation by Rain," *IEEE Trans. Commun.*, Vol.28, no. 6, pp. 1717-1733, 1980
- [68] H. E. Landsburg, World Survey of Climatology, vol. 1-15. Amsterdam, The Netherlands: Elsevier,
- [69] S. Das, A. Maitra and A. K. Shukla, "Rain attenuation modelling in the 10-100 GHz frequency using drop size distributions for different climatic zones in Tropical India," *Progress In Electromagnetics Research B*, Vol. 25, pp. 211-224, 2010.
- [70] M. Marzuki, , W.L. Randeau, M. Schonhuber, V.N. Bringi, T. Kozu and T. Shimomai , "Raindrop size distribution parameters of disdrometer data with different bin sizes," *IEEE Trans., Geosci., Remote Sens*, vol. 48, pp. 3075-3080, 2010..
- [71] P. A. Owolawi: "Derivation of one-minute rain rate from five-minute equivalent for the calculation of rain attenuation in South Africa," *PIERS Online*, Vol.7, No.6, pp 524-535, 2011
- [72] J. S. Marshall and W. Palmer, "The distributions of raindrop with size," *Journal of Meteorology*, 5, pp. 165–166, 1948.
- [73] C. W Ulbrich, "Natural variation in the analytical form of the raindrop size distribution" *J. of Climate and Applied Meteor.*, vol. 23, pp. 1764–1775, 1983.
- [74] D. Atlas and C.W. Ulbrich, 'The physical basis for attenuation-rainfall relationships and the measurement of rainfall parameters by combined attenuation and radar methods,' *J. Rech. Atmos.*, vol. 8, pp. 275–298, 1974.

- [75] M. Sekine and G. Lind, "Rain attenuation of centimeter, millimeter and submillimeter radio waves," *Proc. of 12th European Microwave Conference*, pp. 584–589, 1982.
- [76] H. Jiang, M. Sano, and M. Sekine, "Weibull raindrop-size distribution and its application to rain attenuation," *IEE Proc. Microw. Antennas Propag.* Vol. 144, No. 3, 197-200, June 1997.
- [77] G. Feingold and Z. Levin, "The lognormal fit to raindrop spectra from frontal convective clouds in Israel," *J. Appl. Meteorol.*, vol. 25, pp. 1346–1364, 1986:
- [78] T. Kozu and K. Nakamura, "Rainfall parameter estimation from dual-radar measurements combining reflectivity profile and path-integrated attenuation," *J. of Atmos. and Oceanic tech.*, 259–270.1991.
- [79] T K.I imothy, J. T. Ong and E. B. I. Choo, "Raindrop size distribution using methods of moments for terrestrial and satellite communication applications in Singapore," *IEEE Transactions on Atennas and Propagation*, Vol. 50, No. 10, 140-1424, 2002.
- [80] I. Adimula and G. Ajayi, "Variation in raindrop size distribution and specific attenuation due to rain in nigeria," *Ann. Telecom*, vol. 51, no. 1 - 2, pp. 87–93, 1996.
- [81] O Adetan and TJ Afullo. "Three-parameter raindrop size distribution modeling for microwave propagation in South Africa". *Proceedings of the International Association of Science and Technology for Development (IASTED), International Conference on Modeling and Simulation (Africa MS 2012). 2012*, pp. 155-160.
- [82] L.S. Kumar and Y.H. Lee, "Shape Slope parameter distribution modelling for electromagnetic scattering by rain drops," *Progress In Electromagnetics Research B*, Vol. 25, pp. 191-209, 2010
- [83] C.H. Tseng, K.S. Chen and C.H. Chu, "Prediction of KA-band terrestrial rain attenuation using 2-year raindrop size distribution measurements in Northern Taiwan," *J. of Electromagn. Waves and Appl.*, vol. 19, No. 13, pp. 1833-1841, 2005.
- [84] G. J Zhang, J. Vivekanandan and E. Brandes, "A method of estimating rain rate and drop size distribution from polarimetric radar measurements." *IEEE Transactions on Geoscience and Remote Sensing Conference*, 2000.
- [85] A. A Alonge. and T. J. Afullo, "Seasonal analysis and prediction of rainfall effects in eastern South Africa at Microwave Frequencies," *Progress in Electromagnetics Research B*, Vol. 40, pp. 279-303, 2012.
- [86] M. L. Yakubu, Z. Yusop and F. Yusof, "The modelled raindrop size distribution of Skudai, Peninsular Malaysia, using exponential and lognormal distributions," *The Scientific World Journal*, Vol. 2014, pp. 1-7, 2014.
- [87] J. Joss, J. C. Thams, and A. Waldvogel (1968), the variation of raindrop size distribution at Locarno, in *Proc. Int. Conf. Cloud Physics*, pp. 369 – 373, Toronto, Canada,

- [88] O. Massambani and C.A.M. Rodriguez, "Specific attenuation as inferred from drop size distribution measurements in the tropics," *Proc. URSI Comm. F. Sym. on Regional Factors in predicting Radiowave Attenuation, Rio de Janeiro, Brazil*, pp. 25-28, 1990.
- [89] H. E. Green, "Propagation Impairment on Ka-Band SATCOM links in tropical and equatorial regions," *IEEE Antennas Propag. Magazine*, Vol. 46, no. 2, pp. 31-44, 2004.
- [90] M. Sekine, C. Chen, and T. Musha, "Rain attenuation from lognormal and Weibull raindrop-size distribution," *IEEE Trans. Antennas Propag.*, Vol. 35, No. 3, pp.358-359, March 1987.
- [91] A. A. Alonge. and T. J. Afullo. "Rainfall Drop-Size Estimators for Weibull Probability distribution using Method of Moments Technique," *African Research Journal of SAIEE* 103, no. 2 (2012): 83-93.
- [92] ITU-R, "Specific attenuation model for rain for use in prediction methods," ITU-R P.838-3, Geneva, 1992 - 1999 - 2003 - 2005.
- [93] Freeman, R. L., (2007): *Radio System Design for Telecommunications*, John Wiley and Sons, New York.
- [94] R. L Olsen, D.V. Rogers, D.B. Hodge 1978: 'The aRb Relation in the calculation of rain attenuation,' *IEEE Trans. Antennas Propag.*, 26(2), 1978, pp. 547-556, 1978.
- [95] Rwanda Environment Management Authority (REMA), *Rwanda state of Environment and outlook* (2009 Kigali-Rwanda)
- [96] P.Sirven, J. F. Gontanegre, C. Prioul, *Géographie du Rwanda. (Editions A. DeBoeck, Brussels, Belgium1974)*
- [97] M.C. Peel,B.L. Finlayson, M. Mahon, Updated World Map of the Köppen- Geiger climate classification, *Hydrology and Earth Systems Science Discussions, European Geosciences Union, Vol.11.No 5, 2007.Pages 1633–1644*
- [98] Climate: Rwanda (<http://en.climate-data.org/country/92/>), March, 2016.
- [99] Chebil, J. and T. A. Rahman, "Development of one-minute rain rate contour maps for microwave applications in Malaysia Peninsula," *Electronics Letters*, Vol. 35, No. 20, 30 September, 1999.
- [100] F. Moupfouma and L. Martin, "Modelling of rainfall rate cumulative distribution for the design of satellite and terrestrial communication systems," *International Journal for Satellite Communication*, Vol. 13, 105–115, 1995.
- [101] ITU-R 838-2, Specific Attenuation Model for Rain for Use in Prediction Models, Vol.2003, P Series, *International Telecommunication Union*, Geneva, Switzerland, 2003.
- [102] P. O. Akuon, T. J. O. Afullo, Rain cell sizing for the design of high Capacity radio link systems in South Africa, *Progress in Electromagnetics Research B, Vol. 35, 2011. Pages 263-285.*
- [103] Distromet Ltd., Distrometer RD-80 instructional manual, Basel, Switzerland, June 20, 2002.

- [104] A. Tokay, A. Kruger, and W. F. Krajewski, "Comparison of drop size distribution measurements by impact and optical disdrometer," *Journal of Applied Meteorology*, vol. 40, pp. 2083-2097, 2001.
- [105] I. Adimula and G. Ajayi, "Variations in raindrop size distribution and specific attenuation due to rain in Nigeria," in *Annales des télécommunications*, pp. 87-93, 1996.
- [106] K. I. Timothy, J. T. Ong, and E. B. Choo, "Raindrop size distribution using method of moments for terrestrial and satellite communication applications in Singapore," *Antennas and Propagation, IEEE Transactions on*, vol. 50, pp. 1420-1424, 2002.
- [107] G.O. Ajayi and A. Adimula, "Variations in raindrop size distribution and specific attenuation in a tropical environment," *URSI Comm. F Symposium, La Londe-less Maures, France*, pp. 811-814, September 1989.
- [108] O. Fiser, M. Schoenhuber, and P. Pesice, "First results of DSD measurement by video distrometer in the Czech Republic in 1998–1999," *Studia Geophysica et Geodetica*, 46, 3, 485–505, 2002.
- [109] J.S. Mandeep and K. Tanaka; "Effect of atmospheric parameters on satellite links," *Int. Journal Millimeter wave*, 2007, 28(10), pp. 789-795.
- [110] L.S. Kumar, Y.H. Lee, J.X. Yeo and J.T. Ong., "Tropical rain classification and estimation of rain from Z-R (Reflectivity-rain rate) relationships," *PIER B*, Vol.32, 107-127, 2011.
- [111] Bartholomew, M. J. (2009): *Disdrometer and tipping bucket rain gauge handbook*, DOE/SC-ARM/TR-079, ARM Climate Research Facility.
- [112] S. K. Laskshmi, Y. H. Lee and J. T. Ong "Truncated gamma drop size distribution models for rain attenuation in Singapore," *IEEE Trans Antennas Propag (USA)*, 58 (4), pp. 1325-1335, 2010
- [113] A. A. Alonge and T. J. Afullo, "Estimation of parameters for lognormal rainfall DSD model for various rainfall types in Durban" *Proc. of SATNAC Conf. 2011*, East London, South Africa, September 2011.
- [114] P. A. Owolawi, "Raindrop size distribution model for the prediction of rain attenuation in Durban," *PIERS Online*, Vol. 7, No. 6, 516-523, 2011.
- [115] K. Pearson, "Skew Variation in homogeneous material," *Philosophical Trans., of the Royal Soc, of London*, 186, series A, pp.414-895, 1895.
- [116] L. R Shenton. "Moment estimators and maximum likelihood". *Biometrika*, 45:411–420, 1958.
- [117] C. A Robertson and J G Fryer. "The bias and accuracy of moment estimators". *Biometrika*, 57:57–65, 1970.
- [118] D. Kliche, P. Smith, and R. W. Johnson. L-moment estimators as applied to gamma drop size distributions. *33rd Conf. on Radar Meteorology*, P8A.15, 2007.
- [119] J. Vivekanandan, G. Zhang, and E. Brandes, "Polarimetric radar rain estimators based on



- constrained gamma drop size distribution model," *J. Appl. Meteorology*, Vol. 43, No. 2, 217-230, 2004.
- [120] R. Gunn and G. D. Kinzer, "The terminal velocity of fall for water droplets in stagnant air," *Journal of Meteorology*, vol. 6, pp. 243-248, 1949.
- [121] D. N. Murthy, M. Xie, and R. Jiang, *Weibull Models*, 50-58, 68-74, John Wiley and Sons Inc., New York, 2004.
- [122] G. Casella and R. L. Berger, *Statistical inference* vol. 2: Duxbury Pacific Grove, CA, 2002.
- [123] R. A. Fisher, "On the mathematical foundations of theoretical statistics," *Philosophical Transactions of the Royal Society of London. Series A*, vol. 222, pp. 309-368, 1922.
- [124] UNEP (2011). Rwanda from Post-Conflict to Environmentally Sustainable Development. Kigali-Rwanda. Nairobi: UNEP
- [125] M. Odedina and T. Afullo, "Determination of rain attenuation from electromagnetic scattering by spherical raindrops: Theory and experiment," *Radio Science*, vol. 45, 2010.
- [126] A. Maitra, S. Das, and A. K. Shukla, "Joint statistics of rain rate and event duration for a tropical in India," *Indian Journal of Radio & Space Physics*, Vol.38, No.6, 353-360, December 2009.
- [127] S. J. Malinga and P. A. Owolawi, "Obtaining raindrop size model using the method of moments and its applications for South African radio systems," *PIER B Journal*, Vol. 46, pp. 119-138, 2013.
- [128] T.S. Yeo, P.S. Kooi, M.S. Leong, and L.W. Li, "Tropical raindrop size distribution for the prediction of rain attenuation of microwaves in the 10-40 GHz band," *IEEE Transactions on Antennas and Propagation*, Vol.49, No.1, 80-82, January 2001.
- [129] M.N.O. Sadiku, (2000): *Numerical Techniques in Electromagnetics*, 2nd edition, CRC press, pp. 96–103.
- [130] Van de Hulst, H. C (1957), *Light scattering by Small Particles*, John Wiley & Sons, New York.
- [131] D. Deirmendjian, R. Clasen, and W. Viezee, "Mie scattering with complex index of refraction," *JOSA*, vol. 51, pp. 620-633, 1961.
- [132] C.T Mulangu. and T.J. Afullo 2009: "Variability of the propagation coefficients for microwave links in Southern Africa," *Radio Sci.*, Vol. 44, no. 3, 2009.
- [133] C. F. Bohren and D.R. Huffman (2004): *Absorption and scattering of light particles*, Wienheim: John Wiley.
- [134] C. Mätzler, "MATLAB functions for Mie scattering and absorption," *IAP Res. Rep.* 2002-8, Univ of Bern, Bern, June 2002.
- [135] H. J. Weber and G.B. Arfken, "Essential Mathematical Methods for Physicists", *Academic Press, San Diego*, pp. 523–544, 2003.

- [136] H.J. Liebe, G. A. Hufford, and M. G. Cotton, "Propagation Modelling of Moist Air and Suspended Water/Ice particles at frequencies below 1000 GHz", on Atmospheric Propagation Effects through Natural and Man-made obscurants for Visible to MM-Wave Radiation, May, 1993.
- [137] J. D. Munyeshyaka, *Assessing the Socio-economic Vulnerability of Smallholder Farmers to Climate Variability in Rwanda: Case Study of Rice Farmers in Bugesera District*, MSc. Dissertation, in Geo-Information for Environment and Sustainable Development at the University of Rwanda, Butare 2016.
- [138] ITU-R, "Specific attenuation model for rain for use in prediction methods," ITU-R P.838-3, Geneva, 1992 - 1999 - 2003 – 2005.
- [139] L. da Silva Mello and M.S. Pontes., "Unified method for the prediction of rain attenuation in satellite and terrestrial links," *Journal of Microwaves, Optoelectronics and Electromagnetic Applications*, Vol.11, No.1, June 2012.
- [140] E. Bertok, G. D. Renzis, G. Drufulca G, "Estimate of attenuation due to rain at 11-GHz from rain gauge data, URSI Commission F Open Symposium," La Baule, 1997, pp. 295–300.
- [141] G. Drufulca, "Rain attenuation statistics for frequencies above 10-GHz from rain gauge observations", *J. Res. Atmosphere*, 8(1), p.2., 1974 , pp. 399–411
- [142] E. Matricciani, "Physical-mathematical model of the dynamics of rain attenuation based on rate time series and a two-layer vertical structure of precipitation", *Radio Sci.*, Vol. 31, no. 2, pp. 281–295, 1996.
- [143] A. K. Lwas, Md R Islam, J Chebil, M H Habaebi, A F Ismael, A Zyoud and H Dao, "Rain attenuation analysis using Synthetic Storm Technique in Malesysia" *In IOP Conference Series: Materials Science and Engineering*, Vol. 53, No. 1, p. 012045, 2013.
- [144] J.S. Mandeep, "Rain attenuation statistics over a terrestrial link at 32.6 GHz at Malaysia" *IET microwaves, antennas & propagation*, Vol. 3, no. 7, pp. 1086-1093. 2009

## Appendices

### Appendix B-1:

Table B-1: ITU-R Parameters ( $k$  and  $\alpha$ ) for rainfall specific Attenuation Estimation [91]

Frequency (GHz)	$k_H$	$\alpha_H$	$k_V$	$\alpha_V$
1	0.0000259	0.9691	0.0000308	0.9691
1.5	0.0000443	1.0185	0.0000574	1.0185
2	0.0000847	1.0664	0.0000998	1.0664
2.5	0.0001321	1.1209	0.0001464	1.1209
3	0.000139	1.2322	0.0001942	1.2322
3.5	0.0001155	1.4189	0.0002346	1.4189
4	0.0001071	1.6009	0.0002461	1.6009
4.5	0.000134	1.6948	0.0002347	1.6948
5	0.0002162	1.6969	0.0002428	1.6969
5.5	0.0003909	1.6499	0.0003115	1.6499
6	0.0007056	1.59	0.0004878	1.59
7	0.001915	1.481	0.001425	1.481
8	0.004115	1.3905	0.00345	1.3905
9	0.007535	1.3155	0.006691	1.3155
10	0.01217	1.2571	0.01129	1.2571
11	0.01772	1.214	0.01731	1.214
12	0.02386	1.1825	0.02455	1.1825
13	0.03041	1.1586	0.03266	1.1586
14	0.03738	1.1396	0.04126	1.1396
15	0.04481	1.1233	0.05008	1.1233
16	0.05282	1.1086	0.05899	1.1086
17	0.06146	1.0949	0.06797	1.0949
18	0.07078	1.0818	0.07708	1.0818
19	0.08084	1.0691	0.08642	1.0691
20	0.09164	1.0568	0.09611	1.0568
21	0.1032	1.0447	0.1063	1.0447
22	0.1155	1.0329	0.117	1.0329
23	0.1286	1.0214	0.1284	1.0214
24	0.1425	1.0101	0.1404	1.0101
25	0.1571	0.9991	0.1533	0.9991
26	0.1724	0.9884	0.1669	0.9884
27	0.1884	0.978	0.1813	0.978
28	0.2051	0.9679	0.1964	0.9679
29	0.2224	0.958	0.2124	0.958
30	0.2403	0.9485	0.2291	0.9485
31	0.2588	0.9392	0.2465	0.9392
32	0.2778	0.9302	0.2646	0.9302
33	0.2972	0.9214	0.2833	0.9214

Table B-1 Cont'd

Frequency (GHz)	$k_H$	$\alpha_H$	$k_V$	$\alpha_V$
34	0.3171	0.9129	0.3026	0.9129
35	0.3374	0.9047	0.3224	0.9047
36	0.358	0.8967	0.3427	0.8967
37	0.3789	0.889	0.3633	0.889
38	0.4001	0.8816	0.3844	0.8816
39	0.4215	0.8743	0.4058	0.8743
40	0.4431	0.8673	0.4274	0.8673
41	0.4647	0.8605	0.4492	0.8605
42	0.4865	0.8539	0.4712	0.8539
43	0.5084	0.8476	0.4932	0.8476
44	0.5302	0.8414	0.5153	0.8414
45	0.5521	0.8355	0.5375	0.8355
46	0.5738	0.8297	0.5596	0.8297
47	0.5956	0.8241	0.5817	0.8241
48	0.6172	0.8187	0.6037	0.8187
49	0.6386	0.8134	0.6255	0.8134
50	0.66	0.8084	0.6472	0.8084
51	0.6811	0.8034	0.6687	0.8034
52	0.702	0.7987	0.6901	0.7987
53	0.7228	0.7941	0.7112	0.7941
54	0.7433	0.7896	0.7321	0.7896
55	0.7635	0.7853	0.7527	0.7853
56	0.7835	0.7811	0.773	0.7811
57	0.8032	0.7771	0.7931	0.7771
58	0.8226	0.7731	0.8129	0.7731
59	0.8418	0.7693	0.8324	0.7693
60	0.8606	0.7656	0.8515	0.7656
61	0.8791	0.7621	0.8704	0.7621
62	0.8974	0.7586	0.8889	0.7586
63	0.9153	0.7552	0.9071	0.7552
64	0.9328	0.752	0.925	0.752
65	0.9501	0.7488	0.9425	0.7488
66	0.967	0.7458	0.9598	0.7458
67	0.9836	0.7428	0.9767	0.7428
68	0.9999	0.74	0.9932	0.74
69	1.0159	0.7372	1.0094	0.7372
70	1.0315	0.7345	1.0253	0.7345
71	1.0468	0.7318	1.0409	0.7318
72	1.0618	0.7293	1.0561	0.7293
73	1.0764	0.7268	1.0711	0.7268
74	1.0908	0.7244	1.0857	0.7244
75	1.1048	0.7221	1.1	0.7221

Table B-1 Cont'd

Frequency (GHz)	$k_H$	$\alpha_H$	$k_V$	$\alpha_V$
76	1.1185	0.7199	1.1139	0.7199
77	1.132	0.7177	1.1276	0.7177
78	1.1451	0.7156	1.141	0.7156
79	1.1579	0.7135	1.1541	0.7135
80	1.1704	0.7115	1.1668	0.7115
81	1.1827	0.7096	1.1793	0.7096
82	1.1946	0.7077	1.1915	0.7077
83	1.2063	0.7058	1.2034	0.7058
84	1.2177	0.704	1.2151	0.704
85	1.2289	0.7023	1.2265	0.7023
86	1.2398	0.7006	1.2376	0.7006
87	1.2504	0.699	1.2484	0.699
88	1.2607	0.6974	1.259	0.6974
89	1.2708	0.6959	1.2694	0.6959
90	1.2807	0.6944	1.2795	0.6944
91	1.2903	0.6929	1.2893	0.6929
92	1.2997	0.6915	1.2989	0.6915
93	1.3089	0.6901	1.3083	0.6901
94	1.3179	0.6888	1.3175	0.6888
95	1.3266	0.6875	1.3265	0.6875
96	1.3351	0.6862	1.3352	0.6862
97	1.3434	0.685	1.3437	0.685
98	1.3515	0.6838	1.352	0.6838
99	1.3594	0.6826	1.3601	0.6826
100	1.3671	0.6815	1.368	0.6815
120	1.4866	0.664	1.4911	0.664
150	1.5823	0.6494	1.5896	0.6494
200	1.6378	0.6382	1.6443	0.6382
300	1.6286	0.6296	1.6286	0.6296
400	1.586	0.6262	1.582	0.6262
500	1.5418	0.6253	1.5366	0.6253
600	1.5013	0.6262	1.4967	0.6262
700	1.4654	0.6284	1.4622	0.6284
800	1.4335	0.6315	1.4321	0.6315
900	1.405	0.6353	1.4056	0.6353
1 000	1.3795	0.6396	1.3822	0.6396

## Appendix C-1:

Table C-1 Estimated specific attenuation at  $R_{0.01}$  for Ka and Ku bands for all the 60 locations over Rwanda

Province	Station Name	$R_{0.01}$ (mm/h)	Rain Specific attenuation(dB/Km)			
			Vertical Polarization		Horizontal Polarization	
			15GHz	27GHz	15GHz	27GHz
South	Butare airport	102.5	6.3	13.7	8.1	17.4
	Kansi	100.1	6.1	13.4	7.9	17
	Nyamiyaga	98.2	6	13.2	7.7	16.7
	Nyakibanda	101.4	6.2	13.6	8	17.3
	Rubona	100.5	6.1	13.5	7.9	17.1
	Save	98.3	6	13.2	7.8	16.7
	Nyamabuye	97	5.9	13.1	7.6	16.5
	Byimana	102.2	6.3	13.7	8.1	17.4
	Cyeru	97	5.9	13.1	7.6	16.5
	Kanyanza	101.6	6.2	13.6	8.1	17.3
	Gitwe	93.4	5.7	12.6	7.3	15.9
	Kayenzi	98.3	6	13.2	7.8	16.7
	Gikongoro	104.9	6.4	14	8.3	17.8
	Cyanika	104.3	6.4	13.9	8.2	17.7
	Kaduha	105.8	6.5	14.2	8.4	18
North	Kibeho	103.7	6.4	13.9	8.2	17.6
	Kinigi	109.9	6.8	14.7	8.8	18.7
	Ruhengeri airport	104.3	6.4	14	8.3	17.7
	Rwaza	103.3	6.3	13.8	8.2	17.6
	Rwerere	101.5	6.2	13.6	8	17.3
	Byumba	103.4	6.3	13.9	8.2	17.6
	Ruhunde	103.7	6.4	13.9	8.2	17.6
	Rulindo	102.1	6.3	13.7	8.1	17.4
Rutongo	99.8	6.1	13.4	7.9	17	
	murindi	100.1	6.1	13.4	7.9	17

Table C-1 Cont'd

Province	Station Name	R <sub>0.01</sub> (mm/h)	Rain Specific attenuation(dB/Km)			
			Vertical Polarization		Horizontal Polarization	
			15GHz	27GHz	15GHz	27GHz
West	Kamembe airport	106.5	6.6	14.2	8.5	18.1
	Bugarama	100	6.1	13.4	7.9	17.1
	Cyangugu	106.1	6.5	14.2	8.5	18
	Mibirizi	108.2	6.7	14.5	8.6	18.4
	Nyamasheke	104.8	6.4	14	8.3	17.8
	Nyakabuye	104.2	6.4	14	8.3	17.7
	Rubengera	101.1	6.2	13.6	8	17.2
	Kirambo	101.2	6.2	13.6	8	17.2
	Kilinda	103.8	6.4	13.9	8.2	17.7
	Mubuga	105.3	6.5	14.1	8.4	17.9
	Mugonero	105.1	6.5	14.1	8.4	17.9
	Murunda	104.6	6.4	14	8.3	17.8
	Wisumo	109.6	6.7	14.6	8.8	18.6
	Rwankeri	102.7	6.3	13.7	8.1	17.5
	Nyange	105	6.5	14.1	8.3	17.8
	Gisenyi	99.5	6.1	13.4	7.9	17.8
	Kabaya	105	6.5	14.1	8.3	17.8
	Muramba	105.2	6.5	14.1	8.4	17.9
Gatumba	102.9	6.3	13.8	8.1	17.5	
East	Kibungo	95.4	5.8	12.8	7.9	16.3
	Gahororo	99.9	6.1	13.4	7.9	17
	Rukira	96	5.9	12.9	7.5	16.4
	Rusumo	93.1	5.7	12.6	7.2	15.9
	Rwamagana	95.3	5.8	12.8	7.5	16.2
	Zaza	98.3	6	13.2	7.8	16.7
	Rwinkwavu	91.1	5.6	12.3	7.1	15.5
	Nyarubuye	89.2	5.4	12.1	7	15.2
	Gabiro	91.1	5.6	12.3	7.1	15.5
	Kagitumba	89.5	5.5	12.1	7	15.3
	Karama	90.9	5.5	12.3	7.1	15.5
	Kiziguro	93	5.7	12.6	7.2	15.9
Nyamata	98.4	6	13.2	7.8	16.8	
Kigali	Kigali airport	96.1	5.9	12.9	7.5	16.4
	Gikoro	95.2	5.8	12.8	7.5	16.2
	Masaka	95.7	5.9	13	7.5	16.3